

## ABSTRACT

KAPOOR, ASHISH. Fiber-based Sensors for Electronic Textiles. (Under the direction of Dr. Tushar K. Ghosh).

Electronic textiles are textiles integrated with electrical functionalities like sensing, actuation and energy harvesting. Wearable e-textiles with sensing functionality have recently attracted a lot of scientific and commercial interest because of their uses in healthcare, security systems and other areas. Electronic sensing capabilities can be integrated into textiles at fiber, yarn, or fabric level but unobtrusive integration of sensing capabilities while preserving all desirable textile qualities like comfort and flexibility requires introduction of desired electrical characteristics at the fiber level. In this research, I have demonstrated a transformative sensing technology through the design of a multimodal and multifunctional woven sensor array by employing dumbbell shaped bicomponent fibers consisting of insulating and electrically conducting segments. Each cross-over point in the woven fabric structure acts as a sensing pixel. These fibers have been fabricated using sequential extrusion printing method and coextrusion method. The insulating segments are made using an ultraviolet (UV) curable poly(dimethyl siloxane) (PDMS) while the conducting segments are made from a conducting polymer composite (CPC) containing PDMS and carbon black (CB). The multimodal characteristic of the sensors is demonstrated through the measurement of capacitive and resistive response while multifunctional capabilities were explored by measuring tactile (normal force), tensile, and shear deformations, as well as wetness and biopotential (heart rate). As a potential biomedical application, these fiber based sensing arrays were integrated into prosthesis socket to monitor pressure within inner socket environment of lower limb amputees. Also, a large channel sensor array was fabricated and its potential for contactless sensing of gestures was demonstrated as a potential textile-based human-machine interface. Although this dimensionally scaled-up elastomeric fiber poses challenges for textile fabrication using

conventional fabric formation techniques, this fiber based sensing approach can be used for scalable manufacturability of advanced e-textile products.

© Copyright 2020 by Ashish Kapoor

All Rights Reserved

Fiber-based Sensors for Electronic Textiles

by  
Ashish Kapoor

A dissertation submitted to the Graduate Faculty of  
North Carolina State University  
in partial fulfillment of the  
requirements for the degree of  
Doctor of Philosophy

Fiber and Polymer Science

Raleigh, North Carolina  
2020

APPROVED BY:

---

Dr. Tushar K. Ghosh  
Committee Chair

---

Dr. Alper Bozkurt

---

Dr. Ericka Ford

---

Dr. Xiangwu Zhang

## **DEDICATION**

To my parents Mr. Narinder Kapoor and Mrs. Urvashi and my brother Aayush Kapoor  
along with my teachers.

## **BIOGRAPHY**

Ashish Kapoor received his Bachelor's degree in Textile Engineering in 2013 from Jawaharlal Nehru Government Engineering College, India followed by Master's degree in Textile Engineering from Indian Institute of Technology Delhi, India in 2015. He joined the Fiber and Polymer Science Ph.D. program at Wilson College of Textiles, North Carolina State University in August 2015 and started working under the direction of Dr. Tushar K. Ghosh in the field of electronic textiles. He worked towards the development of fiber based multimodal and multifunctional active sensory textiles. He received the NC State University's Provost Doctoral Recruitment Fellowship for 2015-16, DAAD (German Academic Exchange Service) RISE Professional Scholarship in 2018 and NC State University's Graduate School Summer Fellowship in 2019. Upon completion of PhD, he will be joining Intel in Hillsboro, Oregon as TD Etch Module Engineer.

## ACKNOWLEDGMENTS

I would like to thank my advisor Dr. Tushar Ghosh for giving me the opportunity to work in the growing field of electronic textiles and inspiring me do quality research work so that I can make valuable contribution to the overall body of knowledge in this field.

I would like to thank Dr. Alper Bozkurt for serving as a Graduate School Representative on my committee and for his insights on electrical characterization of sensors and support at every step in the degree program. I also extend my thanks to Dr. Helen Huang for providing useful suggestions in navigating the experiments with prosthetics and supporting my efforts in this regard. I would also like to thank Dr. Ericka Ford and Dr. Xiangwu Zhang for serving on my committee and for their suggestions on improving my work.

I would like to thank my Textile research teammates, Kony and Jordan. Kony helped in assembling the extrusion printing setup and created the extrusion die design which were significant tasks for the progress of my research work. I would like to thank Jordan for helping with the initial coextrusion experiments. I would like to thank the ECE teammates, Michael and Talha without whom this research would not have been possible. Michael helped in developing methods for testing sensing response of fibers and Talha fabricated the printed circuit boards and algorithms for data collection for various experiments. I would also like to thank Hannah for helping with experiments with extrusion printed fibers and Brendan for his help in data collection and plotting of prosthetic experiments. I would like to thank Aaron for setting up the artificial limb test bench and his support in executing prosthetic experiments. I would also like to thank Dr. Ming Liu for his support in prosthetic experiments. I thank Judy Elson for helping with the optical microscopy of fibers and Dr. Philip Bradford for allowing to use the laser cutting machine. I am thankful to

Dr. Shannon Madden for her support in revisions and overall support during the writing process and Parth Chansoria for helping with creating designs on SolidWorks.

I would like to thank my past and current lab-mates; Xiaomeng, Kony, Shuzhen, Jordan and Aaloka for their support at every step. I am also grateful to the funders who supported my PhD work namely the Provost Fellowship, NSF and Graduate School Summer Fellowship. I would also like to thank Dr. John Rust, Dr. Andre West and Dr. Kavita Mathur for supporting me in my final years of PhD as without their support this journey would not have been possible.

Lastly, I express sincere thanks to my wonderful parents and lovely brother who always encouraged, inspired and supported me throughout this process.

## TABLE OF CONTENTS

LIST OF TABLES .....	viii
LIST OF FIGURES .....	ix
<b>Chapter 1: Introduction .....</b>	<b>1</b>
<b>Chapter 2: Textile-based Sensors: A Critical Review .....</b>	<b>5</b>
2.1 Introduction .....	5
2.2 Sensing Mechanisms and Performance Characteristics .....	8
2.3 Materials .....	24
2.4 Applications of E-textile Sensors .....	29
2.5 Summary and outlook .....	47
<b>Chapter 3: Extrusion printed multimodal and multifunctional sensors .....</b>	<b>64</b>
3.1 Abstract .....	64
3.2 Introduction .....	64
3.3 Materials and Methods .....	73
3.4 Results and Discussion .....	76
3.4.1 Electromechanical characterization.....	76
3.4.2 Sensory response .....	77
3.5 Conclusion.....	85
<b>Chapter 4: Fabrication of Multimodal Fiber-based Sensors via Coextrusion: A Microfluidics-Inspired Approach.....</b>	<b>91</b>
4.1 Introduction .....	91
4.2 Materials and Methods .....	92
4.3 Results and Discussion.....	100
4.4 Conclusion.....	110
<b>Chapter 5: Prosthetic Environment Monitoring using Fiber Sensor arrays .....</b>	<b>116</b>
5.1 Introduction .....	116
5.2 Materials and Methods .....	118
5.2.1 Fabrication.....	118
5.2.2 Electromechanical characterization.....	121
5.2.3 Prosthetic environment monitoring.....	122
5.3 Results and Discussion.....	128

5.3.1 Sensor array fabrication.....	128
5.3.2 Benchtop characterization of normal force-capacitance response .....	130
5.3.3 Artificial limb testing .....	133
5.3.4 Able-bodied testing .....	134
5.3.5 Human subject testing .....	137
5.4 Conclusion.....	140
5.5 Supplementary information.....	141
<b>Chapter 6: Woven Fiber-based Sensor Array for Contactless Sensing.....</b>	<b>145</b>
6.1 Introduction .....	145
6.2 Results and Discussion.....	147
6.2.1 Fabrication.....	147
6.2.2 Benchtop sensor characterization.....	150
6.2.3 Gesture recognition .....	155
6.3 Conclusion.....	166
6.4 Supplementary information.....	167
<b>Chapter 7: Summary and Future work.....</b>	<b>172</b>

## LIST OF TABLES

<b>Table 1</b>	Summary of sensor performance metrics of stretchable strain sensors.....	21
<b>Table 2</b>	Properties of PDMS used for insulating and conducting segments fabrication .....	93
<b>Table 3</b>	Dimensions of dumbbell shaped orifice of extrusion channels.....	95
<b>Table 4</b>	Optimized coextrusion process parameters .....	100
<b>Table 5</b>	Comparison of fiber dimensions .....	101
<b>Table 6</b>	Selected locations for placing sensors in artificial limb.....	123

## LIST OF FIGURES

<b>Figure 1</b>	(a) Remote health monitoring system based on sensors integrated in textiles and (b) Use of sensors collected big data for personalized and preventive healthcare ....	7
<b>Figure 2</b>	Classification of sensors .....	9
<b>Figure 3</b>	Resistor with current flowing along length .....	10
<b>Figure 4</b>	Configuration of a parallel plate capacitor .....	12
<b>Figure 5</b>	Surface capacitance based touch sensor .....	13
<b>Figure 6</b>	Self capacitance sensing principle: untouched sensor pad with parasitic capacitance $C_0$ , touched sensor pad with additional touch capacitance $C_T$ .....	14
<b>Figure 7</b>	Mutual capacitance between two electrodes .....	14
<b>Figure 8</b>	Schematic of occurrence of electric dipole moments in response to mechanical force, $F$ in a piezoelectric material .....	16
<b>Figure 9</b>	FBG structure showing incident, transmitted and reflected optical spectra .....	17
<b>Figure 10</b>	Macrobending sensor implemented on a stretchable substrate .....	18
<b>Figure 11</b>	Working of inductive sensor .....	19
<b>Figure 12</b>	(a) Hysteresis curve and (b) Hysteresis in electrical resistance change as a function of strain change from 0%–200%–0% .....	23
<b>Figure 13</b>	Ranges of conductivity .....	25
<b>Figure 14</b>	Conductive filler fraction dependence on conductivity of a composite .....	27
<b>Figure 15</b>	Capacitive fibers: (a) Sandwich fiber cross section with CNT electrodes separated by dielectric core. (b) 20 cm long fiber woven into a glove. (c) Zoomed in images before and after application of 60% tensile strain [89]. (d) Multicore-shell printing process. (e) Capacitive fiber with ionically conductive fluid as conductor. (f) Sensor integration with textiles via sewing (top) and weaving (bottom) [90] .....	30

<b>Figure 16</b>	Sensors made by treatment of pre-fabricated yarns: (a) Steps in the fabrication of bisheath fiber, NTSm@rubber@fiber. The yellow, red, and gray colors are for the SEBS core, the SGE layer, and the NTS sheath, respectively. (3) represents the single sheath fiber, NTSm@fiber [91] (b) Schematics of the fabrication of the wire-shaped strain sensor: (1) cotton thread, (2) CT (carbon thread), (3) CT with electrodes, (4) PDMS resin and (5) CT/PDMS sensor [92](c) Schematic of conductive polymer composite coated polyurethane yarn(top) and cross section (bottom) [93].....	32
<b>Figure 17</b>	(a) Textile structure is similar to that of multitouch capacitive panels used in tablets and mobile phones [94] (b) Schematic illustration of the fabrication of the textile-based pressure sensor [95] (c) Textile pressure sensor based on Pt-coated cotton fiber on a polyethylene terephthalate (PET) substrate .....	34
<b>Figure 18</b>	(a) Twisted fabric based capacitive sensor (left) and diagram of electromechanical test setup and cross-sectional image of the capacitive sensor (right) [96] (b) Schematic illustration of the sensing mechanism of resistive fabric based pressure sensor (left) and current response during loading (right) [97]. (c) Behavior of reduced graphene oxide layer on cotton fabric during tensile and compressive strain .....	36
<b>Figure 19</b>	(a) Schematic of a stretchable graphene thermistor. (b) Resistance variation with temperature at 0% strain showing a nonlinear relationship. (c) Resistance variation with temperature (30-1000C) within 0-50% strains [101] (d) Thermistor structure (left) and flexible temperature sensor on yarn with contact connectors (right).....	38
<b>Figure 20</b>	(a) Swelling of MWCNT/PVA coating layer of a composite yarn during moisture absorption process. (b) Resistances of various test samples as a function of relative humidity [109]. (c) Humidity and temperature sensor in a woven textile band (left) and schematic for measuring a sensor unit in a textile (right) .....	40
<b>Figure 21</b>	Metal organic frameworks (MOFs) coated on textiles.....	42

<b>Figure 22</b>	(a) Biosignals grouped according to sensing locations on body. (b) Description of symbols representing biosignals. (c) CNT/PDMS electrodes and the Ag/AgCl electrode for ECG monitoring. (d) Textile based respiration belt worn by the subject .....	44
<b>Figure 23</b>	a) Monitoring finger motion while bending. (b) Capturing gait cycle of wearer. (c) Strain sensor attached on knee for different walking patterns involving extending, squatting and marching .....	45
<b>Figure 24</b>	Wearable sensors used as interactive devices: (a) Glove with embedded strain sensors (left) showing electrical resistance change at different hand positions [43]. (b) Control of avatar using smart glove having sensors .....	47
<b>Figure 25</b>	Potential sensing locations for a long sleeve top. (a) Arm and wrist areas are suitable for pulse rate monitoring. (b) Skin electrodes for biopotential measurement can be placed on the chest. (c) Underarm can provide information on bodily fluids. (d) Tactile input panels can be placed on the inner arm .....	66
<b>Figure 26</b>	Fiber design. Schematic of (a) Bicomponent fiber showing insulating and conducting segments, (b) Woven fabric made of bicomponent fibers, and (c) Sensing pixel formed at crossover point, compared to a parallel plate capacitor....	67
<b>Figure 27</b>	Sensing pixel for pressure sensing .....	68
<b>Figure 28</b>	(a) Shear forces acting on pixel, (b) Diagram showing change in area due to shear .....	70
<b>Figure 29</b>	Conducting segment of fiber acting as piezoresistor.....	71
<b>Figure 30</b>	Sensing pixel for wetness detection by impedance measurement.....	72
<b>Figure 31</b>	(a) Conducting segment of fiber in contact with skin acting as biopotential electrode and (b) longer floats in woven structure for biopotential recording .....	73

<b>Figure 32</b>	(a) Schematic representation of the fabrication of sensory fibers; 1) etched acrylic substrate, 2) extrusion of insulating segments, and 3) deposition of CPC. (b) Custom built sequential extrusion printing setup.....	74
<b>Figure 33</b>	Percolation behavior of the CPC with the cross-sectional shape of the sensory fibers shown in the inset .....	75
<b>Figure 34</b>	(a) Stress–strain behavior of a sensory fiber subjected to 30 cycles of 40% strain. 1st, 10th, and 30th cycles are shown; (b) Strain–resistance response of the fiber subjected to 20 cycles of 30% strain; (c) 1st, 10th, and 20th cycles of the strain–resistance response of the fiber shown in (b), and (d) Resistance of the fiber under 30% strain for 20 s .....	77
<b>Figure 35</b>	(a) Stress–strain behavior of a texel subjected to 30 cycles of 50% strain in compression. 1st, 10th, and 30th cycles are shown; (b) Force–capacitance response of a texel subjected to 20 cycles of 0–4 N compressive loading; (c) 1st, 10th, and 20th cycles of the force–capacitance response of the texel shown in (b), and (d) capacitive response of the texel under 4 N sustained compressive load for 60 s .....	79
<b>Figure 36</b>	Demonstration of the multitouch sensing capabilities of a texel array .....	80
<b>Figure 37</b>	(a) Schematic representations of the deformation of a texel array subjected to a specific shear angle $\theta$ , and (b) Capacitive response and resulting change in the area (calculated) of the overlap region in a texel, subjected to shear. ....	81
<b>Figure 38</b>	Impedance response of a texel in a wetting–drying cycle using saline.....	82
<b>Figure 39</b>	(a) Three-electrode ECG measurement setup and (b) Measured signal.....	83
<b>Figure 40</b>	(a) Experimental set-up for simultaneous capacitance and resistance measurements of a fiber texel. The set-up allows application of directional in-plane tensile strains as well as compression of the texel. (b) Capacitive ( $\square$ ) and resistive (along bottom fiber: $\circ$ , along top fiber: $\Delta$ ) response of a texel 1) under	

	no-load, 2) only compression, 3) in-plane tension, and 4) simultaneous tension and compression. The arrows point to the corresponding axis.....	84
<b>Figure 41</b>	Schematic of bicomponent dumbbell fiber and a capacitive crossover where ‘h’ is height of insulating segments ‘t’ is thickness of conductor, ‘C’ is capacitance with ‘s’ as conductor separation and ‘A’ as overlapping area of electrode.....	92
<b>Figure 42</b>	Steps in creating conducting material for extrusion: (a) CB pellets. (b) CB pellets dispersed in hexane. (c) CB dispersion mixed with PDMS. Note: Image magnification = 40X.....	94
<b>Figure 43</b>	TEM images of conducting polymer composite showing the nanostructures of CB dispersed in silicone at (a) 50 nm and (b) 20 nm.....	94
<b>Figure 44</b>	Schematic of extrusion channel; (a) before assembling with three fluid flow channels, (b) after assembling the two parts, (c) top view showing three inlets for delivering insulating and conducting materials and (d) bottom view showing dumbbell shaped orifice.....	95
<b>Figure 45</b>	3D printed extrusion device assembled together with metal plates (a) before and (b) after the tubing is inserted.....	96
<b>Figure 46</b>	Schematic of fiber coextrusion process.....	97
<b>Figure 47</b>	Stages of fiber production; firstly (a) insulating sides are extruded, secondly, (b) middle conducting stream is extruded and lastly, (c) UV light is turned ON.....	99
<b>Figure 48</b>	Image of fiber extrusion process showing tunable process parameter where ‘d’ is drop height, ‘l’ is distance between UV light and fluid stream and ‘h’ represents distance from orifice where UV light illuminates the fluid stream and curing begins.....	99
<b>Figure 49</b>	(a) Longitudinal images of all fibers and cross sectional image of (b) large, (c) medium and (d) small fiber.....	100

<b>Figure 50</b>	(a) Breaking elongation response of all fibers. Strain cycling response of (b) large, (c) medium, and (d) small fibers.....	102
<b>Figure 51</b>	Optical microscope images of (a, b) large, (c, d) medium and (e, f) small fibers after tensile failure showing broken conducting bridge and insulating segment...	103
<b>Figure 52</b>	Force –capacitance testing of fibers. (a) Insulating tip attached to load applicator before compressing one of the pixels of woven array. (b) Load-strain response of pixel showing decrease in conductor separation. (c) Load displacement cyclic response of pixel and (d) capacitance response of pixel compressed 10 times .....	104
<b>Figure 53</b>	Piezoresistive response. (a) Resistance change with extension for 40% strain cycling and corresponding (b) 30 cycles of 40 % strain cycling. (c) Images of bending and relaxing of finger onto which fiber is mounted for strain sensing and (d) resistive response (6 cycles) of fiber sensor when the finger is bent and relaxed.....	105
<b>Figure 54</b>	(a) 10 $\mu$ l droplet inside the crossover. (b) Equivalent circuit model for wetness detection. (c) Impedance response to different saline concentrations .....	106
<b>Figure 55</b>	Schematic of test setup for temperature resistance response measurement .....	107
<b>Figure 56</b>	Resistive response of conductive composite of fiber under temperature. (a) Increase in sample temperature under IR light for 10 cycles. (b) Change in electrical resistance of sample when heated and cooled plotted for all 10 cycles. (c) Representative average stabilized resistive response of sample for cycles 4, 6, 8 and 10. (d) Decrease in sample resistance in range of 30 to 35oC showing sensitivity in smaller range. ....	109
<b>Figure 57</b>	(a) Pressure analysis distribution of the stump-to-socket interface using the Pliance system [17] and (b) F-Socket System [18].....	116
<b>Figure 58</b>	(a) Below the knee (BK or lower limb or transtibial amputation and (b) Schematic of prosthetic environment monitoring concept using fiber sensor arrays.....	118

<b>Figure 59</b>	Fiber based sensing pixel .....	118
<b>Figure 60</b>	Schematic of the extrusion channel used for fiber fabrication. (a) Isometric view of two-part extrusion channel with three inlets at the top for injecting fiber forming materials. (b) Bottom view of extrusion channel showing dumbbell shaped orifice. (c) Dimensions of the dumbbell orifice.....	119
<b>Figure 61</b>	Schematic of the fiber extrusion process.....	120
<b>Figure 62</b>	Different steps involved in sensor array fabrication .....	121
<b>Figure 63</b>	Three phases of sensor testing within the socket. (a) Benchtop testing using an artificial limb. (b) Able-bodied testing with bent knee adaptor. (c) Human subject testing.....	122
<b>Figure 64</b>	Inverted pendulum analogy for the stance leg during walking .....	124
<b>Figure 65</b>	(a) Front and (b) top view of sensors attached to the socket at 4 locations.....	124
<b>Figure 66</b>	Guide diagram of sensor locations with respect to the limb .....	125
<b>Figure 67</b>	Artificial limb testing experiment showing (a) mounting frame setup and (b) socket with attached sensors indicating their placement with respect to heel and toe of the prosthetic foot .....	125
<b>Figure 68</b>	Sign conventions used for artificial limb experiment showing (a) negative tilt, and (b) positive tilt.....	126
<b>Figure 69</b>	Able-bodied testing. (a) Sensor attached on front thigh, above liner, and (b) Subject wearing bent knee adaptor on right leg.....	127
<b>Figure 70</b>	Human subject testing: (a) Sensor attached at the Patellar Tendon (PT) location of left residual limb. (b) Amputee standing on the treadmill after wearing socket onto sensor .....	128

<b>Figure 71</b>	Optical microscopic images of the extruded bicomponent fiber. (a) Cross-sectional view showing dumbbell shape and (b) longitudinal view. ....	129
<b>Figure 72</b>	Photograph of fabricated sensor arrays .....	129
<b>Figure 73</b>	(a) Load-capacitance response of sensor array to 12% compression. (b) Capacitance response of sensor array subjected to two different degrees of compression namely 12% and 20%. (c) Load and (d) capacitance response of sensor array compressed by applying a 16% compression at three different test speeds.....	131
<b>Figure 74</b>	(a) Load and (b) capacitance response of sensor array subjected to compression with 2 minutes hold. (c) Load and (d) capacitance response of sensor array compressed for 65 cycles.....	132
<b>Figure 75</b>	Artificial limb testing results where average capacitive response of sensors, (a) S1, (b) S2, (c) S3, and (d) S4, to negative and positive tilting of the limb is displayed. ....	134
<b>Figure 76</b>	(a) Backward (left) and forward (right) weight shift during able bodied testing, and (b) corresponding capacitance sensor response during forward-backward weight shifting for multiple cycles. ....	135
<b>Figure 77</b>	Walking test while wearing bent knee adaptor during able bodied testing. Different stages of walking are shown namely (a) heel strike, (b) support, (c) toe-off, and (d) swing along with (e) ground reaction force generated during one walk cycle highlighting different stages of walking.....	136
<b>Figure 78</b>	Able bodied testing walking results. (a) Ground reaction force recorded by treadmill. (b) Capacitive response of sensor.(c) Comparison of variation of ground reaction force and capacitance in one walk cycle.....	136
<b>Figure 79</b>	Side-to-side leaning/weight shifting by amputee; (a) loading stance, (b) unloading stance, (c) capacitive sensor response during weight shift, and (d)	

	capacitive sensor response during weight shift with stance being held at both loading and unloading points for 5 seconds .....	138
<b>Figure 80</b>	(a) Stances of the prosthetic leg of amputee during walking: 1-heel strike, 2-support, 3-toe-off, 4 &5-swing. (b) Ground reaction force recorded by treadmill. (c) Capacitance response of sensor .....	139
<b>Figure 81</b>	Variation of ground reaction force and capacitance with time during single cycle of walking .....	140
<b>Figure 82</b>	Custom-designed printed circuit board for Capacitance measurement connected to sensor array .....	141
<b>Figure 83</b>	Schematic of capacitive proximity sensing concept. (a) Sensor array integrated into the garment of the user for contactless gesture sensing. (b) Isometric view of the plain woven sensor array. (c) Single sensing pixel showing fringe field of capacitor coupling with human finger .....	147
<b>Figure 84</b>	Schematic of fiber extrusion process.....	149
<b>Figure 85</b>	Schematic of sensor array fabrication process: (a) Fabrication of three channel extrusion device. (b) Fiber extrusion. (c) Weaving, and (d) Fabrication of electrical interconnects.....	150
<b>Figure 86</b>	Effect of the proximity of grounded conductive object on capacitance. (a) Schematic of the experimental setup showing grounded copper tip attached to movable crosshead. (b) Effect of three different proximity distances. (c) Zoomed in single cycles of three different proximity distances shown in (b). (d) Proximity to sensor and change in capacitance plotted as a function of time .....	152
<b>Figure 87</b>	a) Capacitive response of 100 cycles of 2mm proximity of conductive copper tip to the sensor. (b) Capacitive response of sensor when the conductive copper tip is held 2mm away for 2 minutes for 10 cycles. (c) Effect of three different speeds of approaching of conductive copper tip 2mm away from the sensor.....	153

- Figure 88** Dual-mode operation of the capacitive sensor. (a) Capacitance change during approaching, pressing and distancing from the sensor showing capacitance decrease during the approach, capacitance increase when pressed and capacitance recovery during retraction of the crosshead. (b) Force recorded during the pressing of the sensor. (c) 10 cycles of approaching-pressing of the sensor ..... 154
- Figure 89** Two finger simultaneous approach detection. (a) Index and long finger in proximity of pixel 10 and pixel 19 respectively. (b) Heatmap of change in capacitance of sensor array with pixel 10 and pixel 19 displaying a lower capacitance compared to other pixels. (c) Change in capacitance of pixel 10 and pixel 19 with time when approached by index and long finger simultaneously. (d) 5 cycles of approach and retraction of index and long finger from pixel 10 and pixel 19..... 156
- Figure 90** Three finger simultaneous approach detection. (a) Index, long and ring finger in proximity of pixel 10, pixel 21 and pixel 28 respectively. (b) Heatmap of change in capacitance of sensor array with pixel 10, pixel 21 and pixel 28 displaying a lower capacitance compared to other pixels. (c) Change in capacitance of pixel 10, pixel 21 and pixel 28 with time when approached by index, long and ring finger simultaneously. (d) 5 cycles of approach and retraction of index, long and ring finger from pixel 10, pixel 21 and pixel 28. .... 157
- Figure 91** Touchless swipe gesture using index finger. (a) Swipe motion on column 3 with images of index finger at every pixel from pixel 21 to pixel 17 during swipe. (b) Swipe gesture on column 3 represented in the form of heatmap. (c) Drop in capacitance of pixels 21 to 17 during swipe with time. (d) Change in capacitance of pixels 21 to 17 during 3 swipe gestures..... 159
- Figure 92** Touchless addition sign gesture using index finger. (a) Vertical and horizontal swipe motions on column 3 and row 4 respectively with images of index finger at every pixel of interest in that region. (b) Addition sign gesture represented in

	the form of heatmap. (c) Drop in capacitance of pixels of interest during vertical and horizontal swipes with time. ....	161
<b>Figure 93</b>	Touchless check mark sign gesture using index finger. (a) Images of the index finger at different pixels across columns creating a check mark sign. (b) Check mark sign gesture represented in the form of heatmap. (c) Drop in capacitance of pixels of interest during creating a check mark sign with time. ....	163
<b>Figure 94</b>	Touchless writing of word HI using index finger. (a) Images of the index finger at different pixels during creating a pattern of the word HI where hovering from pixel 6 to 2 represents left bar of letter H (top left), hovering from pixel 4 to 20 represents middle bridge of letter H (top right), hovering from pixel 22 to 18 represents right bar of letter H (bottom left) and hovering from pixel 38 to 34 represents letter I (bottom right). (b) Word HI represented in the form of a heatmap. (c) Drop in capacitance of pixels of interest during writing word HI with time. ....	165
<b>Figure 95</b>	(a) Image of 96 channel sensor array showing 8 rows and 12 columns connected to breakout board. (b) Electrical connection of fiber to copper tape with CPC paste (black) encapsulated by silicone.....	167
<b>Figure 96</b>	Different parts of data collection system to record capacitance from 96 channels	168
<b>Figure 97</b>	Schematic of the 96 (8 rows x 12 columns) sensor proximity sensing array with each pixel assigned a particular number for data analysis during gesture decoding.....	168
<b>Figure 98</b>	Core-sheath fiber design. Image shows a hollow silicone tube filled with carbon-black silicone composite. ....	174
<b>Figure 99</b>	Capacitance increase of pixels of sensor array due to force exerted by left foot of the subject upon stepping, plotted as heatmap.....	174

<b>Figure 100</b> Fluid flow simulation using COMSOL multiphysics .....	175
<b>Figure 101</b> Sensing fiber placement on silicone tubing for hoop and longitudinal stress sensing.....	176
<b>Figure 102</b> (a) Placement of electrodes on right gastrocnemius muscle. (b) Maximum Voluntary Contraction (MVC) of the gastrocnemius muscle of the leg by rising on toes. (c) Voltage response of commercial sensor during multiple cycles of rising on toes and relaxing. (d) Voltage response of custom developed (CPC-conductive polymer composite) sensor during multiple cycles of rising on toes and relaxing. (e) Zoomed in 3 cycles of commercial sensor. (f) Zoomed in 3 cycles of CPC sensor indicative of S/N ratio.....	177
<b>Figure 103</b> Light actuation of conductive polymer composite film. (a) Initial flat configuration of film taped at both ends, and (b) Buckling response of both sides taped film when illuminated by UV light. ....	178

## CHAPTER 1: Introduction

Electronic (e)-textiles are textile products with integrated electronic capabilities of devices such as sensors, actuators, energy harvesting and storage devices, and communication devices. E-textiles fall under the category of wearable electronics which are increasingly becoming a part of our daily lives. E-textiles offer potential to produce large area distributed electronic systems in a roll-to-roll fashion. E-textiles have attracted significant commercial interest in the last 30 years and the market for e-textiles is predicted to reach over \$2 billion by 2029 [1]. Key market sectors for e-textile products include medical & healthcare, sports & fitness, military & space, personal protective equipment and fashion. The motivation to integrate electronic capabilities in textiles to create e-textiles comes from the obvious potential of textiles capable of sensing and communicating data to provide useful information about our health. Sensor-embedded e-textiles could be used to monitor vital signs of soldiers in the combat field, health condition of firefighters and physiological condition of top athletes [2]. Some of the current commercial e-textile products in the market include commuter jacket from Google [3], heating clothing [4], smart underwear with multifunctional sensing [5], vibrating yoga pants [6] and touch screen gloves [7].

The primary challenge in producing e-textiles is to enable electrical functionalities in textiles while preserving the desirable textile qualities such as softness, comfort, flexibility, porosity and texture. These unique and desirable properties of textiles are derived mostly from their hierarchical structure with fibers as building blocks. While electronic capabilities can be integrated into any of these hierarchical levels, the integration of electronic capabilities at fiber level is the most practical approach to create seamlessly-integrated e-textile products, using processes that are compatible with textiles. Accordingly, integration of sensing functionality within fibers creates fiber-based sensors which is the focus of this research. These fiber-based

sensors detect and measure the magnitude of stimuli such as strain, pressure, temperature and humidity by converting it into an electrical signal. Current fiber-based sensors are mostly limited to a single sensing functionality and only a few that are currently available have mechanical and dimensional compatibility with textiles. A multifunctional fiber-based sensor can offer unobtrusive integration of sensing capabilities into textiles enabling many practical systems in physiological monitoring, comfort, medicine, security, surveillance and protection. The objective of this research is to create a sensor using polymeric fibers within a woven fabric structure that can generate an electrical response under various stimuli like tactile forces, wetness and biopotentials with the potential of large-scale manufacturability through use of existing fiber and fabric manufacturing technologies.

In this research, a bicomponent fiber was fabricated consisting of insulating and conducting components. The individual fiber acts as a resistive sensor and woven assembly of the fibers forms a capacitive sensor at each cross-over point in the fabric leading to more than one sensing functionality along with multimodality. This approach allows us to harness inherent orthogonal interlacement of fibers/yarns in a woven textile structure. These fiber based sensors were used as capacitive sensors to monitor tactile forces, impedance sensors to detect wetness/moisture and as dry electrodes to monitor biopotentials like ECG (heart rate). In terms of material for e-textile fabrication, polymers are an obvious choice because of their mechanical flexibility. In this work, silicone elastomer was used as the base fiber forming material and carbon black-silicone polymer composite as conductive material to fabricate the fibers. Conductive polymer composites (CPCs) are commonly used conductive materials in making flexible sensors. The bicomponent fibers were fabricated using custom developed extrusion based benchtop techniques. Capacitance and

resistance were the primary electrical measurements conducted to characterize the sensing response of fibers.

This thesis consists of seven chapters. In chapter 1, e-textiles, importance of sensor integrated e-textiles and preference of fiber based sensors followed by motivation of this research and approach are explained, followed by a detailed literature review of flexible sensors for e-textiles in Chapter 2. Chapter 3 discusses sensor design and extrusion printing approach of bicomponent fiber fabrication. Chapter 4 outlines the improved one step approach of coextruding bicomponent fibers in terms of production time and yield. Chapter 5 presents a real world application in biomedical field where fiber based sensors were used for inner prosthetic environment monitoring. Chapter 6 demonstrates contactless sensing for gesture recognition. Lastly, Chapter 7 concludes with summary along with limitations of this work and directions for future research.

## References

- [1] “E-Textiles 2019-2029: Technologies, Markets and Players: IDTechEx,” 21-May-2019. [Online]. Available: <https://www.idtechex.com/en/research-report/e-textiles-2019-2029-technologies-markets-and-players/671>. [Accessed: 18-Jul-2019].
- [2] R. F. Service, “Electronic Textiles Charge Ahead,” *Science*, vol. 301, no. 5635, pp. 909–911, Aug. 2003, doi: 10.1126/science.301.5635.909.
- [3] “Home,” *Jacquard by Google*. [Online]. Available: <https://atap.google.com/jacquard/>. [Accessed: 25-Nov-2018].
- [4] “Our Products,” *LOOMIA Soft Circuit Systems | E-textiles*. [Online]. Available: <https://loomia.com/our-products>. [Accessed: 18-Jul-2019].
- [5] “<https://skiin.com/>,” *SKIIN Connected Apparel*. [Online]. Available: <https://skiin.com/>. [Accessed: 18-Jul-2019].
- [6] “How It Works - Wearable Tech Company,” *Wearable X*. [Online]. Available: <https://www.wearablex.com/pages/how-it-works>. [Accessed: 18-Jul-2019].
- [7] “Touch Screen Gloves - Shop Gloves | Gray Digits by Moshi.” [Online]. Available: <https://www.moshi.com/en/product/touch-screen-gloves-digits/light-gray-s>. [Accessed: 18-Jul-2019].

## CHAPTER 2: Textile-based Sensors: A Critical Review

### 2.1 Introduction

Textiles have been around for thousands of years. In the recent efforts to achieve wearable electronics, textiles have become one of the most attractive choices because they are an essential need at all times for humans. This combination of conventional textiles and electronic devices has led to the development of electronic (e) textiles. Electronic (e)-textiles are textile products with integrated electronic capabilities of devices such as sensors, transistors, antennas, energy harvesters and actuators. E-textiles are different from wearables because the emphasis is on seamless integration of electronics with textiles. Wearable e-textiles have wearable capabilities like any other garment along with sensing, computation and communication capabilities. E-textiles are the next generation of truly wearable electronics as they allow electronic devices to be worn on human body without compromising comfort of user. E-textiles with sensing functionality particularly, can significantly improve area of health and fitness management via continuous health monitoring [1]–[4]. E-textile sensors for human health monitoring can be imagined as fabrics embedded with various sensors such as heart rate sensor, respiratory sensor and motion sensor (see Figure 1a), continuously collecting data in form of electrical signals over healthy and sick states, which is stored on the cloud and can be accessed by health care provider using internet anytime. The vast quantities of human health data can be further analyzed using big-data techniques to find correlations between sensor response and health state enabling early detection of developing health conditions (Figure 1b). Therefore, a sensor integrated textile can play a pivotal role in functioning of complete wearable healthcare system to enable prevention, diagnosis, therapy and even rehabilitation. Additionally, such textile-based sensors will enable individuals to monitor their state of health without trained professionals just through their daily use garments in a comfortable

manner. In addition to health monitoring, textiles with sensing functionality can also be used to monitor sports performance and to create human-computer interfaces. Another advantage of using textiles as platform for sensor integration is that sensors can be strategically placed at desired target locations such as chest or wrist. Initial versions of e-textiles for sensing applications consisted of attaching rigid off the shelf sensors to clothing. But it was soon realized that this approach hindered the comfort and other desirable properties of textiles like feel, conformability and breathability. As a result, efforts then shifted towards converting the textile itself into a sensor which included focusing on approaches that utilize the structural hierarchy of textiles from fiber or yarn level to fabric level as this structural hierarchy is responsible for the inherent textile properties. Within this, electrical functionalization of fibers or yarns has attracted attention because creating sensors in form of fibers does not hinder desirable textile properties as fibers are the lowest primary level in textile formation and have high flexibility due to their aspect ratio. These fiber-based sensors can be directly assembled into fabrics through conventional fabric formation techniques like weaving and knitting to create area-scalable e-textiles in a cost effective roll-to-roll fashion. This review provides an overview of textile based sensors in form of fibers, yarns and fabrics for e-textile applications. Here, sensing principles required to detect various stimuli, sensor materials, stimuli based sensing and major on-body applications are covered.

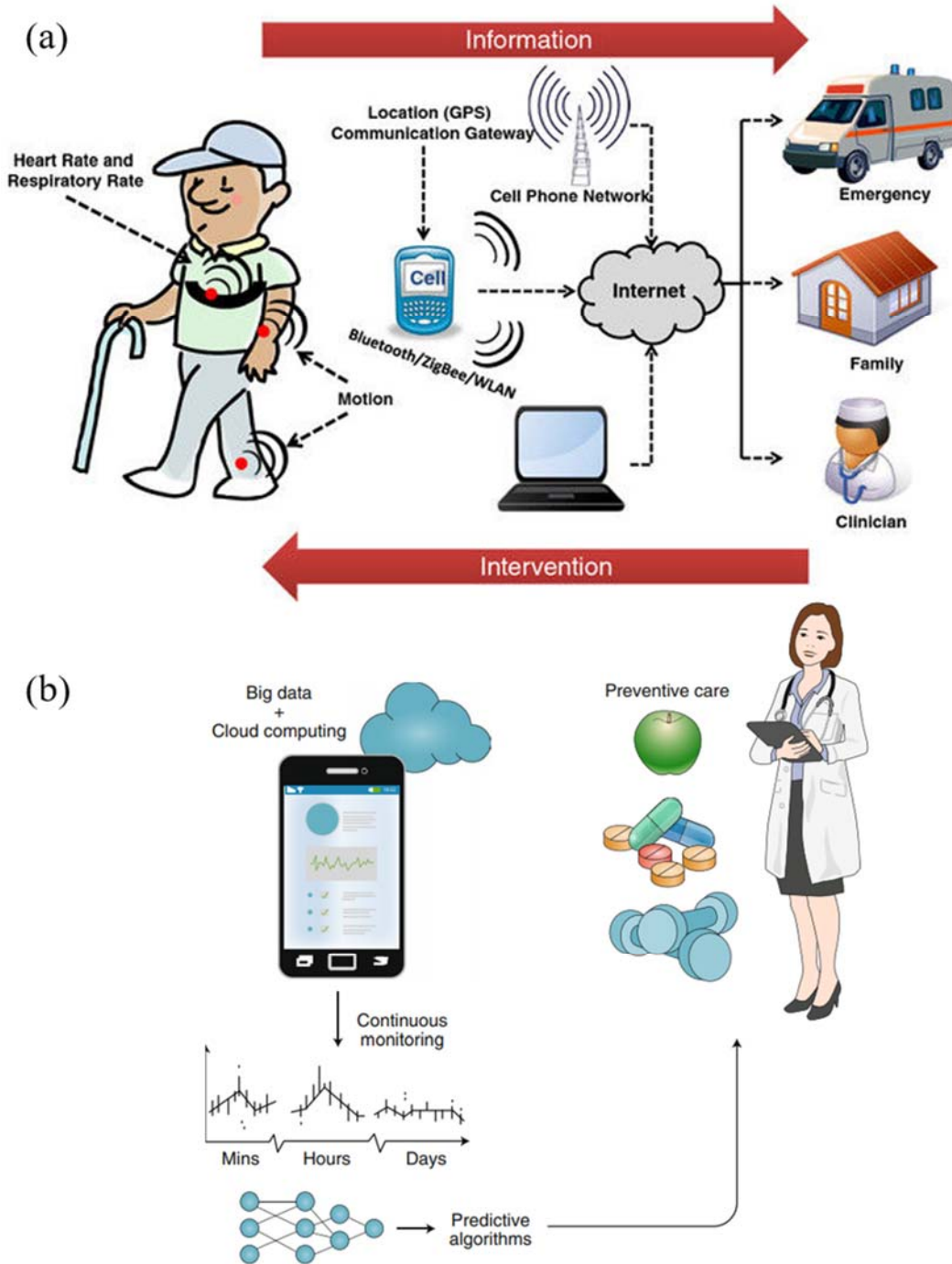


Figure 1: (a) Remote health monitoring system based on sensors integrated in textiles [5] and (b) Use of sensors collected big data for personalized and preventive healthcare [6].

## 2.2 Sensing Mechanisms and Performance Characteristics

Sensors detect a change in physical (or chemical) stimulus (such as pressure, heat) and turn that stimulus into a signal that can be measured or recorded. Sensors can be classified in a number of ways (refer Figure 2 ) depending on the requirement of external power, distance to the object, chosen reference, and sensing principle [7].

- **Active and Passive sensors:** Active sensors are those which require external source of power to operate whereas sensors that generate their own electrical signal and do not require a power source are defined as passive sensors [7].
- **Contact and Non-Contact sensors:** A sensor that requires physical contact with the stimulus, e.g. strain gauge and temperature sensor is a contact sensor and one that requires no physical contact, e.g. optical and magnetic sensor are non-contact sensors.
- **Absolute and Relative sensors:** An absolute sensor reacts to a stimulus on an absolute scale, e.g. a thermistor always reads the absolute temperature whereas a relative sensor measures stimulus relative to a fixed or variable reference, e.g. thermocouple measures the temperature difference.

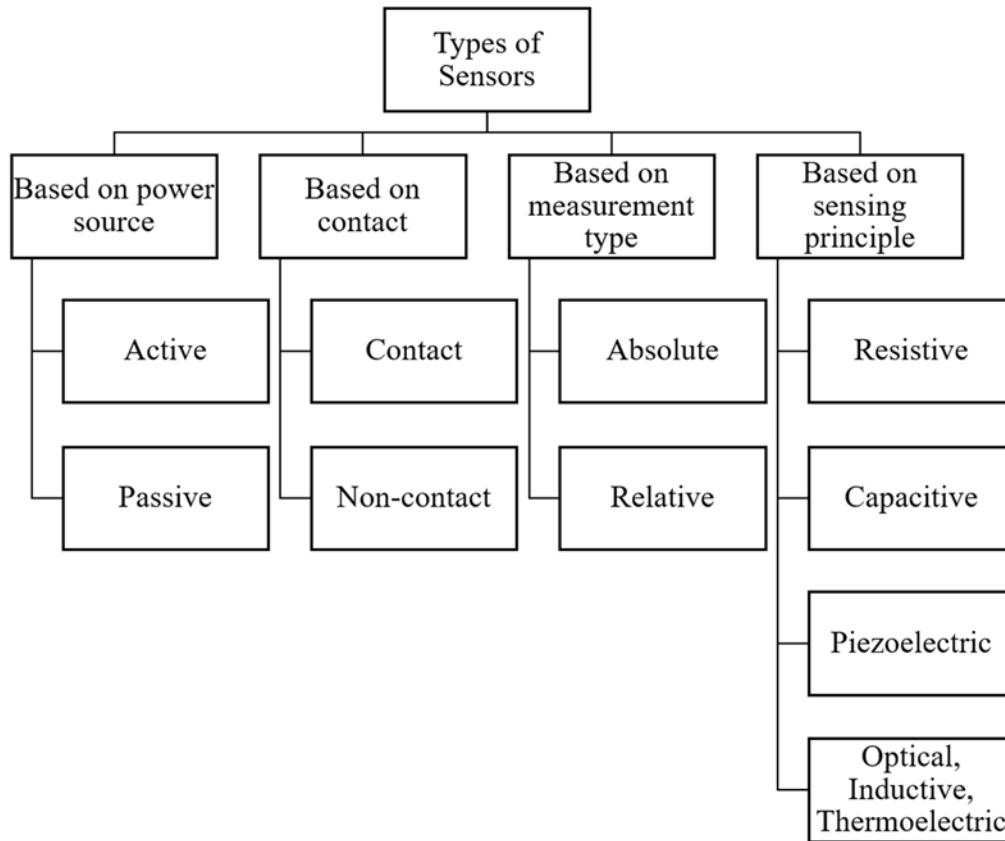


Figure 2: Classification of sensors [7]

In order to detect and measure the magnitude of stimuli (such as strain, pressure, temperature, humidity) it has to be converted into a measurable and processable signal. The major principles of sensing and methods for this conversion are described in this section.

***Resistive***

A resistive sensor responds to a stimulus by change in electrical resistance. The electrical resistance of an object depends on type of material and its shape. Piezoresistive behavior refers to change in electrical resistance of materials under applied strain. This change can be due to dimensional change or change in resistivity, which is an intrinsic property of material. Resistivity governs the electrical resistance experienced by charge carriers within the material when an

external electric field is applied across its ends. Consider a resistor with length (L), width (W) and height (H) with current (I) flowing along length direction as shown in Figure 3.

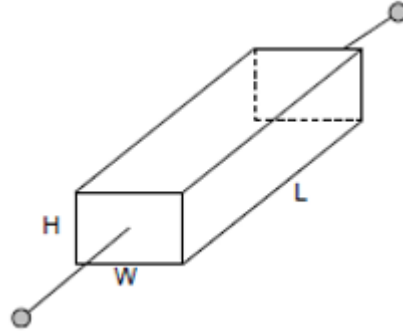


Figure 3: Resistor with current flowing along length [8]

The resistance R of the conductor can be expressed as,

$$R = \frac{\rho L}{A}$$

Where  $\rho$  is resistivity of material and A is area ( $A = W \times H$ ). The unit of resistance is Ohm ( $\Omega$ ) and resistivity, ( $\Omega \cdot m$ ).

Differentiating above equation;

$$dR = \frac{\rho}{A} dL + \frac{L}{A} d\rho - \frac{\rho L}{A^2} dA$$

Dividing by R;

$$\frac{dR}{R} = \frac{dL}{L} + \frac{d\rho}{\rho} - \frac{dA}{A}$$

The term  $dL/L$  represents fractional change in length,  $dA/A$  is fractional change in area and  $d\rho/\rho$  represents fractional change in resistivity of conductor due to external strain.

Here,  $(dA/A)$  can be written as;

$$\frac{dA}{A} = \frac{dW}{W} + \frac{dH}{H}$$

Since, axial strain  $\epsilon_{axial}$  or  $\epsilon$  is,

$$\epsilon = \frac{dL}{L}$$

and lateral strain

$$\epsilon_{lateral} = \frac{dW}{W} = \frac{dH}{H}$$

Then  $(dA/A)$  in terms of strain can be written as;

$$\frac{dA}{A} = 2 \epsilon_{lateral}$$

Also, we know, Poisson's ratio ( $\nu = -\frac{\epsilon_{lateral}}{\epsilon_{axial}}$ ),

$$\Rightarrow \frac{dA}{A} = -2\nu\epsilon$$

Then,

$$\frac{dR}{R} = \epsilon + \frac{d\rho}{\rho} - (-2\nu\epsilon)$$

$$\Rightarrow \frac{dR}{R} = (1 + 2\nu)\epsilon + \frac{d\rho}{\rho}$$

The terms  $(1 + 2\nu)\epsilon$  and  $\frac{d\rho}{\rho}$  represent the geometric and material components of piezoresistivity,

respectively.

The gauge factor (GF) of a piezoresistive sensor is the ratio of relative change in electrical resistance R, to the mechanical strain  $\epsilon$ .

$$GF = \frac{\frac{dR}{R}}{\epsilon} = (1 + 2\nu) + \frac{\frac{d\rho}{\rho}}{\epsilon}$$

In metals, a change in resistance under strain is largely controlled by geometric changes since the band structure responsible for the conductivity (or resistivity) in metals is not altered so

$$GF_{metals} \cong 1 + 2\nu$$

Since, Poisson's ratio  $\nu$  cannot be greater than 0.5 so  $GF_{metals} \sim 2$ . In semiconducting materials like silicon and germanium, the fractional change in resistivity  $\frac{d\rho}{\rho}$  is predominant source of piezoresistive behavior and their GF is  $\sim 100$  [9]. In case of electrically conducting polymer composites, piezoresistivity is a combination of both effects [10].

### **Capacitive**

A capacitor is a passive electronic component that stores energy in the form of an electrostatic field. The basic configuration of a capacitor is a pair of conducting electrodes separated by a dielectric as shown in Figure 4 where changes in dielectric constant ( $\epsilon_r$ ), area of electrode (A) and separation (d) between electrodes directly affect the capacitance by relation;

$$C = \epsilon_0 \epsilon_r \frac{A}{d}$$

where  $\epsilon_0$  is permittivity of free space.

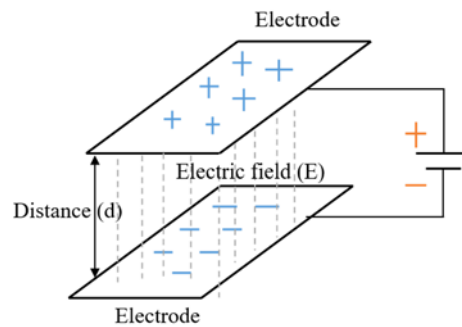


Figure 4: Configuration of a parallel plate capacitor

For a parallel plate capacitor as a sensor, the three controlling variables in capacitance formula are separation ( $d$ ), overlapping area ( $A$ ) and dielectric constant ( $\epsilon_r$ ). The change in dielectric constant may be due to different chemical fluids or different humidity [8]. Besides, the parallel plate configuration, cylindrical and spherical capacitors are also used. Capacitive sensors based on variation in separation 'd' are commonly used for the detection of pressure [11], [12]. A capacitive touch sensor can be based on principle of surface or projected capacitance [13], [14]. Surface capacitive sensor as shown in Figure 5 consists of a conductive coating on a glass substrate on one side and contact is made on other side. A small voltage signal is applied to all four corners of the coated side that produces a uniform electrostatic field and when a conductive object or a human finger touches the uncoated side, it forms a capacitor.

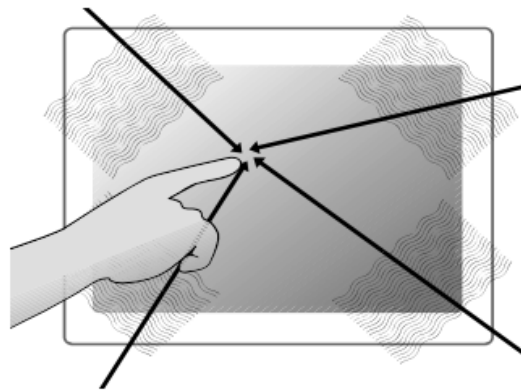


Figure 5: Surface capacitance based touch sensor [15]

Projected capacitive technologies [16] detect touch by measuring the capacitance at each addressable electrode. When a finger or a conductive stylus approaches an electrode, it disturbs the electromagnetic field and alters the capacitance. This can be further divided into self-capacitance and mutual capacitance. In self capacitance, one electrode of a capacitor forms a

parasitic capacitor with environment ( $C_0$ ) and when a conductive object like a human finger touches the cover material of sensor, it disturbs the electromagnetic field and alters the capacitance with respect to ground, generating an additional touch capacitance  $C_T$  [17] as shown in Figure 6. In a self-capacitance sensor, the current on each electrode to ground is measured individually [18]. Mutual capacitance requires two electrodes (refer Figure 7), such that an approaching finger steals some charge, reducing capacitance between electrodes. This approach is useful for detection of proximity, touch and pressure [19].

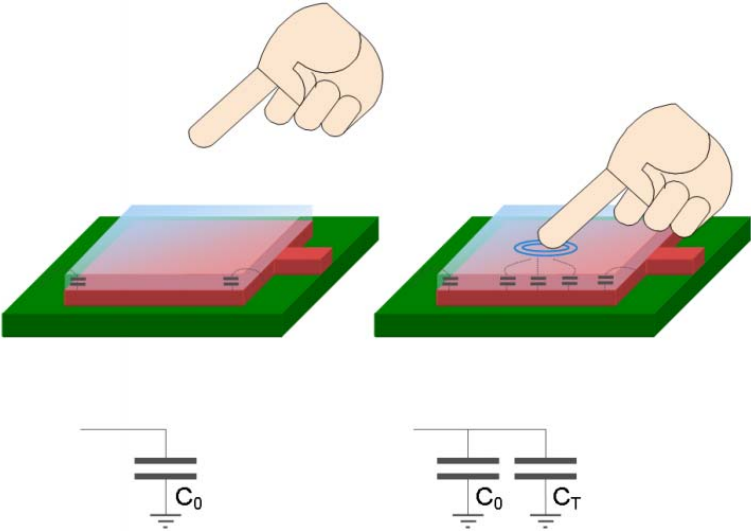


Figure 6: Self capacitance sensing principle: untouched sensor pad with parasitic capacitance  $C_0$ , touched sensor pad with additional touch capacitance  $C_T$  [17]

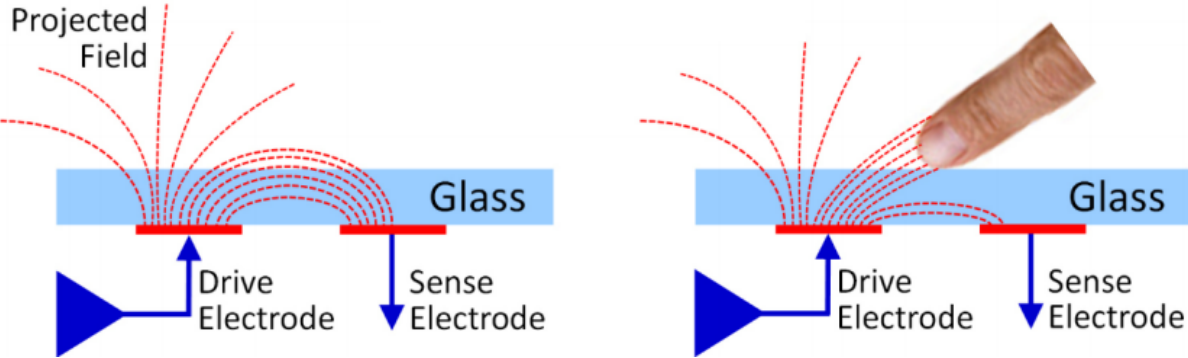


Figure 7: Mutual capacitance between two electrodes [14], [18]

## *Piezoelectric*

Piezoelectrics convert an applied force into an electrostatic charge. When a piezoelectric material is stressed, a charge is induced across the material's faces in response to the magnitude and direction of the strain that can be measured [20]–[22]. The electricity arises either from asymmetric movement of cations and anions under deformation or alignment of permanent dipole moment (refer Figure 8) in molecules of crystal [23], [24]. Piezoelectric sensors respond to various physical stimuli (not limited to pressure, tensile force, and torsion) by producing voltages ranging from tens of millivolts to hundreds of volts depending upon the type and magnitude of stimuli [25]. Polymeric piezoelectric materials are most suitable for fabrication of flexible sensors. In case of polymers, piezoelectricity arises from polymer chain distribution and molecular orientation [26]. Some of the common examples of piezoelectric polymers are poly(vinylidene fluoride) (PVDF), poly(vinylidene fluoride-co-trifluoroethylene) (P(VDF-TrFE)) and polyimide. PVDF has been used in multitude of flexible sensor fabrication because of its ease of processing, chemical inertness and comparative piezoelectric efficiency [27], [28]. The force to electrical charge conversion in piezoelectric materials is quantified using piezoelectric constant,  $d$  (Coulomb/Newton or C/N) given by;

$$d = \frac{\sigma}{p}$$

where ' $\sigma$ ' is the charge density and ' $p$ ' is mechanical pressure applied [26], [29]–[31].

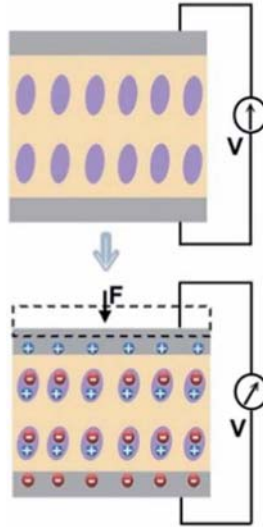


Figure 8: Schematic of occurrence of electric dipole moments in response to mechanical force,  $F$  in a piezoelectric material [32]

### *Optical*

Optical sensors detect light or change in property of light and convert it into an electrical signal. The advantage of optical sensors is their immunity to electromagnetic interference. These sensors consist of a light source, transmission medium and detector [33]. When the semiconductor absorbs the light with energy larger than its bandgap, electrons in valence band of semiconductors can be excited into conduction band, forming free electrons. The process achieves the transformation from light to electronic signals. Different transduction techniques used for measurement of electromagnetic radiation include photovoltaic, photoconduction and photoelectric. In a photovoltaic or photodiode, light is incident upon a junction between dissimilar materials and a voltage is generated. This technique can be used to measure the intensity of a light source. In photoconduction, there is a change in the resistance or conductance of a semiconductor material due to a change in the amount of illumination incident upon the material. In photoelectric, an incident photon causes the emission of an electron [20].

Optical sensors are classified into two major types, intrinsic and extrinsic. In case of intrinsic type an external stimuli changes the light transmission, reflectance wavelength etc. but not the path of light. On the other hand, in extrinsic type there is a change in path of light [23]. Optical techniques used for sensing applications may be based on fiber bragg gratings (FBG), optical time-domain reflectometry (OTDR) and macrobending effects. A FBG is an in-line periodic variation of refractive index of fiber core which reflects a particular wavelength of light, called Bragg wavelength ( $\lambda_B$ ) and transmits all other wavelengths as a filter (refer Figure 9).

The Bragg wavelength is given by;

$$\lambda_B = 2 \times n_{eff} \times \Lambda$$

Where ' $n_{eff}$ ' is effective refractive index and ' $\Lambda$ ' is grating period [34]. The deformation of optical fiber constituted assembly causes a shift in Bragg wavelength towards higher or lower wavelength which can be detected.

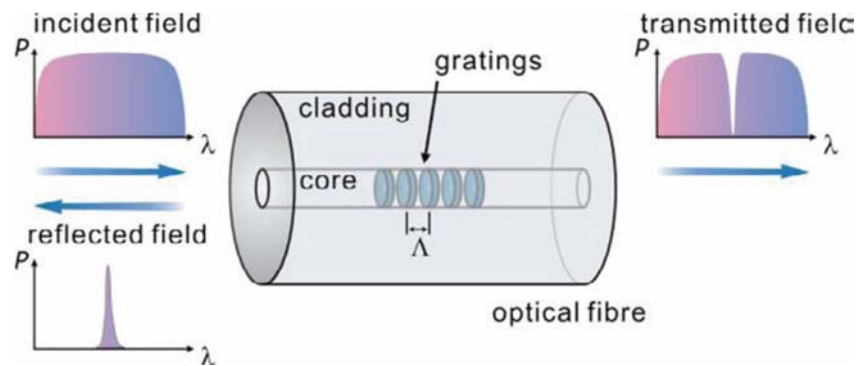


Figure 9: FBG structure showing incident, transmitted and reflected optical spectra [34]

The optical time-domain reflectometry sensor is based on the measurement of time and intensity. The incident light passing through fiber undergoes Fresnel reflection due to refractive index

difference and Rayleigh scattering due to material's microscopic inhomogeneities and the scattered light is detected [35]. In case of macrobending, bending causes loss of power of light because of light coupling from guided modes into radiation modes [36]. Macrobending sensors can be easily integrated into textiles as shown in

Figure 10 where stretching the substrate will decrease bend loss in fiber.

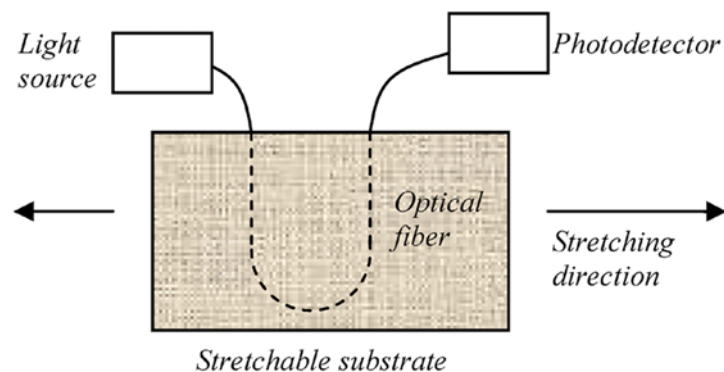


Figure 10: Macrobending sensor implemented on a stretchable substrate [36]

### ***Inductive***

Inductive sensors use magnetic field to measure position and proximity in a contactless manner. Also known as eddy current sensors. Inductive sensor has four components: inductive coil, oscillator, detection circuit, and output circuit. Their operating principle is based on an inductive coil and oscillator that creates an electromagnetic field which penetrates and induces small electrical currents (eddy currents) in the material so target material has a minimum thickness requirement (refer Figure 11). These small currents generate their own electromagnetic fields which react with the sensor probe's field such that the driver electronics can measure them. The

closer the probe, more the interaction between the eddy currents and sensing probe electromagnetic fields and greater the driver's output [37]. The output of an inductive sensor is affected by; (1) size of probe coil and target material, (2) distance between them and (3) target material. Due to its sensitivity to material changes, this sensor is used to detect defects and cracks. A common use case of inductive sensors is monitoring rotating targets such as crankshafts and drive shafts [37].

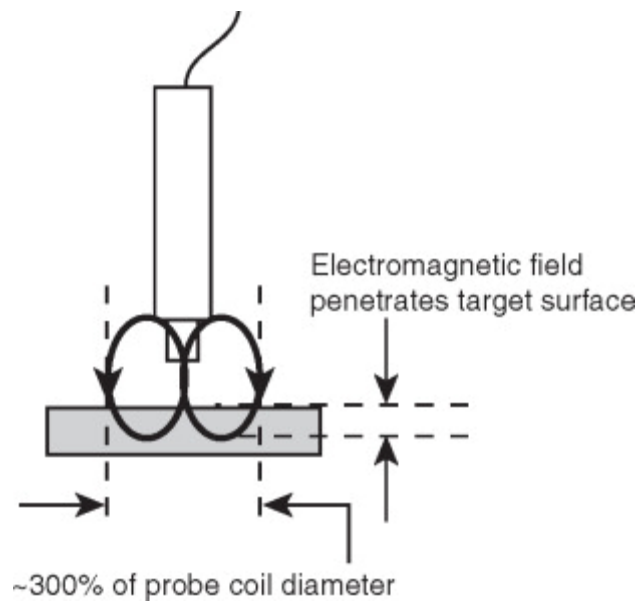


Figure 11: Working of inductive sensor [37]

### ***Electrochemical***

In electrochemical sensors, there is an electrochemical reaction between the measurand of interest and the functional material on the device which is used to measure the degree of that interaction via the measurement of an electrical property of the active layer in the device or the direct electrical signal that is produced from the reaction [20]. There are two major types: potentiometric (involving measurement of potential) and amperometric (involving measurement

of current). Common devices used as sensors are chemoresistor and chemFET (chemically-sensitive field-effect transistor).

### ***Thermoelectric***

Thermoelectricity based sensors convert temperature gradients into a voltage. This potential difference is generated between the junctions of two dissimilar materials due to the Seebeck effect which is used in thermocouples[20]. Due to Seebeck effect, as the temperature of the junction changes, the voltage (V) across the junction changes which is described by the equation;

$$V = \frac{S_B - S_A}{T_2 - T_1}$$

Where  $S_A$  and  $S_B$  are the Seebeck coefficients of materials  $A$  and  $B$ , respectively and  $T_1$  and  $T_2$  are the temperatures of the two junctions.

### **Sensor Performance Characteristics**

The common performance indicators to evaluate a sensor and compare sensor performances such as sensitivity, linearity, hysteresis, response time, measurand range, offset, operating life, output format, resolution, selectivity, speed of response and signal to noise ratio are discussed here [38]. These are crucial for assessing the sensor performance and reliability in end applications.

The *gauge factor (GF)* is a common figure of merit for the sensitivity of transduction from an external stimulus to electrical signal. In case of a resistive or capacitive strain sensor where there is a change in electrical resistance or capacitance with applied strain, GF is written as;

$$GF = \left( \frac{\Delta R}{R_0} \right) \times \varepsilon \text{ and}$$

$$GF = \left( \frac{\Delta C}{C_0} \right) \times \varepsilon$$

where  $\frac{\Delta R}{R_0}$  and  $\frac{\Delta C}{C_0}$  is normalized change in resistance and capacitance respectively,  $R_0$ ,  $C_0$  are initial values of resistance and capacitance respectively before application of stimuli and  $\epsilon$  is applied mechanical strain. The GF of metals is  $\sim 2$  and that of semiconductors is  $\sim 100$ . In case of flexible and stretchable sensors, the value of gauge factor depends on sensing mechanism, materials and structure of sensor [39], [40]. GF may be constant (linear) or varying over the sensor range (non-linear). The gauge factors of some stretchable strain sensors are mentioned in Table 1.

Table 1: Summary of sensor performance metrics of stretchable strain sensors [39]

Material [Ref.]	Sensing principle	Gauge factor	Stretchability	Linearity
CB-PDMS [41]	Resistive	29.1	30	Linear
CB-TPE [42]	Resistive	20	80	Non linear
Carbon grease-Ecoflex 00-30 [43]	Resistive	3.8±0.6	400	Non linear
MWCNTs-Ecoflex [44]	Resistive	1-2.5	500	Linear
Aligned SWCNTs-PDMS [45]	Resistive	0.82	280	2 linear regimes
CNTs-Silicone rubber [46]	Capacitive	0.97	300	Linear
CNTs-Ecoflex [47]	Capacitive	1	150	Linear
CNTs-Silicone elastomer [48]	Capacitive	0.99	100	Linear
Graphene foam-PDMS [49]	Resistive	15-29	70	Linear
Graphene-Natural rubber [50]	Resistive	10-35	800	Non linear
AgNWs-PDMS [51]	Resistive	2-14	70	Linear up to 40%
AgNWs-Ecoflex [52]	Capacitive	0.7	50	Linear
AuNWs-Latex rubber [53]	Resistive	6.9-9.9	350	Linear
Pt-PUA [54]	Resistive	2000	2	Non linear

CB: carbon black, TPE: thermoplastic elastomer, PUA: polyurethane acrylate, Ecoflex: silicone rubber, MWCNT: multiwall carbon nanotube, SWCNT: single wall carbon nanotube, AgNW-silver nanowire, AuNW: gold nanowire, Pt: platinum

The extent of the deviation of actual sensor output from the ideal response is characterized by *linearity* which implies that the output is directly proportional to input signal over complete

range and slope of the response curve is a straight line. The linearity of a sensor indicates the extent to which measured response curve departs from ideal curve [55]. Linearity is expressed as percent non-linearity given by;

$$\text{Nonlinearity \%} = \left( \frac{D_{in,max}}{IN_{f.s.}} \right) \times 100$$

where  $D_{in,max}$  is maximum input deviation and  $IN_{f.s.}$  is full scale input. Nonlinearity of sensors makes sensor calibration complex. An ideal sensor should be able to produce the same response to the same level of the measurand regardless of whether the measurand is increasing or decreasing. *Hysteresis* is the difference between output readings for same input parameter depending on the direction of operation of sensor (increasing or decreasing input) [55], [56]. Hysteresis can lead to errors such as the input value B in Figure 12a can be represented by  $F(X)_1$ ,  $F(X)_2$ , or  $F(X)_3$ . Large hysteresis effect leads to irreversible sensing performance [57]. This effect becomes crucial when sensors are subjected to dynamic load during wearable applications. Figure 12b shows hysteresis in electrical resistance response of a flexible strain sensor consisting of a gold film on elastomer when stretched from 0% to 200% and relaxed [53]. Polymer based sensors show this behavior due to viscoelastic nature of polymers.

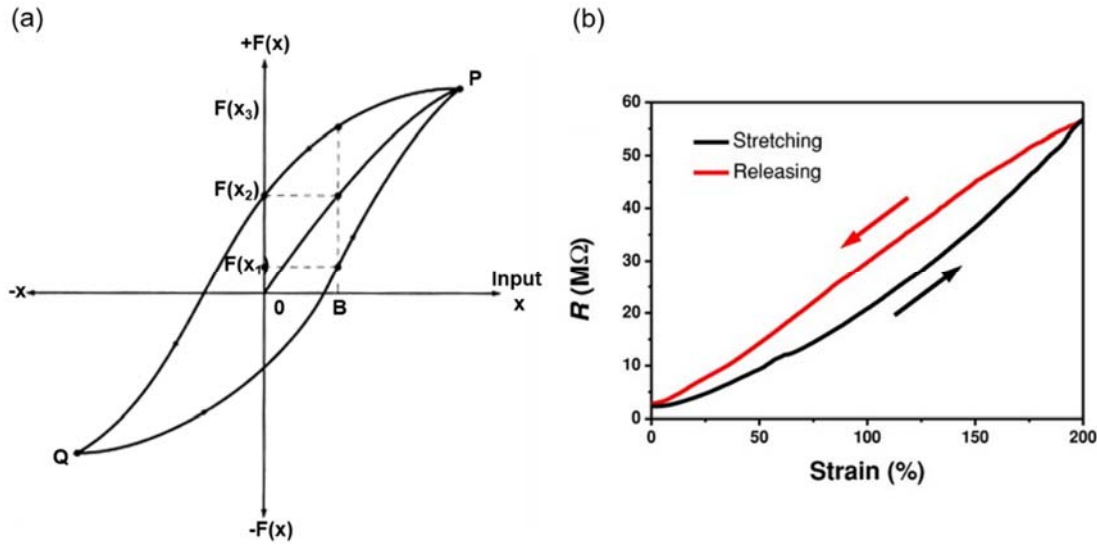


Figure 12: (a) Hysteresis curve [55], [58] and (b) Hysteresis in electrical resistance change as a function of strain change from 0%–200%–0% [53].

The time required by a sensor to change the output to a final settled or steady state value within tolerance band, when an input parameter is changed is called *response time*. The response time is different from time constant of sensor system [55], [58], [59]. Polymer based flexible sensors are associated with large response delays due to inherent viscoelastic nature of polymers [53]. The maximum and minimum values of measurand that can be measured with a sensor specified by upper and lower limits is known as measurand range or span or dynamic range of sensor. All sensors are designed to work over a specified range. If a sensor is operated outside its range it may produce inaccurate results like constant output at maximum input, significant change in sensitivity or cause permanent damage to the sensor [38], [55], [56]. The *accuracy* of a sensor is the maximum difference between sensor output value and true value of a measurand. For example, an oxygen ( $O_2$ ) gas sensor installed in a room operating with 25%  $O_2$  concentration is more accurate if it outputs 25.1% than 24.1% or 26%. To evaluate the sensor accuracy, either it is

benchmarked against a standard measurand or the output value is compared to a measurement system with higher accuracy [56]. Accuracy is measured by absolute and relative error defined as;

- Absolute Error = Sensor output-True value

- Relative Error =  $\frac{\text{Absolute error}}{\text{True Value}}$

*Resolution* is the smallest change of the measurand value necessary to produce a detectable change at the output of the sensor [38]. It is expressed either as a proportion of the reading or in absolute terms. The electrical noise in a sensor's output is the primary factor limiting its resolution. In real use scenario, a sensor or transducer will respond to the measurand under investigation and will also respond to other energy sources that act on the sensor that are not of interest. These are considered sources of noise, for example, when measuring strain with a piezoresistor, the resistance will also change with temperature. *Signal to noise ratio (SNR)* is defined as the ratio of signal power to noise power. SNR considers noise from all sources such as electrical, thermal, optical, environment etc. SNR compares the level of a desired signal to the level of background noise.

## 2.3 Materials

In order to fabricate textiles capable of sensing, we need to impart electrical conductivity to inherently insulating textiles. Electrical conductivity is indicative of charge carrier mobility and is a key requirement for good overall electrical performance of the device. Based on electrical conductivity, materials can be classified as insulators ( $\sigma=10^{-22}$  to  $10^{-12}$  S cm<sup>-1</sup>), semiconductors ( $\sigma=10^{-9}$  to  $10^{-2}$  S cm<sup>-1</sup>), conductors ( $\sigma > 10^2$  S cm<sup>-1</sup>) and superconductors ( $\sigma \sim 10^{20}$  S cm<sup>-1</sup>) [60]. The ranges of conductivity are shown in Figure 13. The choice of materials is critical for development of flexible textile based sensors. Polymer based materials have been used extensively

for fabrication of flexible sensors because of their intrinsic flexibility and tunable chemical and mechanical properties as they are synthesized from basic molecular level. Two major classes of conductive polymers namely intrinsically conducting polymers and conducting polymer composites are discussed here.

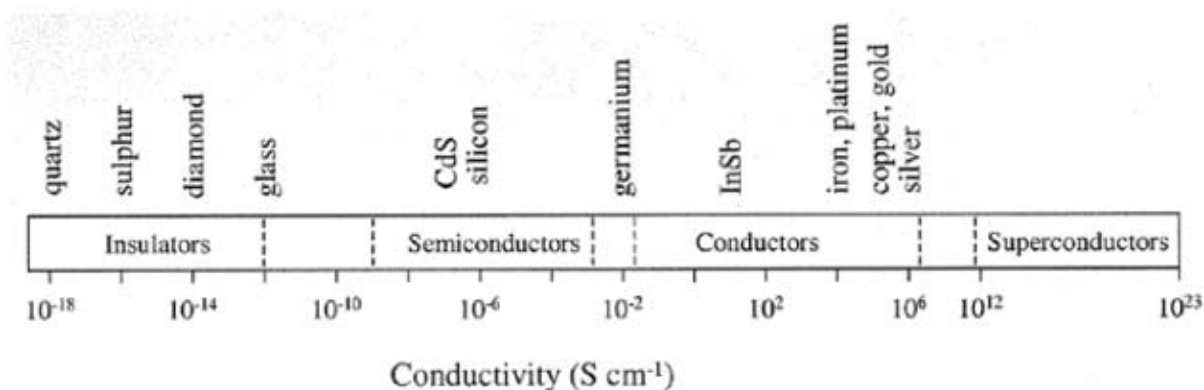


Figure 13: Ranges of conductivity [60]

### ***Intrinsically conducting polymers***

Intrinsically conducting polymers (ICPs) combine the advantages of metals and conventional polymers in terms of electrical conductivity and stretchability respectively [61]. The conductivity of intrinsically conducting polymers lies in the range of semiconductors and conductors ( $\sigma=10^{-9}$  to  $10^6$  S cm<sup>-1</sup>). ICPs have attracted much interest as sensing materials despite their low charge carrier mobility and instability, compared to inorganic semiconductors because of their tunable physical and chemical properties. Most polymers are “saturated” and act as electrical insulators because all available electrons in their structure, which can carry electrical current, are located in the  $\sigma$ -bonds. Intrinsically conducting polymers are characterized by a backbone chain of alternating double and single bonds. These are conducting due to the presence of delocalized  $\pi$ - $\pi$  interactions across their backbone that are able to move more easily along the polymer backbone, because  $\pi$ -electrons are less strongly bound than the  $\sigma$ -electrons [62]–[64].

Another primary factor behind high conductivity of these polymers is the dopant, which introduces, heteroatoms or charge carriers, modifying the  $\pi$  and  $\pi - p$  electron systems, rendering it conductive [65]–[68]. Examples of ICPs are polyaniline (PANI), polypyrrole (PPy), polythiophene (PTh) and poly-(3,4- ethylenedioxythiophene) or PEDOT. PEDOT is one of the most commonly used conducting polymer due to its high conductivity and solution processability [69].

### ***Conducting polymer composites***

Conducting polymer composites refer to insulating polymeric materials that have been made electrically conductive through the incorporation of electrically conducting fillers. In this section only carbon based conducting polymer composites are discussed. Zero, one and two dimensional carbon based materials have extensively been used in flexible sensor fabrication. Zero dimensional materials are spherical particles, one dimensional materials include nanotubes, nanorods, nanowires and two dimensional materials are single layered materials consisting of single layer of atoms [70]. Carbon particles (CP) like carbon black[71], carbon nanotubes (CNTs)[72] and graphene[73] are commonly used carbon compounds in flexible sensors.

The piezoresistive response of a conducting polymer composite (CPC) depends on following factors: (1) characteristics of the fillers like type of the filler, aspect ratio, homogeneity of distribution within the composite; (2) strength of interaction with the polymer chains and percent loading; (3) properties of matrix such as modulus etc.; (4) characteristics of composite like processing technique etc.; and (5) type of external force applied like tensile, compressive etc.

The conduction of electricity in non-conducting polymer with the presence of conductive fillers occurs due to a phenomenon called percolation. Percolation thresholds were first studied by Broadbent and Hammersley in 1957 who introduced lattice models for the flow of fluid through a

static random medium, and showed that no fluid will flow if the concentration of active medium is smaller than some nonzero threshold value[74]. For the polymer composite to be conducting, the conducting network has to be formed from one end of the composite to the other end. A conducting network is formed when electrons can travel from one point to another. This electrical conduction is a function of the concentration of the fillers (reinforcements) which is explained below. The percolation graph has various regimes as shown in Figure 14.

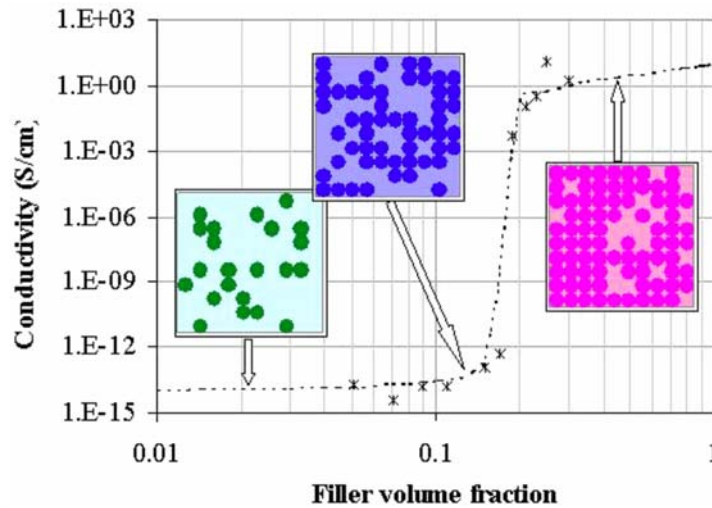


Figure 14: Conductive filler fraction dependence on conductivity of a composite [75]

At low filler concentration, the average distance between particles is large and the composite conductivity is primarily governed by the polymer matrix. With increase in concentration, at a specific volume fraction of the fillers, the distance between particles decreases forming a network that extends across the entire composite. This concentration is called percolation threshold and at this point, there is a substantial increase in the conductivity. Frisch and Hammersley [76] proposed the equation governing conduction;

$$\sigma(\phi) \propto (\phi - \phi_c)^t$$

which shows that just above percolation threshold, the conductivity ( $\sigma$ ) is found to increase with filler concentration ( $\phi$ ). The parameter ‘ $t$ ’ is termed as percolation exponent and is generally between 1.65 and 2 for three dimensional lattices. Those percolating systems with a value of  $t=2$  are termed as universally percolating and  $t=2$  is called universal percolation constant. This definition of percolation applies only for ideal systems which assume infinite resistivity of matrix and infinite conductance in conducting fillers with spherical geometry[32]. This exponential increase in conductivity is due to electron transfer occurring via quantum mechanical tunneling indicating that the distance between conducting particles is  $\leq 10$  nm which is required for tunneling [77]. Addition of conductive fillers beyond percolation threshold does not change the conductivity a lot and theoretically approaches the conductivity of the filler particle. Since, conductivity  $\sigma = e \times n \times \mu$  where ‘ $e$ ’ is the charge, ‘ $n$ ’ the charge carrier concentration and ‘ $\mu$ ’ the mobility of the carrier so beyond percolation threshold even when carrier concentration increases, mobility of the carriers show slow decrease because of increasing interface area between matrix and fillers [74], [76]–[82].

When an external strain is applied onto CPCs, it may lead to the breakdown or the reformation of the conducting network by rotation, alignment and translation of the fillers. If the dominant behavior is the filler separation, resistance will increase, referred as positive piezoresistance but if fillers get closer and form new conducting networks, resistance will decrease which is referred as negative piezoresistance [83]. The only drawback of a conductive elastomeric composite is the sensitivity to environmental temperature and creep due to viscoelastic nature [27]. Individual CNTs and network of CNTs have also been employed directly to create flexible electronics [84], [85]. Graphene[86], [87] is another promising material for flexible sensors due to its unique properties like high intrinsic carrier mobility, remarkable mechanical behavior and high

optical transmittance [21], [27]. The application adaptable electromechanical performance arises from its atomic structure, which consists of atomically thin material made of  $sp^2$  hybridized carbon atoms [32], [33].

## **2.4 Applications of E-textile Sensors**

E-textiles sensors find unique applications wherever flexibility and conformability are required. E-textile sensors are developed for measuring a specific measurand involved in that application, for example, a textile carpet for sensing weight is a force sensor. This section reviews relevant literature with focus on materials, sensor design and working principle of textile based sensors for strain, pressure, temperature, humidity, chemical and gas sensing.

### ***Strain and pressure sensing***

Strain and pressure sensors are two most important mechanical deformation based sensing mechanisms. These sensors detect and transduce any kind of mechanical deformation due to pressing, stretching, bending or twisting into electrical signal. The pressures encountered during daily routine fall into two categories; low pressure regime of less than 10 kPa which is equivalent to gentle touch and medium pressure regime ranging from 10 to 100 kPa which is associated to object manipulation [88]. Here we focus on piezoresistive and capacitive sensing mechanisms only, for strain and pressure sensing because they are used in a large number of flexible sensors and can easily be implemented. This section discusses sensors consisting of fibers and fibrous assemblies (fabrics) used to create strain and pressure sensing e-textiles.

The approach of producing fibers with unique cross-section having a conducting component as one of the constituent is used to fabricate soft sensors for easy integration into textiles. Changsoon, et al fabricated rectangular cross-section capacitive fibers (refer Figure 15 a)

by sandwiching a compliant dielectric layer between conductive materials for strain sensing [89]. Buckled CNT sheets were used as electrodes with silicone rubber as dielectric. Under 200% tensile strain, fibers generated approximately 116% change in capacitance due to decrease in thickness of dielectric layer. The fibers were sewn into glove (Figure 15 b, c) to demonstrate weavability. Frutiger, A. et al. produced fibers consisting of alternating layers of ionically conductive fluid (composed of glycerol, sodium chloride, and polyethylene glycol) as conductors and silicone elastomer as dielectric and encapsulant using custom-designed print head consisting of four coaxially aligned cylindrical nozzles (refer Figure 15 d, e) [90]. These capacitive fibers were used for recording elongation strains and had a gauge factor of 0.35. These fibers were integrated into textiles by sewing and weaving. The fibers sewn into fabric across knee was used to capture the gate cycle of a wearer (shown in Figure 15 f).

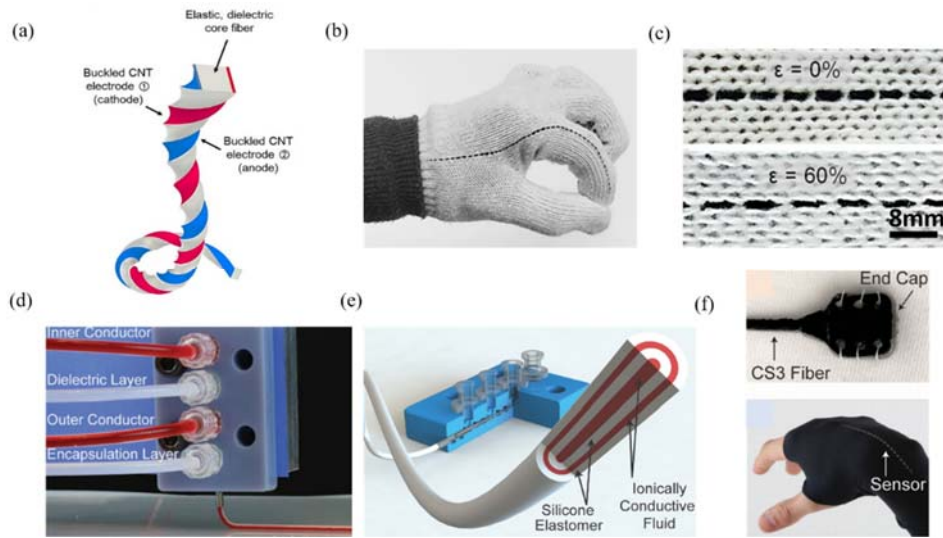


Figure 15 : Capacitive fibers: (a) Sandwich fiber cross section with CNT electrodes separated by dielectric core. (b) 20 cm long fiber woven into a glove. (c) Zoomed in images before and after application of 60% tensile strain [89]. (d) Multicore-shell printing process. (e) Capacitive fiber with ionically conductive fluid as conductor. (f) Sensor integration with textiles via sewing (top) and weaving (bottom) [90].

Electrically functionalizing pre-fabricated yarns with conducting materials is another common technique to create sensors. Wang, R. et al made a core bi-sheath fiber based resistive sensor with buckled multi-walled carbon nanotube sheets (NTS) and buckled rubber on styrene-ethylene-butylene-styrene (SEBS) block copolymer based rubber core elastic fiber [91]. Figure 16 a shows  $\text{NTS}_m@rubber@fiber$  bi-sheath sensor where  $m$  indicates number of NTS layers. When strain decreases, there is an increase in number of buckle contacts by rubber intermediate layer, causing a decrease in resistance. The buckled bi-sheath fiber could be reversibly stretched to 600% strain with linear resistance increase with strain. The sensitivity of these fibers could be tuned by varying the buckling structure. Yuan-Qing, et al fabricated a strain sensor by pyrolysing cotton thread to render it conductive and encapsulating with polydimethylsiloxane (PDMS) elastomer (refer Figure 16 b). This simple wire shaped composite strain sensor showed a highly sensitive piezo-resistive behavior with the gauge factors (GF) 8.7 and 18.5 at low strain of 0–4% and high strain of 8–10%, respectively [92]. In another research, direct coating of conductive composite consisting of carbon black and natural rubber onto polyurethane yarn produced a highly sensitive strain sensor as shown in (refer Figure 16 c) with a gauge factor of 39 [93]. External strains cause variation of the percolated conductive network within sensor, giving electrical signal output and making them possible to detect external stimuli. This yarn strain sensor could detect very small strains as low as 0.1%.

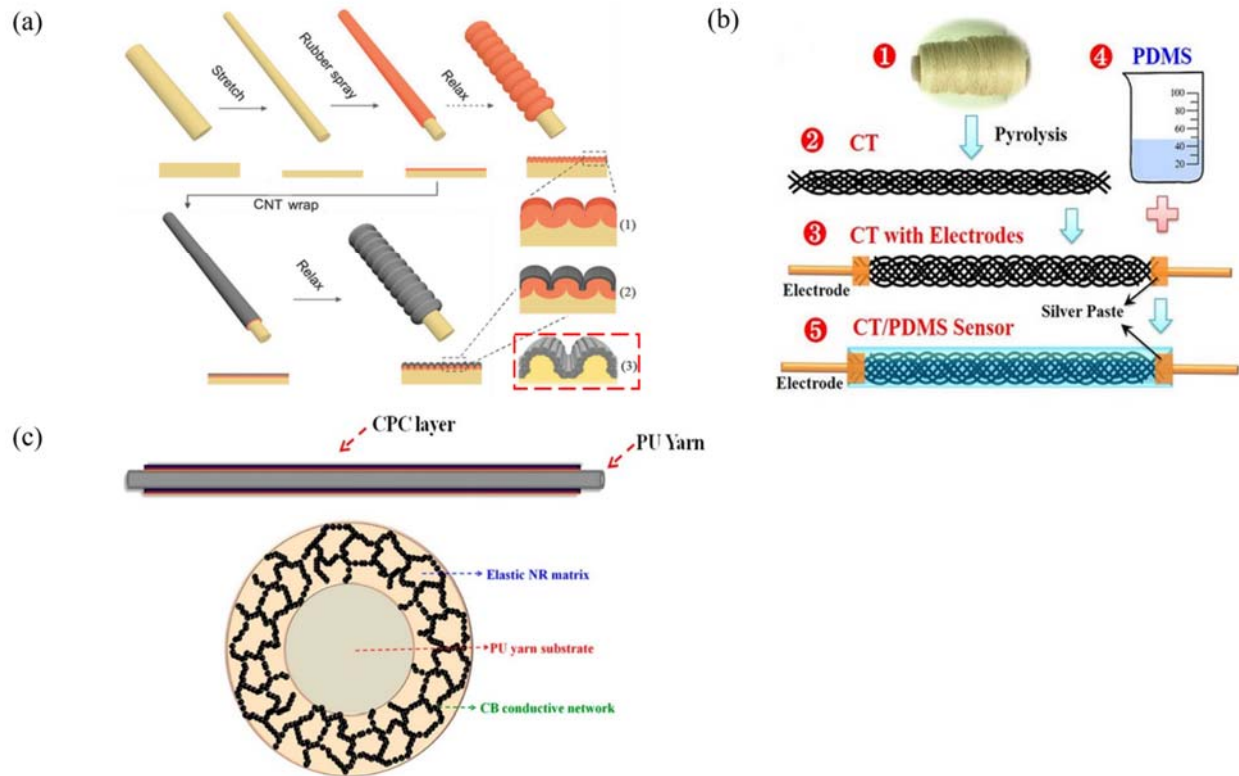


Figure 16 : Sensors made by treatment of pre-fabricated yarns: (a) Steps in the fabrication of bisheath fiber,  $\text{NTS}_m@rubber@fiber$ . The yellow, red, and gray colors are for the SEBS core, the SGE layer, and the NTS sheath, respectively. (3) represents the single sheath fiber,  $\text{NTS}_m@fiber$  [91] (b) Schematics of the fabrication of the wire-shaped strain sensor: (1) cotton thread, (2) CT (carbon thread), (3) CT with electrodes, (4) PDMS resin and (5) CT/PDMS sensor [92] (c) Schematic of conductive polymer composite coated polyurethane yarn (top) and cross section (bottom) [93].

Woven fabric structures provide surface area to create large area sensor arrays and inspired by the structure, where yarns cross each other, researchers have created sensing pixels such that intersection of two electrically functional fibers forms a sensor. This section mentions cross-over configuration based sensors. The structure of woven textiles is considered analogous to multitouch sensor panels in mobile phones and tablets as compared in Figure 17a. Project Jacquard has exploited this characteristic to create touch-sensitive interactive textiles [94]. Lee, J. et al developed a textile based pressure sensor where the crossover point of two conductive fibers formed a capacitive sensor. The conductive fibers were fabricated by coating poly(styrene-block-

butadiene-styrene) (SBS)/silver nanoparticle composite on the surface of Kevlar fiber. The conductive fibers were then coated by poly(dimethyl siloxane) (PDMS) acting as a dielectric layer (refer Figure 17 b) [95]. The capacitance at the crossover point is a function of the load induced thickness change of dielectric layer. The sensor shows two different levels of sensitivity; high sensitivity of  $0.21\text{kPa}^{-1}$  in low pressure range of 0-2kPa and reduced sensitivity of  $0.06\text{kPa}^{-1}$  above 2kPa. This difference is attributed to variation in fiber structure in contact area of orthogonal cross-section of fibers. In another work, conductive cotton fibers made by atomic layer deposition of platinum were coated with a PDMS dielectric layer, creating a capacitive sensor at the intersection of two fibers (refer Figure 17c [12]. These sensors were sewn into cotton fabric to create a large area textile pressure sensor  $50 \times 40\text{ cm}$  for detecting spatial pressure distribution as seat sensor. The sensor showed very high sensitivity due to simultaneous change in contact area of PDMS coated conductive fibers and dielectric thickness.

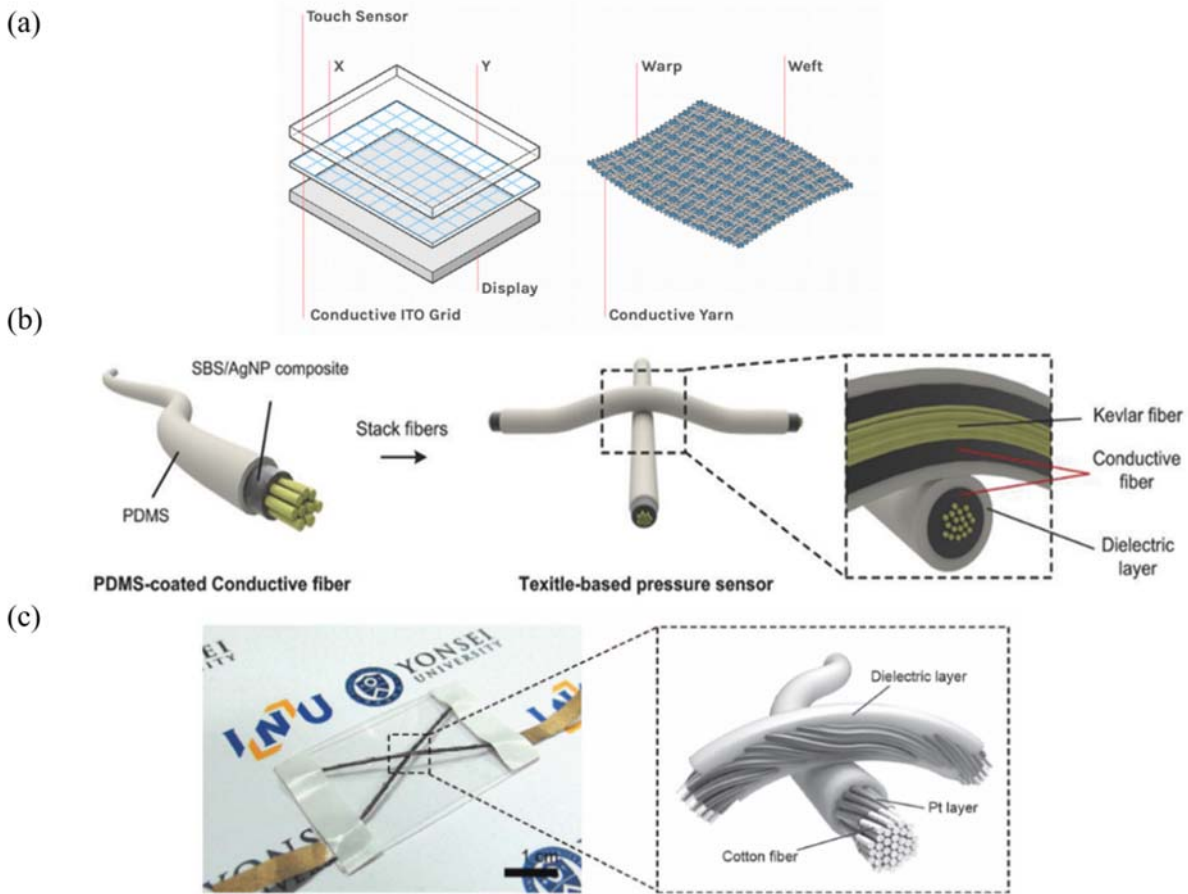


Figure 17 : (a) Textile structure is similar to that of multitouch capacitive panels used in tablets and mobile phones [94] (b) Schematic illustration of the fabrication of the textile-based pressure sensor [95] (c) Textile pressure sensor based on Pt-coated cotton fiber on a polyethylene terephthalate (PET) substrate [12]

Lastly, there are fabric based sensors which here refer to sensors consisting of pre-woven or knit fabric as one of the components of sensor. An alternative viable method for creating large area sensors within garments was proposed by Asli, et al who fabricated a fabric-based capacitive strain sensor where two highly stretchable silver-plated knitted fabrics were separated by a silicone elastomer dielectric layer (refer Figure 18a) [96]. The capacitive response of this sensor depended on two major components: fabric electrode area and silicone dielectric thickness. The capacitive sensor had a gauge factor of 1.23. Ying-Chih, et al developed a resistive fabric sensor consisting

of two stainless-steel threads woven into a textile and a suspended (AgNW (silver nanowire)/PDMS) conducting film (refer Figure 18b) [97]. This is an example of a hybrid system where fiber and film based flexible sensors have been used to create an e-textile. When a pressure is applied, there is current flow due to contact between suspended AgNW network and stainless steel threads. This is referred to as the contact resistance mechanism. The sensor showed very high sensitivity of  $1.04 \times 10^4$  to  $6.57 \times 10^6 \text{ kPa}^{-1}$  in low-pressure regime of less than 3kPa. The surface roughness of conductive film and conductive threads enhanced the sensitivity of contact resistance to applied pressures. Coating fabrics with a conductive material is considered a cost-effective route. A flexible fabric strain sensor was fabricated by deposition of reduced graphene oxide (r-GO) on cotton fabric (refer Figure 18c) [98]. The fabric showed different resistive response under tensile and compressive strain due to variation in structure of conductive layer. The primary reason behind resistance increase to  $\sim 3500 \text{ k}\Omega$  during tensile straining is cracking of r-GO film. In case of compressive strain, the resistance decreased to  $\sim 10 \text{ k}\Omega$ . This is because of reduction in distance between the cotton fibers, causing narrowing of cracks and overlapping of r-GO film in that region.

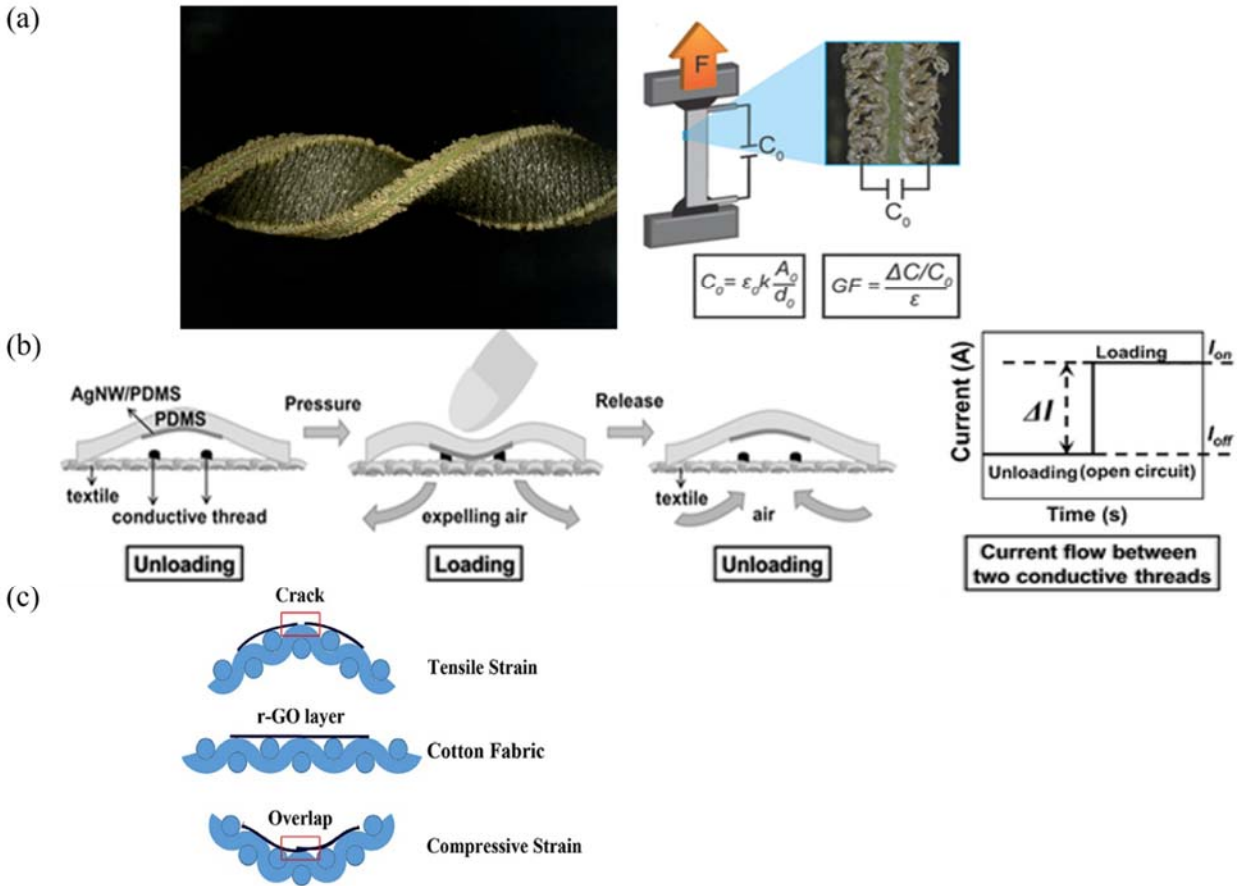


Figure 18 : (a) Twisted fabric based capacitive sensor (left) and diagram of electromechanical test setup and cross-sectional image of the capacitive sensor (right) [96] (b) Schematic illustration of the sensing mechanism of resistive fabric based pressure sensor (left) and current response during loading (right) [97]. (c) Behavior of reduced graphene oxide layer on cotton fabric during tensile and compressive strain [98].

### Temperature and humidity sensing

The human body temperature is an indicator of health condition and determinant factor of performance in various physical activities [11]. Flexible and wearable temperature and humidity sensors can be useful in monitoring temperature and humidity at skin surface or in the ambient environment. There are three major type of temperature sensors namely; resistive temperature detectors, thermistors and pyroelectric detectors.

The resistive temperature detector (RTD) works on principle of change in electrical resistance of metal with temperature. RTDs consist of elements like platinum (Pt), nickel (Ni), copper (Cu), nichrome (NiCr) and related materials [99]. If a semiconductor material such as oxides of nickel, manganese or cobalt replaces the sensing component, metal in RTD, a thermistor is derived [27]. The thermistors whose resistance decreases with an increase in temperature have a negative temperature coefficient of resistance (NTC) and if resistance increases with increase in temperature, it has a positive temperature coefficient of resistance (PTC). A pyroelectric detector generates a transient voltage when a temperature change is applied due to electric polarization. A large number of flexible temperature sensors have been developed on elastomeric substrates or using conducting composites. This is because the conductive elastomeric composites consisting of CNTs, CB or metallic particles display temperature sensitivity due to thermal expansion or contraction of polymer matrix, thereby modifying the percolating conductive network. The temperature coefficient of resistance (TCR),  $\alpha$  can be calculated by:

$$\alpha = (\Delta R / R_0) / (T - T_0)$$

where  $T_0$  is the ambient temperature, and  $R_0$  is the initial resistance.

Wen-Pin, et al fabricated a temperature sensor by depositing a graphite-PDMS composite on polyimide film whose resistance changes with ambient temperature variation. The TCRs of the composites are  $0.042 \text{ K}^{-1}$  and  $0.286 \text{ K}^{-1}$  for the graphite volume fractions of 25% and 15%, respectively [100]. In another work, a stretchable thermistor using graphene as thermal detector and silver nanowires as electrodes, embedded in PDMS matrix was fabricated (refer Figure 19a). The sensor displayed a negative temperature coefficient (NTC) behavior as shown in Figure 19b where at a fixed voltage of 10 V, the current of the device increased from  $0.79 \mu\text{A}$  at  $30^\circ\text{C}$  to  $1.34 \mu\text{A}$  at  $100^\circ\text{C}$ . There was a decrease in resistance with increasing temperature indicating NTC

behavior and this functionality was maintained even at high strains (refer Figure 19c) [101]. Sibinski, et al manufactured flexible sensors for e-textiles on polyvinylidene fluoride (PVDF) monofilament (refer Figure 19d) operating in temperature range of 30–42 °C. PVDF was chosen primarily because of its sufficient thermal resistance and coating adhesion. The temperature sensitive layer consisted of 2% multiwalled carbon nanotubes filled poly (methyl methacrylate) (PMMA) polymer. The sensor displayed a negative temperature coefficient response and had a TCR of 0.13%/K [102].

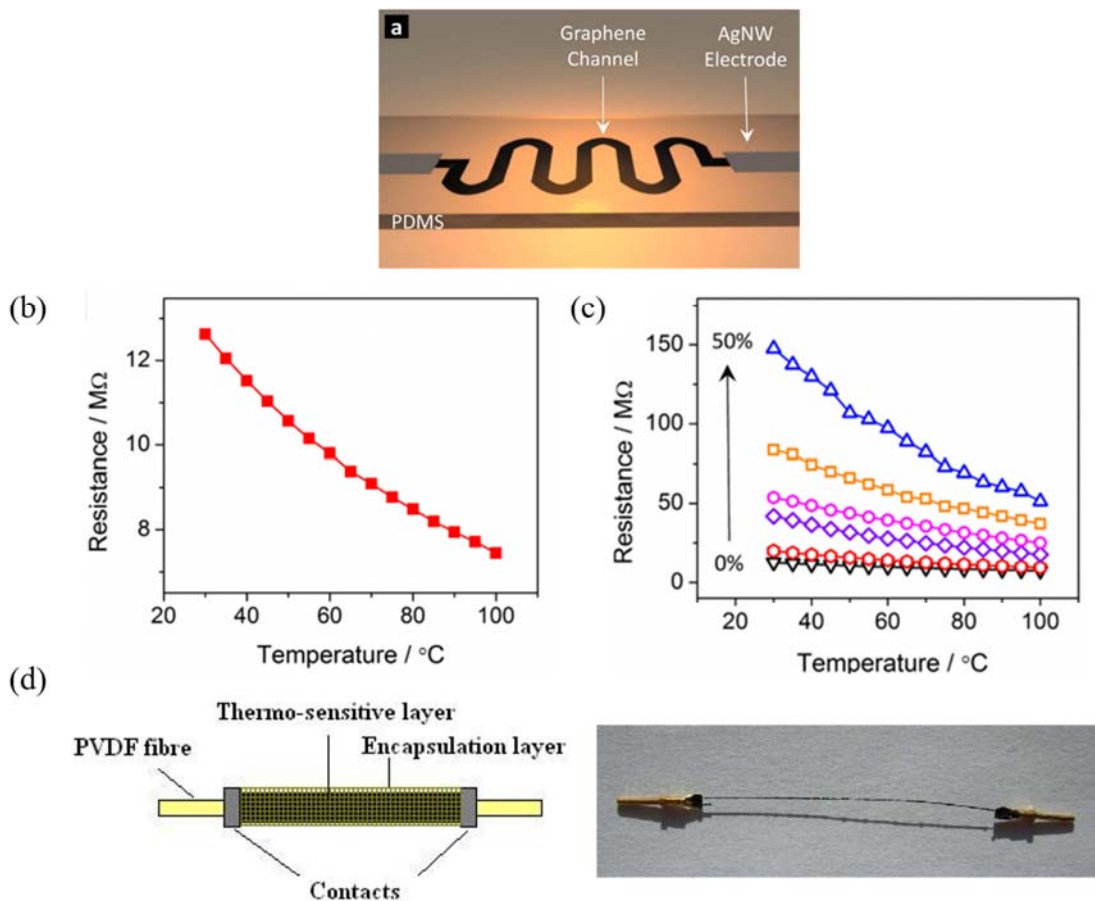


Figure 19: (a) Schematic of a stretchable graphene thermistor. (b) Resistance variation with temperature at 0% strain showing a nonlinear relationship. (c) Resistance variation with temperature (30-100°C) within 0-50% strains [101] (d) Thermistor structure (left) and flexible temperature sensor on yarn with contact connectors (right) [102]

Flexible humidity sensors based on resistive and capacitive sensing principles have received much attention because of their high sensitivity and simple circuitry [103]. The resistive humidity sensors show a change in electrical conductivity or impedance with moisture variation [69]. The underlying mechanism causing resistance variation may be proton conduction [104], [105], electron tunneling due to change in average tunneling barrier width [106] or polymer swelling due to absorption of water molecules [107]. Most of the organic humidity sensors consist of conductive fillers like CB [108], CNTs [109] and swellable polymers such as polyvinyl alcohol (PVA) [108], polyacrylic acid (PAA) [110] and cellulose[111]. A humidity sensing yarn was fabricated by dipping MWCNT yarn into a PVA solution and drying. CNTs were selected due to their high electrical conductivity and sensitivity to water vapor. The electrical resistance of sensing yarns was constant at low relative humidity (RH) but showed a sharp increase at or beyond 75% which is good humidity switch characteristic [109]. The reason behind the decrease of electrical resistance was increased number of conductive paths in presence of water. This is attributed to swelling of PVA matrix leading to electronic donation of absorbed water molecules on the CNTs surface (refer Figure 20a). There was an increase in initial resistance of composite yarns with increase in PVA content as shown in Figure 20b due to presence of electrically insulating PVA between MWCNTs [109]. A flexible ambient environment monitoring sensing system was fabricated on PI substrate with gold resistance temperature sensor (RTDs) and PEDOT-PSS resistive type humidity sensor (refer *Figure 20c*). The sensor showed an increase in resistance up to 60% RH due to presence of water molecules between PEDOT chains. There was decrease in sensitivity at higher RH levels due to dissolution of PSS (polystyrenesulfonate) protons. The sensor was also woven into a textile using band weaving machine [112].

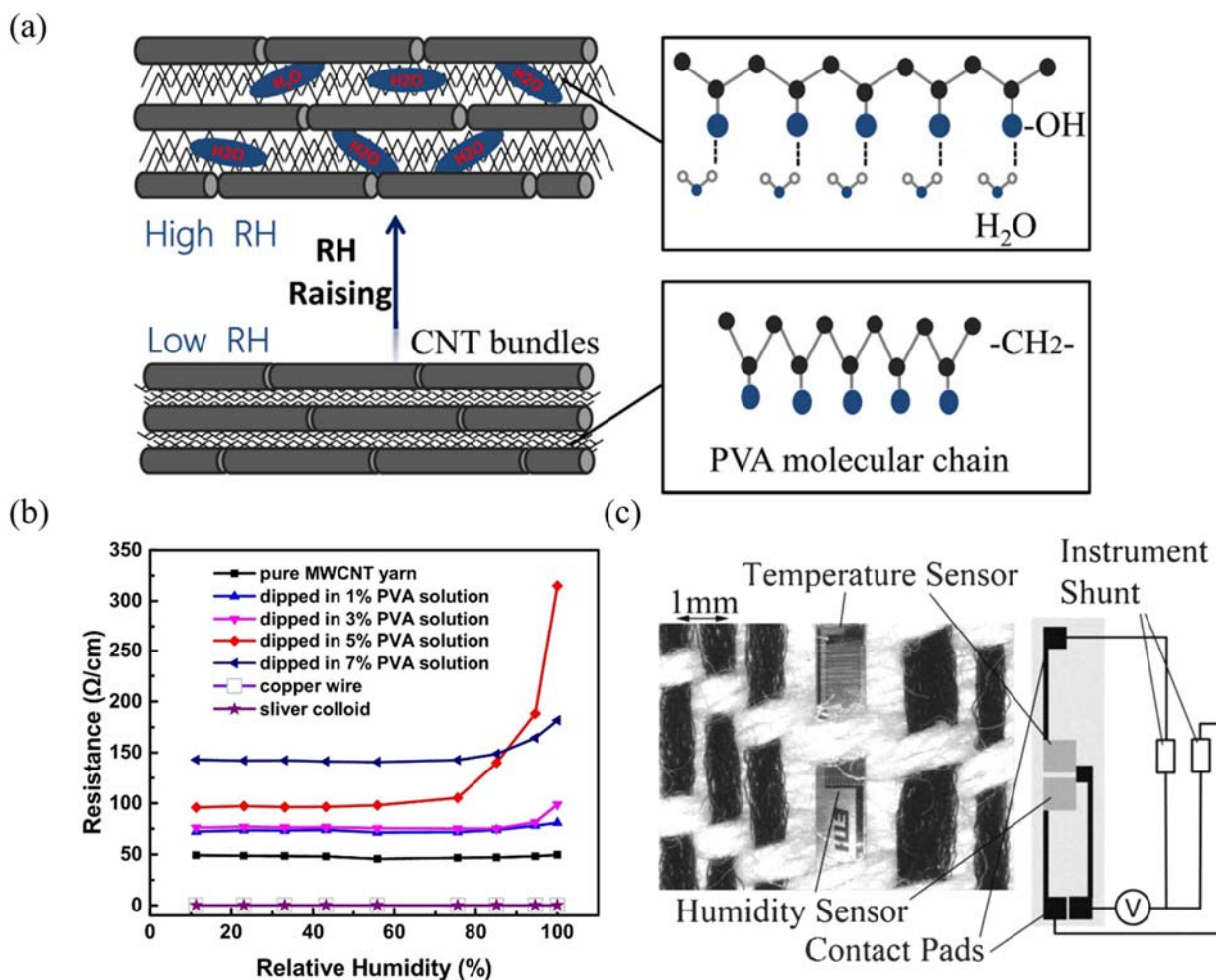


Figure 20: (a) Swelling of MWCNT/PVA coating layer of a composite yarn during moisture absorption process. (b) Resistances of various test samples as a function of relative humidity [109]. (c) Humidity and temperature sensor in a woven textile band (left) and schematic for measuring a sensor unit in a textile (right) [112].

### Chemical and Gas sensing

Detection of toxic gases and chemicals is of importance in the workplace and as a safety measure in unknown environments. For any kind of chemical sensing integrated with electronic devices, a binding event or reaction is transduced to a change in conductance of device. The devices primarily used for chemical and gas sensing include: electrochemical electrodes,

chemically sensitive resistors or chemiresistors and transistors [99] but only chemiresistors are discussed here. Sensitivity for these sensors can be calculated as;

$$(R_{\text{gas}} - R_{\text{air}})/R_{\text{gas}} \times 100,$$

where  $R_{\text{gas}}$  and  $R_{\text{air}}$  are the electrical resistances in presence of gas to be detected and clean air, respectively. Fabric based chemical sensors made by coating conducting polymer provide a wide dynamic range of sensing due to their large surface area [113]. A fabric based ammonia gas sensor was fabricated by in situ polymerization of polyaniline (PANI), on the surface of nylon 6. PANI is an intrinsically conducting polymer and a promising candidate for gas sensing due to observable physical property changes at room temperature. There was an increase in resistance of PANI–nylon 6 composite fabrics in presence of  $\text{NH}_3$  gas because PANI is a p-type conductor and  $\text{NH}_3$ , as a strong reductant, eliminates free hole charge carriers, causing a drop in conductivity. The fabric sensor could be reversed after blowing fresh air [114]. In a recent work, metal organic frameworks (MOFs), were employed as sensing materials at fiber level to create textile based chemiresistive sensors (refer Figure 21). MOFs consist of coordination bonds between transition-metal cations and multidentate organic linkers and are used for gas storage, catalysis and sensing applications. A conformal coating of MOFs on cotton and polyester fabrics was obtained by direct solution phase self-assembly. These e-textiles could detect target gaseous analytes,  $\text{H}_2\text{S}$  and  $\text{NO}$  which are considered as dangerous pollutants [115].

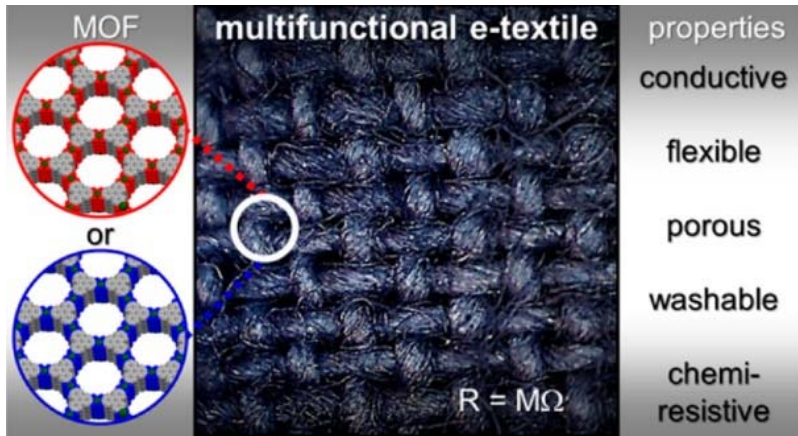


Figure 21 : Metal organic frameworks (MOFs) coated on textiles [115]

The above-discussed textile based sensing technologies for quantifying measurands like strain, pressure, temperature and humidity find three major on body applications; namely, biosignal monitoring, human motion detection and interactive wearables.

### ***Biosignal monitoring***

Biosignals are the vital signs which are the indicators of health and fitness of an individual. These include body temperature, heart rate, respiration rate, blood pressure and pulse. Wearable sensors provide the facility of long term, continuous monitoring of these vital signs, which can be useful in early diagnosis. Sensors can be mounted on different locations on body to retrieve the biosignal of interest as shown in *Figure 22 a, b*. Wrist and chest are two prime body locations, which can provide multiple signals. For measurement of body temperature, thermistor configuration is most common in wearable sensors [116]–[118]. Heart rate, expressed as beats per minute (b.p.m.) is the sequence of cycling deoxygenated blood through lungs and pumping newly oxygenated blood through aorta. The technique of picking up depolarization signal from heart muscles using skin electrodes is electrocardiography (ECG) [117]. Silver/Silver Chloride (Ag/AgCl) gel electrode is the gold standard for ECG measurement. Dry elastomer based [119], [120] (refer *Figure 22c*) and textile based[121] ECG electrodes have been implemented but they

have yet not been completely accepted for medical use because of inferior quality signal owing to high skin to electrode impedance due to poor contact and susceptibility to motion artifacts [122], [123]. Respiration rate is another critical vital sign involving inflow of oxygen and removal of carbon dioxide. In order to measure respiration rate, sensing element should physically expand and contract with lungs so strain or pressure sensing mechanism is suitable [117]. A comfortable respiration belt consisting of a knitted sensor and an inelastic textile strap as shown in Figure 22d was realized, where volume change induced strain during respiration, was transduced by resistive sensing [124]. Another textile based respiration belt working on principle of capacitive sensing was designed where there was a capacitive response due to overlapping area change during respiration [125]. Similar sensing and transduction principles can be used to monitor blood pressure and pulse. Blood pressure is represented by two numbers referring to peak pulse pressure (systolic) and lowest pressure (diastolic).

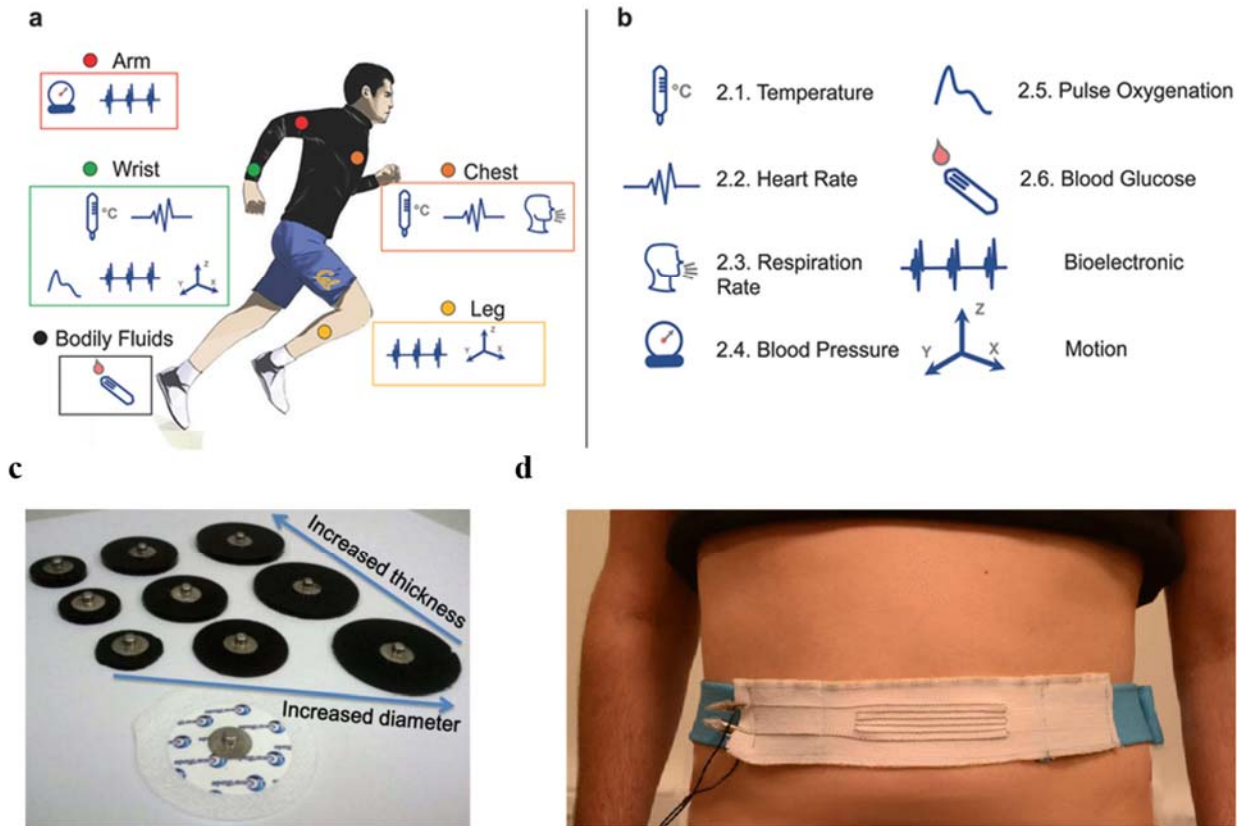


Figure 22: (a) Biosignals grouped according to sensing locations on body. (b) Description of symbols representing biosignals [117]. (c) CNT/PDMS electrodes and the Ag/AgCl electrode [120] for ECG monitoring. (d) Textile based respiration belt worn by subject [124].

### ***Human motion detection***

Wearable sensors can be used to monitor human activity and retrieve useful information related to posture, walking and flexibility which can be used in clinical evaluation and for studying body movement during sports and rehabilitation practices. There can be two kinds of human body motions, one involving tiny displacements or strains for example while speaking and other involving large strains such as gait cycle of a person. Resistive sensors are preferred in low strain motions due to high sensitivity and capacitive for high strain motions due to linearity and low hysteresis [39]. Skin mountable sensors have been used to record and study tiny motions like finger bending (*Figure 23a*) [92], wrist bending [41], throat movement while speaking [53] and elbow

joint movement [44]. In case of large strain motions, capacitive fibers were sewn onto textiles and were used to capture gait cycle of wearer (refer *Figure 23b*) [90]. Strain sensors attached on knee were also used to study different walking patterns involving extending, squatting and marching (refer *Figure 23c*). These motions are common in daily physical activities and involve different anatomical strains in different regions of body [45], [91].

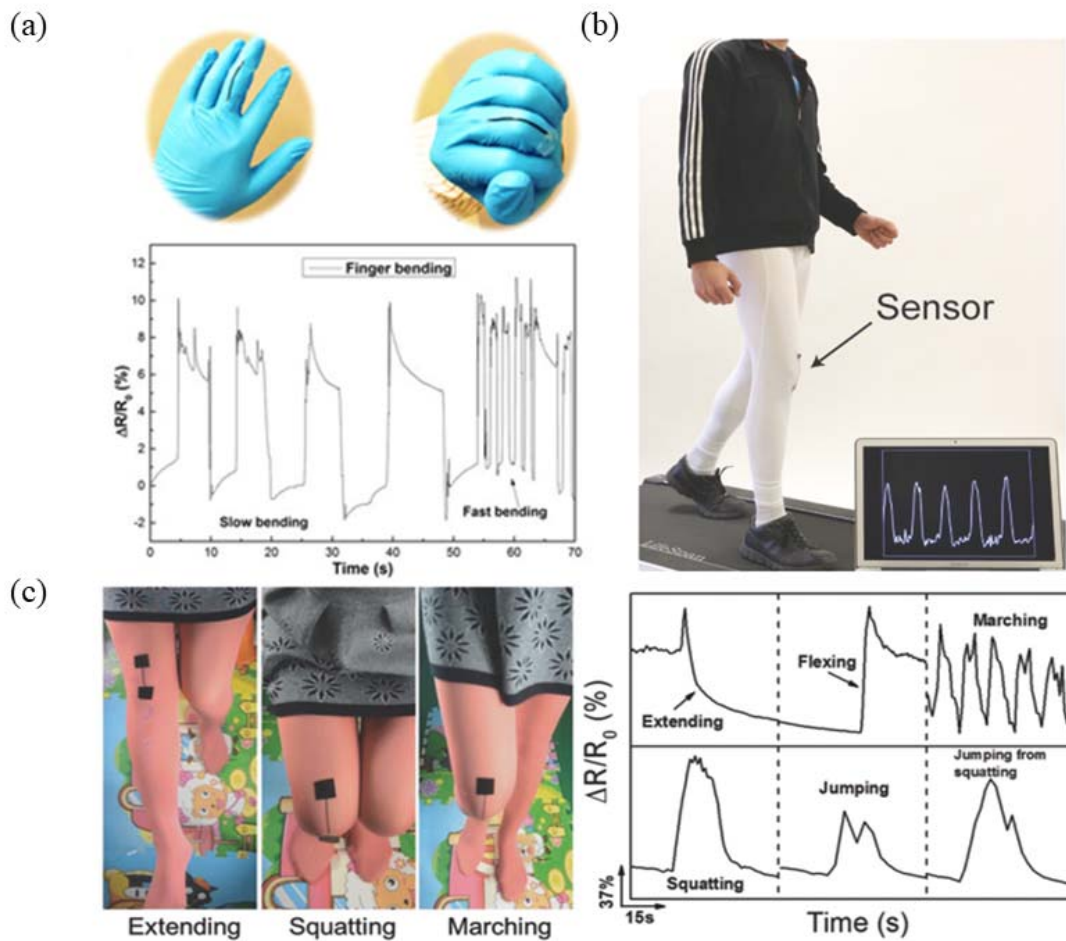


Figure 23: a) Monitoring finger motion while bending [92]. (b) Capturing gait cycle of wearer [90]. (c) Strain sensor attached on knee for different walking patterns involving extending, squatting and marching [91].

### *Interactive wearables*

The signals from wearable sensors can be used to build smart human-computer interfaces and control robots. Current technologies focus a lot on user interactivity via human gesture. In this regard, stretchable and conformable wearable sensors embedded with user interactivity can be useful in medical training and therapy applications besides wearable robotics. The most common way is to incorporate sensors in gloves and track hand motions [43], [126]. An elastomeric strain sensor was embedded in glove which showed a particular pattern of resistance change for different hand positions (refer Figure 24a) [43]. Morteza, et al used the similar concept and used the finger motion to control an avatar in virtual environment where bending of fingers by user leads to bending of avatar fingers [51] as shown in Figure 24b. This was possible by a custom-made data acquisition system along with Bluetooth communication circuit. Sewing fiber based pressure sensors onto fingers of a textile glove created a smart glove capable of controlling a drone [95]. Each finger motion corresponded to a particular motion of drone.

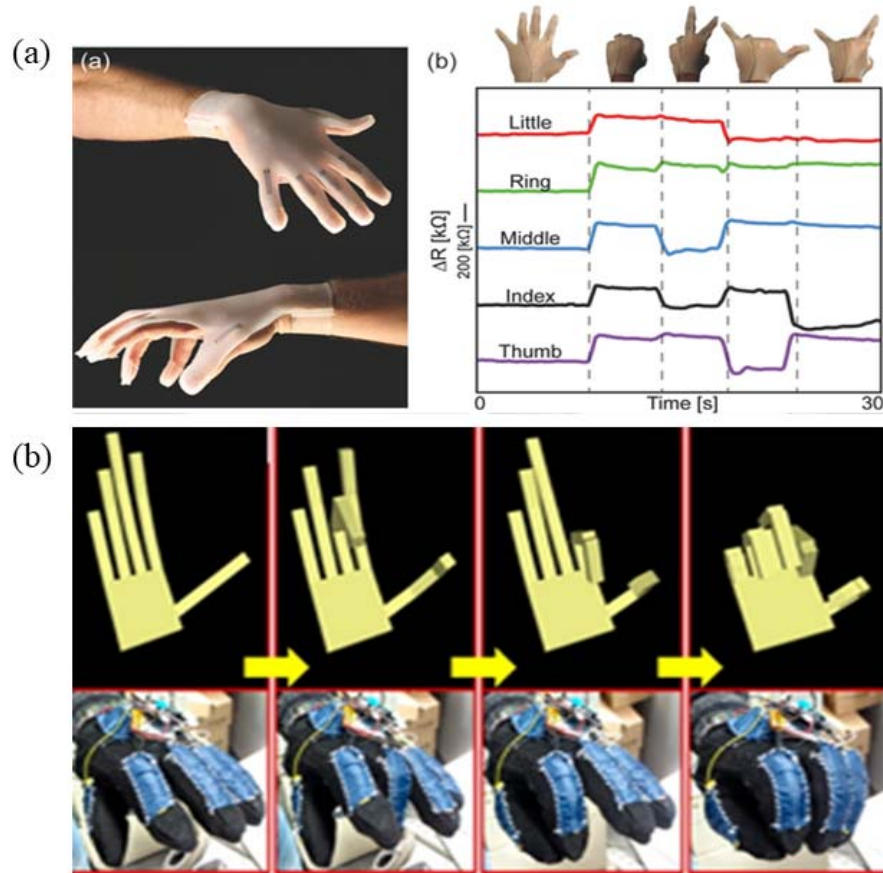


Figure 24: Wearable sensors used as interactive devices: (a) Glove with embedded strain sensors (left) showing electrical resistance change at different hand positions [43]. (b) Control of avatar using smart glove having sensors [51].

## 2.5 Summary and outlook

In this review, e-textiles with sensing functionality were focused. It highlights different sensing principles like resistive, capacitive, piezoelectric, optical, etc. Conducting materials used to fabricate flexible sensors were introduced namely; intrinsically conducting polymers and conducting polymer composites. The common performance indicators for sensor evaluation and comparison such as, hysteresis, linearity, sensitivity, speed of response, etc. are discussed. In the later part, applications of e-textile sensors for strain, pressure, temperature, humidity and chemical

sensing are discussed with focus on materials, structure and their working principle. For temperature sensing, RTDs are primarily used. Flexible humidity sensors based on resistive principle are common. The devices primarily used for chemical sensing are chemically sensitive resistors or chemiresistors. In the last section, three primary, on body applications of all the above discussed flexible and e-textile based sensing technologies were discussed, namely, biosignal monitoring, human motion detection and interactive wearables.

Based on this review, it was found that most of the sensors had one sensing functionality and were manufactured using batch fabrication techniques. There was also no focus on comfort aspect of fabrics when electrical properties are imparted. Enabling electrical functionalities in textiles while preserving the desirable textile qualities such as softness, comfort, flexibility, porosity and texture, is one of the biggest challenges in developing e-textiles. Also, the current high cost of available e-textile products hinders large-scale consumer adoption. The cost can be lowered by focusing on roll-to-roll processing of these products at large scale. Multifunctional e-textiles capable of sensing more than one property, like pressure along with temperature, will further help in this regard by providing more value within a single product. These gaps have motivated this thesis research which focuses on producing multifunctional fiber based sensors in roll-to-roll fashion which can be manufactured using conventional fiber formation techniques and woven to produce e- textiles capable of sensing more than one property.

## References

- [1] S. Coyle *et al.*, “BIOTEX—Biosensing Textiles for Personalised Healthcare Management,” *IEEE Transactions on Information Technology in Biomedicine*, vol. 14, no. 2, pp. 364–370, Mar. 2010, doi: 10.1109/TITB.2009.2038484.
- [2] R. Paradiso, G. Loriga, N. Taccini, A. Gemignani, and B. Ghelarducci, “WEALTHY – a wearable healthcare system: new frontier on e-textile,” p. 9.
- [3] “Fitness | DuPont™ Intexar™.” [Online]. Available: <http://electronicmaterials.dupont.com/intexar-performance>. [Accessed: 27-Nov-2018].
- [4] C. T. inc (Hexoskin), “Hexoskin Smart Shirts - Cardiac, Respiratory, Sleep & Activity Metrics,” *Carre Technologies inc (Hexoskin)*. [Online]. Available: <https://www.hexoskin.com/>. [Accessed: 27-Nov-2018].
- [5] S. Patel, H. Park, P. Bonato, L. Chan, and M. Rodgers, “A review of wearable sensors and systems with application in rehabilitation,” *Journal of NeuroEngineering and Rehabilitation*, vol. 9, p. 21, Apr. 2012, doi: 10.1186/1743-0003-9-21.
- [6] M. Bariya, H. Y. Y. Nyein, and A. Javey, “Wearable sweat sensors,” *Nat Electron*, vol. 1, no. 3, pp. 160–171, Mar. 2018, doi: 10.1038/s41928-018-0043-y.
- [7] “(PDF) Introduction and Classification of Sensors,” *ResearchGate*. [Online]. Available: [https://www.researchgate.net/publication/321625555\\_Introduction\\_and\\_Classification\\_of\\_Sensors](https://www.researchgate.net/publication/321625555_Introduction_and_Classification_of_Sensors). [Accessed: 24-Oct-2018].
- [8] K.-S. CHEN, “PART 7. TRANSDUCTION PRINCIPLE,” 1999.
- [9] Y. Sun, S. E. Thompson, and T. Nishida, *Strain Effect in Semiconductors: Theory and Device Applications*. Springer Science & Business Media, 2009.

- [10] M. Taya, W. J. Kim, and K. Ono, "Piezoresistivity of a short fiber/elastomer matrix composite," *Mechanics of Materials*, vol. 28, no. 1, pp. 53–59, Jul. 1998, doi: 10.1016/S0167-6636(97)00064-1.
- [11] T. Q. Trung and N.-E. Lee, "Flexible and Stretchable Physical Sensor Integrated Platforms for Wearable Human-Activity Monitoring and Personal Healthcare," *Adv. Mater.*, vol. 28, no. 22, pp. 4338–4372, Jun. 2016, doi: 10.1002/adma.201504244.
- [12] J. Lee *et al.*, "Highly conductive and flexible fiber for textile electronics obtained by extremely low-temperature atomic layer deposition of Pt," *NPG Asia Mater*, vol. 8, no. Journal Article, p. e331, 2016.
- [13] P. Madaan and P. Kaur, "CAPACITIVE SENSING MADE EASY, Part 1: An Introduction to Different Capacitive Sensing Technologies," p. 8, 2012.
- [14] G. Walker, "A review of technologies for sensing contact location on the surface of a display," *Jnl Soc Info Display*, vol. 20, no. 8, pp. 413–440, Aug. 2012, doi: 10.1002/jsid.100.
- [15] J. Schöning *et al.*, "Multi-Touch Surfaces: A Technical Guide," p. 19.
- [16] G. Barrett, "Projected-Capacitive Touch Technology," p. 6.
- [17] D. Fischer, "Capacitive Touch Sensors," p. 12.
- [18] G. Walker, "Part 1: Fundamentals of Projected-Capacitive Touch Technology," p. 315.
- [19] M. S. Sarwar, Y. Dobashi, C. Preston, J. K. M. Wyss, S. Mirabbasi, and J. D. W. Madden, "Bend, stretch, and touch: Locating a finger on an actively deformed transparent sensor array," *Science Advances*, vol. 3, no. 3, p. e1602200, Mar. 2017, doi: 10.1126/sciadv.1602200.
- [20] J. Fortin, "Transduction Principles," in *Functional Thin Films and Nanostructures for Sensors: Synthesis, Physics and Applications*, A. Zribi and J. Fortin, Eds. Boston, MA: Springer US, 2009, pp. 17–29.

- [21] X. Wang, Z. Liu, and T. Zhang, "Flexible Sensing Electronics for Wearable/Attachable Health Monitoring," *Small*, vol. 13, no. 25, p. 1602790, Jul. 2017, doi: 10.1002/sml.201602790.
- [22] W. G. Cady, "Piezoelectricity McGraw-Hill Book Co," *Inc., New York*, vol. 125, 1946.
- [23] F. Wang, "Soft Tactile Sensors for Human-Machine Interaction," *Handbook of Smart Textiles*, pp. 317–355, 2015.
- [24] A. Lund, C. Jonasson, C. Johansson, D. Haagenen, and B. Hagström, "Piezoelectric polymeric bicomponent fibers produced by melt spinning," *J. Appl. Polym. Sci.*, vol. 126, no. 2, pp. 490–500, Oct. 2012, doi: 10.1002/app.36760.
- [25] J. Edmison, M. Jones, Z. Nakad, and T. Martin, "Using piezoelectric materials for wearable electronic textiles," in *Proceedings. Sixth International Symposium on Wearable Computers*, 2002, pp. 41–48, doi: 10.1109/ISWC.2002.1167217.
- [26] D. V. Bayramol, N. Soin, T. Shah, E. Siores, D. Matsouka, and S. Vassiliadis, "Energy Harvesting Smart Textiles," in *Smart Textiles*, Springer, Cham, 2017, pp. 199–231.
- [27] T. Yang, D. Xie, Z. Li, and H. Zhu, "Recent advances in wearable tactile sensors: Materials, sensing mechanisms, and device performance," *Materials Science and Engineering: R: Reports*, vol. 115, no. Supplement C, pp. 1–37, May 2017, doi: 10.1016/j.mser.2017.02.001.
- [28] W. H. Liew, M. S. Mirshekarloo, S. Chen, K. Yao, and F. E. H. Tay, "Nanoconfinement induced crystal orientation and large piezoelectric coefficient in vertically aligned P(VDF-TrFE) nanotube array," *Scientific Reports*, vol. 5, p. 09790, May 2015, doi: 10.1038/srep09790.
- [29] J. Hillenbrand and G. M. Sessler, "Piezoelectricity in cellular electret films," *IEEE Transactions on Dielectrics and Electrical Insulation*, vol. 7, no. 4, pp. 537–542, Aug. 2000, doi: 10.1109/94.868074.

- [30] X. Zhang, J. Hillenbrand, and G. M. Sessler, “Ferroelectrets with improved thermal stability made from fused fluorocarbon layers,” *Journal of Applied Physics*, vol. 101, no. 5, p. 054114, Mar. 2007, doi: 10.1063/1.2562413.
- [31] S. R. Moheimani and A. J. Fleming, “Fundamentals of piezoelectricity,” *Piezoelectric transducers for vibration control and damping*, pp. 9–35, 2006.
- [32] Y. Zang, F. Zhang, C. Di, and D. Zhu, “Advances of flexible pressure sensors toward artificial intelligence and health care applications,” *Materials Horizons*, vol. 2, no. 2, pp. 140–156, 2015, doi: 10.1039/C4MH00147H.
- [33] M. L. Hammock, A. Chortos, B. C.-K. Tee, J. B.-H. Tok, and Z. Bao, “25th Anniversary Article: The Evolution of Electronic Skin (E-Skin): A Brief History, Design Considerations, and Recent Progress,” *Adv. Mater.*, vol. 25, no. 42, pp. 5997–6038, Nov. 2013, doi: 10.1002/adma.201302240.
- [34] C. Yan, E. Ferraris, and D. Reynaerts, “A pressure sensing sheet based on optical fibre technology,” *Procedia Engineering*, vol. 25, no. Supplement C, pp. 495–498, Jan. 2011, doi: 10.1016/j.proeng.2011.12.123.
- [35] A. J. Rogers, “Polarization-optical time domain reflectometry: a technique for the measurement of field distributions,” *Appl. Opt., AO*, vol. 20, no. 6, pp. 1060–1074, Mar. 1981, doi: 10.1364/AO.20.001060.
- [36] A. Grillet *et al.*, “Optical Fiber Sensors Embedded Into Medical Textiles for Healthcare Monitoring,” *IEEE Sensors Journal*, vol. 8, no. 7, pp. 1215–1222, Jul. 2008, doi: 10.1109/JSEN.2008.926518.
- [37] M. Kretschmar and S. Welsby, “Chapter 8—Capacitive and Inductive Displacement Sensors,” *Sensor Technology Handbook (Jon Wilson, Newnes)*, vol. 2, pp. 103–222, 2005.

- [38] S. M. Sze and others, *Semiconductor sensors*, vol. 55. Wiley New York, 1994.
- [39] M. Amjadi, K.-U. Kyung, I. Park, and M. Sitti, “Stretchable, Skin-Mountable, and Wearable Strain Sensors and Their Potential Applications: A Review,” *Adv. Funct. Mater.*, vol. 26, no. 11, pp. 1678–1698, Mar. 2016, doi: 10.1002/adfm.201504755.
- [40] M. Hempel, D. Nezich, J. Kong, and M. Hofmann, “A Novel Class of Strain Gauges Based on Layered Percolative Films of 2D Materials,” *Nano Lett.*, vol. 12, no. 11, pp. 5714–5718, Nov. 2012, doi: 10.1021/nl302959a.
- [41] N. Lu, C. Lu, S. Yang, and J. Rogers, “Highly Sensitive Skin-Mountable Strain Gauges Based Entirely on Elastomers,” *Advanced Functional Materials*, vol. 22, no. 19, pp. 4044–4050, Oct. 2012, doi: 10.1002/adfm.201200498.
- [42] C. Mattmann, F. Clemens, and G. Tröster, “Sensor for Measuring Strain in Textile,” *Sensors*, vol. 8, no. 6, pp. 3719–3732, Jun. 2008, doi: 10.3390/s8063719.
- [43] J. T. Muth *et al.*, “Embedded 3D Printing of Strain Sensors within Highly Stretchable Elastomers,” *Adv. Mater.*, vol. 26, no. 36, pp. 6307–6312, Sep. 2014, doi: 10.1002/adma.201400334.
- [44] M. Amjadi, Y. J. Yoon, and I. Park, “Ultra-stretchable and skin-mountable strain sensors using carbon nanotubes–Ecoflex nanocomposites,” *Nanotechnology*, vol. 26, no. 37, p. 375501, 2015, doi: 10.1088/0957-4484/26/37/375501.
- [45] T. Yamada *et al.*, “A stretchable carbon nanotube strain sensor for human-motion detection,” *Nat Nano*, vol. 6, no. 5, pp. 296–301, May 2011, doi: 10.1038/nnano.2011.36.
- [46] L. Cai *et al.*, “Super-stretchable, Transparent Carbon Nanotube-Based Capacitive Strain Sensors for Human Motion Detection,” *Scientific Reports*, vol. 3, p. 3048, Oct. 2013, doi: 10.1038/srep03048.

- [47] U.-H. Shin, D.-W. Jeong, S.-M. Park, S.-H. Kim, H. W. Lee, and J.-M. Kim, “Highly stretchable conductors and piezocapacitive strain gauges based on simple contact-transfer patterning of carbon nanotube forests,” *Carbon*, vol. 80, pp. 396–404, Dec. 2014, doi: 10.1016/j.carbon.2014.08.079.
- [48] D. J. Cohen, D. Mitra, K. Peterson, and M. M. Maharbiz, “A Highly Elastic, Capacitive Strain Gauge Based on Percolating Nanotube Networks,” *Nano Lett.*, vol. 12, no. 4, pp. 1821–1825, Apr. 2012, doi: 10.1021/nl204052z.
- [49] Y. R. Jeong, H. Park, S. W. Jin, S. Y. Hong, S.-S. Lee, and J. S. Ha, “Highly Stretchable and Sensitive Strain Sensors Using Fragmentized Graphene Foam,” *Advanced Functional Materials*, vol. 25, no. 27, pp. 4228–4236, Jul. 2015, doi: 10.1002/adfm.201501000.
- [50] C. S. Boland *et al.*, “Sensitive, High-Strain, High-Rate Bodily Motion Sensors Based on Graphene–Rubber Composites,” *ACS Nano*, vol. 8, no. 9, pp. 8819–8830, Sep. 2014, doi: 10.1021/nm503454h.
- [51] M. Amjadi, A. Pichitpajongkit, S. Lee, S. Ryu, and I. Park, “Highly stretchable and sensitive strain sensor based on silver nanowire–elastomer nanocomposite,” *ACS nano*, vol. 8, no. 5, pp. 5154–5163, 2014.
- [52] S. Yao and Y. Zhu, “Wearable multifunctional sensors using printed stretchable conductors made of silver nanowires,” *Nanoscale*, vol. 6, no. 4, pp. 2345–2352, 2014, doi: 10.1039/C3NR05496A.
- [53] S. Gong *et al.*, “Highly Stretchy Black Gold E-Skin Nanopatches as Highly Sensitive Wearable Biomedical Sensors,” *Adv. Electron. Mater.*, vol. 1, no. 4, p. n/a-n/a, Apr. 2015, doi: 10.1002/aelm.201400063.

- [54] D. Kang *et al.*, “Ultrasensitive mechanical crack-based sensor inspired by the spider sensory system,” *Nature*, vol. 516, no. 7530, pp. 222–226, Dec. 2014, doi: 10.1038/nature14002.
- [55] *Sensor Terminology - National Instruments*. .
- [56] K. Kalantar-zadeh, “Sensors Characteristics,” in *Sensors: An Introductory Course*, K. Kalantar-zadeh, Ed. Boston, MA: Springer US, 2013, pp. 11–28.
- [57] C.-X. Liu and J.-W. Choi, “Analyzing resistance response of embedded PDMS and carbon nanotubes composite under tensile strain,” *Microelectronic Engineering*, vol. 117, no. Supplement C, pp. 1–7, Apr. 2014, doi: 10.1016/j.mee.2013.11.013.
- [58] J. J. Carr, “Sensors and circuits,” *PTR Prentice Hall, Englewood Cliffs, New Jersey*, vol. 7632, p. 75, 1993.
- [59] “Sensor Fundamentals.” [Online]. Available: <http://www.mfg.mtu.edu/cyberman/machtool/machtool/sensors/fundamental.html>. [Accessed: 22-Nov-2017].
- [60] J. Pionteck, J. Pionteck, and G. Wypych, *Handbook of Antistatics*. ChemTec Publishing, 2007.
- [61] S. Koul, R. Chandra, and S. K. Dhawan, “Conducting polyaniline composite for ESD and EMI at 101GHz,” *Polymer*, vol. 41, no. 26, pp. 9305–9310, Dec. 2000, doi: 10.1016/S0032-3861(00)00340-2.
- [62] R. Balint, N. J. Cassidy, and S. H. Cartmell, “Conductive polymers: Towards a smart biomaterial for tissue engineering,” *Acta Biomaterialia*, vol. 10, no. 6, pp. 2341–2353, Jun. 2014, doi: 10.1016/j.actbio.2014.02.015.
- [63] L. Brehmer, “Electrical and Electronic Properties of Polymers: A State-of-the-Art Compendium. Encyclopedia Reprint Series. Hg. von J. I. KROSCHWITZ. ISBN 0-471-

- 60896-3. New York/Chichester/Brisbane/Toronto/Singapore: John Wiley & Sons 1988.
- XXVI, 330 S., geb. £ 38.95,” *Acta Polymerica*, vol. 40, no. 5, pp. 361–361, May 1989, doi: 10.1002/actp.1989.010400518.
- [64] L. Rupprecht, *Conductive Polymers and Plastics: In Industrial Applications*. William Andrew, 1999.
- [65] H. Shirakawa, E. J. Louis, A. G. MacDiarmid, C. K. Chiang, and A. J. Heeger, “Synthesis of electrically conducting organic polymers: halogen derivatives of polyacetylene, (CH)<sub>x</sub>,” *J. Chem. Soc., Chem. Commun.*, vol. 0, no. 16, pp. 578–580, Jan. 1977, doi: 10.1039/C39770000578.
- [66] A. Facchetti, “ $\pi$ -Conjugated Polymers for Organic Electronics and Photovoltaic Cell Applications,” *Chem. Mater.*, vol. 23, no. 3, pp. 733–758, Feb. 2011, doi: 10.1021/cm102419z.
- [67] “Introduction of Conducting Polymers,” in *Conducting Polymers with Micro or Nanometer Structure*, Springer, Berlin, Heidelberg, 2008, pp. 1–15.
- [68] J. Foroughi, G. M. Spinks, and G. G. Wallace, “Conducting Polymer Fibers,” *Handbook of Smart Textiles*, pp. 31–62, 2015.
- [69] W. Zeng, L. Shu, Q. Li, S. Chen, F. Wang, and X.-M. Tao, “Fiber-Based Wearable Electronics: A Review of Materials, Fabrication, Devices, and Applications,” *Advanced Materials*, vol. 26, no. 31, pp. 5310–5336, 2014.
- [70] C. Cao, Y. Chu, Y. Zhou, C. Zhang, and S. Qu, “Recent Advances in Stretchable Supercapacitors Enabled by Low-Dimensional Nanomaterials,” *Small*, vol. 0, no. 0, p. 1803976, doi: 10.1002/sml.201803976.

- [71] N. C. Das, T. K. Chaki, and D. Khastgir, "Effect of axial stretching on electrical resistivity of short carbon fibre and carbon black filled conductive rubber composites," *Polym. Int.*, vol. 51, no. 2, pp. 156–163, Feb. 2002, doi: 10.1002/pi.811.
- [72] N. Hu, Y. Karube, C. Yan, Z. Masuda, and H. Fukunaga, "Tunneling effect in a polymer/carbon nanotube nanocomposite strain sensor," *Acta Materialia*, vol. 56, no. 13, pp. 2929–2936, Aug. 2008, doi: 10.1016/j.actamat.2008.02.030.
- [73] D. A. Dikin *et al.*, "Graphene-based composite materials," *Nature*, vol. 442, no. 7100, p. 282, Jul. 2006, doi: 10.1038/nature04969.
- [74] S. R. Broadbent and J. M. Hammersley, "Percolation processes: I. Crystals and mazes," *Mathematical Proceedings of the Cambridge Philosophical Society*, vol. 53, no. 3, pp. 629–641, Jul. 1957, doi: 10.1017/S0305004100032680.
- [75] I. J. Youngs, "Exploring the universal nature of electrical percolation exponents by genetic algorithm fitting with general effective medium theory," *J. Phys. D: Appl. Phys.*, vol. 35, no. 23, p. 3127, 2002, doi: 10.1088/0022-3727/35/23/314.
- [76] H. Frisch and J. Hammersley, "Percolation Processes and Related Topics," *Journal of the Society for Industrial and Applied Mathematics*, vol. 11, no. 4, pp. 894–918, Dec. 1963, doi: 10.1137/0111066.
- [77] R. D. Sherman, L. M. Middleman, and S. M. Jacobs, "Electron transport processes in conductor-filled polymers," *Polymer Engineering & Science*, vol. 23, no. 1, pp. 36–46, Jan. 1983, doi: 10.1002/pen.760230109.
- [78] S. Kirkpatrick, "Percolation and Conduction," *Rev. Mod. Phys.*, vol. 45, no. 4, pp. 574–588, Oct. 1973, doi: 10.1103/RevModPhys.45.574.
- [79] P. Jeraldo, *Critical Phenomena in Percolation Theory*. 2005.

- [80] G. Grimmett, “What is Percolation?,” in *Percolation*, G. Grimmett, Ed. Berlin, Heidelberg: Springer Berlin Heidelberg, 1999, pp. 1–31.
- [81] P. B. Jana, S. Chaudhuri, A. K. Pal, and S. K. De, “Electrical conductivity of short carbon fiber-reinforced polychloroprene rubber and mechanism of conduction,” *Polymer Engineering & Science*, vol. 32, no. 6, pp. 448–456, Mar. 1992, doi: 10.1002/pen.760320611.
- [82] J.-B. Donnet, *Carbon Black: Science and Technology, Second Edition*. CRC Press, 1993.
- [83] R. Hull, *Properties of Crystalline Silicon*. IET, 1999.
- [84] W. Guo, C. Liu, X. Sun, Z. Yang, H. G. Kia, and H. Peng, “Aligned carbon nanotube/polymer composite fibers with improved mechanical strength and electrical conductivity,” *J. Mater. Chem.*, vol. 22, no. 3, pp. 903–908, Dec. 2011, doi: 10.1039/C1JM13769G.
- [85] Y. He, W. Chen, C. Gao, J. Zhou, X. Li, and E. Xie, “An overview of carbon materials for flexible electrochemical capacitors,” *Nanoscale*, vol. 5, no. 19, pp. 8799–8820, Sep. 2013, doi: 10.1039/C3NR02157B.
- [86] M. J. Allen, V. C. Tung, and R. B. Kaner, “Honeycomb Carbon: A Review of Graphene,” *Chem. Rev.*, vol. 110, no. 1, pp. 132–145, Jan. 2010, doi: 10.1021/cr900070d.
- [87] K. Kim, K. S. Novoselov, L. Colombo, M. G. Schwab, P. R. Gellert, and V. I. Fal’ko, “A roadmap for graphene,” *Nature*, vol. 490, no. 7419, p. 192, Oct. 2012, doi: 10.1038/nature11458.
- [88] S. C. Mannsfeld *et al.*, “Highly sensitive flexible pressure sensors with microstructured rubber dielectric layers,” *Nature materials*, vol. 9, no. 10, pp. 859–864, 2010.
- [89] C. Choi, J. M. Lee, S. H. Kim, S. J. Kim, J. Di, and R. H. Baughman, “Twistable and Stretchable Sandwich Structured Fiber for Wearable Sensors and Supercapacitors,” *Nano Lett.*, vol. 16, no. 12, pp. 7677–7684, 2016, doi: 10.1021/acs.nanolett.6b03739.

- [90] A. Frutiger *et al.*, “Capacitive Soft Strain Sensors via Multicore–Shell Fiber Printing,” *Adv. Mater.*, vol. 27, no. 15, pp. 2440–2446, Apr. 2015, doi: 10.1002/adma.201500072.
- [91] R. Wang *et al.*, “A Bi-Sheath Fiber Sensor for Giant Tensile and Torsional Displacements,” *Adv. Funct. Mater.*, p. n/a-n/a, doi: 10.1002/adfm.201702134.
- [92] Y.-Q. Li, P. Huang, W.-B. Zhu, S.-Y. Fu, N. Hu, and K. Liao, “Flexible wire-shaped strain sensor from cotton thread for human health and motion detection,” *Scientific Reports*, vol. 7, p. srep45013, Mar. 2017, doi: 10.1038/srep45013.
- [93] X. Wu, Y. Han, X. Zhang, and C. Lu, “Highly Sensitive, Stretchable, and Wash-Durable Strain Sensor Based on Ultrathin Conductive Layer@Polyurethane Yarn for Tiny Motion Monitoring,” *ACS Appl. Mater. Interfaces*, vol. 8, no. 15, pp. 9936–9945, Apr. 2016, doi: 10.1021/acsami.6b01174.
- [94] I. Poupyrev, N.-W. Gong, S. Fukuhara, M. E. Karagozler, C. Schwesig, and K. E. Robinson, “Project Jacquard: Interactive Digital Textiles at Scale,” in *Proceedings of the 2016 CHI Conference on Human Factors in Computing Systems*, New York, NY, USA, 2016, pp. 4216–4227, doi: 10.1145/2858036.2858176.
- [95] J. Lee *et al.*, “Conductive Fiber-Based Ultrasensitive Textile Pressure Sensor for Wearable Electronics,” *Advanced Materials*, vol. 27, no. 15, pp. 2433–2439, 2015.
- [96] A. Atalay *et al.*, “Batch Fabrication of Customizable Silicone-Textile Composite Capacitive Strain Sensors for Human Motion Tracking,” *Adv. Mater. Technol.*, vol. 2, no. 9, p. n/a-n/a, Sep. 2017, doi: 10.1002/admt.201700136.
- [97] Y.-C. Lai *et al.*, “Extraordinarily Sensitive and Low-Voltage Operational Cloth-Based Electronic Skin for Wearable Sensing and Multifunctional Integration Uses: A Tactile-Induced

- Insulating-to-Conducting Transition,” *Advanced Functional Materials*, vol. 26, no. 8, pp. 1286–1295, 2016, doi: 10.1002/adfm.201503606.
- [98] J. Ren *et al.*, “Environmentally-friendly conductive cotton fabric as flexible strain sensor based on hot press reduced graphene oxide,” *Carbon*, vol. 111, pp. 622–630, Jan. 2017, doi: 10.1016/j.carbon.2016.10.045.
- [99] L. M. Castano and A. B. Flatau, “Smart fabric sensors and e-textile technologies: a review,” *Smart Mater. Struct.*, vol. 23, no. 5, p. 053001, 2014, doi: 10.1088/0964-1726/23/5/053001.
- [100] W.-P. Shih *et al.*, “Flexible Temperature Sensor Array Based on a Graphite-Polydimethylsiloxane Composite,” *Sensors*, vol. 10, no. 4, pp. 3597–3610, Apr. 2010, doi: 10.3390/s100403597.
- [101] C. Yan, J. Wang, and P. S. Lee, “Stretchable Graphene Thermistor with Tunable Thermal Index,” *ACS Nano*, vol. 9, no. 2, pp. 2130–2137, Feb. 2015, doi: 10.1021/nn507441c.
- [102] M. Sibinski, M. Jakubowska, M. Sloma, M. Sibinski, M. Jakubowska, and M. Sloma, “Flexible Temperature Sensors on Fibers,” *Sensors*, vol. 10, no. 9, pp. 7934–7946, Aug. 2010, doi: 10.3390/s100907934.
- [103] H. Farahani, R. Wagiran, and M. N. Hamidon, “Humidity Sensors Principle, Mechanism, and Fabrication Technologies: A Comprehensive Review,” *Sensors*, vol. 14, no. 5, pp. 7881–7939, Apr. 2014, doi: 10.3390/s140507881.
- [104] T. Zhang *et al.*, “Study on humidity sensing properties based on composite materials of Li-doped mesoporous silica A-SBA-15,” *Sensors and Actuators B: Chemical*, vol. 128, no. 2, pp. 482–487, Jan. 2008, doi: 10.1016/j.snb.2007.07.012.

- [105] J. H. Anderson and G. A. Parks, “Electrical conductivity of silica gel in the presence of adsorbed water,” *J. Phys. Chem.*, vol. 72, no. 10, pp. 3662–3668, Oct. 1968, doi: 10.1021/j100856a051.
- [106] T. S. Sreeprasad *et al.*, “Electron-Tunneling Modulation in Percolating Network of Graphene Quantum Dots: Fabrication, Phenomenological Understanding, and Humidity/Pressure Sensing Applications,” *Nano Lett.*, vol. 13, no. 4, pp. 1757–1763, Apr. 2013, doi: 10.1021/nl4003443.
- [107] K.-P. Yoo, L.-T. Lim, N.-K. Min, M. J. Lee, C. J. Lee, and C.-W. Park, “Novel resistive-type humidity sensor based on multiwall carbon nanotube/polyimide composite films,” *Sensors and Actuators B: Chemical*, vol. 145, no. 1, pp. 120–125, Mar. 2010, doi: 10.1016/j.snb.2009.11.041.
- [108] K. Jiang, T. Fei, F. Jiang, G. Wang, and T. Zhang, “A dew sensor based on modified carbon black and polyvinyl alcohol composites,” *Sensors and Actuators B: Chemical*, vol. 192, no. Supplement C, pp. 658–663, Mar. 2014, doi: 10.1016/j.snb.2013.11.004.
- [109] W. Li, F. Xu, L. Sun, W. Liu, and Y. Qiu, “A novel flexible humidity switch material based on multi-walled carbon nanotube/polyvinyl alcohol composite yarn,” *Sensors Actuators B: Chem.*, vol. 230, no. Journal Article, pp. 528–535, 2016, doi: 10.1016/j.snb.2016.02.108.
- [110] S. Wu, F. Li, Y. Zhu, and J. Shen, “The switch-type humidity sensing properties of polyacrylic acid and its copolymers,” *Journal of Materials Science*, vol. 35, no. 8, pp. 2005–2008, Apr. 2000, doi: 10.1023/A:1004787007579.
- [111] H. Qi, E. Mäder, and J. Liu, “Unique water sensors based on carbon nanotube–cellulose composites,” *Sensors and Actuators B: Chemical*, vol. 185, no. Supplement C, pp. 225–230, Aug. 2013, doi: 10.1016/j.snb.2013.04.116.

- [112] T. Kinkeldei, C. Zysset, K. H. Cherenack, and G. Tröster, “A textile integrated sensor system for monitoring humidity and temperature,” in *2011 16th International Solid-State Sensors, Actuators and Microsystems Conference*, 2011, pp. 1156–1159, doi: 10.1109/TRANSDUCERS.2011.5969238.
- [113] G. E. Collins and L. J. Buckley, “Conductive polymer-coated fabrics for chemical sensing,” *Synthetic Metals*, vol. 78, no. 2, pp. 93–101, Mar. 1996, doi: 10.1016/0379-6779(96)80108-1.
- [114] K. H. Hong, K. W. Oh, and T. J. Kang, “Polyaniline–nylon 6 composite fabric for ammonia gas sensor,” *J Appl Polym Sci*, vol. 92, no. 1, pp. 37–42, 2004, doi: 10.1002/app.13633.
- [115] M. K. Smith and K. A. Mirica, “Self-Organized Frameworks on Textiles (SOFT): Conductive Fabrics for Simultaneous Sensing, Capture, and Filtration of Gases,” *J. Am. Chem. Soc.*, Oct. 2017, doi: 10.1021/jacs.7b08840.
- [116] A. Behnaz *et al.*, “Ultrathin conformal devices for precise and continuous thermal characterization of human skin,” *Nature Materials*, vol. 12, no. 10, p. 938, Oct. 2013, doi: 10.1038/nmat3755.
- [117] Y. Khan, A. E. Ostfeld, C. M. Lochner, A. Pierre, and A. C. Arias, “Monitoring of Vital Signs with Flexible and Wearable Medical Devices,” *Adv. Mater.*, vol. 28, no. 22, pp. 4373–4395, Jun. 2016, doi: 10.1002/adma.201504366.
- [118] B. Xu *et al.*, “Epidermal photonic devices for quantitative imaging of temperature and thermal transport characteristics of the skin,” *Nature Communications*, vol. 5, p. 4938, Sep. 2014, doi: 10.1038/ncomms5938.
- [119] D.-H. Baek *et al.*, “Solderable and electroplatable flexible electronic circuit on a porous stretchable elastomer,” *Nature Communications*, vol. 3, p. 977, Jul. 2012, doi: 10.1038/ncomms1980.

- [120] H. C. Jung *et al.*, “CNT/PDMS Composite Flexible Dry Electrodes for Long-Term ECG Monitoring,” *IEEE Transactions on Biomedical Engineering*, vol. 59, no. 5, pp. 1472–1479, May 2012, doi: 10.1109/TBME.2012.2190288.
- [121] J. Yoo, L. Yan, S. Lee, H. Kim, and H. J. Yoo, “A Wearable ECG Acquisition System With Compact Planar-Fashionable Circuit Board-Based Shirt,” *IEEE Transactions on Information Technology in Biomedicine*, vol. 13, no. 6, pp. 897–902, Nov. 2009, doi: 10.1109/TITB.2009.2033053.
- [122] N. Meziane, J. G. Webster, M. Attari, and A. J. Nimunkar, “Dry electrodes for electrocardiography,” *Physiol Meas*, vol. 34, no. 9, pp. R47-69, Sep. 2013.
- [123] A. Searle and L. Kirkup, “A direct comparison of wet, dry and insulating bioelectric recording electrodes,” *Physiol. Meas.*, vol. 21, no. 2, p. 271, 2000, doi: 10.1088/0967-3334/21/2/307.
- [124] O. Atalay, W. R. Kennon, and E. Demirok, “Weft-Knitted Strain Sensor for Monitoring Respiratory Rate and Its Electro-Mechanical Modeling,” *IEEE Sensors Journal*, vol. 15, no. 1, pp. 110–122, Jan. 2015, doi: 10.1109/JSEN.2014.2339739.
- [125] C. R. Merritt, H. T. Nagle, and E. Grant, “Textile-Based Capacitive Sensors for Respiration Monitoring,” *IEEE Sensors Journal*, vol. 9, no. 1, pp. 71–78, Jan. 2009, doi: 10.1109/JSEN.2008.2010356.
- [126] C. Yan *et al.*, “Highly Stretchable Piezoresistive Graphene–Nanocellulose Nanopaper for Strain Sensors,” *Adv. Mater.*, vol. 26, no. 13, pp. 2022–2027, Apr. 2014, doi: 10.1002/adma.201304742.

## Chapter 3: Extrusion Printed Multimodal and Multifunctional Sensors

Kapoor, Ashish, Michael McKnight, Kony Chatterjee, Talha Agcayazi, Hannah Kausche, Alper Bozkurt, and Tushar K. Ghosh. "Toward Fully Manufacturable, Fiber Assembly–Based Concurrent Multimodal and Multifunctional Sensors for e-Textiles." *Advanced Materials Technologies* 4, no. 1 (2019): 1800281.

### 3.1 Abstract

Soft polymer-based sensors as an integral part of textile structures have attracted considerable scientific and commercial interest recently because of their potential use in healthcare, security systems, and other areas. While electronic sensing functionalities can be incorporated into textiles at one or more of the hierarchical levels of molecules, fibers, yarns, or fabrics, arguably a more practical and inconspicuous means to introduce the desired electrical characteristics is at the fiber level, using processes that are compatible to textiles. Here, a prototype multimodal and multifunctional sensor array formed within a woven fabric structure using bicomponent fibers with ordered insulating and conducting segments is reported. The multifunctional characteristics of the sensors are successfully demonstrated by measuring tactile, tensile, and shear deformations, as well as wetness and biopotential. While the unobtrusive integration of sensing capabilities offers possibilities to preserve all desirable textile qualities, this scaled-up fiber-based approach demonstrates the potential for scalable and facile manufacturability of practical e-textile products using low-cost roll-to-roll processing of large-area flexible sensor systems and can be remarkably effective in advancing the field of e-textiles.

### 3.2 Introduction

Wearable sensors for monitoring human health or peripersonal environment can be deployed as electronic skin (e-skin) or electronic textiles (e-textile). While e-skin is likely to become important for future generations of robots and medical devices, e-textiles offer tremendous opportunities in many applications including physiological monitoring, comfort, security systems,

and in large-area deployment of electronic systems. The challenge, however, is to engender electrical functionalities in textiles while preserving the desirable textile qualities such as softness, comfort, flexibility, and texture that arise from its hierarchical structure through the complex interaction of inherent fiber material properties and the characteristic textile structural features at multiple length scales. To this end, among all the different potential routes of incorporating electronic functionalities into textiles, integration of textile fibers performing as electrical devices, on its own or when assembled, seems to provide the most obvious, unobtrusive, and practical means. Appropriately designed flexible fiber-based electronics are fundamentally transformational; they present very attractive possibilities of ease of manufacturing using standard fiber-extrusion, roll-to-roll textile processing technologies, and enable high spatial sensing density with redundancy within the textile structure.

The utility of fiber-based electronics has been recognized as a key step for truly mass-produced e-textiles. Accordingly, the constituents (e.g., fibers or yarns) of textile products have been directly fashioned into electrical devices by incorporating appropriate functional design and materials. These include “fiber”-shaped photovoltaic devices [1], [2], transistors [3]–[5], logic circuits [6], [7], sensors [8], [9], actuators [10], [11], other electronic/optical devices [12]–[14] in addition to fabric-based devices [15], [16]. Modulation of resistance and/or capacitance have been the two most common strategies to sense various physical stimuli, such as applied forces [9], [17] and moisture [18], [19]. Piezoresistive sensors in the form of fibers/yarns and printed layers on fabrics have been proposed for monitoring motion, posture, and various physiological signals for patient monitoring and rehabilitation [20], [21]. For pressure measurements, multicore fibers consisting of layers of soft dielectric and conductive polymers or thin metal films [22], [23], sets of orthogonal fibers [24], [25], or fabric-like structures with soft dielectric and conductive fibers

[26] have been employed to form capacitive structures. While remarkable progress has been made in e-textiles, practical real-life products in e-textiles remain elusive. Arguably, the most difficult challenge has been the development of truly textile/fiber-compatible materials/devices and practical methods, instead of complex fabrication methods that are often impractical and inappropriate for textile products and processes.

In this work, we demonstrate a potentially transformative technology through the design of a multimodal and multifunctional sensor array formed within a woven fabric structure using extrusion printed bicomponent fibers. While the multimodal characteristic of the sensors is demonstrated through capacitive and resistive response, their ability to measure tactile, tensile, and shear deformations, as well as wetness and biopotential, demonstrates the multifunctional characteristics; see Figure 25 . Although we use a dimensionally scaled-up fiber made of an elastomer that is not commonly used as a textile fiber, our fiber-based approach demonstrates the potential for scalable and facile manufacturability of practical e-textile products.



Figure 25: Potential sensing locations for a long sleeve top. (a) Arm and wrist areas are suitable for pulse rate monitoring. (b) Skin electrodes for biopotential measurement can be placed on the chest. (c) Underarm can provide information on bodily fluids. (d) Tactile input panels can be placed on the inner arm. [Adapted from: Kapoor, Ashish, et al. *Advanced Materials Technologies* 4.1 (2019): 1800281.]

The novelty of this research lies in the fact that inherent orthogonal interlacement of fibers/yarns in a woven textile structure is used to enable sensing. This is achieved by the unique cross sectional geometry of the fiber which consists of two circular insulating segments bridged by an electrically conducting segment. Once woven, the cross-over point, referred as sensing pixel allows for capacitive measurements while resistive measurements can be made along the length of fiber (see Figure 26). Due to this multimodality, the fiber based sensor can be used for concurrent detection of pressure, strain, shear, moisture and biopotentials in a single woven structure. This section briefly elucidates the principle of above measurements.

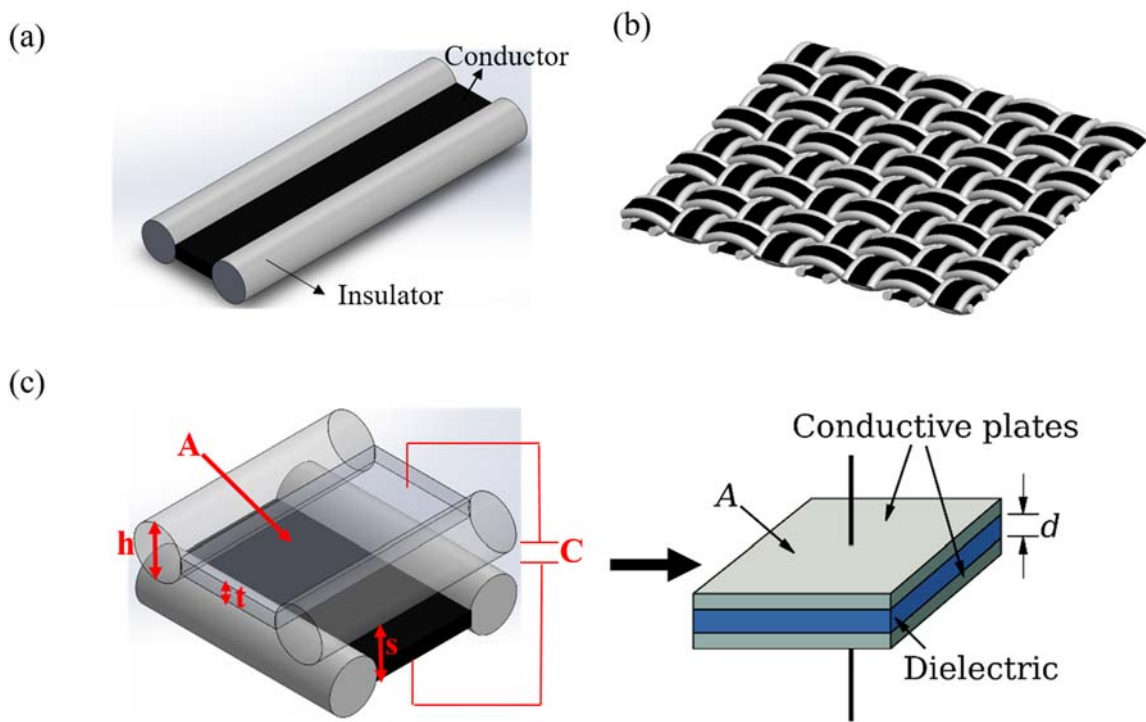


Figure 26: Fiber design. Schematic of (a) Bicomponent fiber showing insulating and conducting segments, (b) Woven fabric made of bicomponent fibers, and (c) Sensing pixel formed at crossover point, compared to a parallel plate capacitor.

### *Capacitance based pressure sensing*

The sensing pixel formed at the crossover point of two bicomponent fibers can be simplified as a parallel plate capacitor (refer Figure 27). The capacitance ( $C$ ) of this parallel plate capacitor is given by  $C = \epsilon A/s$ , where  $\epsilon$  is the dielectric constant of medium separating the conducting segments,  $A$  is the overlapping area, and  $s$  is the separation between conducting segments. When a normal force is applied there is a change in the separation between conducting segments due to compression of insulating segments which can be detected by the modified capacitance.

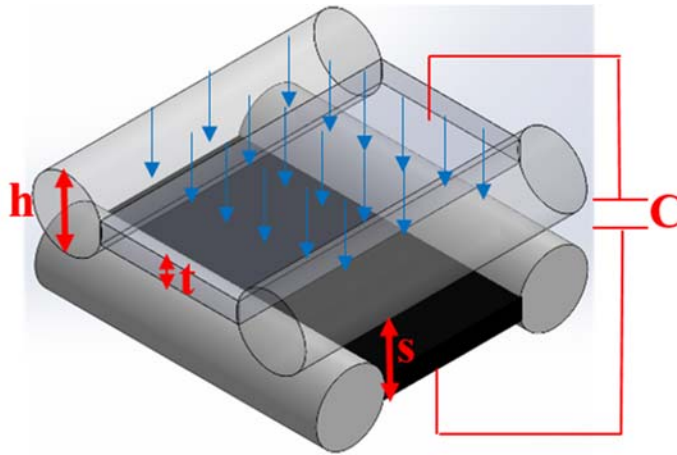


Figure 27: Sensing pixel for pressure sensing

Let us consider, height of insulating segment =  $h$ , thickness of conducting segment =  $t$ , separation between top and bottom conducting segments ( $s$ ) =  $h-t$ , initial capacitance =  $C_0$ , capacitance under applied force =  $C_1$  and separation under applied force =  $s_1$ .

Then, using the Hooke's law and the parallel plate capacitance equation, we can derive  $\Delta C/C_0$  as below.

$$C_0 = \frac{\epsilon A}{s}$$

$$C_1 = \frac{\epsilon A}{s_1}$$

$$\sigma = E\epsilon$$

Here  $\sigma$  and  $\epsilon$  are the applied stress and strain and  $E$  is the Young's modulus. Strain can be written in terms of change in separation as below.

$$\epsilon = \frac{s - s_1}{s} = 1 - \frac{s_1}{s}$$

$$\sigma = E \left(1 - \frac{s_1}{s}\right)$$

$$s_1 = \left(1 - \frac{\sigma}{E}\right) s$$

Thus, the change in capacitance  $\Delta C$  can be calculated as;

$$\Delta C = \frac{\epsilon A}{s_1} - \frac{\epsilon A}{s} = \frac{\epsilon A}{\left(\left(1 - \frac{\sigma}{E}\right) s\right)} - \frac{\epsilon A}{s} = \frac{\epsilon A}{s} \left(\frac{1}{\frac{E}{\sigma} - 1}\right)$$

$$\therefore \frac{\Delta C}{C_0} = \frac{\epsilon A}{C_0 s} \left(\frac{1}{\frac{E}{\sigma} - 1}\right)$$

If  $\sigma \ll E$ , then,

$$\frac{\Delta C}{C_0} = \frac{\epsilon A \sigma}{C_0 s E}$$

Thus,  $\frac{\Delta C}{C_0}$  increases with increasing pressure as  $E$ ,  $\epsilon$  and  $A$  are considered constants. Also, when the applied pressure ' $\sigma$ ' is much less than Young's modulus ' $E$ ' of material then  $\frac{\Delta C}{C_0}$  is linearly proportional to applied pressure [27].

### Capacitance based shear sensing

The changes in overlapping area of electrodes of capacitor are commonly used to detect shear forces [30]. In this case, when the shear forces are applied to the sensor, the fiber is oriented at an angle  $\theta$  and the overlapping area can be approximated as a parallelogram as shown in

Figure 28

Let shear angle =  $\theta$  and fiber width =  $w$

$$\cos \theta = \frac{w}{CD}$$

Area ABCD =  $w \times CD$  ( $\because$  area of parallelogram = base  $\times$  height )

$$\Rightarrow \text{Area ABCD} = \frac{w^2}{\cos \theta}$$

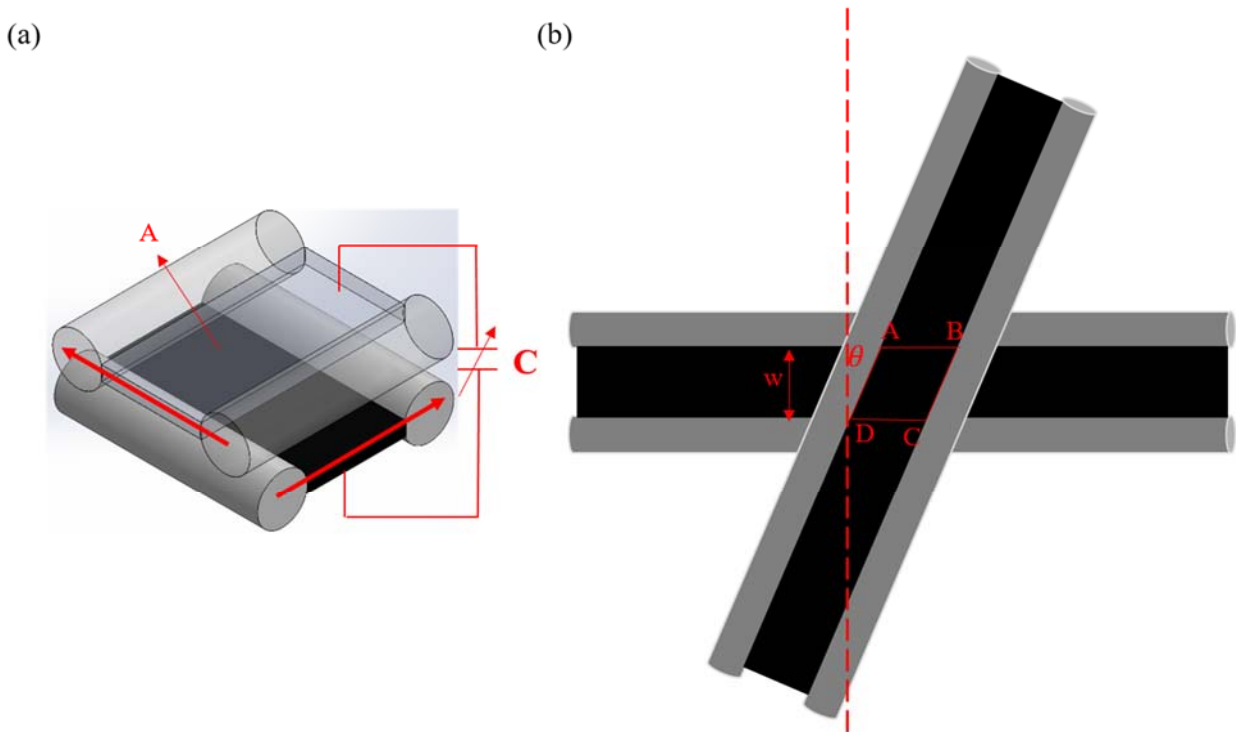


Figure 28: (a) Shear forces acting on pixel, (b) Diagram showing change in area due to shear

### ***Resistance based strain sensing***

The conducting segment of the fiber will be fabricated using a conducting polymer composite (CPC) made by adding spherical carbon black particles to the elastomer beyond percolation threshold. When the fiber is stretched there will be an increase in electrical resistance of the conducting segment (Figure 29) of fiber with increase in applied strain due to dimensional changes as well as disruption of the conducting polymer network which will recover upon removal of strain [31], [32]. Due to this response, the fibers within woven fabric can be used for strain sensing by measurement of resistance.

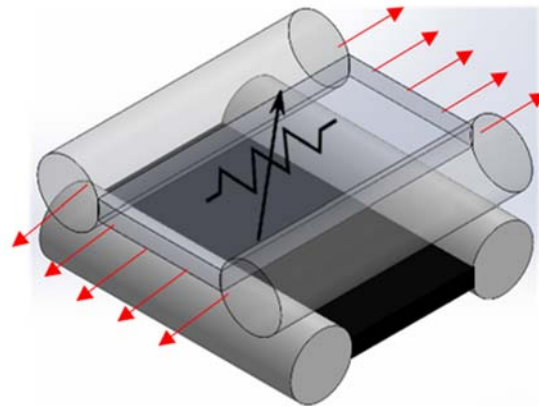


Figure 29: Conducting segment of fiber acting as piezoresistor

### ***Impedance based wetness sensing***

The capacitive sensing pixel formed by the orthogonal placement of fibers consists of air as dielectric. When a liquid like sweat is introduced between the fiber electrodes (

Figure 30), the air dielectric is replaced by a material which has a higher dielectric constant and is more conductive due to presence of ions. The simplified equivalent circuit for this test configuration consists of a parallel RC circuit in series with R. In this circuit model, the resistive element in parallel RC circuit corresponds to the sweat or any other fluid and the series resistance

corresponds to the resistance of fibers. For the parallel RC circuit, the impedance ‘Z’ is given by the relation,

$$Z = \frac{R}{1 + j\omega RC_0}$$

Where ‘j’ is the imaginary unit,  $\omega = 2\pi f$  where ‘f’ is frequency, R is resistance and  $C_0$  is initial base capacitance. This resulting impedance change can be sensed through impedance spectroscopy to determine the presence of liquid like sweat.

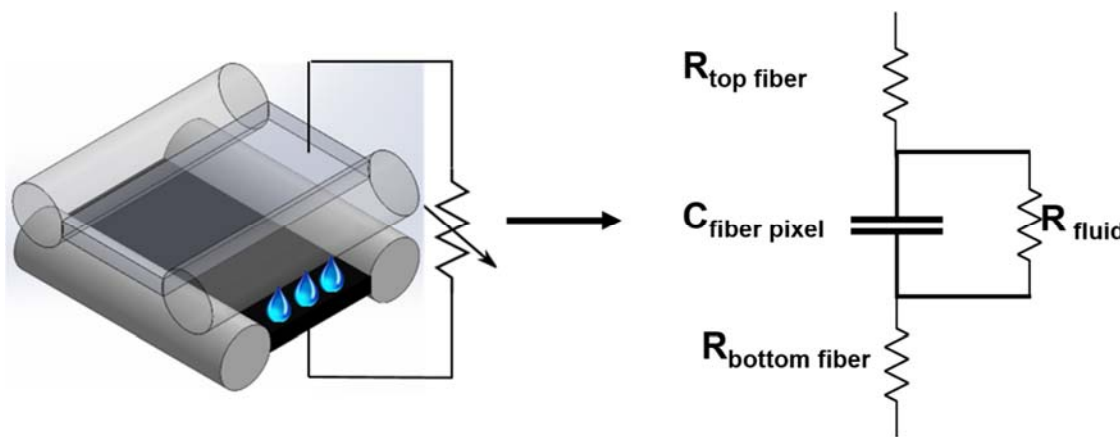


Figure 30: Sensing pixel for wetness detection by impedance measurement

### ***Biopotential recording***

The sensing pixels can be used to record biopotentials like ECG (generated by the heart) or EMG (generated by the muscles). The intermediate conducting layer of fiber will be used as surface electrode to record biopotentials (Figure 31a). The conducting segment acts as a biopotential electrode by conducting body potentials to external circuits to get voltage versus time response. The contact impedance of the fiber with the skin can be minimized by more exposure of conductive inner segment through use of woven structures with longer float lengths on skin side of garment (Figure 31b).

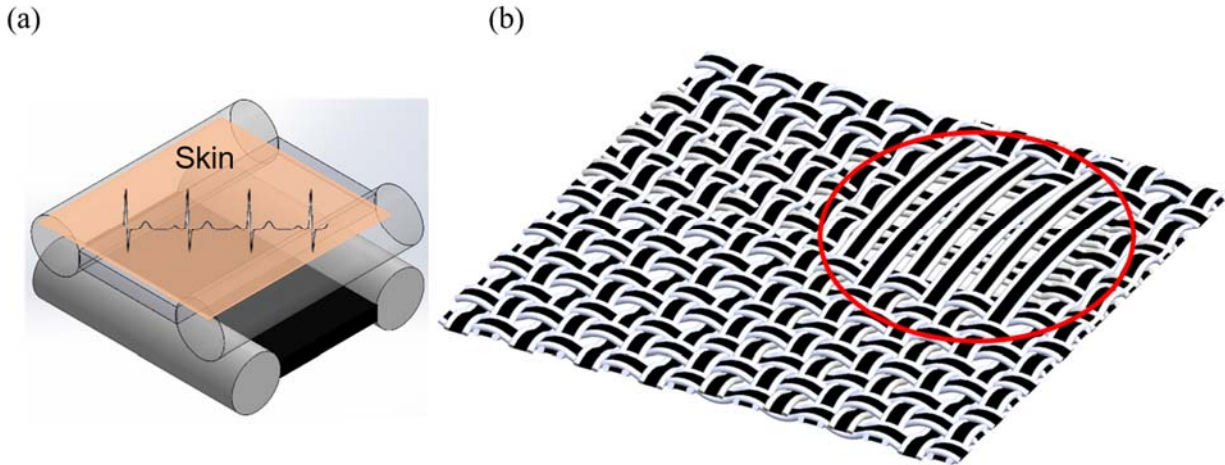


Figure 31: (a) Conducting segment of fiber in contact with skin acting as biopotential electrode and (b) longer floats in woven structure for biopotential recording.

### 3.3 Materials and Methods

The fibers were fabricated using a sequential extrusion printing method shown in Figure 32a using a custom built sequential extrusion printing setup (Figure 32b) that included a computer controlled XY stage (Openbuilds), an ultraviolet (UV) light source (Bluewave 200, Dymax), a syringe pump (Genie Touch, Lucca Technologies, USA) and appropriate tubes and needles. A laser etched acrylic substrate was used as a mold to collect the fiber segments (insulating/conducting) in its tracks to ensure the shape. The print paths were generated using a LabVIEW program.

The insulating segments were extruded from a two-part UV-curing silicone (LSR 225-1, Momentive). The base was mixed with catalyst in a 100:2 ratio using a planetary mixer (Mazerustar, Kurabo KK- 50 S) for 60 seconds and subsequently degassed. 10% of silicone fluid, Xiameter PMX-200 of 50 centipoise viscosity was used as viscosity modifier. The conducting segments were extruded from a percolative conducting polymer composite (CPC) containing PDMS and carbon black (CB). The CPC consisted of two-part heat-curing silicone (Sylgard-184,

Dow Corning) with a base to catalyst ratio of 10:1, filled with 9wt% carbon black (Ketjenblack EC-300J, AkzoNobel). 9% (w/w) CB was chosen based on observation of the percolation behavior [20], [33] of the CPC, see Figure 33. A four-point probe setup consisting of a nanovoltmeter (model 2182A, Keithley, Cleveland, OH) and a current source (model 6221, Keithley, Cleveland, OH) was used to measure the electrical resistance of the CPC.

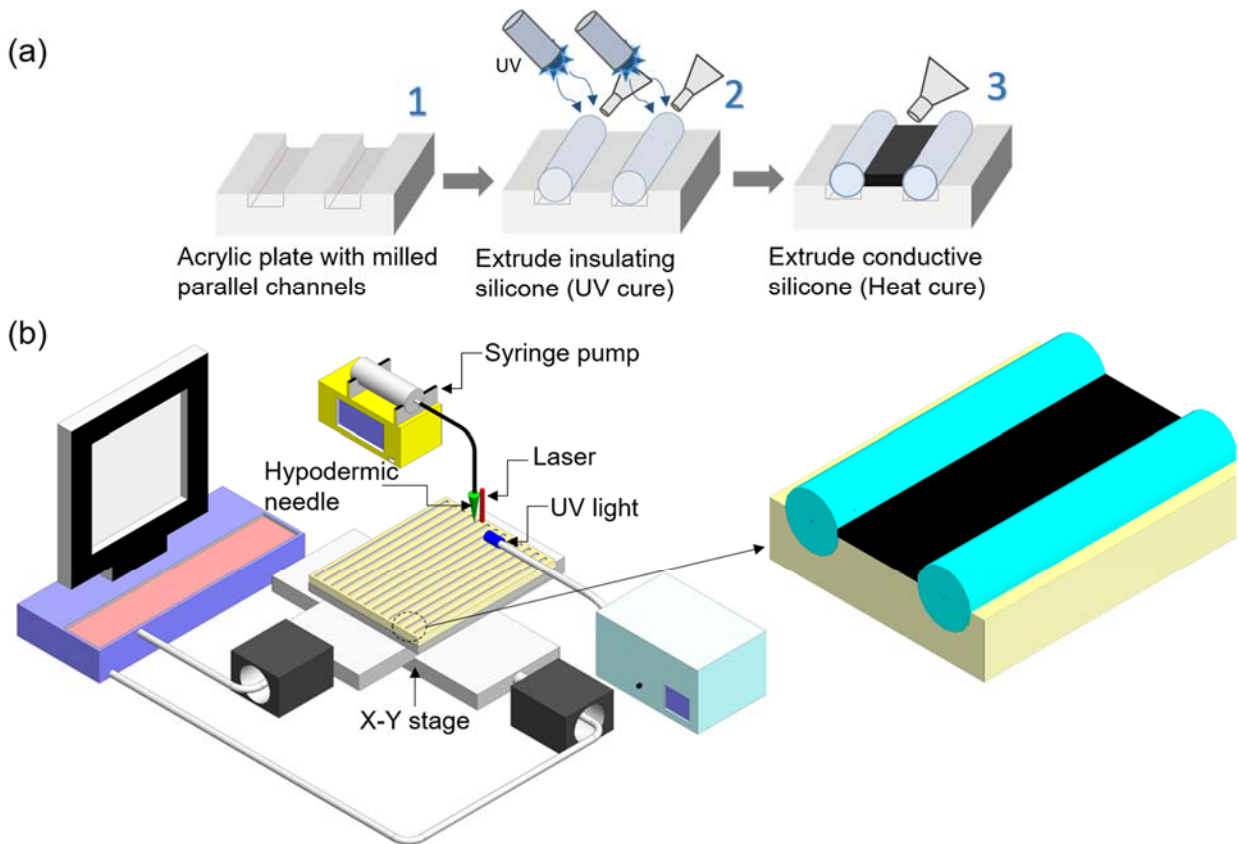


Figure 32: (a) Schematic representation of the fabrication of sensory fibers; 1) etched acrylic substrate, 2) extrusion of insulating segments, and 3) deposition of CPC. (b) Custom built sequential extrusion printing setup. [Adapted from: Kapoor, Ashish, et al. *Advanced Materials Technologies* 4.1 (2019): 1800281.]

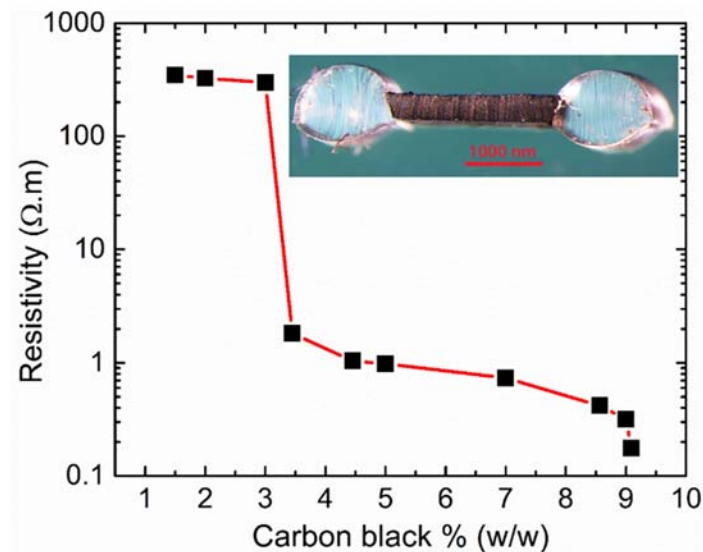


Figure 33: Percolation behavior of the CPC with the cross-sectional shape of the sensory fibers shown in the inset. [Adapted from: Kapoor, Ashish, et al. "Toward Fully Manufacturable, Fiber Assembly-Based Concurrent Multimodal and Multifunctional Sensors for e-Textiles." *Advanced Materials Technologies* 4.1 (2019): 1800281.]

For fiber fabrication, the as prepared insulating and conducting materials were then transferred to 5ml syringes (BD, USA) fitted with flexible tubing of appropriate size with hypodermic needles on the other end and mounted onto the syringe pump. Once the needle head was aligned with the etched tracks on the mold using a laser beam, the syringe pump was programmed to pump at  $1\text{ ml min}^{-1}$  flow rate and the stage was programmed to move at  $1\text{ cm s}^{-1}$  while extruding insulating segments. For the insulating segments, the UV light beam was positioned near the needle exit such that the exiting polymer stream is exposed to UV light, before it contacts the mold to ensure circular cross section. After laying the two insulating segments in the mold tracks before the CB-silicone mixture was extruded at  $2\text{ ml min}^{-1}$  and was laid in between the insulator lines to bridge the space with the stage speed set at  $2\text{ cm s}^{-1}$ . At the end of the extrusion runs, the acrylic mold with the fiber segments was transferred to a vacuum oven (Model 280A Fisher Scientific) set at  $100^{\circ}\text{C}$  for 35 minutes, for curing of the conducting segments.

## 3.4 Results and Discussion

### 3.4.1 Electromechanical characterization

To establish a relationship between the piezoresistive response of the fibers under axial strain while in the fabric, and their mechanical behavior, we performed cyclic uniaxial tensile tests on the fibers on a load frame (MTS-30G fitted with a 10 N load cell) using 40% strain amplitude, of which a limited but representative response is provided in Figure 34a. The stress–strain behavior of the fibers stabilizes after a few cycles. The response of individual fiber's electrical resistance under mechanical strain was evaluated using a four-point probe while applying 20 uniaxial strain cycles. The same 4 point probe setup was used to measure the strain–resistance relation of the fiber specimens fitted with four equispaced (10 mm probe-spacing) copper leads (attached by CPC silicone adhesive) on the computer-controlled uniaxial load-frame set at an extension rate of 30 mm min<sup>-1</sup>. The electrical resistance is plotted as a function of time in Figure 34b for all 20 cycles and for clarity the corresponding 1st, 10th, and 20th strain cycles are shown separately in Figure 34c. Several general features of this figure warrant discussion. The first cycle exhibits a large unrecoverable change in electrical resistance due primarily to the morphological changes observed earlier in the mechanical hysteresis in the first cycle stress–strain behavior; see Figure 34a. In the subsequent cycles, however, the fibers show good strain-reversible piezoresistive behavior, implying that the CPC morphology is robust with little mechanical/electrical hysteresis. In each cycle, the resistance is observed to increase with increasing strain due to dimensional changes as well as physical disruption of the conductive percolating network [20] and recover upon removal of strain, particularly beyond cycle 5. The piezoresistive sensitivity or the gage factor for the fibers was  $\approx 2.0$ . Additionally, when the sensory fiber was held under uniaxial strain for 20 s, there was no appreciable change in its electrical resistance; see Figure 34d. This indicates the potential of

using this fiber as a piezoresistive strain sensor, especially in applications where typical axial strain is less than 20%.

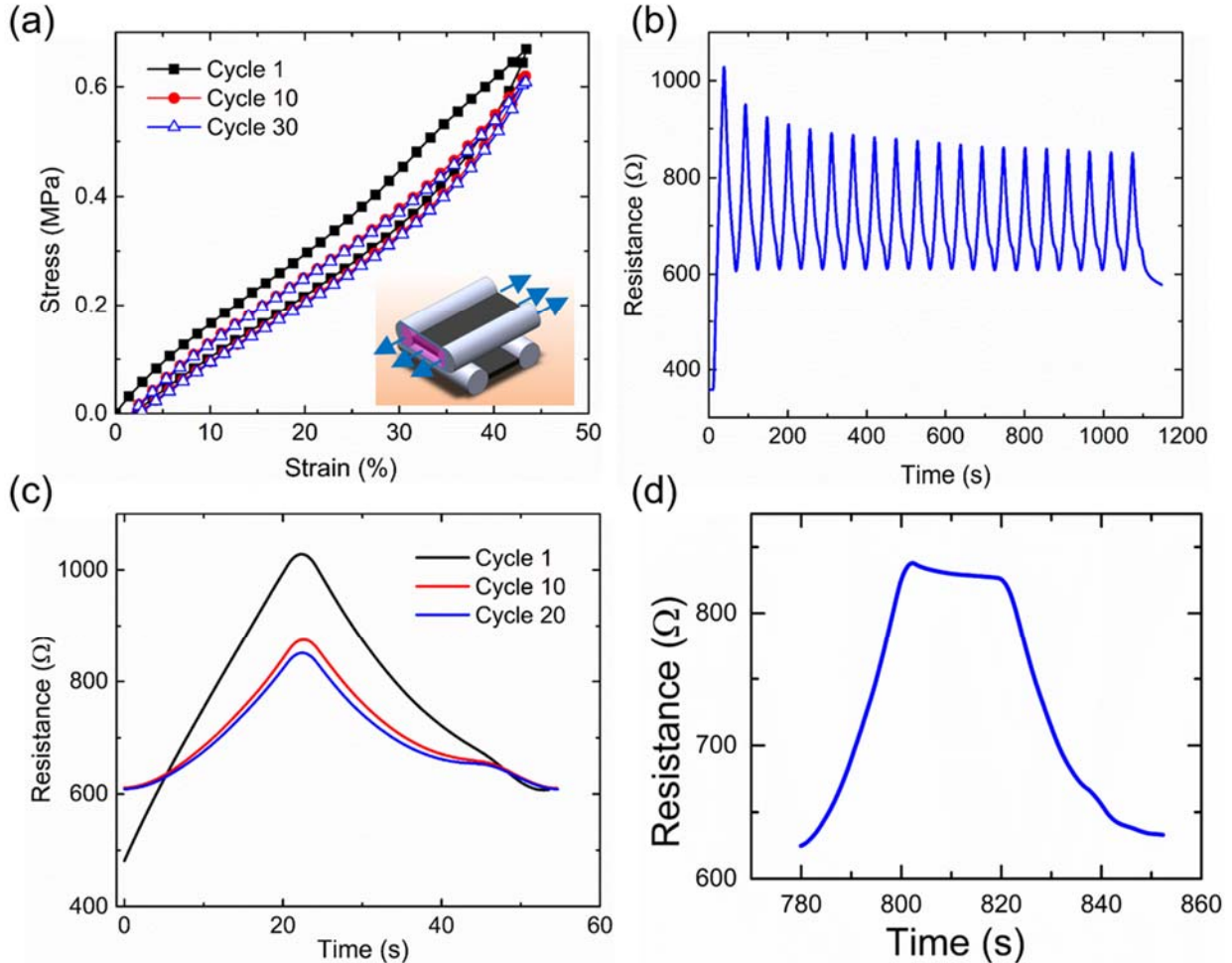


Figure 34: (a) Stress–strain behavior of a sensory fiber subjected to 30 cycles of 40% strain. 1st, 10th, and 30th cycles are shown; (b) Strain–resistance response of the fiber subjected to 20 cycles of 30% strain; (c) 1st, 10th, and 20th cycles of the strain–resistance response of the fiber shown in (b), and (d) Resistance of the fiber under 30% strain for 20 s. [Adapted from: Kapoor, Ashish, et al. *Advanced Materials Technologies* 4.1 (2019): 1800281.]

### 3.4.2 Sensory Response

While similarly strain-reversible piezoresistive behavior has been previously reported for carbonaceous composites [34], [35], our sensory texels can also be used for tactile sensing. Texel deformation due to compression should determine its tactile response; therefore, its cyclic stress–

strain behavior under compression was determined (see Figure 35a). The response clearly exhibits low mechanical hysteresis following 30 loading/unloading cycles at 50% strain amplitude. Note that the stress–strain response of the texel under compression is that of the insulating segments which could be changed to alter its sensory response. Tactile sensing capabilities of the texel were evaluated by applying a normal force 4 N on a single texel, while recording the capacitance using a custom-printed circuit board (PCB). Once again, we present the capacitive response as a function of time in Figure 35b for all 20 cycles and the corresponding 1st, 10th, and 20th strain cycles in Figure 35c. It is clear that the unique fiber cross section enables highly sensitive measurement ( $0.25 \text{ pF N}^{-1}$ ) of tactile forces. No significant change in its electrical capacitance is observed under static compressive loading of 4 N over 1 min, see Figure 35d. The change in capacitance is very consistent and reversible over a large number of cycles indicating the efficacy of the woven texel as a tactile sensor.

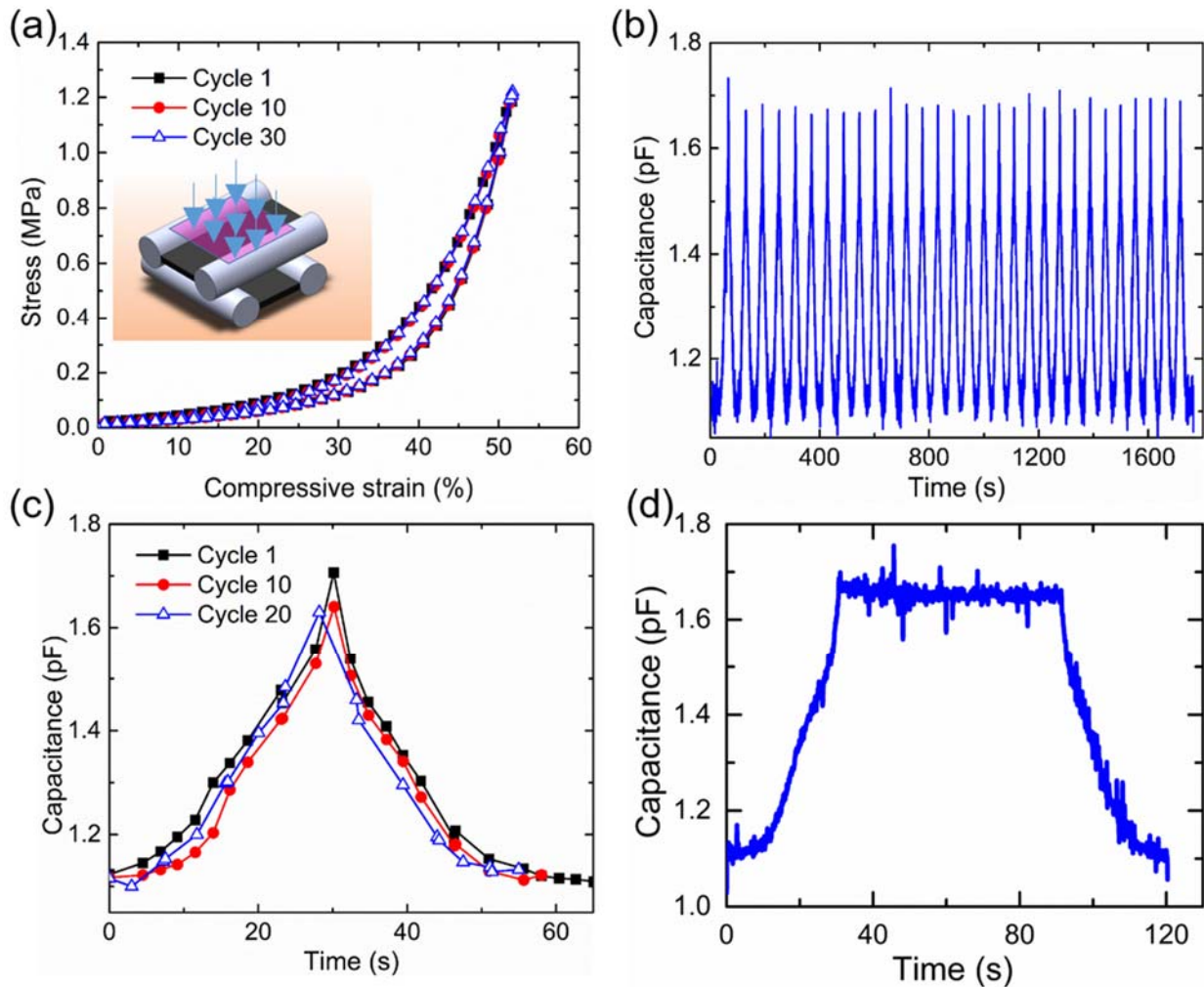


Figure 35: (a) Stress–strain behavior of a texel subjected to 30 cycles of 50% strain in compression. 1st, 10th, and 30th cycles are shown; (b) Force–capacitance response of a texel subjected to 20 cycles of 0–4 N compressive loading; (c) 1st, 10th, and 20th cycles of the force–capacitance response of the texel shown in (b), and (d) capacitive response of the texel under 4 N sustained compressive load for 60 s. [Adapted from: Kapoor, Ashish, et al. *Advanced Materials Technologies* 4.1 (2019): 1800281.]

The multitouch capability of our sensory patch was probed using a tactile array consisting of 36 texels woven in a 1-up, 1-down pattern. The capacitive response of the woven texels was measured using a custom PCB, housing the analog-to-digital conversion circuitry. The fibers in the woven array were attached to a flexible PCB made of polyimide film using a combination of Ag/AgCl conductive epoxy (8331, MG Chemicals,) and silicone adhesive (Sugru Moldable glue).

The flex PCB was then attached to the custom wireless circuitry using a commercial flexible flat cable. Various weighted letter blocks made of acrylonitrile butadiene styrene (ABS) plastic were manually pressed onto various locations on the array and the resulting change in texel capacitance values were displayed; see *Figure 36*. The simple demonstration illustrates the multitouch sensitivity of our texel array.

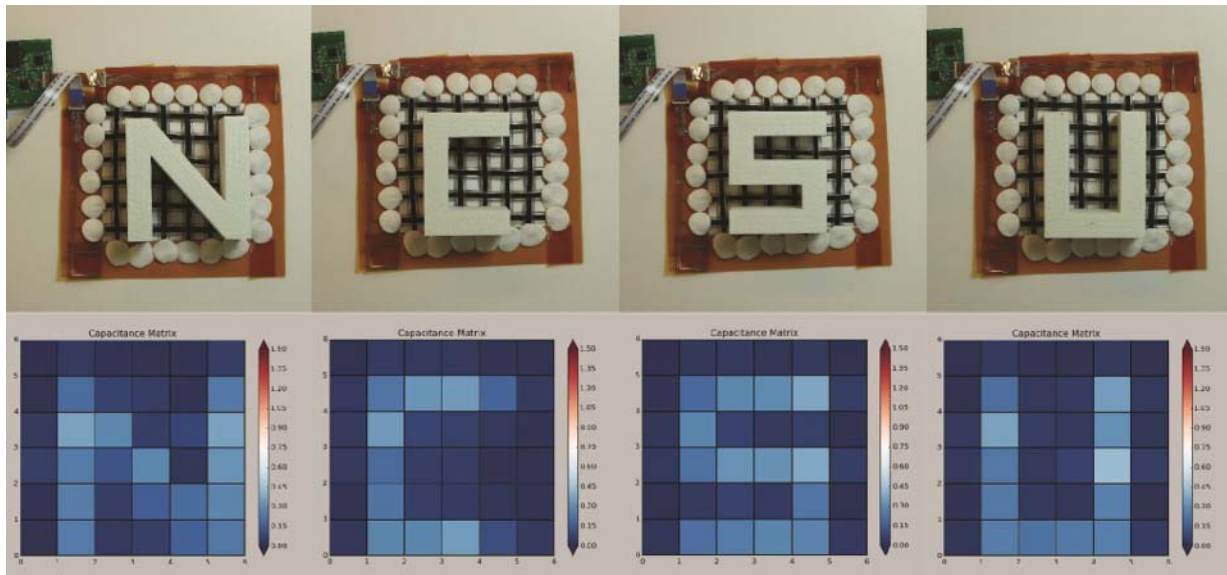


Figure 36: Demonstration of the multitouch sensing capabilities of a texel array. [Adapted from: Kapoor, Ashish, et al. *Advanced Materials Technologies* 4.1 (2019): 1800281.]

The unique texels can also be used to evaluate in-plane shear strain experienced by a fabric. We measured the change in capacitance of a texel under shear strain by applying edge forces to our sensory patch and recording its capacitive response at discrete points of shear strain (angle) (see *Figure 37a*). The shear strain–capacitance data plotted in indicate strong sensory response of the fabric texel as a shear sensor (see *Figure 37b*). While this indicates potential use of the fiber in textile-based sensing of shear, it also underlines the need for fabric designs that are less susceptible to shear deformation if tensile and tactile measurements are the primary requirements.

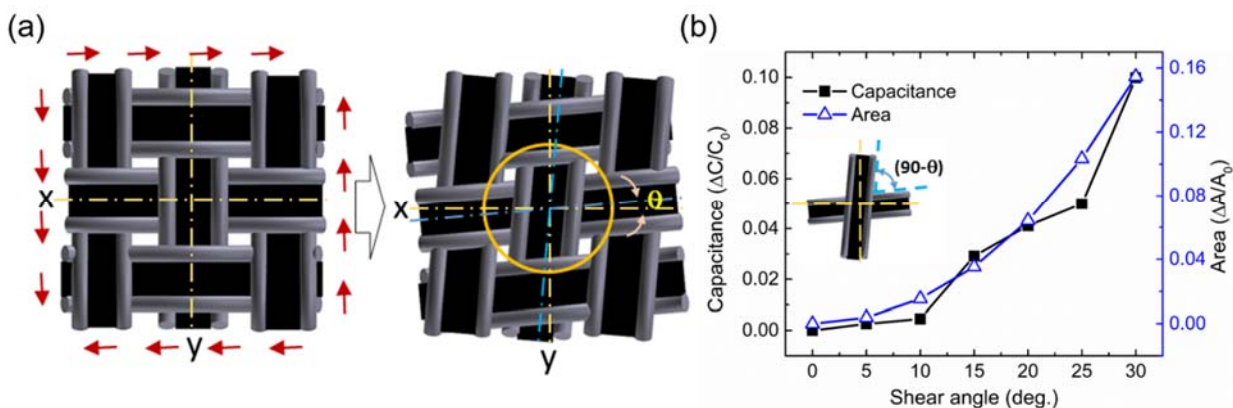


Figure 37: (a) Schematic representations of the deformation of a texel array subjected to a specific shear angle  $\theta$ , and (b) Capacitive response and resulting change in the area (calculated) of the overlap region in a texel, subjected to shear. [Adapted from: Kapoor, Ashish, et al. *Advanced Materials Technologies* 4.1 (2019): 1800281.]

Wetness sensing capabilities were evaluated by performing electrochemical impedance spectroscopy between fibers at a crossover point. Spectroscopy was first performed on a dry texel, and subsequently on the same wetted with saline (1.2 wt. % by volume NaCl). The spectroscopy was repeated at regular time intervals until the texel was visibly dry due to evaporation. The impedance of the dry sensing texels was found to be more than two orders of magnitude larger ( $>10^7 \Omega$ ) than that wetted with saline solution ( $<10^4 \Omega$ ) (see Figure 38). The texels rapidly detected the presence of a small amount of saline solution (12  $\mu\text{L}$ ), as capillary action quickly pulled the saline to its interior. Once the texel was saturated, the impedance level dropped substantially and slowly recovered to the dry sensor level when left to dry in ambient conditions (20  $^\circ\text{C}$ , relative humidity of 65%) for 2 h (Figure 38).

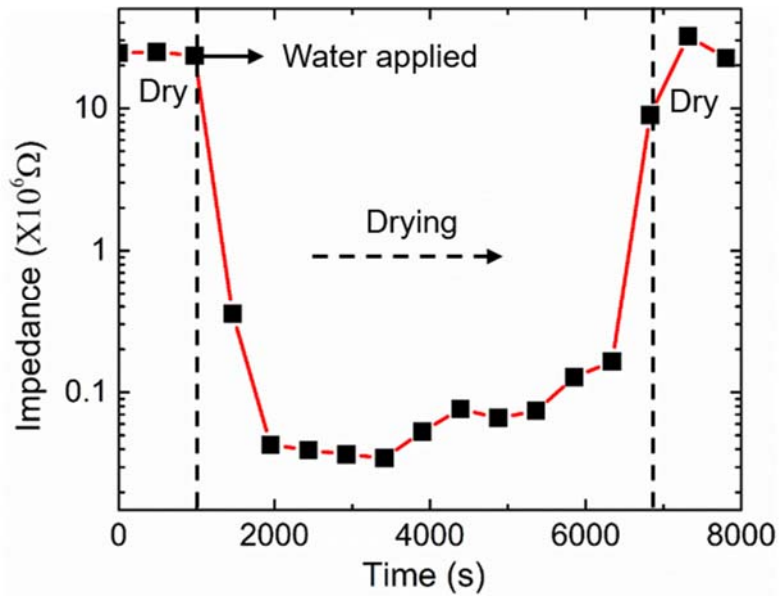


Figure 38: Impedance response of a texel in a wetting–drying cycle using saline. [Adapted from: Kapoor, Ashish, et al. *Advanced Materials Technologies* 4.1 (2019): 1800281.]

These fibers can also be arranged to emulate a woven structure with floats, to work as skin electrodes for electrocardiography (ECG). Although ECG measurements are conventionally done using 12 leads, we recorded the signal using three electrodes (see Figure 39a) each made up of three fibers in parallel arranged in the same manner as they will be in a woven fabric and placed following chest patch/strap recording systems [36], [37]. The recorded signal shows the expected  $Q$ ,  $R$ , and  $S$  waveforms (Figure 39b).

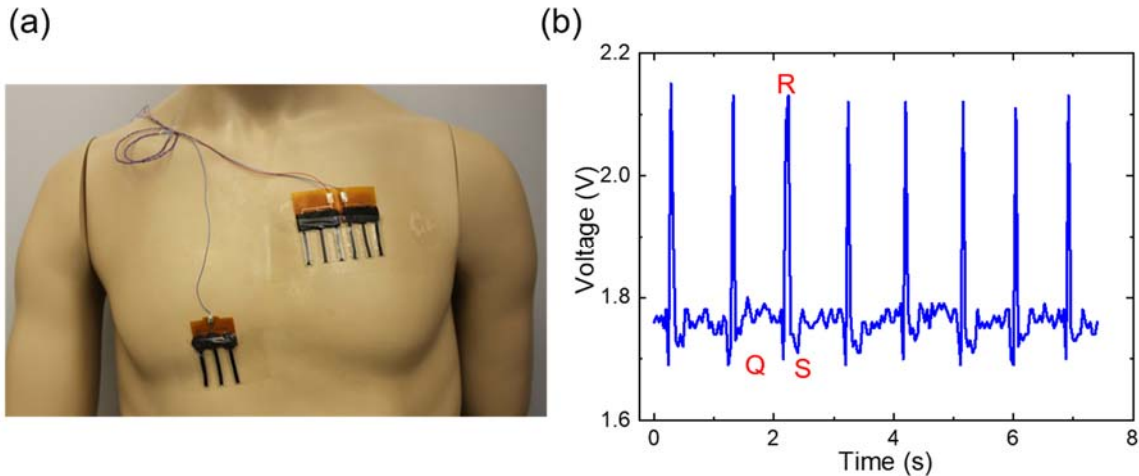


Figure 39: (a) Three-electrode ECG measurement setup and (b) Measured signal. [Adapted from: Kapoor, Ashish, et al. "Toward Fully Manufacturable, Fiber Assembly-Based Concurrent Multimodal and Multifunctional Sensors for e-Textiles." *Advanced Materials Technologies* 4.1 (2019): 1800281.]

Now that we have demonstrated the multimodal capabilities of our sensing texel, it is important to explore if the texels are capable of distinguishing between, for example, capacitive response originating from in-plane tensile deformation of the fibers in a texel array and that from tactile pressure. To examine this, simultaneous capacitance and resistance measurements of a fiber texel were carried out in an experimental setup that allows application of directional in-plane tensile strains as well as compression of the texel, independently (Figure 40a). The capacitance and resistance data plotted in Figure 40b in four side-by-side panels represent response under no-load (panel 1), only compression (panel 2), in-plane tension (panel 3), and simultaneous tension and compression (panel 4). Several key features are evident from these results. Notably, compression-only mode causes significant capacitance change with no change in resistance. In case of tension (biaxial), significant resistance change is accompanied by minor change in capacitance. Lastly, simultaneous application of compression and in-plane tension causes notable change in both resistance and capacitance. The data clearly demonstrate the unique potential of

our fibers in applications where characterization of complex deformation may be necessary. The resistance/capacitance data can be analyzed to determine if the texel is experiencing normal pressure or in-plane strain, locally.

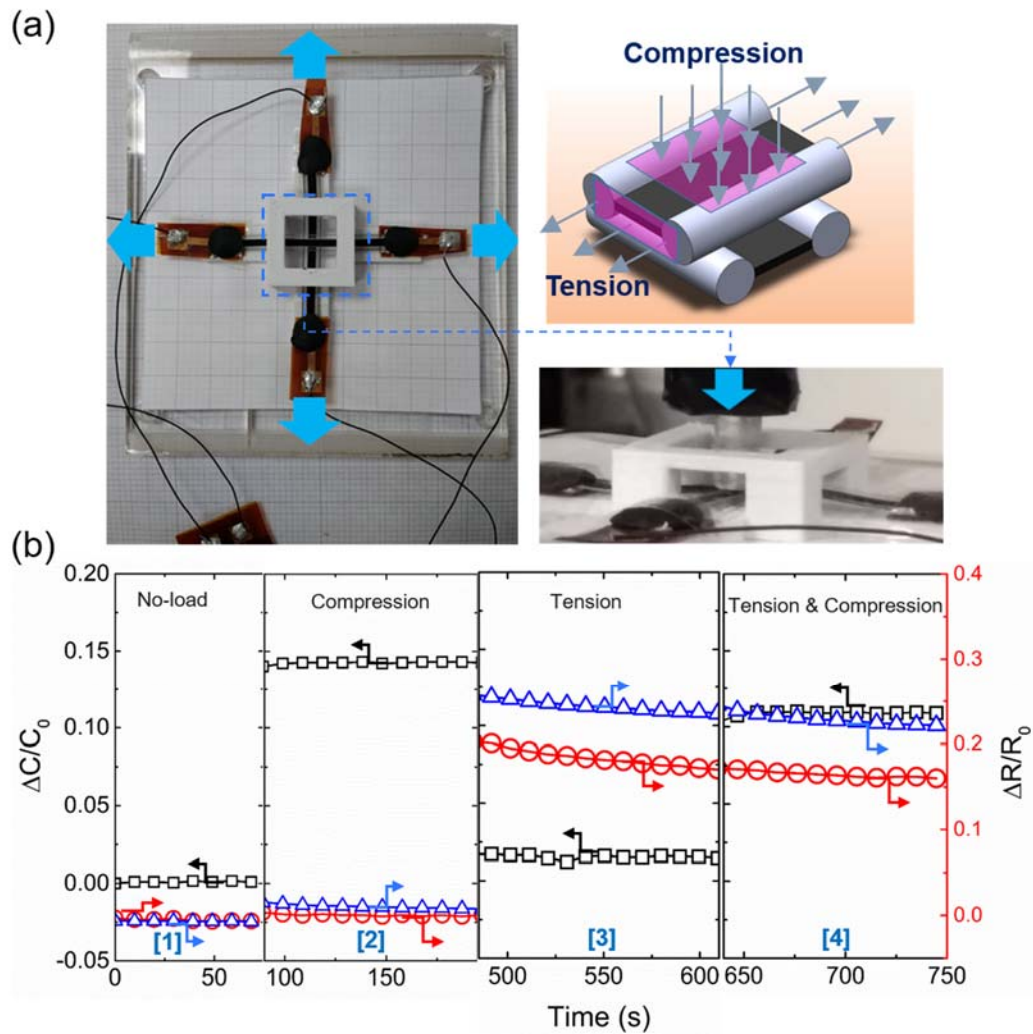


Figure 40: (a) Experimental set-up for simultaneous capacitance and resistance measurements of a fiber texel. The set-up allows application of directional in-plane tensile strains as well as compression of the texel. (b) Capacitive ( $\square$ ) and resistive (along bottom fiber:  $\circ$ , along top fiber:  $\Delta$ ) response of a texel 1) under no-load, 2) only compression, 3) in-plane tension, and 4) simultaneous tension and compression. The arrows point to the corresponding axis. [Adapted from: Kapoor, Ashish, et al. *Advanced Materials Technologies* 4.1 (2019): 1800281.]

### 3.5 Conclusion

This work demonstrated a platform technology in the form of stretchable and conformable texel arrays made of our polymeric bicomponent fibers produced via a benchtop extrusion process at room temperature. These fibers are capable of multiple sensing modalities and can be used for monitoring various forces (tactile/tensile/shear), biopotentials, and wetness. While an array of these fiber texels can detect the location and magnitude of multiple point forces (tactile) as well as wetness, a parallel set of these fibers in a woven structure can be used as skin electrodes for ECG. In all cases, the sensing exhibited stable performance using our wireless Bluetooth-enabled circuitry, so an array of these fibers could be woven as part of a textile fabric for remote sensing of the aforementioned parameters together with their spatial resolution. The exceptional strength of our approach is in its facile scalability and its potential to manufacture from a wide variety of materials using simple and time-tested industrial processes. Although we have chosen PDMS for the ease of demonstration, the sensory fibers can be manufactured using commercial bicomponent melt-extrusion systems and can be easily assembled into sensor arrays using commercial roll-to-roll weaving process, thus allowing a simple, cheap, yet robust sensing platform for high-performance, large-area e-textile sensors.

## References

- [1] D. Liu *et al.*, “Solid-State, Polymer-Based Fiber Solar Cells with Carbon Nanotube Electrodes,” *ACS Nano*, vol. 6, no. 12, pp. 11027–11034, Dec. 2012, doi: 10.1021/nn304638z.
- [2] A. (Celik) Bedeloglu, A. Demir, Y. Bozkurt, and N. S. Sariciftci, “A Photovoltaic Fiber Design for Smart Textiles,” *Textile Research Journal*, vol. 80, no. 11, pp. 1065–1074, Jul. 2010, doi: 10.1177/0040517509352520.
- [3] C. Müller *et al.*, “Woven Electrochemical Transistors on Silk Fibers,” *Advanced Materials*, vol. 23, no. 7, pp. 898–901, 2011, doi: 10.1002/adma.201003601.
- [4] S. S. Yoon *et al.*, “Highly Conductive Graphene/Ag Hybrid Fibers for Flexible Fiber-Type Transistors,” *Scientific Reports*, vol. 5, p. 16366, Nov. 2015, doi: 10.1038/srep16366.
- [5] M. Y. Lee *et al.*, “Highly Flexible Organic Nanofiber Phototransistors Fabricated on a Textile Composite for Wearable Photosensors,” *Advanced Functional Materials*, vol. 26, no. 9, pp. 1445–1453, 2016, doi: 10.1002/adfm.201503230.
- [6] P. J. Jeon, S. Lee, Y. T. Lee, H. S. Lee, K. Oh, and S. Im, “Manipulating ZnO nanowires for field-effect device integration by optical-fiber grip coated with thermoplastic copolymer,” *J. Mater. Chem. C*, vol. 1, no. 44, pp. 7303–7307, Oct. 2013, doi: 10.1039/C3TC31303D.
- [7] S. Danto, Z. Ruff, Z. Wang, J. D. Joannopoulos, and Y. Fink, “Ovonic Memory Switching in Multimaterial Fibers,” *Advanced Functional Materials*, vol. 21, no. 6, pp. 1095–1101, 2011, doi: 10.1002/adfm.201002252.
- [8] J. Foroughi *et al.*, “Knitted Carbon-Nanotube-Sheath/Spandex-Core Elastomeric Yarns for Artificial Muscles and Strain Sensing,” *ACS Nano*, vol. 10, no. 10, pp. 9129–9135, 2016, doi: 10.1021/acsnano.6b04125.

- [9] Y. Abdul Samad *et al.*, “From sewing thread to sensor: Nylon® fiber strain and pressure sensors,” *Sensors Actuators B: Chem.*, vol. 240, no. Journal Article, pp. 1083–1090, 2017, doi: 10.1016/j.snb.2016.09.088.
- [10] B. K. Gu, Y. A. Ismail, G. M. Spinks, S. I. Kim, I. So, and S. J. Kim, “A Linear Actuation of Polymeric Nanofibrous Bundle for Artificial Muscles,” *Chem. Mater.*, vol. 21, no. 3, pp. 511–515, Feb. 2009, doi: 10.1021/cm802377d.
- [11] B. Kim, M. G. Lee, Y. P. Lee, Y. Kim, and G. Lee, “An earthworm-like micro robot using shape memory alloy actuator,” *Sensors and Actuators A: Physical*, vol. 125, no. 2, pp. 429–437, Jan. 2006, doi: 10.1016/j.sna.2005.05.004.
- [12] S. L. Kim, K. Choi, A. Tazebay, and C. Yu, “Flexible Power Fabrics Made of Carbon Nanotubes for Harvesting Thermoelectricity,” *ACS Nano*, vol. 8, no. 3, pp. 2377–2386, Mar. 2014, doi: 10.1021/nm405893t.
- [13] S. Bai, L. Zhang, Q. Xu, Y. Zheng, Y. Qin, and Z. L. Wang, “Two dimensional woven nanogenerator,” *Nano Energy*, vol. 2, no. 5, pp. 749–753, Sep. 2013, doi: 10.1016/j.nanoen.2013.01.001.
- [14] B. O’Connor, K. H. An, Y. Zhao, K. P. Pipe, and M. Shtein, “Fiber Shaped Light Emitting Device,” *Advanced Materials*, vol. 19, no. 22, pp. 3897–3900, 2007, doi: 10.1002/adma.200700627.
- [15] A. Jo *et al.*, “Textile Resistance Switching Memory for Fabric Electronics,” *Advanced Functional Materials*, vol. 27, no. 15, p. 1605593, 2017, doi: 10.1002/adfm.201605593.
- [16] S. Jung, J. Lee, T. Hyeon, M. Lee, and D.-H. Kim, “Fabric-Based Integrated Energy Devices for Wearable Activity Monitors,” *Advanced Materials*, vol. 26, no. 36, pp. 6329–6334, 2014, doi: 10.1002/adma.201402439.

- [17] C.-T. Huang, C.-L. Shen, C.-F. Tang, and S.-H. Chang, “A wearable yarn-based piezo-resistive sensor,” *Sensors and Actuators A: Physical*, vol. 141, no. 2, pp. 396–403, 2008, doi: 10.1016/j.sna.2007.10.069.
- [18] W. Li, F. Xu, L. Sun, W. Liu, and Y. Qiu, “A novel flexible humidity switch material based on multi-walled carbon nanotube/polyvinyl alcohol composite yarn,” *Sensors Actuators B: Chem.*, vol. 230, no. Journal Article, pp. 528–535, 2016, doi: 10.1016/j.snb.2016.02.108.
- [19] Q. Lin, Y. Li, and M. Yang, “Investigations on the sensing mechanism of humidity sensors based on electrospun polymer nanofibers,” *Sensors Actuators B: Chem.*, vol. 171–172, no. Journal Article, pp. 309–314, 2012, doi: 10.1016/j.snb.2012.03.082.
- [20] H. A. K. Toprakci, S. K. Kalanadhabhatla, R. J. Spontak, and T. K. Ghosh, “Polymer Nanocomposites Containing Carbon Nanofibers as Soft Printable Sensors Exhibiting Strain-Reversible Piezoresistivity,” *Advanced Functional Materials*, vol. 23, no. 44, pp. 5536–5542, Nov. 2013, doi: 10.1002/adfm.201300034.
- [21] A. Tognetti *et al.*, “Wearable kinesthetic system for capturing and classifying upper limb gesture in post-stroke rehabilitation,” *Journal of NeuroEngineering and Rehabilitation*, vol. 2, no. 1, p. 8, Mar. 2005, doi: 10.1186/1743-0003-2-8.
- [22] J. Lee *et al.*, “Highly conductive and flexible fiber for textile electronics obtained by extremely low-temperature atomic layer deposition of Pt,” *NPG Asia Mater*, vol. 8, no. Journal Article, p. e331, 2016.
- [23] J. Lee *et al.*, “Conductive Fiber-Based Ultrasensitive Textile Pressure Sensor for Wearable Electronics,” *Advanced Materials*, vol. 27, no. 15, pp. 2433–2439, 2015.

- [24] S. Takamatsu, T. Yamashita, and T. Itoh, "Meter-scale large-area capacitive pressure sensors with fabric with stripe electrodes of conductive polymer-coated fibers," *Microsyst Technol*, vol. 22, no. 3, pp. 451–457, Mar. 2016, doi: 10.1007/s00542-015-2498-3.
- [25] S. Takamatsu, T. Kobayashi, N. Shibayama, K. Miyake, and T. Itoh, "Fabric pressure sensor array fabricated with die-coating and weaving techniques," *Sensors and Actuators A: Physical*, vol. 184, pp. 57–63, Sep. 2012, doi: 10.1016/j.sna.2012.06.031.
- [26] B. You, C. J. Han, Y. Kim, B.-K. Ju, and J.-W. Kim, "A wearable piezocapacitive pressure sensor with a single layer of silver nanowire-based elastomeric composite electrodes," *Journal of Materials Chemistry A*, 2016.
- [27] L. Pang *et al.*, "Enhanced pressure & proximity sensitivities of a flexible transparent capacitive sensor with PZT nanowires," *IOP Conf. Ser.: Mater. Sci. Eng.*, vol. 479, p. 012035, Mar. 2019, doi: 10.1088/1757-899X/479/1/012035.
- [28] M. Amjadi, K.-U. Kyung, I. Park, and M. Sitti, "Stretchable, Skin-Mountable, and Wearable Strain Sensors and Their Potential Applications: A Review," *Adv. Funct. Mater.*, vol. 26, no. 11, pp. 1678–1698, Mar. 2016, doi: 10.1002/adfm.201504755.
- [29] O. Atalay, A. Atalay, J. Gafford, H. Wang, R. Wood, and C. Walsh, "A Highly Stretchable Capacitive-Based Strain Sensor Based on Metal Deposition and Laser Rastering," *Advanced Materials Technologies*, vol. 2, no. 9, p. 1700081, 2017, doi: 10.1002/admt.201700081.
- [30] J. A. Dobrzynska and M. A. M. Gijs, "Polymer-based flexible capacitive sensor for three-axial force measurements," *J. Micromech. Microeng.*, vol. 23, no. 1, p. 015009, Nov. 2012, doi: 10.1088/0960-1317/23/1/015009.

- [31] N. C. Das, T. K. Chaki, and D. Khastgir, "Effect of axial stretching on electrical resistivity of short carbon fibre and carbon black filled conductive rubber composites," *Polym. Int.*, vol. 51, no. 2, pp. 156–163, Feb. 2002, doi: 10.1002/pi.811.
- [32] W. Luheng, D. Tianhuai, and W. Peng, "Influence of carbon black concentration on piezoresistivity for carbon-black-filled silicone rubber composite," *Carbon*, vol. 47, no. 14, pp. 3151–3157, Nov. 2009, doi: 10.1016/j.carbon.2009.06.050.
- [33] V. K. S. Shante and S. Kirkpatrick, "An introduction to percolation theory," *Advances in Physics*, vol. 20, no. 85, pp. 325–357, May 1971, doi: 10.1080/00018737100101261.
- [34] Y. Wei, S. Chen, X. Dong, Y. Lin, and L. Liu, "Flexible piezoresistive sensors based on 'dynamic bridging effect' of silver nanowires toward graphene," *Carbon*, vol. 113, pp. 395–403, Mar. 2017, doi: 10.1016/j.carbon.2016.11.027.
- [35] X. Guo, Y. Huang, X. Cai, C. Liu, and P. Liu, "Capacitive wearable tactile sensor based on smart textile substrate with carbon black/silicone rubber composite dielectric," *Measurement Science and Technology*, vol. 27, no. 4, p. 045105, 2016.
- [36] Y. Wang, S. Doleschel, R. Wunderlich, and S. Heinen, "A Wearable Wireless ECG Monitoring System With Dynamic Transmission Power Control for Long-Term Homecare," *J Med Syst*, vol. 39, no. 3, p. 35, Feb. 2015, doi: 10.1007/s10916-015-0223-5.
- [37] Y. Yamamoto *et al.*, "Efficient Skin Temperature Sensor and Stable Gel-Less Sticky ECG Sensor for a Wearable Flexible Healthcare Patch," *Advanced Healthcare Materials*, vol. 6, no. 17, p. 1700495, 2017, doi: 10.1002/adhm.201700495.

## **CHAPTER 4: Fabrication of Multimodal Fiber-based Sensors via Coextrusion: A Microfluidics-Inspired Approach**

### **4.1 Introduction**

With the increase in demand for wearable devices, fiber based sensors [1]–[3] have attracted much attention because of their potential for creating electronic textiles for applications such as health monitoring, interactive interfaces, etc. A lot of the fiber-based sensors have been fabricated using carbon-based electrically functional nanomaterials including carbon black [4], carbon nanotubes [5] and graphene [1]. Though the utility of fiber-based sensors has been recognized as a key step for truly mass-produced electronic textiles, most of the current fiber-based sensors are limited to a single sensing functionality only and only a few have production and dimensional compatibility with textiles. A multimodal and multifunctional fiber-based sensor can offer unobtrusive integration of sensing capabilities into textiles enabling many practical systems in physiological monitoring, comfort, medicine, security, surveillance, and protection. This work demonstrates one-step fabrication of uniquely cross-sectioned bicomponent conductive fibers through an innovative approach, referred as coextrusion. This fiber formation method was inspired from microfluidic fiber formation techniques [8]–[13]. In the coextrusion process, an extrusion die with inbuilt channels was used for shaping the polymeric materials to create the desired fiber shape. This process is versatile as extrusion channels with complex geometries can be fabricated to create desired shape of fiber and variety of materials can be processed. Another advantage is that this process can produce continuous long lengths of fibers just like conventional fiber formation processes. Researchers have used similar approach to create functional fibers for sensing applications such as multicore capacitive fibers for strain sensing [14], optical fibers with core-cladding structures for sensing deformations [15], bicomponent fibers with tunable structures for

wearable devices [16] and electroluminescent fibers for textile displays [17]. The commercial and common bicomponent fiber formation process where two dissimilar materials of different chemical and/or physical properties are processed to form a desired shape of fiber is melt spinning [6], [7] but the advantages of the proposed scalable coextrusion approach include cost effectiveness, flexibility to customization and variety in choice of materials than can be processed. The bicomponent fiber fabricated via coextrusion process has a dumbbell cross-section where side segments are insulating and middle bridge is conducting. When woven, these fibers act as capacitive sensors providing multifunctional sensing capabilities (see Figure 41). For more details refer section 3.2. Previously, sequential extrusion printing process was used to make these fibers but it was a multi-step process with limitation on fiber length. Through this new coextrusion technique, the multimodal fiber was produced in one-step with a higher yield. The fibers were woven into an array and their multifunctional sensing capabilities were evaluated.

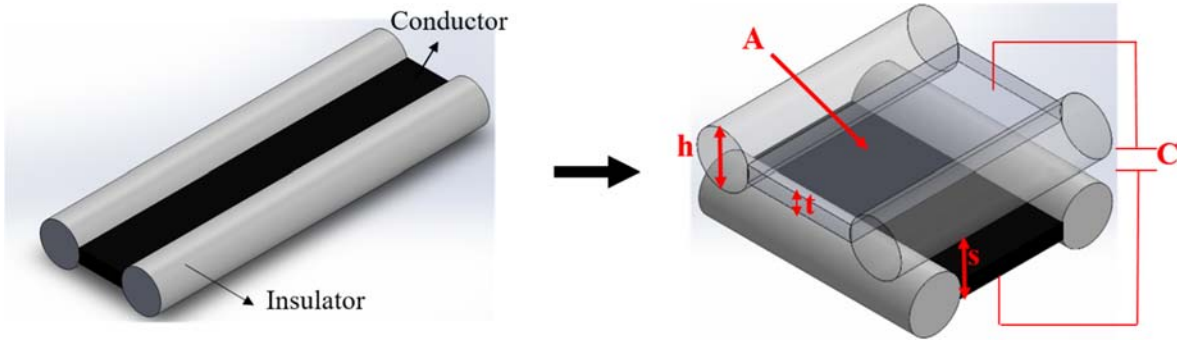


Figure 41: Schematic of bicomponent dumbbell fiber and a capacitive crossover where ‘h’ is height of insulating segments ‘t’ is thickness of conductor, ‘C’ is capacitance with ‘s’ as conductor separation and ‘A’ as overlapping area of electrode

## 4.2 Materials and Methods

Poly(dimethylsiloxane) (PDMS)  $[(CH_3)_2SiO]_n$  elastomer was selected for fiber formation owing to its low Young’s modulus and good elastic recovery [18]. The conductive segment of fiber was fabricated by incorporating carbonaceous particles, carbon black (CB) into PDMS above

percolation threshold [19]–[22]. CB has been widely used for fabricating polymer-matrix composites [23]. CB was chosen because of its ease of processing (dispersion) and commercial availability in a wide range of particle diameters (10-500 nm) and surface area (4.87-981.6 m<sup>2</sup>/g) [24], [25]. PDMS was used as base polymer for both insulating and conducting segments in order to have compatibility in processing as well as interfacial adhesion between the conducting and insulating segments during use. Table 2 lists the properties of PDMS used. The base and catalyst silicone (UV Electro 225-1) were mixed (100:2 ratio) with ≈2.5 % viscosity modifier (Silicone fluid, Xiameter PMX-200) using a planetary mixer (Mazerustar) rotating at speed of 1040 rpm (level 6) for 60s to form the insulating segment material. The conductive segments consisted of a heat-curing silicone (Ecoflex 00-50) filled with 6.4 wt.% carbon black (Ketjenblack EC-300J, Akzo-Nobel), duly dispersed in 20 ml hexane using a planetary mixer at similar conditions using steel balls for homogenous dispersion. *Figure 42* shows the various steps in preparation of conducting mixture where it is seen in *Figure 42b* that steel balls have grinded the CB pellets into fine powder for better dispersion in hexane. The cracks separating clumps of CB dispersion in hexane are due to evaporation of solvent while taking the image. *Figure 42c* shows the final conducting mixture with CB dispersion mixed in PDMS, ready to be used for extrusion. The conducting mixture was subsequently cured to create a film and the film was placed under a transmission electron microscope (TEM) to observe the nanostructure. TEM images (refer *Figure 43*) indicated a high structure CB with spherical primary particles forming aggregates [26], [27].

Table 2: Properties of PDMS used for insulating and conducting segments fabrication

Material	Viscosity (cP)	Pot life	Cure time at RT*
Silopren UV Electro 225-1 (insulator)	70,000	1 day	< 1min by UV light**
Ecoflex 00-50 (conductor)	8,000	18 min	3 hours

\*Room temperature, \*\*depends on UV light intensity



Figure 42: Steps in creating conducting material for extrusion: (a) CB pellets. (b) CB pellets dispersed in hexane. (c) CB dispersion mixed with PDMS. Note: Image magnification = 40X

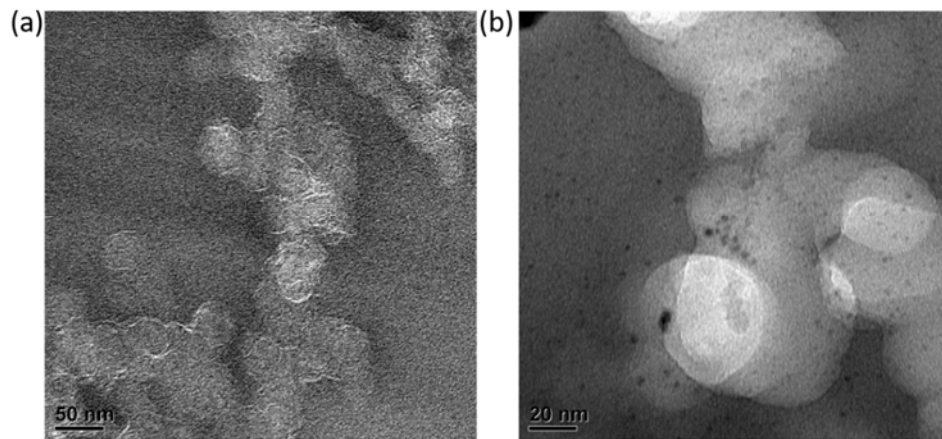


Figure 43: TEM images of conducting polymer composite showing the nanostructures of CB dispersed in silicone at (a) 50 nm and (b) 20 nm

The target dumbbell shaped fiber consists of two circular insulating sides separated by conductive bridge. Therefore, the extrusion channel design consisted of three inlet channels namely two side channels for insulating segments and one channel in middle for conductive segment formation (refer Figure 44). The channels were separated by walls for almost entire length to prevent mixing of fluids but there was a no wall region of 1 mm just before exit for the streams to come in contact to create the target shape without mixing. The length of the no wall region is critical as longer lengths led to mixing of conductive and insulating fluids whereas eliminating no wall region led to three separate streams falling from the orifice exit.

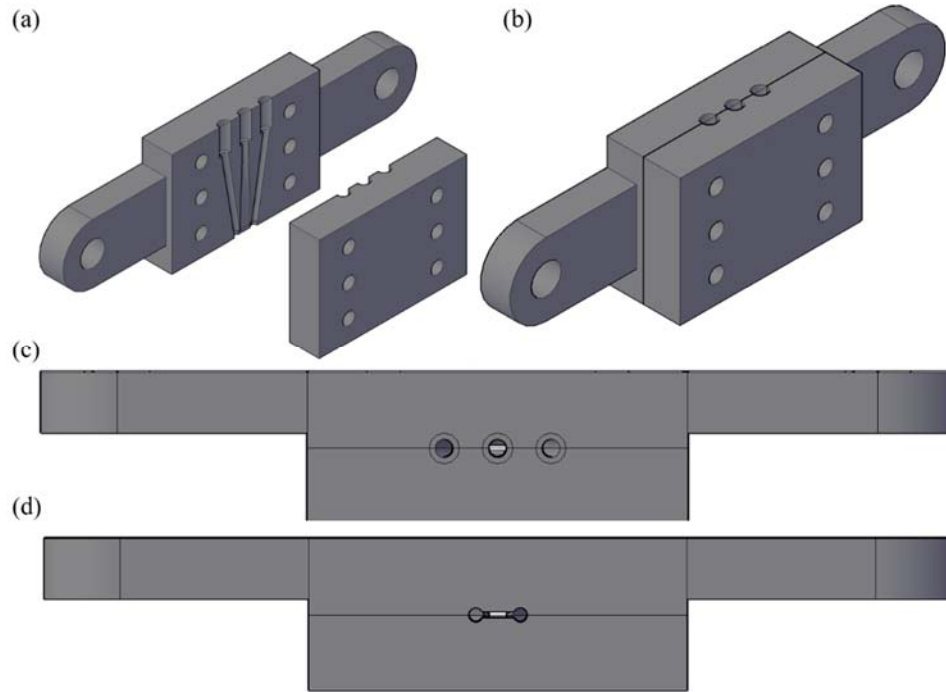


Figure 44: Schematic of extrusion channel; (a) before assembling with three fluid flow channels, (b) after assembling the two parts, (c) top view showing three inlets for delivering insulating and conducting materials and (d) bottom view showing dumbbell shaped orifice.

The extrusion printed fibers fabricated previously provided a reference for deciding target fiber dimensions as well as extrusion channel orifice dimensions. The most significant aspect of this fiber design is the conductor separation when two fibers are orthogonally placed on top of each other which is dictated by the difference in insulator height and conductor thickness and the symmetry of the conducting segment with reference to insulating segments. Three extrusion channels were designed with different orifice dimensions as summarized in Table 3 to create large, medium and small size fibers.

Table 3: Dimensions of dumbbell shaped orifice of extrusion channels

Fiber size	Insulator height	Conductor thickness	Conductor width	Capacitor separation
Large	2	0.85	4	1.15
Medium	1.5	0.5	3	1
Small	1	0.4	3	0.6

The extrusion device was 3D printed using methacrylate clear resin on Formlabs Form 2 printer because of its high print resolution. It was printed in two parts for ease of cleaning. The assembled device was sandwiched between two metal plates to induce pressure to prevent any fluid leakage and polyurethane tubing was inserted in the top inlets for delivering the materials (refer *Figure 45*).

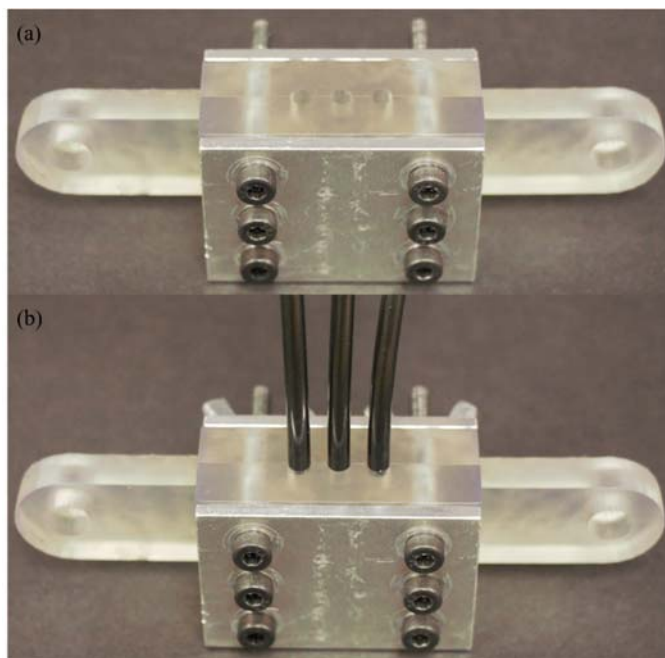


Figure 45: 3D printed extrusion device assembled together with metal plates (a) before and (b) after the tubing is inserted.

The setup (refer *Figure 46* ) consisted of two syringe pumps feeding insulating and conducting polymer into a custom 3D printed three channel extrusion device to form the dumbbell shaped fiber structure. Downstream of the extrusion die orifice, the insulating segment sides of fiber were cured by UV light while middle conducting segment was cured by heat when the fiber was collected on a heated winding drum. The extrusion rate and winding rate along with lateral traverse were matched to achieve continuous deposition of fibers on drum. An Arduino and

LabVIEW program were used to control the drum rotation speed and lateral traverse of drum respectively. The heated winding drum was wrapped by a black Teflon sheet. Teflon helped in easy peel off of fibers while black color minimized any reflection of UV light onto extrusion nozzle, otherwise causing clogging at orifice.

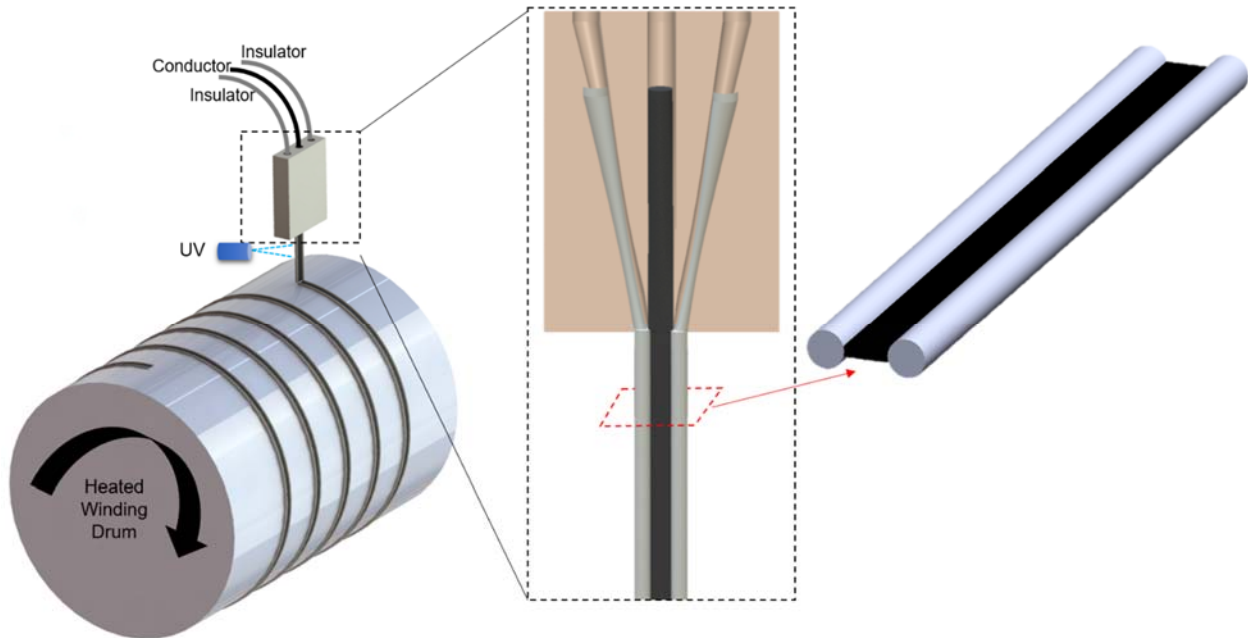


Figure 46: Schematic of fiber coextrusion process

Firstly, the insulating sides are pumped and when they exit at the orifice, the conducting material is pumped (refer Figure 47) because presence of insulator in channel initially, prevents migration of conducting polymer into empty side channels in the no wall region. There were four variables in the coextrusion process as shown in Figure 48 which were tuned to obtain the desired fiber shape. These are discussed below.

*(a) Drop height*

It is the distance between the orifice and the point on the winding drum where the fiber drops. Larger drop height led to breakage of fluid stream under its own weight and the minimum drop

height was defined by the space required to accommodate UV light between winding drum and orifice without curing the fiber at orifice.

*(b) Drop point*

This refers to the position on the drum where the fiber drops. If the fiber was dropped exactly on top of drum (perpendicular) then it led to large bending of fluid stream and disruption of flow continuity so in order to avoid this, the winding drum was offset to displace the fiber drop point away from drum center. This also provided flexibility in changing drop height and accommodating UV light.

*(c) UV light incidence point*

This is the point on the fluid stream where UV light is incident to cure the insulating segments of fiber. Ideally, this point should be as close as possible to the orifice but the light is emitted as a cone covering a larger area compared to light bulb diameter so UV light was placed optimally to cure the fiber before the insulating and conducting streams mixed while preventing clogging at the orifice.

*(d) Winding speed*

Winding speed or fiber take up speed is the rotation speed of drum and it depends on extrusion rate of fiber. In order to have continuous fiber formation, feed per unit time was matched with the length of fiber collected per unit time. Smaller draw ratios were used in this process because the middle conducting stream only cured after dropping on the hot winding drum. High winding speeds led to breakage of fluid stream.

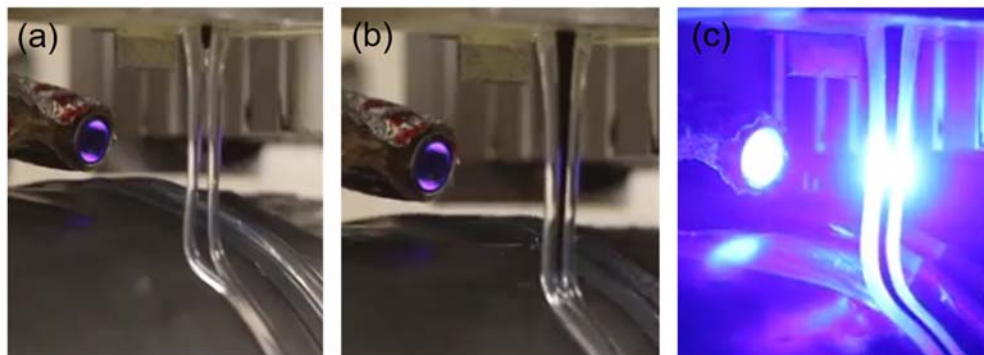


Figure 47: Stages of fiber production; firstly (a) insulating sides are extruded, secondly, (b) middle conducting stream is extruded and lastly, (c) UV light is turned ON.

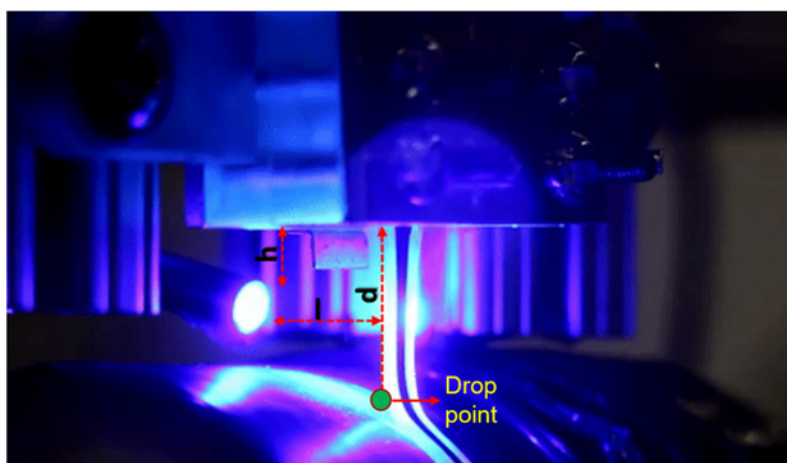


Figure 48: Image of fiber extrusion process showing tunable process parameter where 'd' is drop height, 'l' is distance between UV light and fluid stream and 'h' represents distance from orifice where UV light illuminates the fluid stream and curing begins.

Three fiber sizes, namely, large, medium and small were produced by optimizing the process parameters and the feed rates used to produce these fibers are summarized in *Table 4*. The fiber forming materials were loaded in 10 ml syringes and fibers were collected on a hot winding drum with surface temperature  $\sim 60^{\circ}\text{C}$  at draw ratios 1.2 to 1.6.

Table 4: Optimized coextrusion process parameters

Fiber size	Insulator feed rate (ml/min)	Conductor feed rate (ml/min)	Fiber production rate (mm/min)	Drop height (mm)
Large	0.90	0.97	286.48	28
Medium	0.50	0.42	282.94	26
Small	0.23	0.35	292.85	26

### 4.3 Results and Discussion

The cross-sectional images of fibers as shown in *Figure 49* were obtained using an optical microscope (SMZ 100, Nikon). The images collected in high resolution, digital format were then analyzed using an image analysis software (ImageJ, NIH) to extract geometric features displayed in *Table 5*. It was observed that the conductor width of fiber undergoes largest reduction from the designed conductor width in orifice.

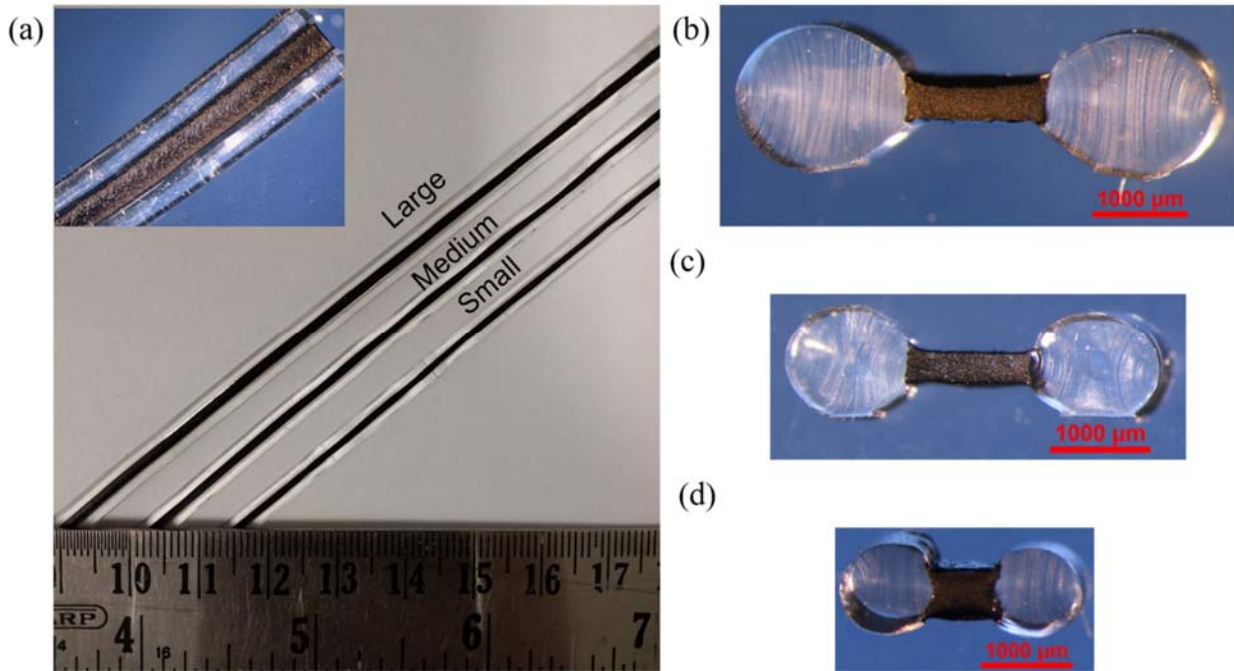


Figure 49: (a) Longitudinal images of all fibers and cross sectional image of (b) large, (c) medium and (d) small fiber.

Table 5: Comparison of fiber dimensions

Fiber size	Insulator height (mm)	Conductor width (mm)	Conductor thickness (mm)	Fiber width (mm)
Large	1.5	1.5	0.4	5
Medium	1.1	1.3	0.3	3.9
Small	1	0.7	0.4	2.7

The tensile properties of fibers were evaluated using load frame (MTS-30G) and 100 N load cell where fibers were stretched till break at a speed of 50mm/min and cycled between 0% and 100% strain to understand their recovery behavior or hysteresis. All the fibers exhibited very high breaking elongation strains, greater than 300% (see Figure 50a). Optical examination of failure points of all fibers showed breakage of conductive segment and one of the insulating segments of the fiber (see Figure 51). The tearing of conducting layer occurs before the breakage of the insulating segments due to lower elongation or higher modulus of conducting material as it consists of carbon black (CB) filled silicone elastomer. This cracking of conducting layer is also confirmed by the irregularities in stress response of fibers at various points before final break (see Figure 50a). Also, the cycling response of fibers stretched and relaxed 30 times showed that all cycles were consistent beyond the first cycle with little hysteresis (see Figure 50b,c,d).

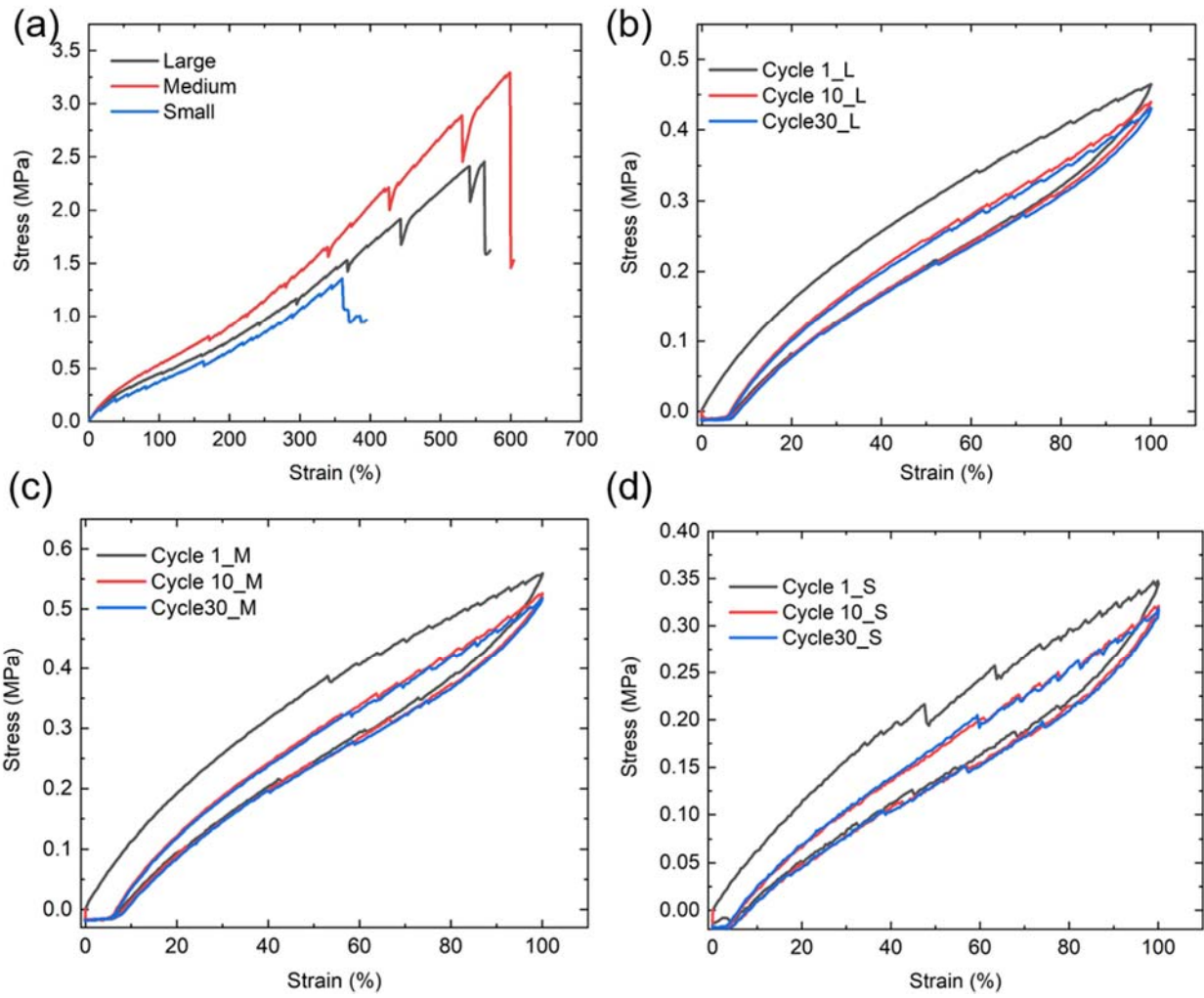


Figure 50: (a) Breaking elongation response of all fibers. Strain cycling response of (b) large, (c) medium, and (d) small fibers.

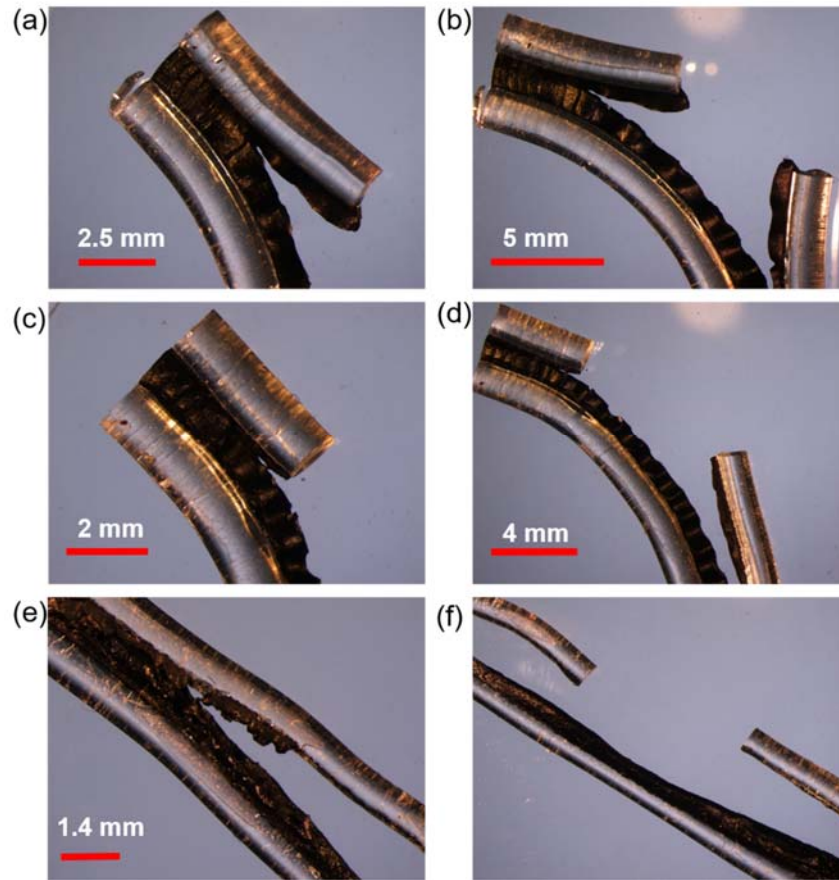


Figure 51: Optical microscope images of (a, b) large, (c, d) medium and (e, f) small fibers after tensile failure showing broken conducting bridge and insulating segment

### ***Sensory Response***

Tactile or pressure sensing capabilities were evaluated by applying normal force using an insulating tip mounted on MTS-30G load frame at the crossover point of two fibers in a nine pixel plain woven array, while recording the capacitance between fibers (*Figure 52 a*). The conductor separation in pixel was decreased by 50% by compressing the pixel at test speed of 5mm/min. Multiple pixels were tested and a representative response is shown in *Figure 52b*. There was a decrease in conductor separation due to compression of insulators which caused an increase in capacitance ( $C$ ) as elucidated before (*Figure 52 c, d*).

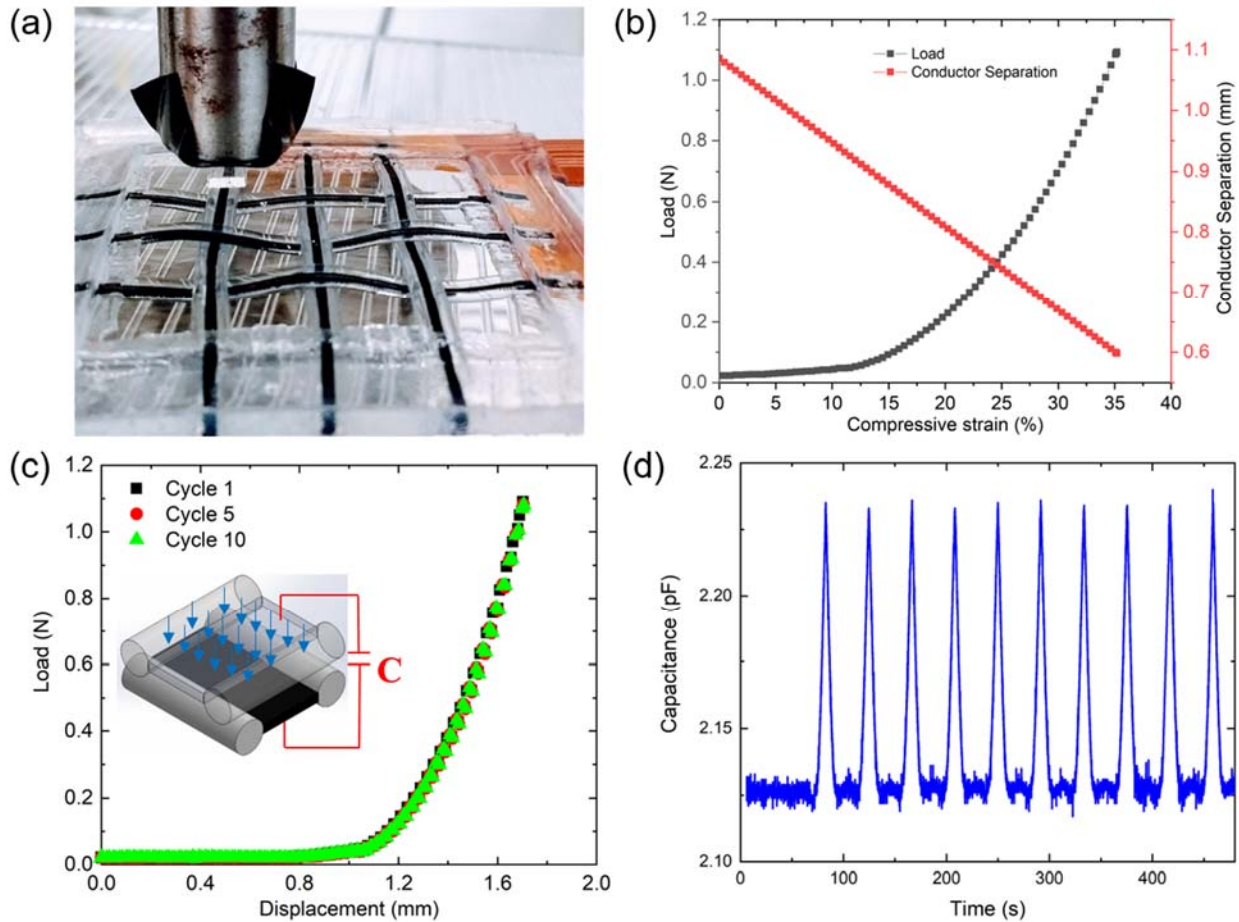


Figure 52: Force –capacitance testing of fibers. (a) Insulating tip attached to load applicator before compressing one of the pixels of woven array. (b) Load-strain response of pixel showing decrease in conductor separation. (c) Load displacement cyclic response of pixel and (d) capacitance response of pixel compressed 10 times.

The response of conducting segment's electrical resistance under mechanical strain was recorded using a four-point probe where a prestrained sample was cycled 30 times between 0% and 40% strain on MTS-30G load frame (see *Figure 53a*). The piezoresistive response showed a stable and reversible resistance change of ~550 ohms under stretch (see *Figure 53b*). This resistive response was used to monitor finger bending motion demonstrating its utility as a strain sensor (refer *Figure 53 c, d*).

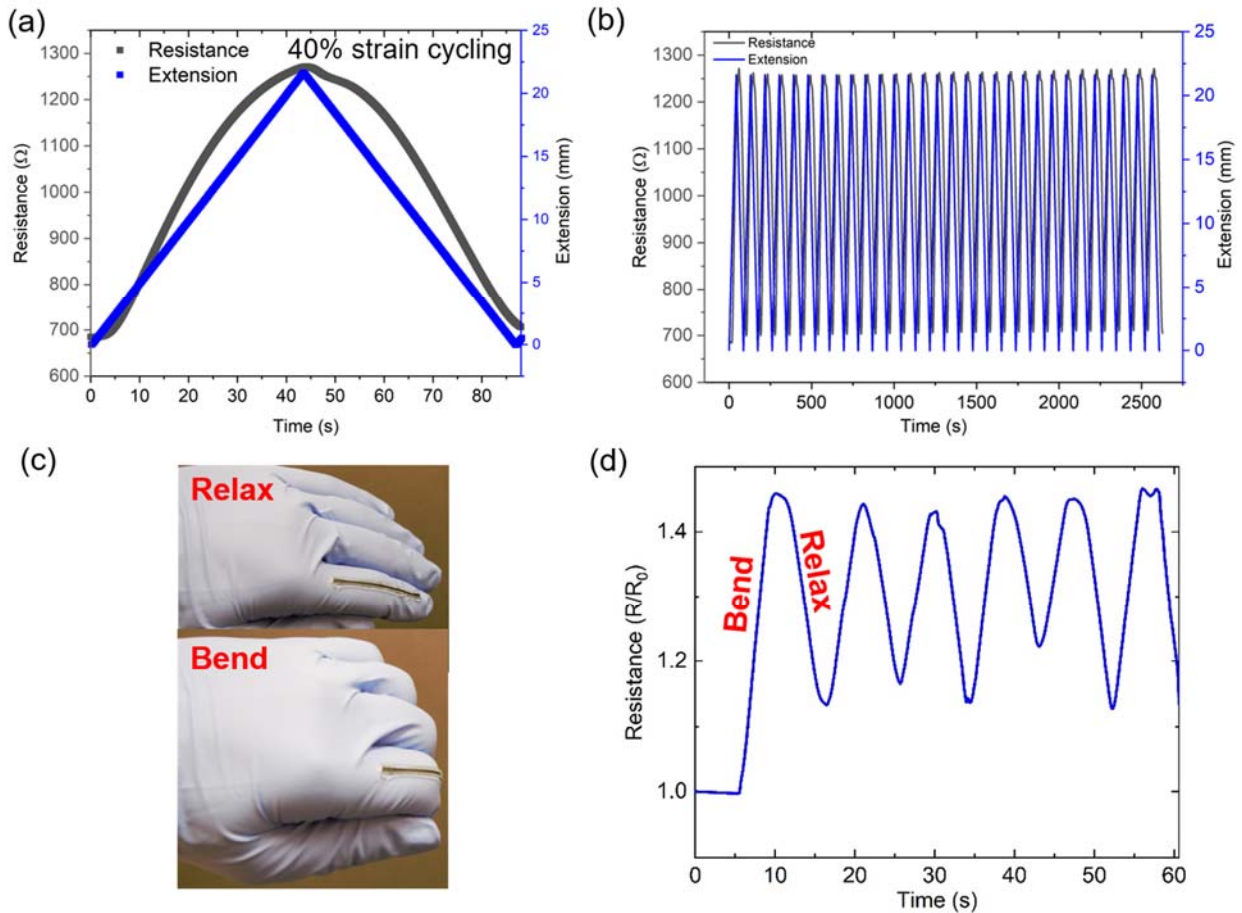


Figure 53: Piezoresistive response. (a) Resistance change with extension for 40% strain cycling and corresponding (b) 30 cycles of 40 % strain cycling. (c) Images of bending and relaxing of finger onto which fiber is mounted for strain sensing and (d) resistive response (6 cycles) of fiber sensor when the finger is bent and relaxed.

Wetness detection was carried out using impedance spectroscopy. Wetness detection was carried out using impedance spectroscopy. Deionized water (DI) and saline solutions were used for this experiment. Saline solutions to simulate sweat were prepared by mixing sodium chloride in water to create 0.5 wt.% and 1.5wt% solutions. A hand held micropipette was used to introduce a 10  $\mu$ l saline droplet in the capacitive crossover between fiber electrodes (see Figure 54a). The simplified equivalent circuit for this test configuration consists of a parallel RC circuit in series with R as shown in Figure 54b. In this circuit model, the resistive element in parallel RC circuit corresponds

to the saline solution and the series resistance corresponds to the resistance of fibers. Potentiostatic Repeating EIS script from Gamry's EIS application package was used to collect the impedance data. The frequency was varied from 1 Hz (initial frequency) to 1MHz (final frequency) during the test with AC voltage set as 10mV rms. The test was run in a low noise mode. It was observed that when 10  $\mu$ l volume of saline solution was introduced into the capacitive pixel, the impedance dropped by 2+ orders of magnitude due to presence of ions, compared to initial state of pixel when only air was present between electrodes. It was also seen that the solution with a higher salt concentration caused larger drop in impedance (Figure 54c). This was because with increase in salinity, there is an increase in ion content which leads to increase in conductivity i.e. lower value of  $R_{\text{saline fluid}}$  in circuit, thus, decreasing impedance. Since at higher frequencies, beyond 1000 Hz, the impedance values merge so only low frequency range of 1 to 1000 Hz is suitable for detecting difference in salinity levels of fluids.

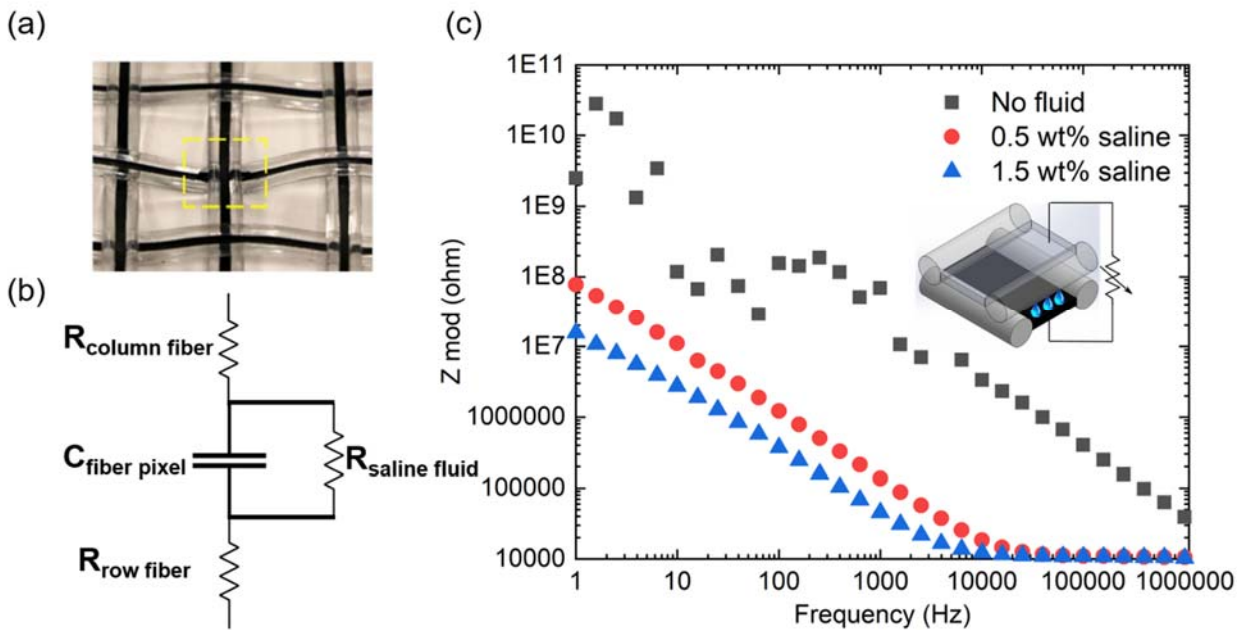


Figure 54: (a) 10  $\mu$ l droplet inside the crossover. (b) Equivalent circuit model for wetness detection. (c) Impedance response to different saline concentrations (0.5 wt. % and 1.5 wt. %).

Since the middle segment of the fiber is made of carbon based conducting polymer composite so the effect of temperature on electrical resistance was studied to identify the multimodal fiber's capability for temperature sensing. The setup for temperature- resistance response measurement consisted of an infrared light (IR) source for heating the sample, an LCR meter for resistance measurement and a contact type thermocouple for temperature measurement. The sample was mounted on a glass slide and copper wires were attached to the two ends of sample using silver conductive epoxy for connecting to LCR meter. The temperature probe was placed in center of sample. The IR source was placed directly above the sample, approximately 6 cm away. Figure 55 shows the test setup for temperature resistance response measurement.

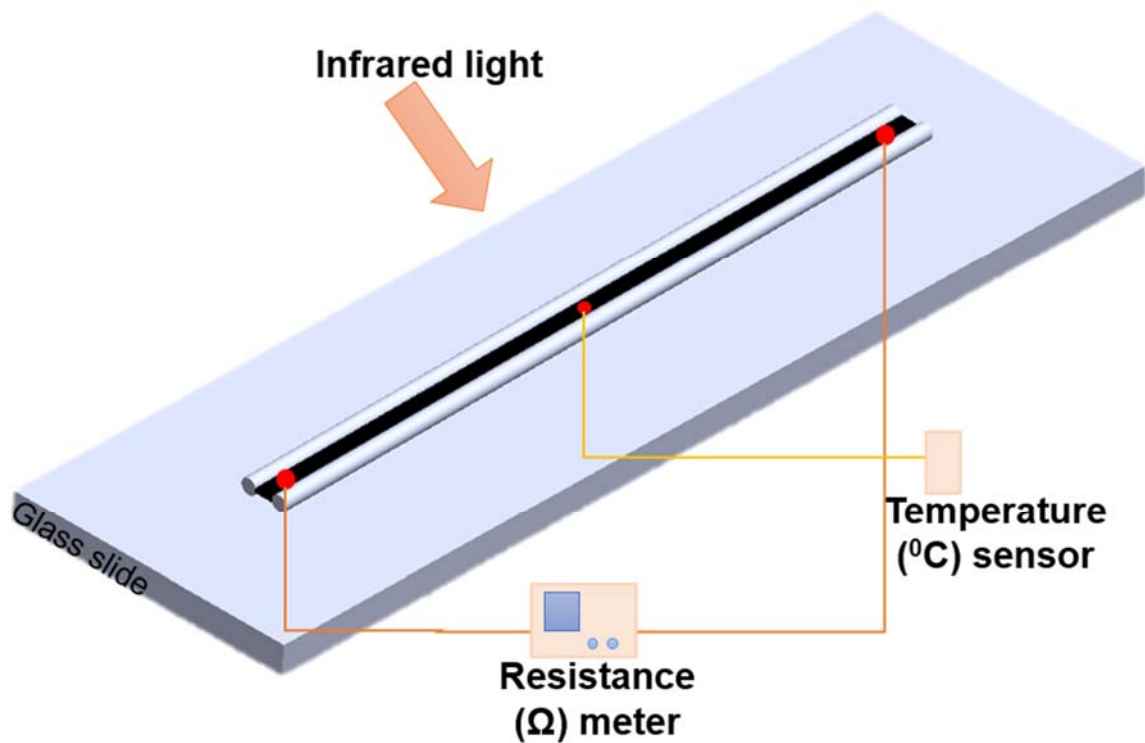


Figure 55: Schematic of test setup for temperature resistance response measurement

For the test, the IR lamp was switched on while the temperature and resistance data was collected simultaneously. The temperature was allowed to increase till 75°C and then the lamp was

turned off. The sample was allowed to cool naturally in ambient environment until it reached 30°C. This process was repeated ten times and resistive response during heating and cooling of sample was recorded. Figure 56a shows sample temperature during heating and cooling cycles plotted with time for all 10 cycles and Figure 56b shows raw resistance as a function of temperature for the same. It was observed that initial cycles (1 to 3) were different and cycle 4 onwards the response of sample was stabilized. That is why the representative average resistance response (change in resistance) of sample for cycles 4, 6, 8 and 10 was plotted in Figure 56c.

The heating and cooling cycles between 30°C to 75°C are marked and it can be seen that as temperature is increased there is a decrease in resistance but at around 55°C it starts increasing up to 75°C. On the other hand, during cooling cycle, the resistance starts decreasing but again at around 55°C it starts increasing till it reaches 30°C. This result indicates that the material exhibits both negative temperature coefficient (NTC) and positive temperature coefficient (PTC) behavior with a switching point at around 55°C marked by a dotted line in Figure 56c. The resistance increase upon increasing temperature is described by a PTC, whereas decrease is indicative of a NTC. This strong dependency of resistance on temperature is observed, primarily, because the composite material has CB concentration in percolation region. The initial decrease in resistance during heating can be attributed to an increase in the activation of the thermal emission of electrons from the CB particles. Beyond switching point, the cause of a PTC is thermal expansion of the silicone polymer matrix, which increases the average distance between CB particles [28]. Another point worth mentioning is the hysteresis in the resistance–temperature curve during the heating-cooling cycle. There are two possible reasons for this behavior i.e. different resistance at same temperature. During cooling, firstly, it is not possible for expanded silicone polymer to recover immediately and completely to its original volume and secondly, reformation of conductive

network might lead to a new distribution of CB particles [28]. This also explains the reason for comparatively larger error bars in the cooling cycle. For use of this temperature response for wearable applications, the sensor material should respond close to normal human skin temperature range. That is why resistance change during heating from 30°C to 35°C for similar cycles was plotted separately in Figure 56d. The result indicated good sensitivity within this useful narrow range of temperature change with repeatable response between cycles.

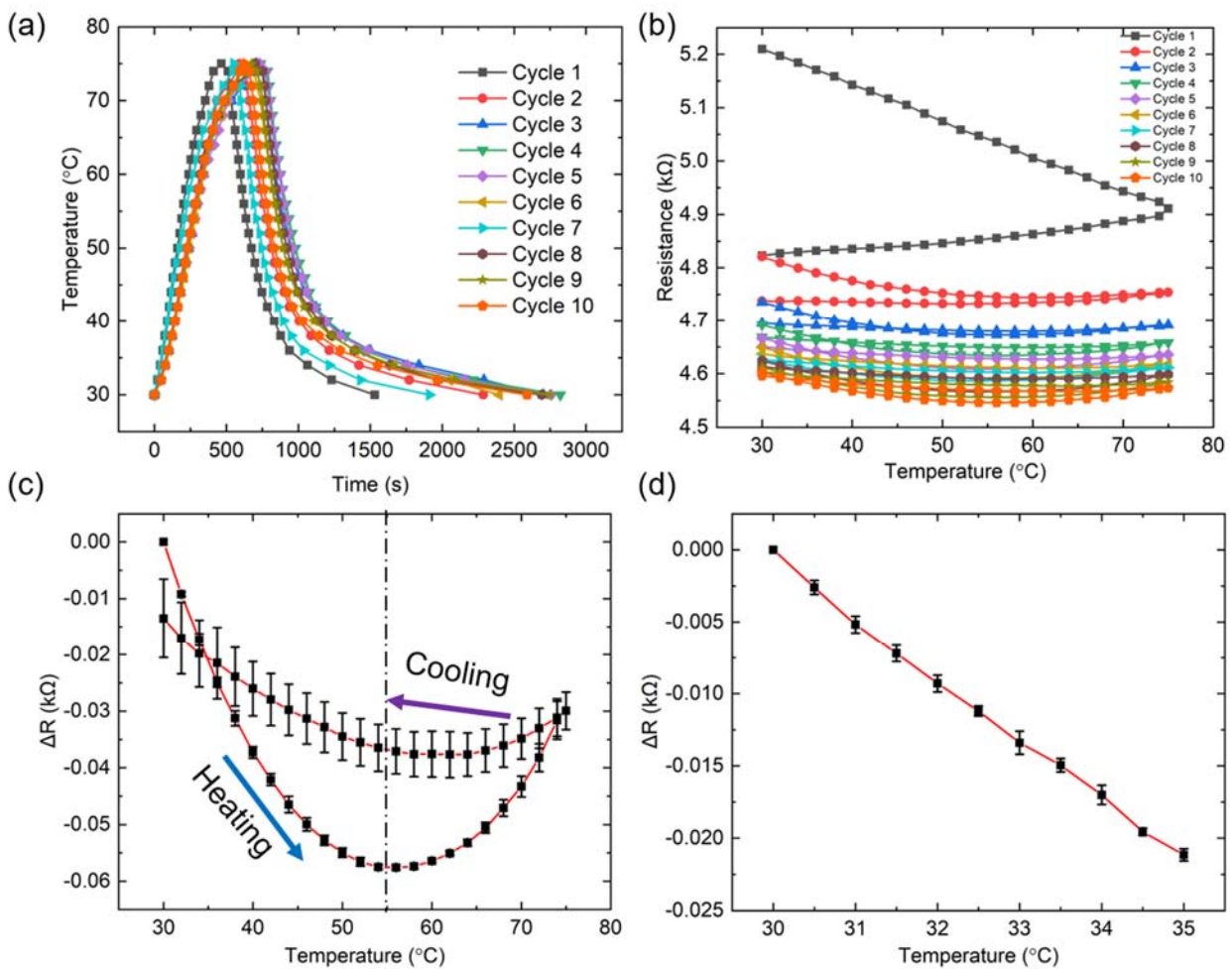


Figure 56: Resistive response of conductive composite of fiber under temperature. (a) Increase in sample temperature under IR light for 10 cycles. (b) Change in electrical resistance of sample when heated and cooled plotted for all 10 cycles. (c) Representative average stabilized resistive response of sample for cycles 4, 6, 8 and 10. (d) Decrease in sample resistance in range of 30 to 35°C showing sensitivity in smaller range.

#### **4.4 Conclusion**

In this research, a new and improved coextrusion approach to make dumbbell shaped multimodal and multifunctional fibers was introduced. Extrusion channel design and coextrusion process were discussed followed by geometrical, mechanical and electrical characterization. The biggest challenge in this coextrusion process was related to the middle conducting stream as it did not cure along with the insulating sides but later after depositing on the hot winding drum. Overall, this fiber forming approach is advantageous compared to previous extrusion printing process because it is a one-step process and produces longer fiber lengths with higher production rate. Another advantage is flexibility in design of fiber because it uses an inexpensive 3D printed extrusion device which can be customized. Fibers with desired dumbbell cross-section in three different widths were produced successfully. The multimodality and multifunctionality of these fibers was demonstrated by force-capacitance, strain-resistance, wetness-impedance and temperature-resistance testing.

## References

- [1] E. T. Alonso *et al.*, “Graphene electronic fibres with touch-sensing and light-emitting functionalities for smart textiles,” *npj Flexible Electronics*, vol. 2, no. 1, p. 25, Sep. 2018, doi: 10.1038/s41528-018-0040-2.
- [2] N. Nan *et al.*, “A Stretchable, Highly Sensitive, and Multimodal Mechanical Fabric Sensor Based on Electrospun Conductive Nanofiber Yarn for Wearable Electronics,” *Advanced Materials Technologies*, vol. 0, no. 0, p. 1800338, doi: 10.1002/admt.201800338.
- [3] J. D. Sandt *et al.*, “Stretchable Optomechanical Fiber Sensors for Pressure Determination in Compressive Medical Textiles,” *Advanced Healthcare Materials*, vol. 7, no. 15, p. 1800293, 2018, doi: 10.1002/adhm.201800293.
- [4] X. Guo, Y. Huang, X. Cai, C. Liu, and P. Liu, “Capacitive wearable tactile sensor based on smart textile substrate with carbon black/silicone rubber composite dielectric,” *Measurement Science and Technology*, vol. 27, no. 4, p. 045105, 2016.
- [5] N. Hu, Y. Karube, C. Yan, Z. Masuda, and H. Fukunaga, “Tunneling effect in a polymer/carbon nanotube nanocomposite strain sensor,” *Acta Materialia*, vol. 56, no. 13, pp. 2929–2936, Aug. 2008, doi: 10.1016/j.actamat.2008.02.030.
- [6] T. Kikutani *et al.*, “High-speed melt spinning of bicomponent fibers: Mechanism of fiber structure development in poly(ethylene terephthalate)/polypropylene system,” *J. Appl. Polym. Sci.*, vol. 62, no. 11, pp. 1913–1924, Dec. 1996, doi: 10.1002/(SICI)1097-4628(19961212)62:11<1913::AID-APP16>3.0.CO;2-Z.
- [7] J. Radhakrishnan, T. Kikutani, and N. Okui, “High-Speed Melt Spinning of Sheath-Core Bicomponent Polyester Fibers: High and Low Molecular Weight Poly(ethylene

- Terephthalate) Systems,” *Textile Research Journal*, vol. 67, no. 9, pp. 684–694, Sep. 1997, doi: 10.1177/004051759706700908.
- [8] R. V. Bell, C. C. Parkins, R. A. Young, C. M. Preuss, M. M. Stevens, and S. A. F. Bon, “Assembly of emulsion droplets into fibers by microfluidic wet spinning,” *J. Mater. Chem. A*, vol. 4, no. 3, pp. 813–818, Jan. 2016, doi: 10.1039/C5TA08917D.
- [9] D. A. Boyd, A. A. Adams, M. A. Daniele, and F. S. Ligler, “Microfluidic fabrication of polymeric and biohybrid fibers with predesigned size and shape,” *Journal of visualized experiments: JoVE*, no. 83, 2014.
- [10] Y. Cheng *et al.*, “Controlled Fabrication of Bioactive Microfibers for Creating Tissue Constructs Using Microfluidic Techniques,” *ACS Appl. Mater. Interfaces*, vol. 8, no. 2, pp. 1080–1086, Jan. 2016, doi: 10.1021/acsami.5b11445.
- [11] T. R. Cuadros, O. Skurtys, and J. M. Aguilera, “Mechanical properties of calcium alginate fibers produced with a microfluidic device,” *Carbohydrate Polymers*, vol. 89, no. 4, pp. 1198–1206, Aug. 2012, doi: 10.1016/j.carbpol.2012.03.094.
- [12] M. A. Daniele, D. A. Boyd, A. A. Adams, and F. S. Ligler, “Microfluidic strategies for design and assembly of microfibers and nanofibers with tissue engineering and regenerative medicine applications,” *Advanced healthcare materials*, vol. 4, no. 1, pp. 11–28, 2015.
- [13] S. Enomoto, Y. Yajima, Y. Watabe, M. Yamada, K. Furusawa, and M. Seki, “One-step microfluidic spinning of collagen microfibers and their application to cell cultivation,” in *2015 International Symposium on Micro-NanoMechatronics and Human Science (MHS)*, 2015, pp. 1–4, doi: 10.1109/MHS.2015.7438257.
- [14] A. Frutiger *et al.*, “Capacitive Soft Strain Sensors via Multicore–Shell Fiber Printing,” *Adv. Mater.*, vol. 27, no. 15, pp. 2440–2446, Apr. 2015, doi: 10.1002/adma.201500072.

- [15] A. Leber, B. Cholst, J. Sandt, N. Vogel, and M. Kolle, “Stretchable Thermoplastic Elastomer Optical Fibers for Sensing of Extreme Deformations,” *Advanced Functional Materials*, vol. 29, no. 5, p. 1802629, 2019, doi: 10.1002/adfm.201802629.
- [16] X. Hu *et al.*, “Structure-tunable graphene oxide fibers via microfluidic spinning route for multifunctional textile,” *Carbon*, Jun. 2019, doi: 10.1016/j.carbon.2019.06.010.
- [17] Z. Zhang *et al.*, “Textile Display for Electronic and Brain-Interfaced Communications.,” *Adv Mater*, pp. e1800323–e1800323, Mar. 2018, doi: 10.1002/adma.201800323.
- [18] M. J. Owen, “Elastomers: Siloxane,” in *Encyclopedia of Materials: Science and Technology*, K. H. J. Buschow, R. W. Cahn, M. C. Flemings, B. Ilschner, E. J. Kramer, S. Mahajan, and P. Veysière, Eds. Oxford: Elsevier, 2001, pp. 2480–2482.
- [19] H. Frisch and J. Hammersley, “Percolation Processes and Related Topics,” *Journal of the Society for Industrial and Applied Mathematics*, vol. 11, no. 4, pp. 894–918, Dec. 1963, doi: 10.1137/0111066.
- [20] S. Kirkpatrick, “Percolation and Conduction,” *Rev. Mod. Phys.*, vol. 45, no. 4, pp. 574–588, Oct. 1973, doi: 10.1103/RevModPhys.45.574.
- [21] P. Jeraldo, *Critical Phenomena in Percolation Theory*. 2005.
- [22] G. Grimmett, “What is Percolation?,” in *Percolation*, G. Grimmett, Ed. Berlin, Heidelberg: Springer Berlin Heidelberg, 1999, pp. 1–31.
- [23] J. Liang and Q. Yang, “Aggregate structure and percolation behavior in polymer/carbon black conductive composites,” *Journal of Applied Physics*, vol. 102, no. 8, p. 083508, Oct. 2007, doi: 10.1063/1.2795674.

- [24] O. A. Moskalyuk, A. N. Aleshin, E. S. Tsobkallo, A. V. Krestinin, and V. E. Yudin, “Electrical conductivity of polypropylene fibers with dispersed carbon fillers,” *Phys. Solid State*, vol. 54, no. 10, pp. 2122–2127, Oct. 2012, doi: 10.1134/S1063783412100253.
- [25] Z. Li, J. Zhang, and S. Chen, “Effect of carbon blacks with various structures on electrical properties of filled ethylene-propylene-diene rubber,” *Journal of Electrostatics*, vol. 67, no. 1, pp. 73–75, Feb. 2009, doi: 10.1016/j.elstat.2008.11.002.
- [26] M. E. Spahr and R. Rother, “Carbon Black as a Polymer Filler,” in *Encyclopedia of Polymers and Composites*, S. Palsule, Ed. Berlin, Heidelberg: Springer Berlin Heidelberg, 2014, pp. 1–24.
- [27] M. Singh and R. L. Vander Wal, “Nanostructure Quantification of Carbon Blacks,” *C*, vol. 5, no. 1, p. 2, Mar. 2019, doi: 10.3390/c5010002.
- [28] J. Zhang and S. Feng, “Temperature effects of electrical resistivity of conductive silicone rubber filled with carbon blacks,” *Journal of Applied Polymer Science*, vol. 90, no. 14, pp. 3889–3895, 2003, doi: 10.1002/app.13127.

## Chapter 5: Prosthetic Environment Monitoring using Fiber Sensor Arrays

### 5.1 Introduction

Prosthetic devices substitute a missing body part such as an arm or leg to help regain the ability to perform various physical activities. Limb loss can occur due to birth defects, diseases like diabetes and physical trauma [1]. While the number of people with limb loss (called amputees) in the United States alone is predicted to reach approximately 3.6 million by 2050 [2], currently, the number of lower-limb amputees exceeds the number of upper limb amputees at a ratio of 4 to 1 [3]. Within lower limb amputees, this research specifically focuses on ‘Below the Knee’ (BK) or transtibial amputees (see Figure 58a). The transtibial prosthesis broadly consists of a socket in which the residual limb is placed and a prosthetic foot. The socket is considered as the most important component responsible for load transfer between the limb and the prosthesis. The residual limb-socket interface is also supplemented by a layer of viscoelastic material, called liners for cushioning and fabric socks for improving socket fit and comfort. The region between the residual limb and the socket, referred here as prosthetic environment exposes the residual limb to various levels of normal and shear stress, increased humidity, and temperature. Among these, the static and dynamic normal pressure distribution of limb within the socket are key considerations in amputee comfort [4]. Currently, the comfort for the prosthetic socket is determined through subjective feedback from amputees, manual palpation, or use of clay in the socket to assess socket contact [5], [6]. Unfortunately, many transtibial amputees complain about their sockets being uncomfortable due to problems associated with fitting and limb volume changes during daily prosthesis use. The discomfort not only leads to poor gait symmetry [7] but of greater concern is the fact that uncomfortable sockets can only be addressed after skin problems appear [8], [9]. This can also lead to decreased prosthesis use by the amputee. Therefore, improved and innovative

inner socket environment monitoring technologies are required to prevent any medical issues and enhance amputee comfort during prosthesis use. The first step towards improving the comfort requires understanding the prosthetic environment, and that is why a sensor technology to quantify inner socket environment (ISE) is needed. Since normal pressure distribution within the socket is one of the key considerations in amputee comfort, a sensor capable of measuring the pressure within socket would be useful. Researchers have been measuring the interface pressure in transtibial prosthesis [10]–[15] for more than 50 years now using a variety of sensing mechanisms including resistive, capacitive, optical and inductive types[16] but there still doesn't exist a fully flexible and unobtrusive solution. The current state of the art in so called flexible sensor technologies (see *Figure 57*) available for monitoring pressure distribution within the ISE include capacitive sensors like Pliance, Novel Inc., Germany [17] and resistive sensors like F-socket, Tekscan, USA [18]. These flexible sensors are expensive, fragile, difficult-to-clean and are not fully conformable.

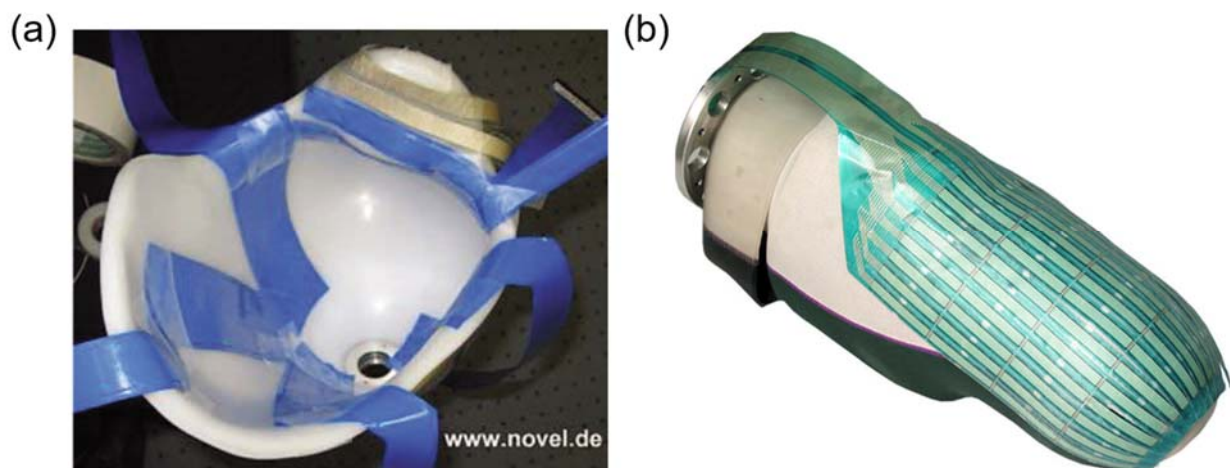


Figure 57: (a) Pressure analysis distribution of the stump-to-socket interface using the Pliance system [17] and (b) F-Socket System [18].

In this work, a novel and flexible woven fabric based sensor is demonstrated where uniquely-shaped conductive polymer fibers are woven to form a multimodal and multifunctional sensor array. The sensor array, when connected to an appropriate electrical circuit, can sense different stimuli like pressure, humidity, temperature and biopotentials. This study focuses only on the measurement of normal force in the ISE using these sensor arrays. This innovation offers a potential unobtrusive way to continuously monitor ISE and objectively measure prosthesis misfit to address amputee discomfort. The resulting data can be used to design prosthesis to better distribute pressure for an individual transtibial amputee.

Figure 58b shows the concept of application of woven fiber-based sensors for prosthetic environment monitoring. The woven sensor arrays can be placed between the liner and the socket in different regions of interest for monitoring force. The sensing capability of these fiber sensor arrays arises from the dumbbell shaped cross-section of the fiber with electrically conducting (black in color) middle bridge and insulating side lobes. In a woven fabric made of these fibers, each crossover point (henceforth referred to as a Texel) acts as a capacitive sensor capable of sensing local forces within the array (see Figure 59). The capacitance of the Texel  $C_0$  can be expressed in terms of the fiber dimensions, as

$$C_0 = \frac{\epsilon A}{s}$$

$$\text{or } C_0 = \frac{\epsilon A}{h - t}$$

Where 'h' is height of insulating segment, 'A' is overlapping area of fibers acting as electrodes of capacitor, 't' is thickness of conducting segment and 's' is the separation between conducting segments of fibers in capacitor, given by  $s=h-t$ .

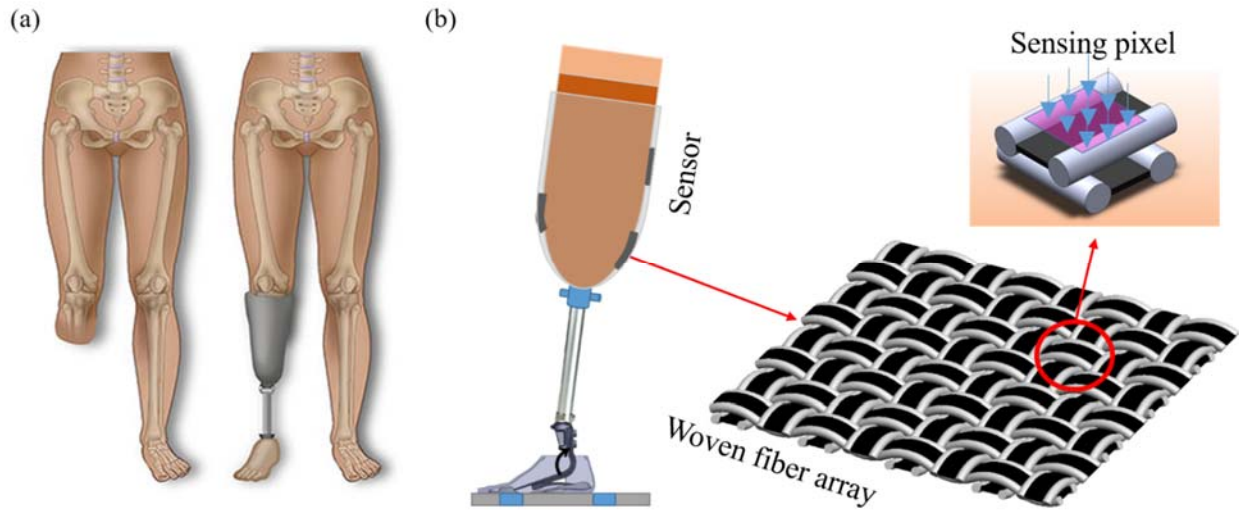


Figure 58: (a) Below the knee (BK or lower limb or transtibial amputation and (b) Schematic of prosthetic environment monitoring concept using fiber sensor arrays

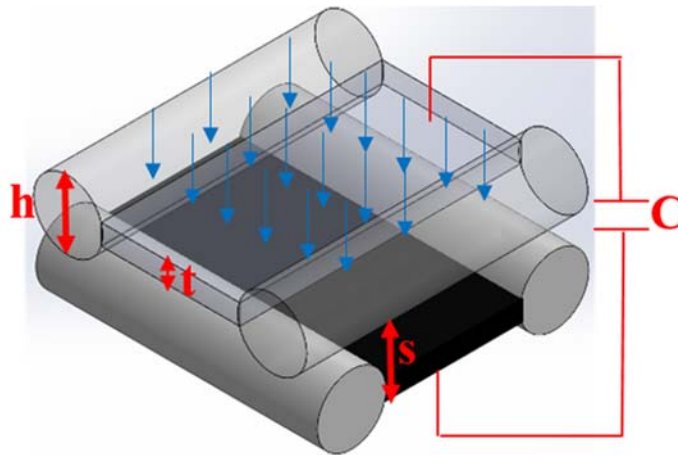


Figure 59: Fiber based sensing pixel

## 5.2 Materials and Methods

### 5.2.1 Fabrication

The insulating part of the bicomponent fiber was fabricated from a two-part UV-curing silicone (LSR 225-1, Momentive) and the middle conducting part was composed of conducting polymer composite (CPC) which consisted of 6.4wt% carbon black (Ketjenblack EC-300J,

AkzoNobel) dispersed in heat-curing silicone (Ecoflex 00-50). These fiber forming materials were fed into an extrusion die (refer *Figure 60*) with three inlets (two for insulating sides and one for middle conductive segment) and a dumbbell shaped orifice to produce fibers at a production rate of 292.85 mm/min. Downstream of the extrusion die orifice, the insulating sides of fiber were cured by UV light since the insulating sides were made of photo crosslinking silicone while middle conducting segment was cured by collecting on a heated winding drum as it was made of thermally curing silicone. The extrusion rate and winding rate along with lateral traverse rate were matched to achieve continuous deposition of fibers on the drum (see *Figure 61*). After extrusion, the fibers were peeled off the winding drum.

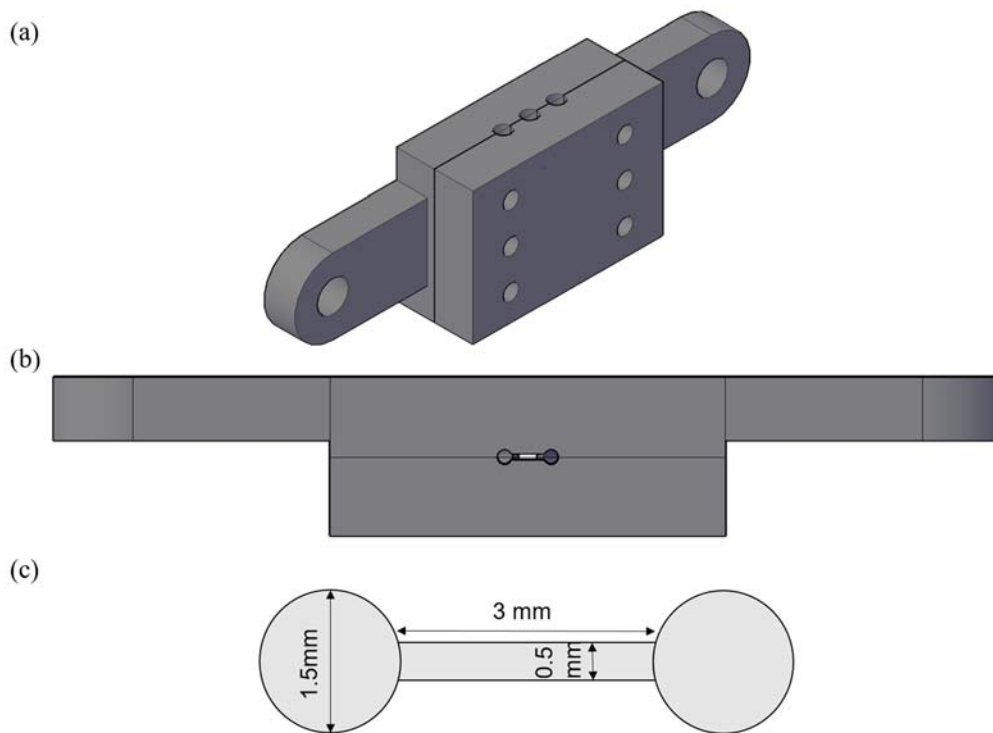


Figure 60 : Schematic of the extrusion channel used for fiber fabrication. (a) Isometric view of two-part extrusion channel with three inlets at the top for injecting fiber forming materials. (b) Bottom view of extrusion channel showing dumbbell shaped orifice. (c) Dimensions of the dumbbell orifice.

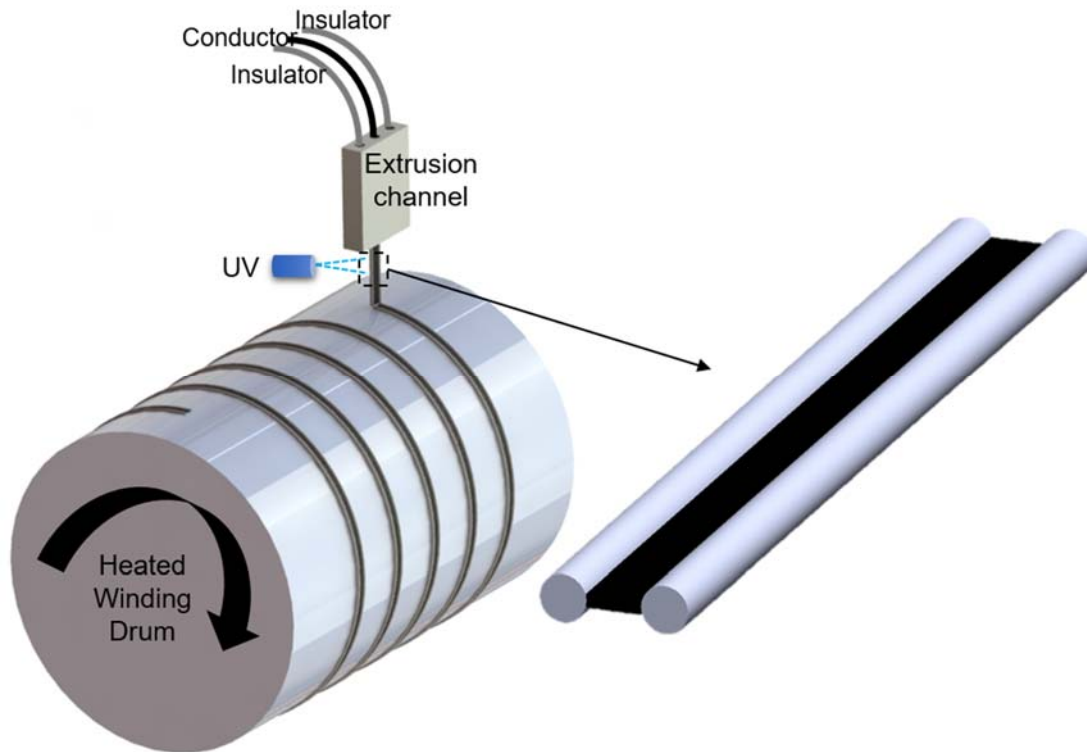


Figure 61: Schematic of the fiber extrusion process.

The extruded fibers were cut into appropriate lengths and were subsequently hand-woven in one-up one-down configuration (plain weave) to create a 3x3 arrays with 9 sensing pixels each to cover target critical location. Electrical connections were made by attaching the fibers to copper pads on polyimide substrate using silver epoxy adhesive such that the middle conducting segment of fiber was electrically connected to copper (see Figure 82 in supplementary section). The woven array was then sandwiched between two polyurethane (PU) films (Polyurethane Deerfield PT6100S) sealed using silicone adhesive (Dow Corning Bio PSA 7-4402) to create packaged sensor array which could easily be integrated within prosthetics. The complete sensor thickness including PU film was 2.5 mm. Four similar arrays with sensing area of 2.5x2.5 cm<sup>2</sup> were made following the steps outlined in Figure 62. The data digitizer board was connected

to copper connection on each sensor array using z-axis tape which was then connected to data aggregator board using a detachable connector.

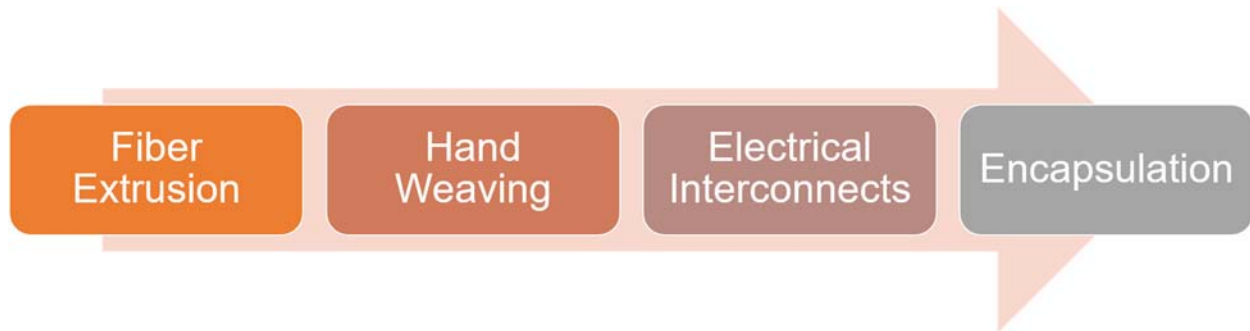


Figure 62: Different steps involved in sensor array fabrication

### ***5.2.2 Electromechanical Characterization***

After the sensors were fabricated these were tested for their force-capacitance response by compressing all pixels in each sensor array on a universal testing machine (MTS 30G) simultaneously because in the intended application all the pixels of sensor will be under load simultaneously. The mechanical response (load vs. displacement) along with the electrical response (capacitance vs. displacement) of the sensor were recorded. The average value of change in capacitance of all pixels was calculated to represent the sensor array response. The capacitive response of the sensor array was recorded under following conditions considering real application scenario: (a) applying two different levels of compression, (b) applying compression at three different test speeds, (c) compressing and holding the load, and (d) compressing sensor array for large number of cycles.

### 5.2.3 Prosthetic environment monitoring

The utility of the fiber sensor arrays for monitoring force within the prosthetic socket was evaluated in three phases (Figure 63), by placing the sensor array in an appropriate socket and using (a) an artificial limb, (b) an able-bodied person, and (c) an amputee (human subject testing).

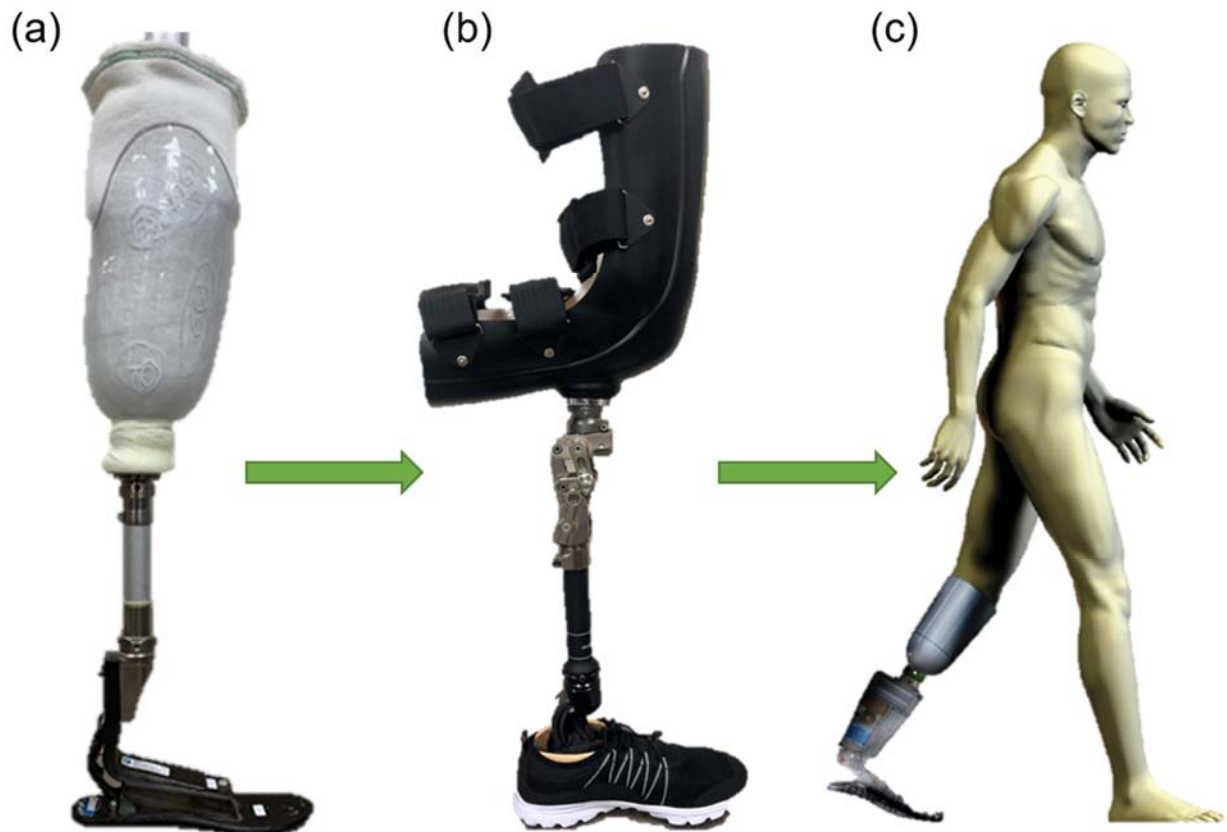


Figure 63: Three phases of sensor testing within the socket. (a) Benchtop testing using an artificial limb. (b) Able-bodied testing with bent knee adaptor. (c) Human subject testing.

#### (a) Sensor Evaluation with Artificial Limb

As the first step that offers a controlled testing environment, an artificial limb made of plaster of Paris was used as a simulated residual limb along with a socket attached to a foot to

validate the capability and suitability of the sensors in this application. The goal of this test was to monitor the changes in force within the socket at different locations while tilting of limb when the foot is fixed to the ground. The tilting motion was chosen because it resembles the motion of the stance leg during walking as described by the inverted pendulum model [19] (see Figure 64). The sensors were placed in four locations listed in Table 6 (see Figure 9a), out of which three (Patella Tendon, Popliteal Fossa, Pre-Tibia) were pressure tolerant locations, and one (Fibular head) was pressure sensitive. Four different sensors arrays were attached at the desired locations in the socket (see Figure 65) using a surgical tape (Transpore, 3M Corp.) and were connected to a data collection board placed outside the socket. To help keep track of the data and its interpretation, the placement of the sensors is represented in Figure 66 as a guide diagram. The set up for this experiment consisted of a metal frame for mounting the artificial limb and keeping the foot fixed (see Figure 67). When the limb was tilted towards heel or toe side it was locked at a particular angle for recording capacitance using an adaptor. During the experiment, the limb was tilted, forward and backward, and the movement was divided into different steps based on the tilt angle. The tilt directions are referred to as negative and positive tilt as shown in Figure 68. In terms of data collection, the capacitance from all texels of each sensor placed in different locations was recorded for 15 seconds and used to calculate average capacitance at reference position and at every angle.

Table 6: Selected locations for placing sensors in artificial limb

<b>Name of location</b>	<b>Type of location</b>	<b>Sensor</b>
Popliteal fossa	Pressure tolerant	S1
Patella Tendon	Pressure tolerant	S2
Pre tibia	Pressure tolerant	S3
Fibular head	Very sensitive	S4

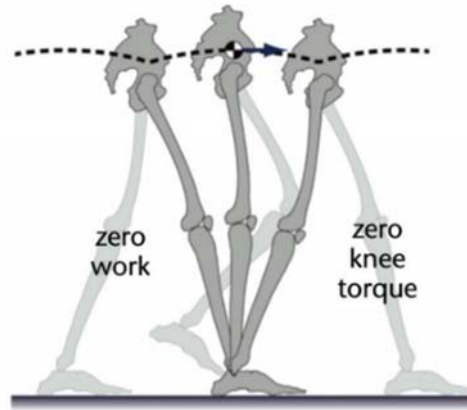


Figure 64: Inverted pendulum analogy for the stance leg during walking [20]

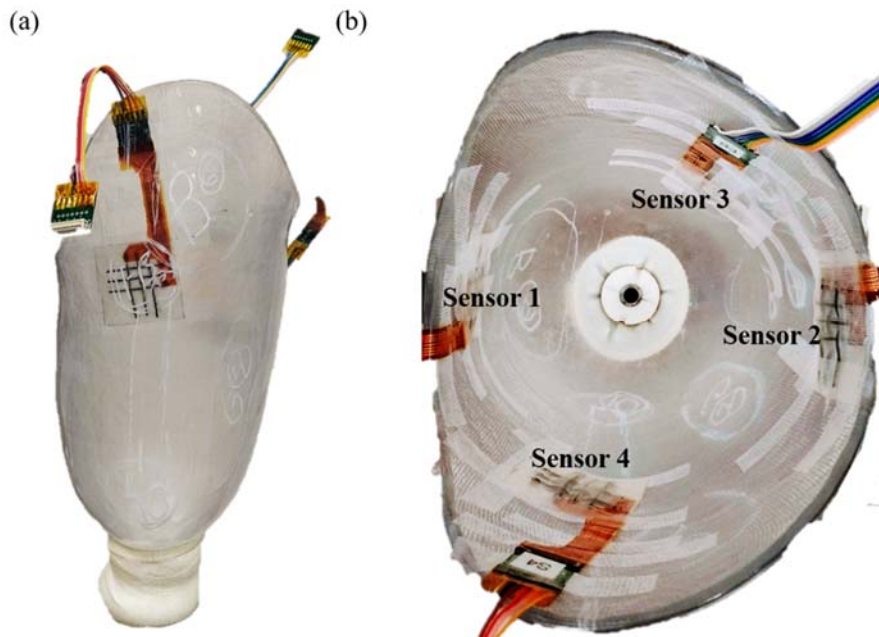


Figure 65: (a) Front and (b) top view of sensors attached to the socket at 4 locations

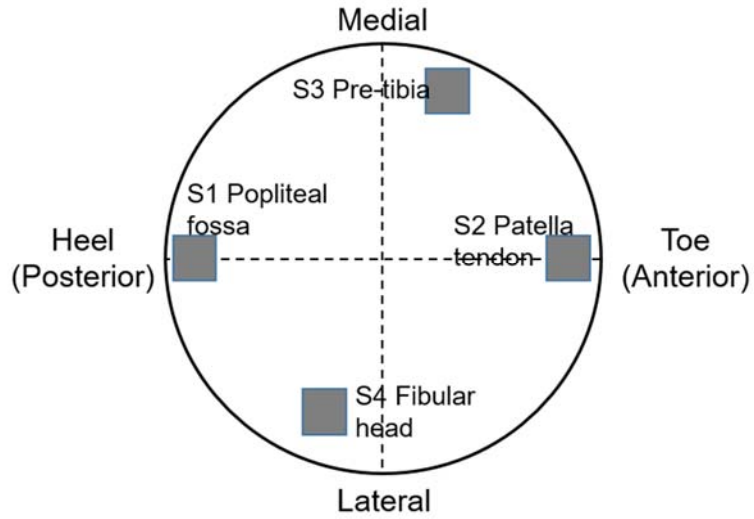


Figure 66: Guide diagram of sensor locations with respect to the limb

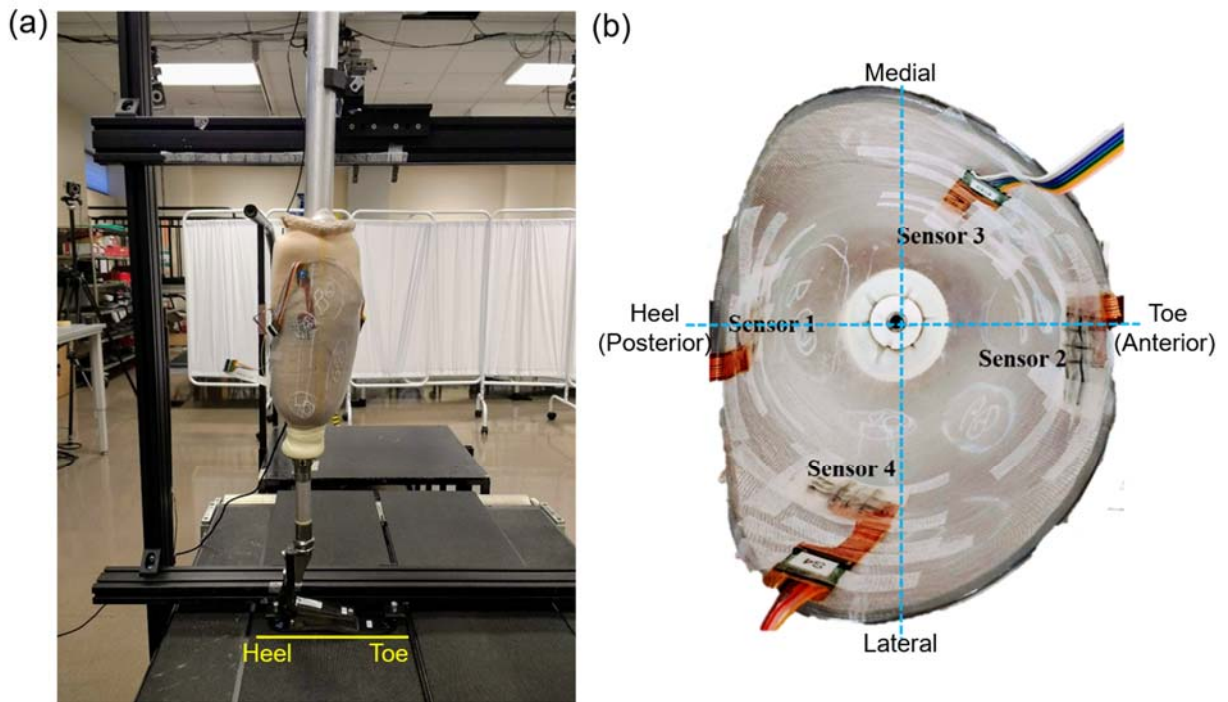


Figure 67: Artificial limb testing experiment showing (a) mounting frame setup and (b) socket with attached sensors indicating their placement with respect to heel and toe of the prosthetic foot.

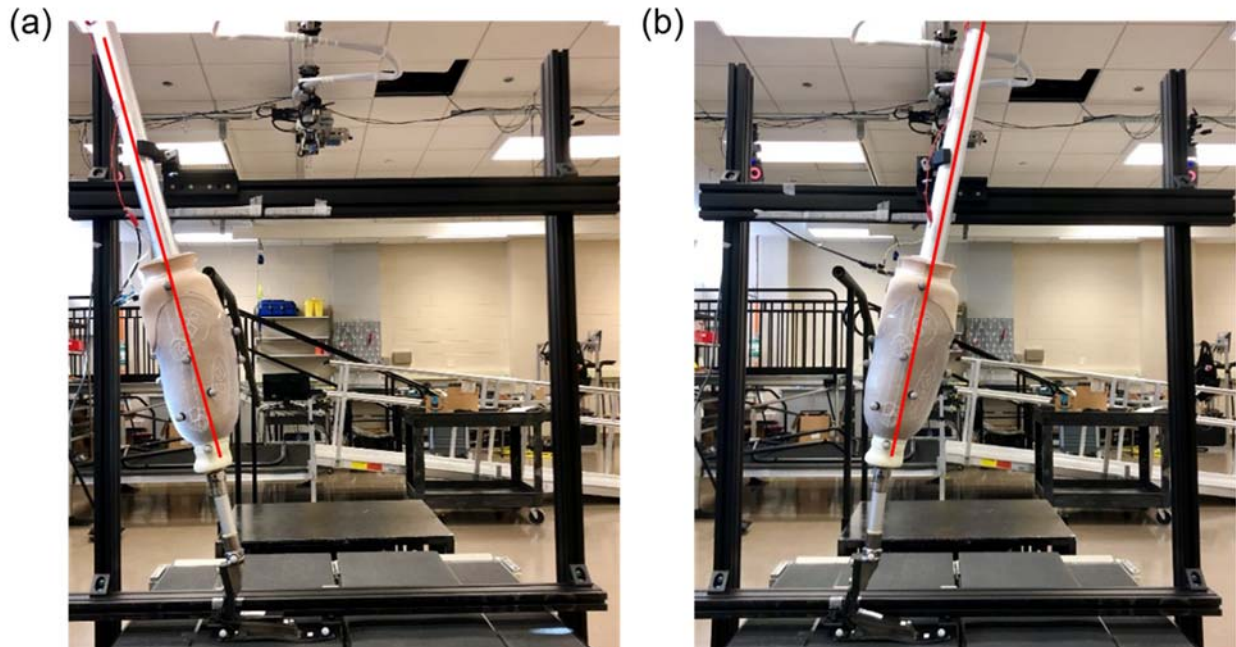


Figure 68: Sign conventions used for artificial limb experiment showing (a) negative tilt (heel side), and (b) positive tilt (toe side)

*(b) Sensor Evaluation with Able-bodied Subject*

In the second stage, able-bodied testing of sensors was performed using a non-physically-disabled human subject donning a bent knee adaptor in order to simulate an amputee. The goals of this test were to ensure sensors are reliable across sessions during activities like walking when loaded with body weight and to determine electrical signal routing from sensor as well as data collection when in contact with human. Unlike the artificial limb test, the sensor was attached by a medical bandage on the liner worn by the subject, 20 cm above the center of the knee cap, on the front thigh of the right leg (see Figure 69) rather than the socket for repeatability in terms of placement. Two tests were conducted during the able-bodied testing; in the first test, the subject performed forward and backward weight shifting and in the second, the subject performed walking on a treadmill at a comfortable pace of 0.45 m/s which was slower than normal walking speed.

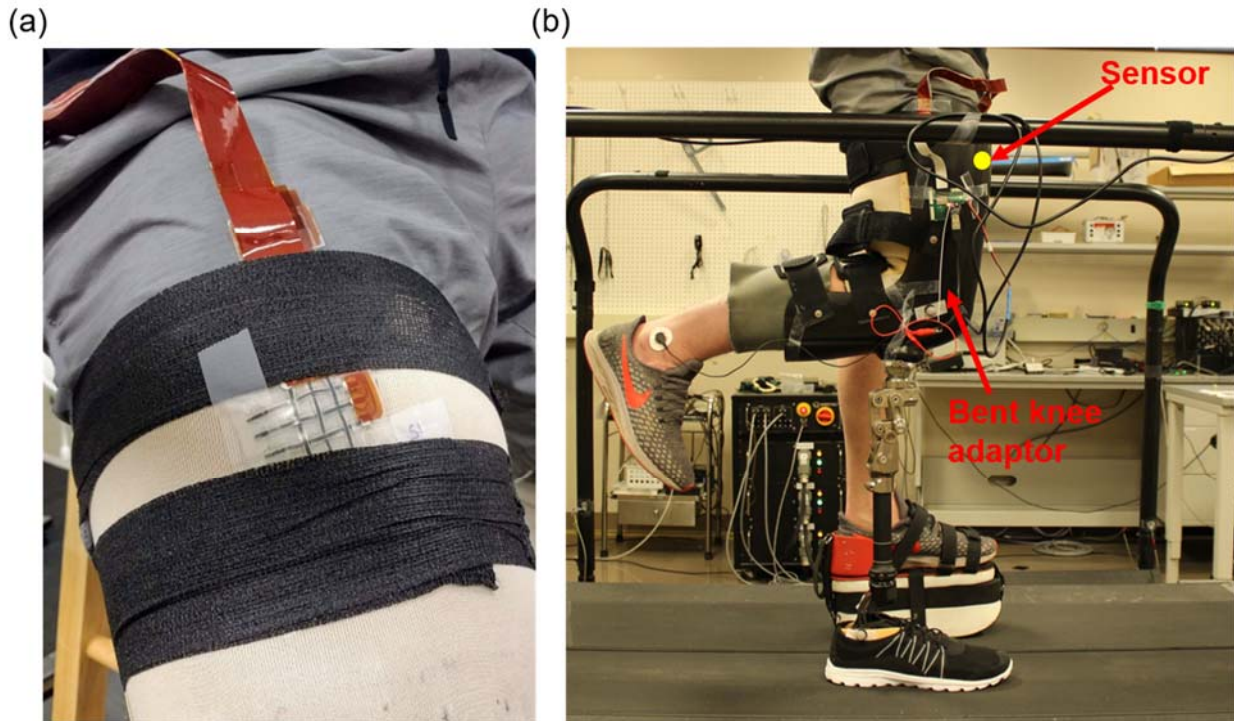


Figure 69: Able-bodied testing. (a) Sensor attached on front thigh, above liner, and (b) Subject wearing bent knee adaptor on right leg.

*(c) Sensor Evaluation using Human Subject.*

A male, bilateral below knee (BK) amputee was chosen as the subject for this study. The sensor was attached at the Patella Tendon (PT) location above liner on the left leg (see Figure 70). The PT was one of the critical locations selected during the earlier artificial limb experiment. After mounting the sensor, the subject donned the socket and walked to confirm that the sensor does not cause any discomfort or interfere with natural walking. The subject was then asked to perform 3 movements, namely (a) side-to-side weight shifting, (b) side-to-side weight shifting with pause for 5 seconds at each side and (c) walking at 0.41m/s for 1 minute.

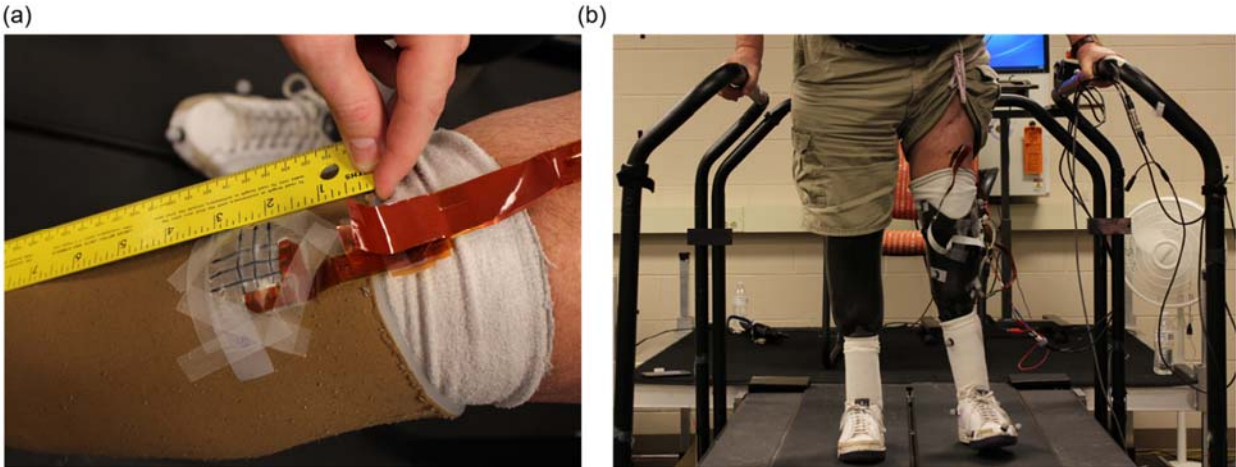


Figure 70: Human subject testing: (a) Sensor attached at the Patellar Tendon (PT) location of left residual limb. (b) Amputee standing on the treadmill after wearing socket onto sensor.

## 5.3 Results and Discussion

### 5.3.1 Sensor array fabrication

The extruded fibers were observed under an optical microscope to ascertain the cross sectional shape and fiber dimensions. The optical micrographs presented in Figure 71 reveal, an overall fiber width of 3.5 mm where height of insulating segment was 1.1 mm, and the thickness of the conducting segment was 0.3 mm. Based on these dimensions, the electrode separation was 0.8mm which is the maximum compressive strain under which these fiber-based sensors can produce a useful capacitive signal before shorting. Figure 72 shows the image of four woven sensing arrays attached to the FPCB (flexible printed circuit board) which are further connected to rigid PCB having capacitance to digital chip (see Figure 82).

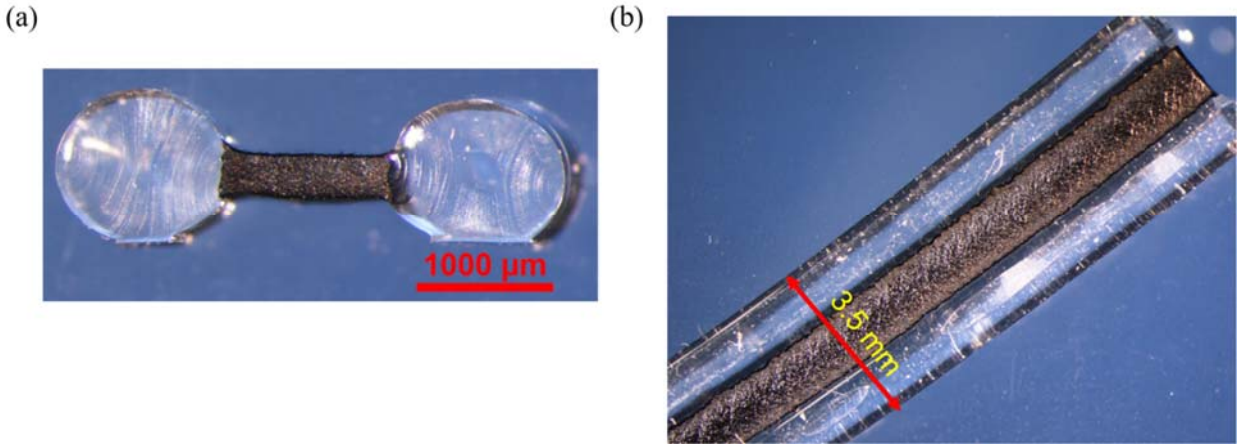


Figure 71: Optical microscopic images of the extruded bicomponent fiber. (a) Cross-sectional view showing dumbbell shape and (b) longitudinal view.

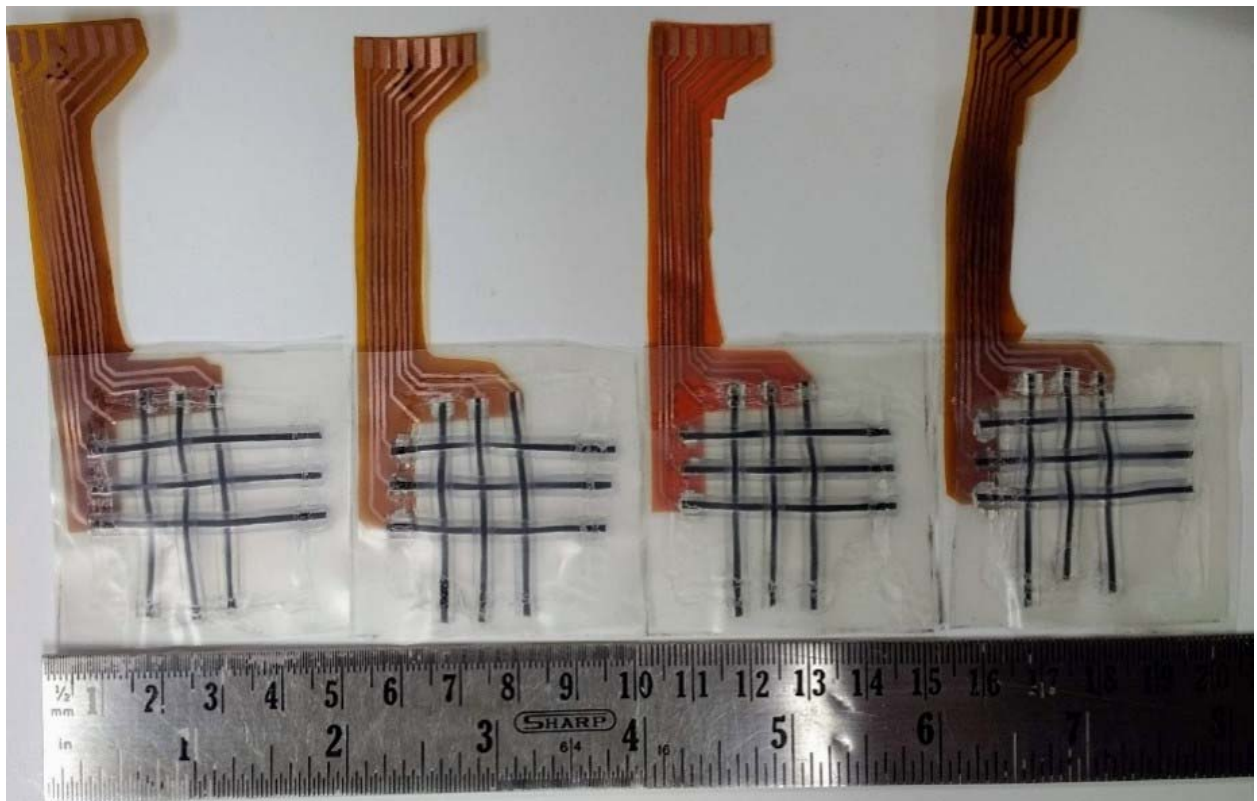


Figure 72: Photograph of fabricated sensor arrays.

### ***5.3.2 Benchtop characterization of Normal force-Capacitance response***

Before using the sensor array in the real application environment it is necessary to evaluate its response under controlled conditions so that is why benchtop characterization of the fiber sensor array on the universal testing machine was conducted. Firstly, a normal force corresponding to 12% compression was applied and capacitance was recorded (see Figure 73a). It was observed that there was an increase in capacitance with applied force due to decrease in separation of conductors. Secondly, capacitance response of two different degrees of compression, 12% and 20% compressive strains was recorded and as seen in Figure 73b, 20% compression clearly shows a 20fF higher capacitance increase ( $\Delta C$ ) than 12% compression indicating that sensor can differentiate between different levels of applied normal force. In another test to explore the influence of the rate of displacement, the compression head (crosshead) was moved down at 20, 30, and 40 mm/min to apply an intermediate compressive strain of 16%, see Figure 73c, d. The plot of  $\Delta C$  versus time for three different compression rates for multiple cycles during 120 seconds showed a stable and repeatable response, indicating the capability of the sensor to respond to varying degrees of compression. Another observation from the mechanical response of the sensor array was that with increasing compression frequency, the compressive force required for the same degree of compression was slightly but consistently higher. The increasing resistance to strain with increasing rate is a characteristic of viscoelastic materials.

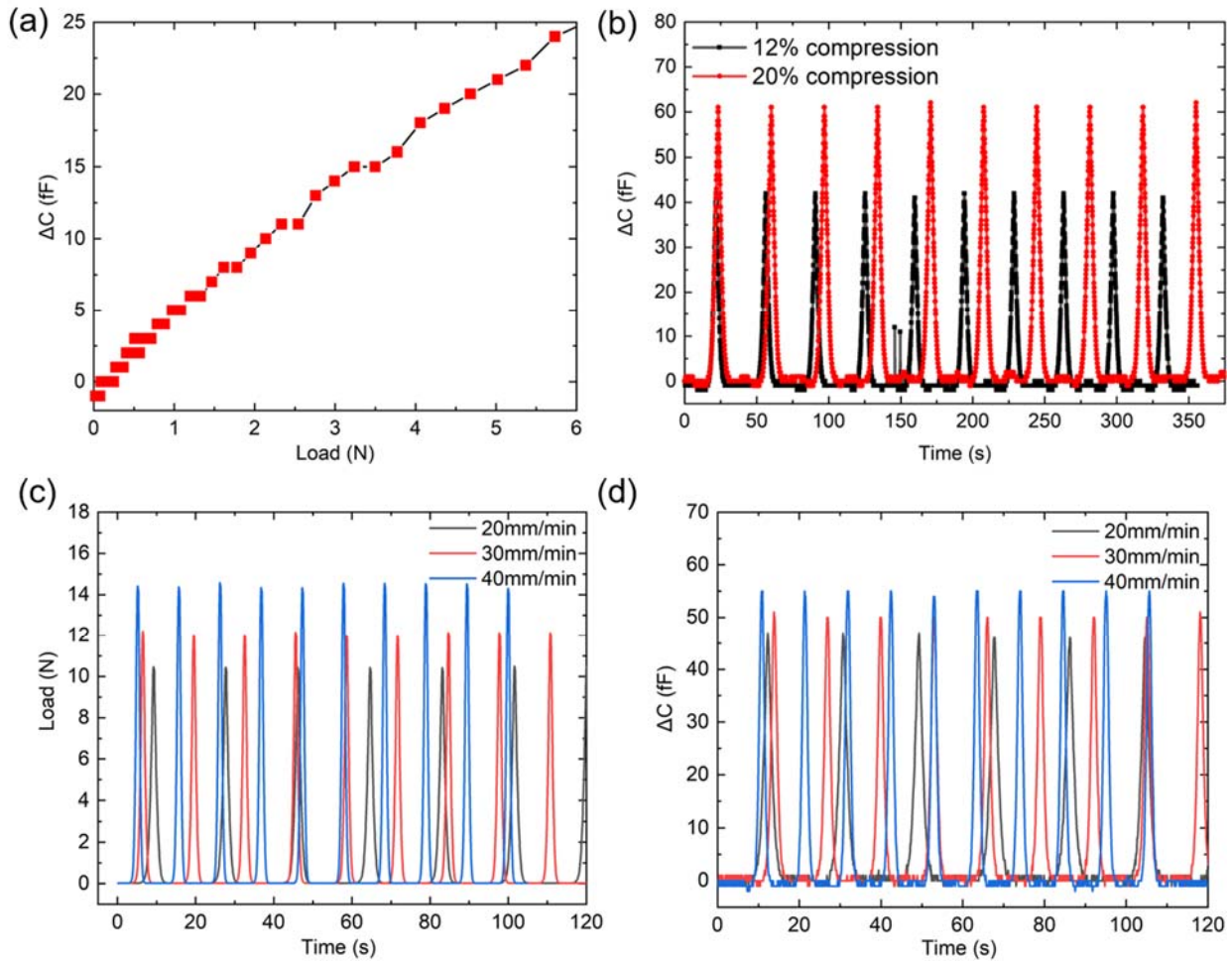


Figure 73: (a) Load-capacitance response of sensor array to 12% compression. (b) Capacitance response of sensor array subjected to two different degrees of compression namely 12% and 20%. (c) Load and (d) capacitance response of sensor array compressed by applying a 16% compression at three different test speeds.

Another important characteristic of an ideal sensor is the drift. It is a measure of sensor output while the input remains constant. Though it is often associated with sensor ageing, in this instance material related drift maybe significant. During practical use, the applied compression might not be instantaneous like if the subject is leaning on one leg and during that time period the output signal should not change with time so drift characterization was conducted. To evaluate the

sensor for drift, the load frame crosshead was lowered onto the sensor to apply a constant compressive strain of 16 % over 2 minutes for few cycles. The force-time data presented in Figure 74a, and b show no change in capacitive response over time in all cycles indicating a stable response with no obvious drift. Lastly, the ability of sensor to perform consistently for longer time durations was tested by performing 65 strain-cycles under 16% strain amplitude. The response shows no change in signal amplitude during the test indicating that the sensor can perform reliably during long periods of testing when used in an application (see Figure 74c, d).

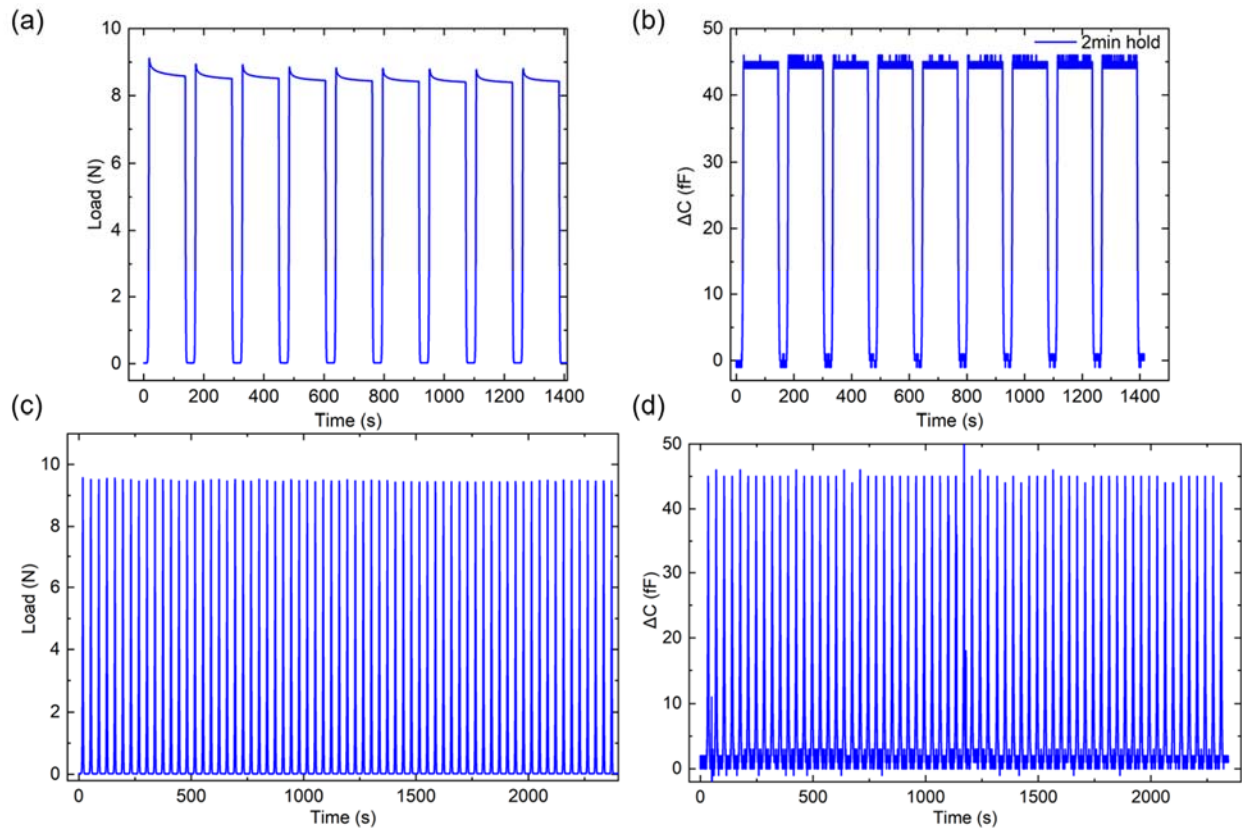


Figure 74: (a) Load and (b) capacitance response of sensor array subjected to compression with 2 minutes hold. (c) Load and (d) capacitance response of sensor array compressed for 65 cycles.

### 5.3.3 Artificial Limb Testing

The sensor data collected from all of the sensors simultaneously and continuously for ~15 seconds for tilt angles 3,6,9,12,14 degrees during backward (*Dorsi flexion*) and for tilt angles of 3,6,and 9 degrees for forward tilting (*Plantar flexion*) of the artificial limb is shown in Figure 75. The guide diagram (inset) shows the placement of the sensors in the socket. The negative values of the angle of tilt plotted as an independent variable (x-axis) correspond to the heel side tilt whereas the positive values indicate the toe side tilt. The number of negative tilt angles are more than the number of positive tilt angles because the artificial limb allowed more degrees of tilting towards the heel side than towards toe side due to its inherent design. The values of average change in capacitance ( $\Delta C$ ) of all nine pixels in the sensor array are plotted as the dependent variable with error bars corresponding to variation between four trials. A higher value of  $\Delta C$  implies a higher force acting on the sensor array at that tilt angle. The response of sensor S1 placed at the heel (posterior) or the popliteal fossa position displayed in Figure 75a shows an increase in  $\Delta C$  only when the limb is tilted towards heel side. The  $\Delta C$  is also found to increase with increase in tilt angle in the same direction. This data indicates increasing compression between the socket and the liner when the limb is tilted towards heel side as seen in the inset diagram. For the same reason, the sensor S2 placed at toe (anterior) or the patella tendon shows a very sharp increase in  $\Delta C$  when the limb is tilted toward the toe side (see Figure 75b). The sensors at other two locations namely S3 at pretibia and S4 at fibular head do not lie exactly in the front or back side of limb but their response is what would be expected in light of the data S1 and S2 locations, noted earlier. The sensor S3 responds more like S2 as its location is closer to the toe side and S4 responds like S1 as it is closer to heel side (see Figure 75c, d).

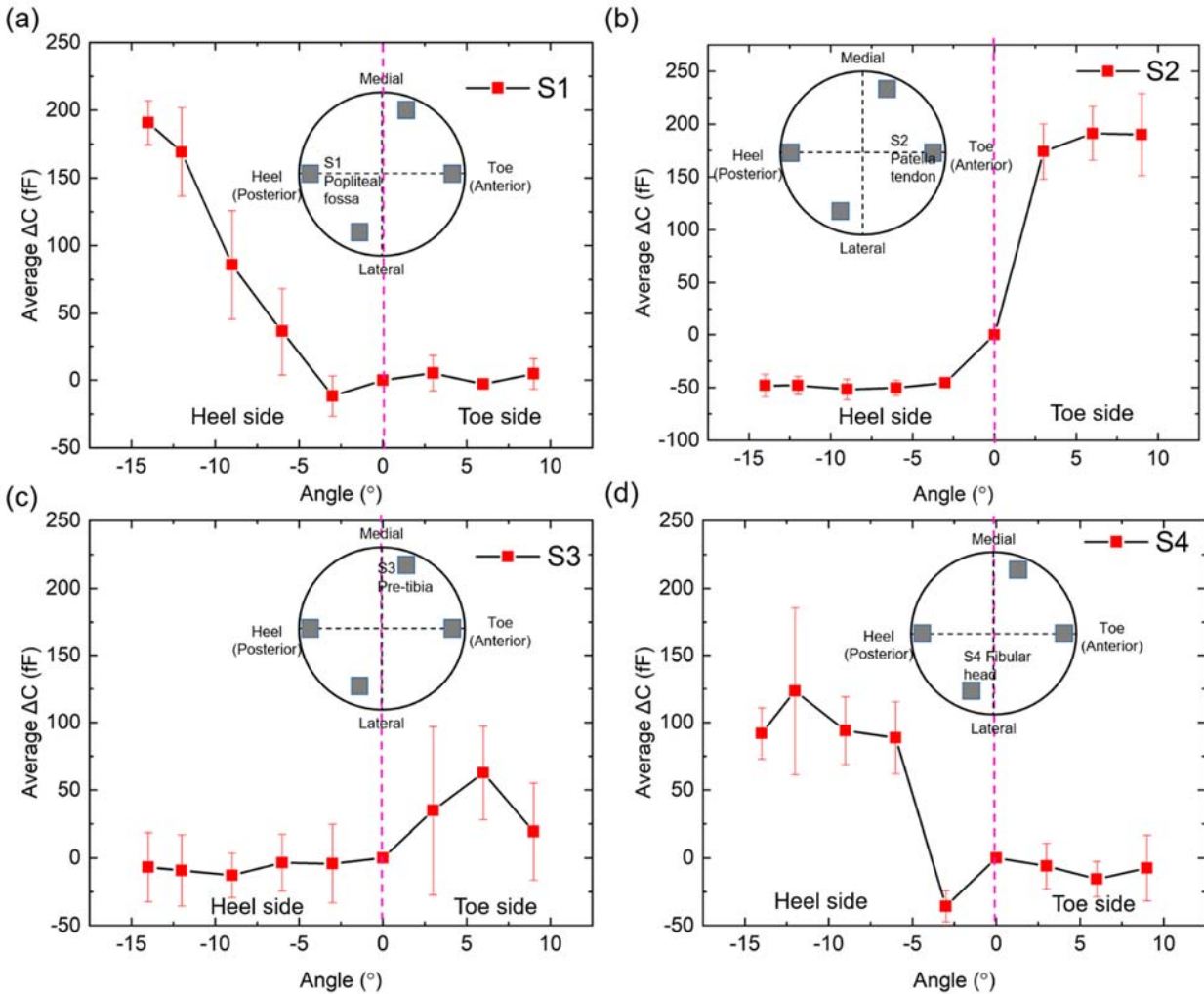


Figure 75: Artificial limb testing results where average capacitive response of sensors, (a) S1, (b) S2, (c) S3, and (d) S4, to negative and positive tilting of the limb is displayed.

### 5.3.4 Able-bodied testing

In the able-bodied testing, the response of sensor placed in the front thigh of right leg as shown previously in Figure 69 was observed. During backward and forward weight shifting by leaning (see Figure 76a), the sensor array showed an increase and decrease in average capacitance, respectively (see Figure 76b). There was an increase in capacitance during backward weight shift as at that point the sensor was pressed against socket. This phenomenon was also confirmed from

subject's verbal feedback. In the second test, capacitance of the sensor was recorded when the subject walked on a treadmill at a speed of 0.45 m/s. During this test, the ground reaction force produced by the foot of the bent knee adaptor which is monitored by the embedded sensor under the treadmill belt and the capacitance signal from the woven sensor array due to movement of the subject were recorded simultaneously during multiple cycles of walking (see Figure 78 a, b). In order to understand the sensor response Figure 77 shows the different stages of walking and ground reaction force (GRF) profile produced by the sensor under the treadmill belt for one walk cycle. A single walking cycle (see Figure 77e) shows that the GRF increases when there is a heel strike which decreases when the toe is lifted off the ground and stays zero during swing phase during which there is no ground contact. When single cycles of GRF and capacitance were plotted together on same time scale (see Figure 78 c) it was observed that the largest increase in average capacitance occurred at the heel strike.

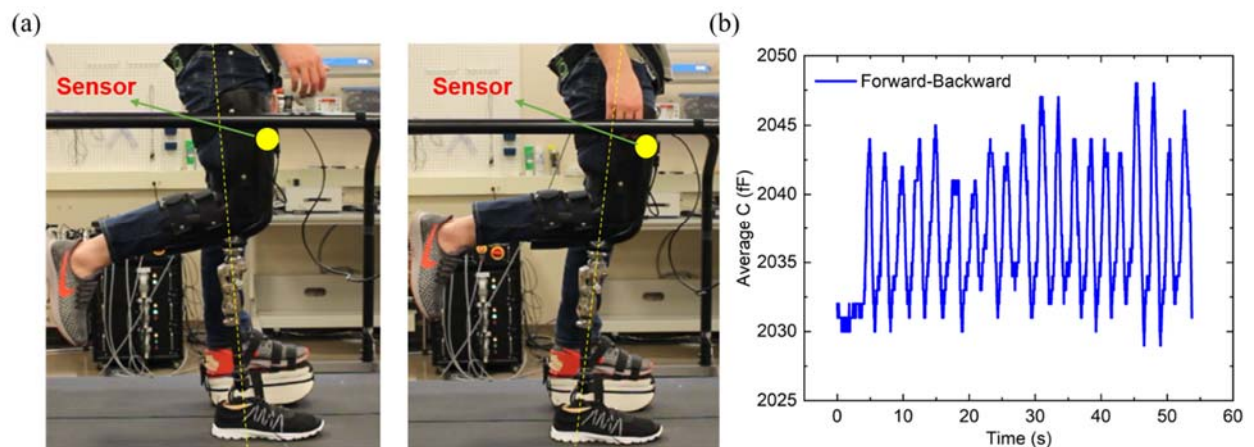


Figure 76: (a) Backward (left) and forward (right) weight shift during able-bodied testing, and (b) corresponding capacitance sensor response during forward-backward weight shifting for multiple cycles.

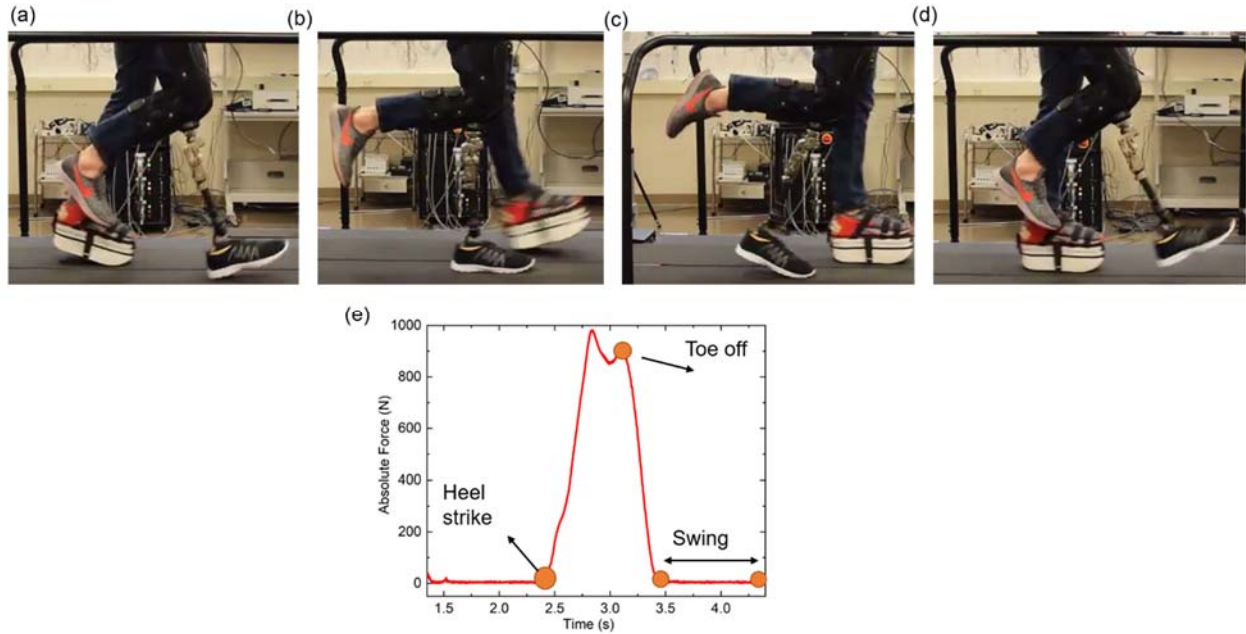


Figure 77: Walking test while wearing bent knee adaptor during able-bodied testing. Different stages of walking are shown namely (a) heel strike, (b) support, (c) toe-off, and (d) swing along with (e) ground reaction force generated during one walk cycle highlighting different stages of walking.

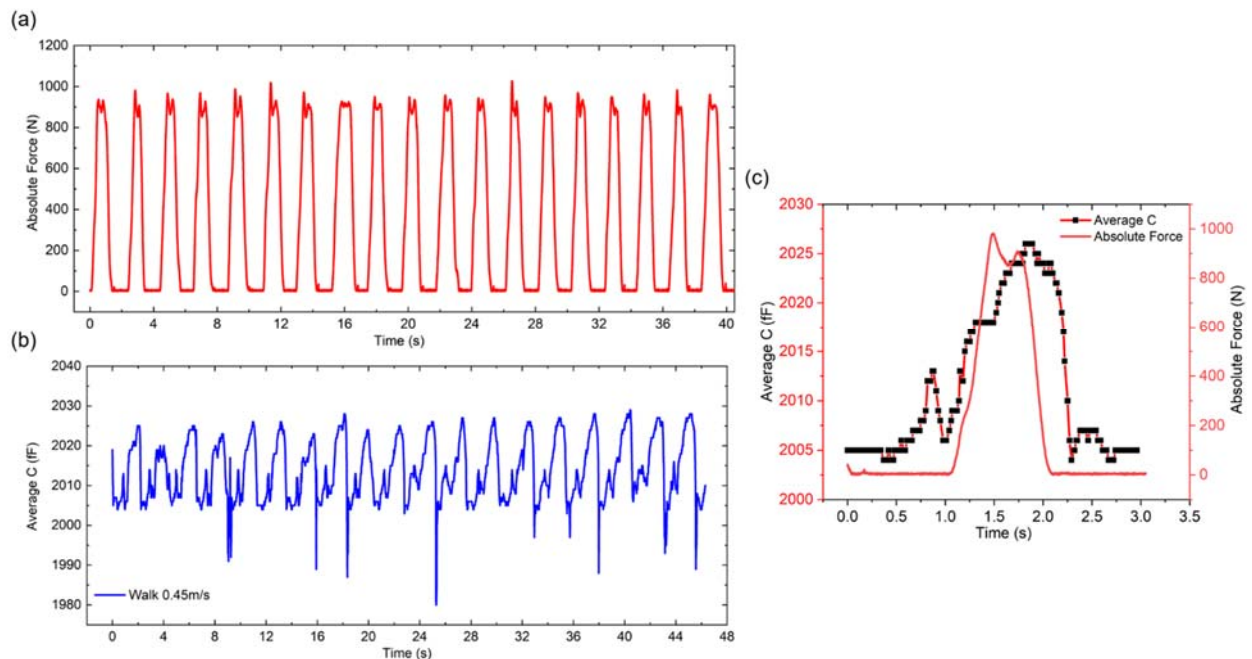


Figure 78: Able-bodied testing walking results. (a) Ground reaction force recorded by treadmill. (b) Capacitive response of sensor.(c) Comparison of variation of ground reaction force and capacitance in one walk cycle.

### ***5.3.5 Human Subject Testing***

In the human subject testing, the response of the sensor attached at the Patella Tendon (PT) location on the left leg of the human amputee was studied. In the static experiment, the response of the woven sensor array due to the simple side-to-side leaning with and without holding the stance for about 5 seconds was recorded (see Figure 79a, b). There was an increase in average capacitance of sensor array when the subject was leaning on the left leg on which the sensor was mounted which recovered during relaxing phase (see Figure 79c). This was due to the body weight acting on the sensor during the leaning phase. Similar average capacitance change was observed for multiple cycles of side-to-side leaning. Within the same static experiment, the subject also held his stance for 5s while leaning onto side of sensor mounted limb as well as relaxing. During this test an ~5s plateau region in capacitance value was observed both at the highest and lowest value of average capacitance of sensor indicating that the sensor response is constant over time, verifying no drift in sensor response as characterized before during benchtop testing of sensor. The ~5s constant capacitance value corresponds to the condition where subject was not performing any movement and was holding the stance. In the dynamic testing, the subject walked on a treadmill at a speed of 0.41m/s for 1 minute while the GRF and capacitance data was collected (Figure 80b, c). The results showed a repeatable increase and decrease in capacitance of sensor placed at the Patellar Tendon (PT) during walking (see Figure 80b) indicating that the Patellar Tendon (PT) was affected by various stances of walking. In order to understand the sensor response, the average capacitance change and GRF during one walk cycle were plotted on same time scale and it was observed that the capacitance value increased after the heel strike and recovered during toe off. This information indicates that a force is exerted at the PT location of the residual limb whenever there is a heel strike during walking (see Figure 81). Another interesting feature which can be observed from Figure 81 is that the sensor also responds to changes in force at the PT location

during swing phase of walking when the GRF is zero. This is because the woven sensor array is made of low modulus materials which are sensitive to small levels of applied forces.

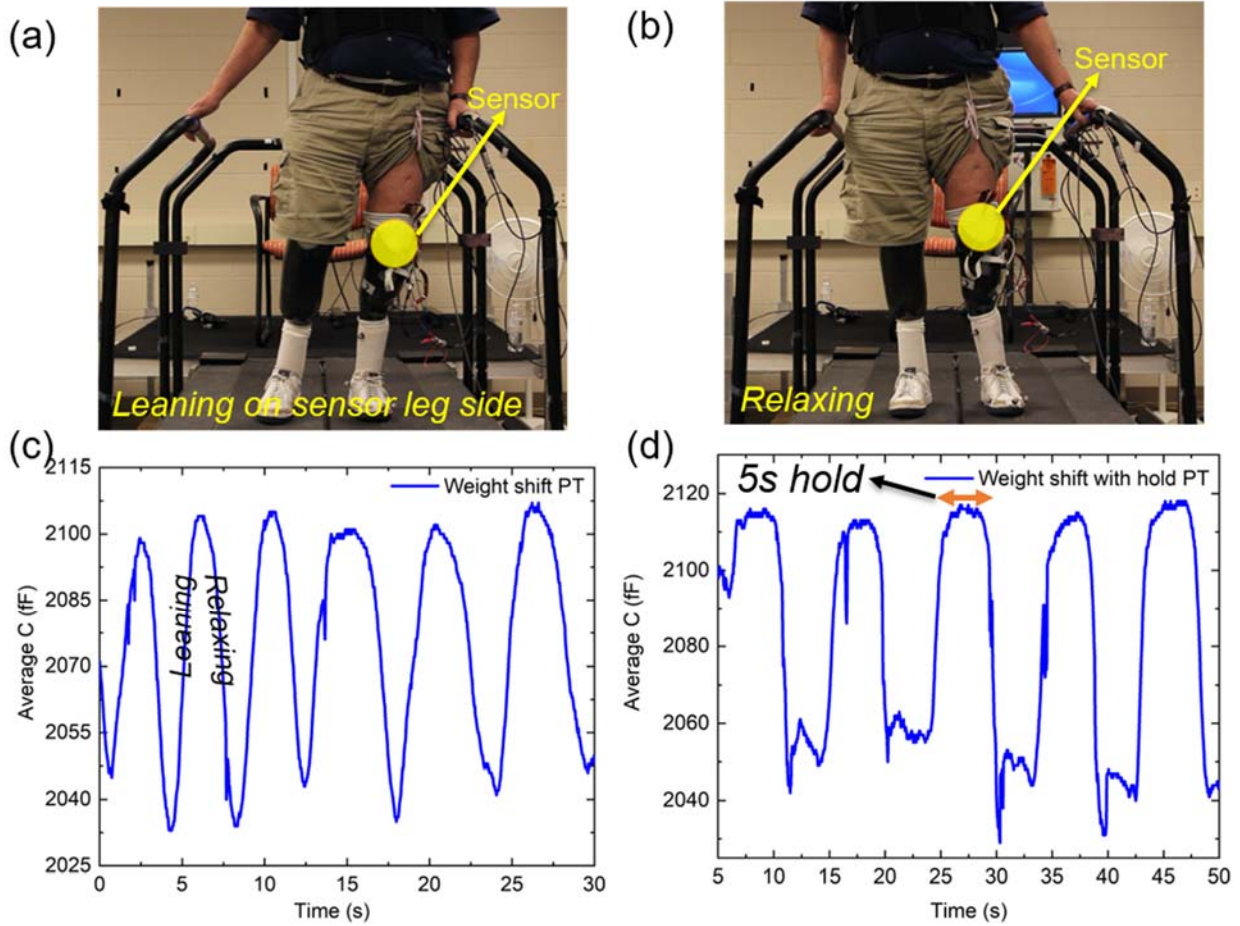
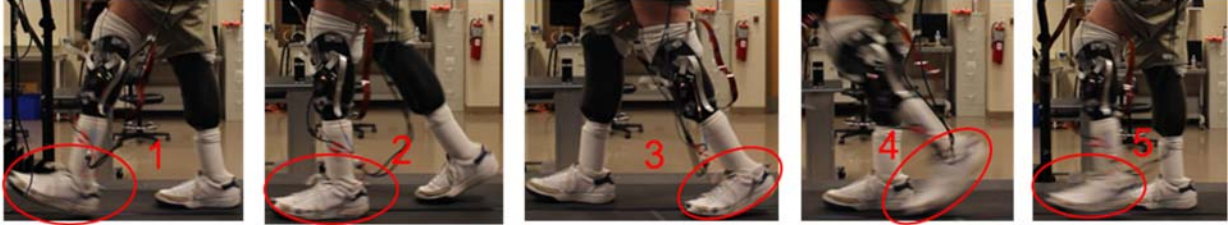
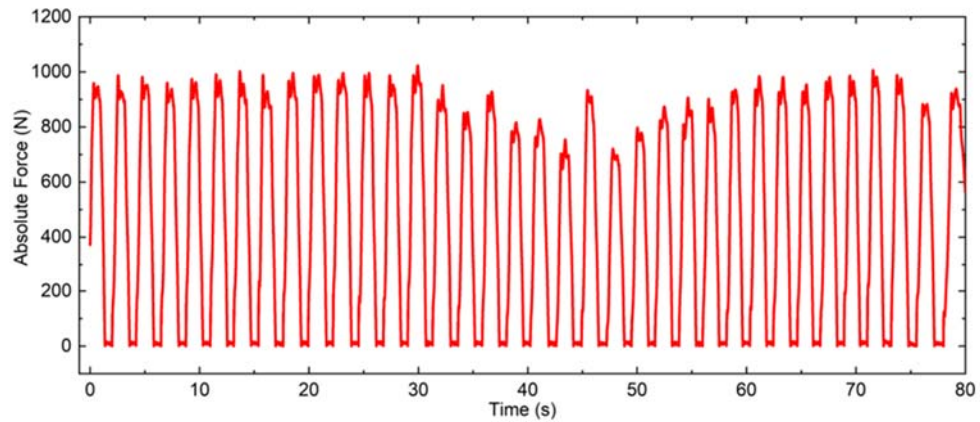


Figure 79: Side-to-side weight shifts by amputee; (a) loading stance, (b) unloading stance, (c) sensor response during weight shift, and (d) capacitive sensor response during weight shift with stance being held at both loading and unloading points for 5 seconds.

(a)



(b)



(c)

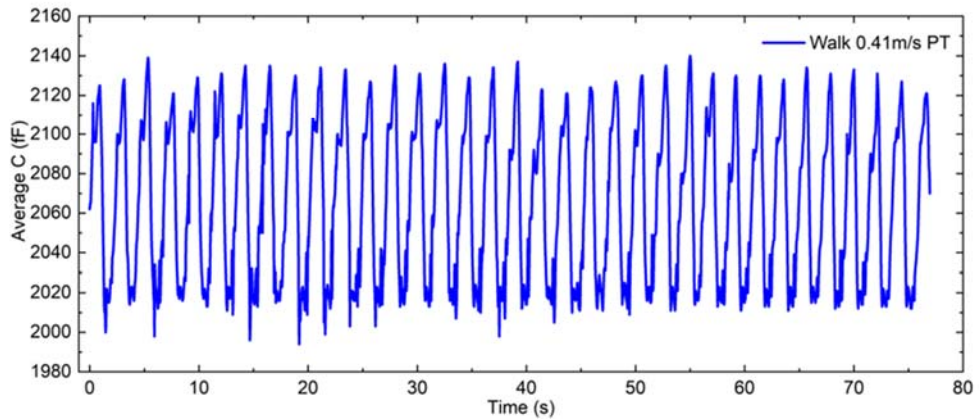


Figure 80: (a) Stances of the prosthetic leg of amputee during walking: 1-heel strike, 2-support, 3-toe-off, 4 &5-swing. (b) Ground reaction force recorded by treadmill. (c) Capacitive response of sensor.

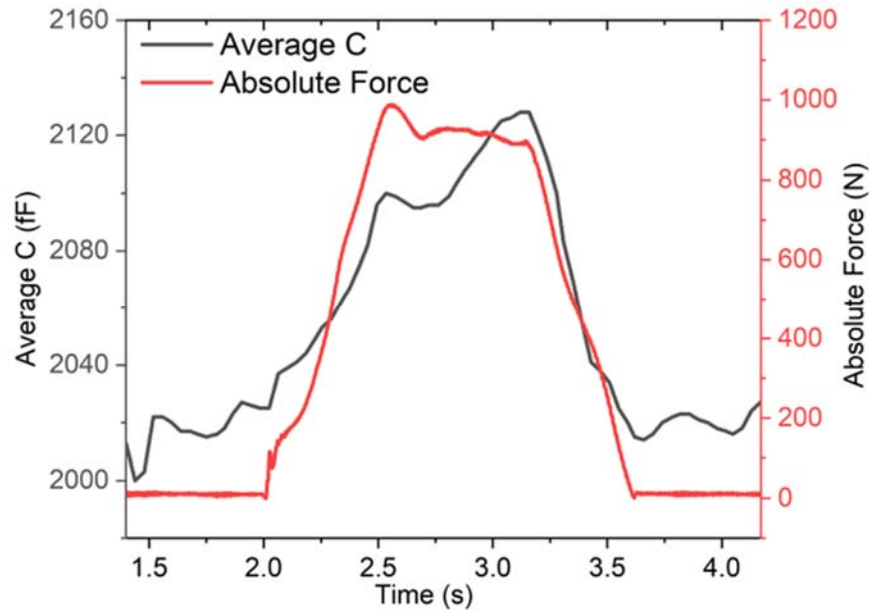


Figure 81: Variation of ground reaction force and capacitance with time during single cycle of walking

## 5.4 Conclusion

In this work, the application of woven fiber sensor array made of PDMS base polymer, in monitoring force in prosthetic socket environment was demonstrated. Benchtop characterization of sensors established their characteristics like sensitivity to compression, fast response, no drift and consistency during prolonged testing. The sensor arrays were tested in three phases namely, artificial limb testing, able-bodied testing, and amputee testing. These tests showed that fiber based sensors integrated within prosthetic environment can successfully track weight shifts as well as walking. This research is a proof of concept of implementation of fiber-based sensors for ISE for the first time. These sensors are conformable, resilient, and low cost and provide a promising potential solution to quantify the pressure at various points within prosthesis to offer individual customized solutions to design better fitting and comfortable sockets.

## 5.5 Supplementary information

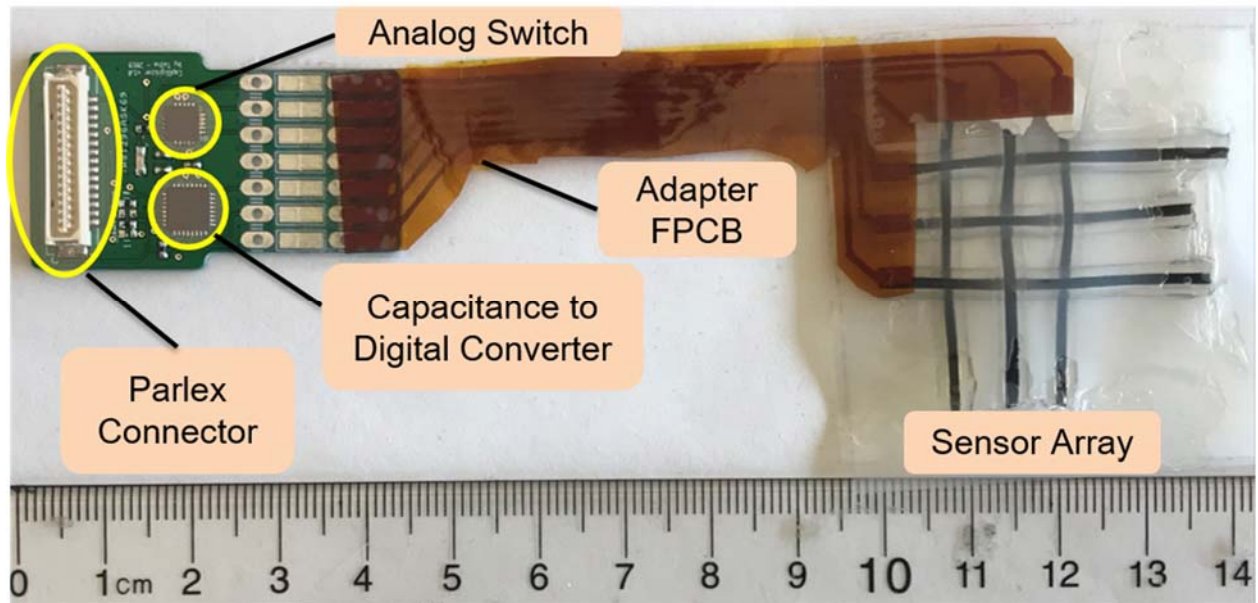


Figure 82: Custom-designed printed circuit board for Capacitance measurement connected to Sensor array

## References

- [1] “Artificial Limbs.” [Online]. Available: <https://medlineplus.gov/artificiallimbs.html>. [Accessed: 12-Aug-2019].
- [2] “Lower-Extremity Amputations: Background, Indications, Contraindications,” Apr. 2019.
- [3] “Statistics on hand and arm loss.” [Online]. Available: <https://www.ishn.com/articles/97844-statistics-on-hand-and-arm-loss>. [Accessed: 12-Aug-2019].
- [4] P. M. Stevens, R. R. DePalma, and S. R. Wurdeman, “Transtibial Socket Design, Interface, and Suspension: A Clinical Practice Guideline,” *JPO: Journal of Prosthetics and Orthotics*, vol. 31, no. 3, p. 172, Jul. 2019, doi: 10.1097/JPO.0000000000000219.
- [5] K. Carroll, *Prosthetics and Patient Management: A Comprehensive Clinical Approach*. SLACK Incorporated, 2006.
- [6] M. M. Lusardi, M. Jorge, and C. C. Nielsen, *Orthotics and Prosthetics in Rehabilitation - E-Book*. Elsevier Health Sciences, 2013.
- [7] S. A. Gard, “Use of Quantitative Gait Analysis for the Evaluation of Prosthetic Walking Performance,” *JPO: Journal of Prosthetics and Orthotics*, vol. 18, no. 6, p. P93, Jan. 2006.
- [8] S. W. Levy, “Skin problems of the leg amputee,” *Prosthet Orthot Int*, vol. 4, no. 1, pp. 37–44, Apr. 1980, doi: 10.3109/03093648009103113.
- [9] C. C. Lyon, J. Kulkarni, E. Zimerson, E. Van Ross, and M. H. Beck, “Skin disorders in amputees,” *Journal of the American Academy of Dermatology*, vol. 42, no. 3, pp. 501–507, Mar. 2000, doi: 10.1016/S0190-9622(00)90227-5.
- [10] E. A. Al-Fakih, N. A. Abu Osman, and F. R. Mahmad Adikan, “Techniques for Interface Stress Measurements within Prosthetic Sockets of Transtibial Amputees: A Review of the

- Past 50 Years of Research,” *Sensors*, vol. 16, no. 7, p. 1119, Jul. 2016, doi: 10.3390/s16071119.
- [11] A. F. T. Mak, M. Zhang, and D. A. Boone, “State-of-the-art research in lower-limb prosthetic biomechanics-socket interface: A review,” *Journal of Rehabilitation Research and Development*, vol. 38, no. 2, pp. 161–74, Apr. 2001.
- [12] J. C. H. Goh, P. V. S. Lee, and S. Y. Chong, “Stump/socket pressure profiles of the pressure cast prosthetic socket,” *Clinical Biomechanics*, vol. 18, no. 3, pp. 237–243, Mar. 2003, doi: 10.1016/S0268-0033(02)00206-1.
- [13] P. Davenport, S. Noroozi, P. Sewell, and S. Zahedi, “Systematic Review of Studies Examining Transtibial Prosthetic Socket Pressures with Changes in Device Alignment,” *J. Med. Biol. Eng.*, vol. 37, no. 1, pp. 1–17, Feb. 2017, doi: 10.1007/s40846-017-0217-5.
- [14] V. Rajtukova, R. Hudak, J. Zivcak, P. Halfarova, and R. Kudrikova, “Pressure Distribution in Transtibial Prostheses Socket and the Stump Interface,” *Procedia Engineering*, vol. 96, pp. 374–381, Jan. 2014, doi: 10.1016/j.proeng.2014.12.106.
- [15] L. Armitage, A. Buller, G. Rajan, G. Prusty, A. Simmons, and L. Kark, “Clinical utility of pressure feedback to socket design and fabrication,” *Prosthet Orthot Int*, p. 0309364619868364, Nov. 2019, doi: 10.1177/0309364619868364.
- [16] K. M. Henrikson, E. J. Weathersby, B. G. Larsen, J. C. Cagle, J. B. McLean, and J. E. Sanders, “An Inductive Sensing System to Measure In-Socket Residual Limb Displacements for People Using Lower-Limb Prostheses,” *Sensors (Basel)*, vol. 18, no. 11, Nov. 2018, doi: 10.3390/s18113840.

- [17] S. A. Curran and A. Kalpen, “Research and development at novel GmbH, Germany for prosthetics and paraplegics,” *Prosthet Orthot Int*, vol. 36, no. 3, pp. 376–379, Sep. 2012, doi: 10.1177/0309364612453252.
- [18] “F-Socket System,” *Tekscan*. [Online]. Available: <https://www.tekscan.com/products-solutions/systems/f-socket-system>. [Accessed: 12-Aug-2019].
- [19] G. A. Cavagna, H. Thys, and A. Zamboni, “The sources of external work in level walking and running,” *The Journal of Physiology*, vol. 262, no. 3, pp. 639–657, 1976, doi: 10.1113/jphysiol.1976.sp011613.
- [20] A. D. Kuo and J. M. Donelan, “Dynamic Principles of Gait and Their Clinical Implications,” *Phys Ther*, vol. 90, no. 2, pp. 157–174, Feb. 2010, doi: 10.2522/ptj.20090125.

## Chapter 6: Woven Fiber-based Sensor Array for Contactless Sensing

### 6.1 Introduction

Human-machine interfaces based on wearable electronics have recently attracted tremendous interest because of the increasing focus on weaving interactivity into daily use objects and advancements in technologies capable of exchanging information between people and electronics. Wearable electronics aims to merge the physical and digital world. In accomplishing the vision of weaving interactivity in our daily lives, textiles are an obvious choice as they are the most fundamental and universal constituents used to build the world around us. This has led to the development of electronic textiles with sensing functionality. Clothing based sensing interfaces for gesture recognition have promising potential applications in creating novel human machine interfaces and electronic skin for robots. One of the earliest attempts of integrating interactivity to clothing was done by Orth with the development of Musical Jacket in 1998 with an embroidered keypad to play music where the principle of touch detection was based on capacitive sensing method [1], [2]. Since then, fabrics as sensors for detecting tactile pressure through capacitance measurement have been explored extensively [3]–[6]. Most of the textile based pressure sensors are capacitive sensors because of their ease of implementation, multifunctionality and ability to run in low power mode. Most capacitive gesture sensors require contact between finger and the sensor interface but if action of contact is not required then it can open new possible applications. Contactless gesture sensing is desirable in many instances because it offers the freedom and simplicity of hand motion to enrich user experience. Various capacitive gesture sensing systems [7]–[15] have been proposed but there hasn't been any fully textile based contactless sensor with potential application in gesture sensing.

The work reported here demonstrates a capacitive woven sensor array capable of sensing conductive objects in the vicinity in a contactless manner. The sensor array consists of multiple capacitors created at the crossover points of fibers in the fabric, due to the unique fiber cross-sectional shape and the fringe capacitance is used as tool for the contactless sensing. The fabric acts as a proximity sensor by showing a drop in capacitance when a conducting object like human finger approaches it due to local variations in the fringe fields of the capacitor array [11]. In this unique approach the sensing functionality comes from the fiber shape as well as their structure of interlacement without compromising inherent textile properties of fabrics like conformability. The advantage of this approach is that it utilizes woven configuration which resembles the structure of the capacitive touch sensor panels [16] as both are based on grid structure and also it can be manufactured at low cost using conventional textile weaving technologies to create large area sensor surfaces. Another advantage of the proposed array is that since it utilizes capacitance based sensing, it is possible to merge contact based pressure sensing along with contactless proximity sensing capabilities in one device [9], [10], [12], [13]. This paper focuses on proximity sensing capability of these fiber based woven sensing arrays. As a proof of concept, millimeter scale sensing fibers were fabricated in a cost-effective manner through simple benchtop extrusion procedure and hand woven to create a 96 pixel sensor array. A schematic of potential application of such proximity sensing array is shown in Figure 83a where the sleeve of the garment is the interactive sensor area that would allow user to activate some functionality like answer a phone call simply by contactless drawing of a specific pattern. A similar idea of using fabric as an interactive surface can be found in Google-Levi's trucker jacket [16] but that requires touch contact. Figure 83b shows the plain woven sensor array consisting of sensing fibers. The bicomponent sensing fibers developed in this research have dumbbell-like cross-section consisting

of electrically insulating and conducting components where circular side lobes are insulating and the middle bridge is conducting. Figure 83c shows one sensing crossover point made by the fibers as well as the fiber cross-section. The conducting segment of the two fibers is separated due to height of the insulating segments creating a capacitive sensor with air as the dielectric medium. The diagram also shows electric field lines outside the electrodes running from positively charged electrode to negatively charged electrode of the capacitor which couple with human finger.

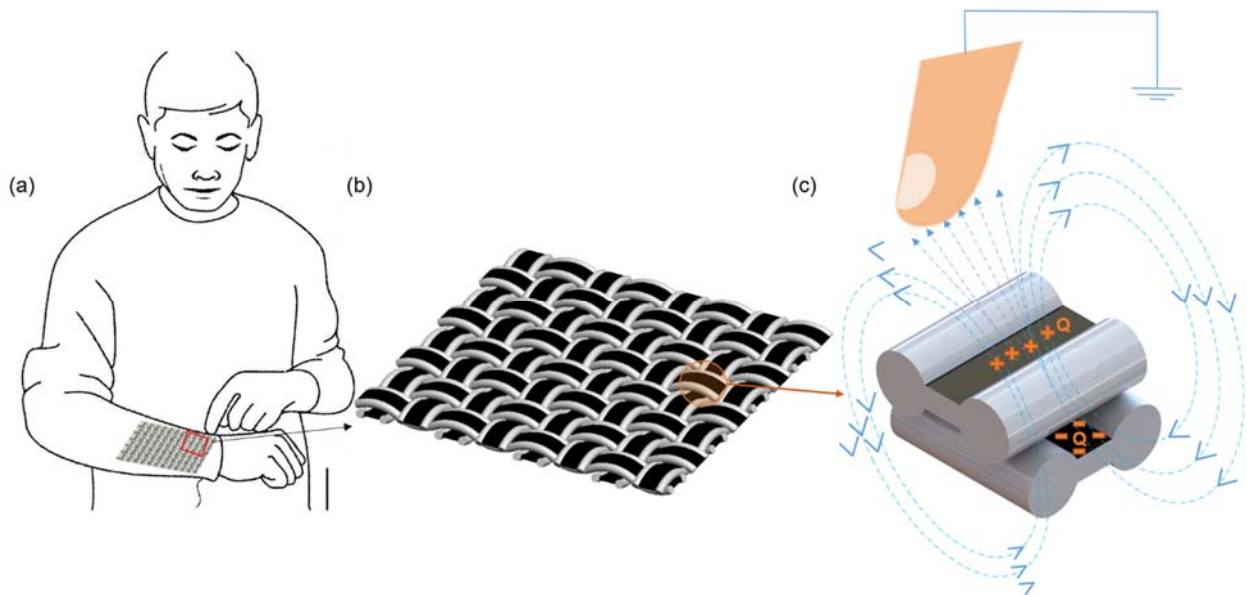


Figure 83: Schematic of capacitive proximity sensing concept. (a) Sensor array integrated into the garment of the user for contactless gesture sensing. (b) Isometric view of the plain woven sensor array. (c) Single sensing pixel made by bicomponent sensing fibers showing fringe field of capacitor coupling with human finger.

## 6.2 Results and Discussion

### 6.2.1 Fabrication

The insulating part of the bicomponent fiber was fabricated from a two-part UV-curing silicone (LSR 225-1, Momentive) and the middle conducting part was composed of conducting

polymer composite (CPC) which consisted of 6.4wt% carbon black (Ketjenblack EC-300J, AkzoNobel) dispersed in heat-curing silicone (Ecoflex 00-50). These fiber forming materials were fed into an extrusion die with three inlets (two for insulating sides and one for middle conductive segment) and a dumbbell shaped orifice to produce fibers at a production rate of 292.85 mm/min. Downstream of the extrusion die orifice, the insulating sides of fiber were cured by UV light since the insulating sides were made of photo crosslinking silicone while middle conducting segment was cured by collecting on a heated winding drum as it was made of thermally curing silicone. The extrusion rate and winding rate along with lateral traverse rate were matched to achieve continuous deposition of fibers on the drum (refer Figure 84). After extrusion, the fibers were peeled off the winding drum. Optical microscopy of fibers revealed that the overall width of fibers was 2.7mm where insulating segment height was 1mm and conducting segment dimensions were 0.7mm (width) x 0.4mm (thickness). The fibers were assembled in a plain woven configuration to create a 96 pixel sensor array with 8 rows and 12 columns which was defined by the data processing capability. The total spatial area of sensor array was 261 cm<sup>2</sup> (27.5 cm x 9.5cm) where column and row separations was 2.5 cm and 1.5 cm respectively. The minimum spacing between sensing pixels was kept larger than dimensions of the index finger which can be approximated by a circle of diameter of 13mm [17]. This was done to prevent the index finger used for making gestures from overlapping multiple pixels simultaneously as a spacing lower than index finger dimension would lead to more than one sensor response for a single finger proximity so the simplest configuration was chosen to demonstrate the proof of concept and ease of data interpretation. Electrical interconnects were created to connect fibers to the custom designed printed circuit board for recording capacitance. Firstly, fibers were attached to copper tape using the thermally curing CPC paste used for fiber extrusion and encapsulated by silicone (Ecoflex 00-

35 Fast) to secure connections. Secondly, thin wires were soldered onto the same copper pad and routed to the circuit board housing the capacitance to digital convertor chip (Analog Devices AD 7142) (refer Figure 95 and Figure 96 in supplementary information ). A USB cable was used to connect the circuitry to the computer for recording capacitance. Figure 85 shows diagram of various steps involved in sensory array fabrication, namely, extrusion, weaving and electrical interconnect fabrication.

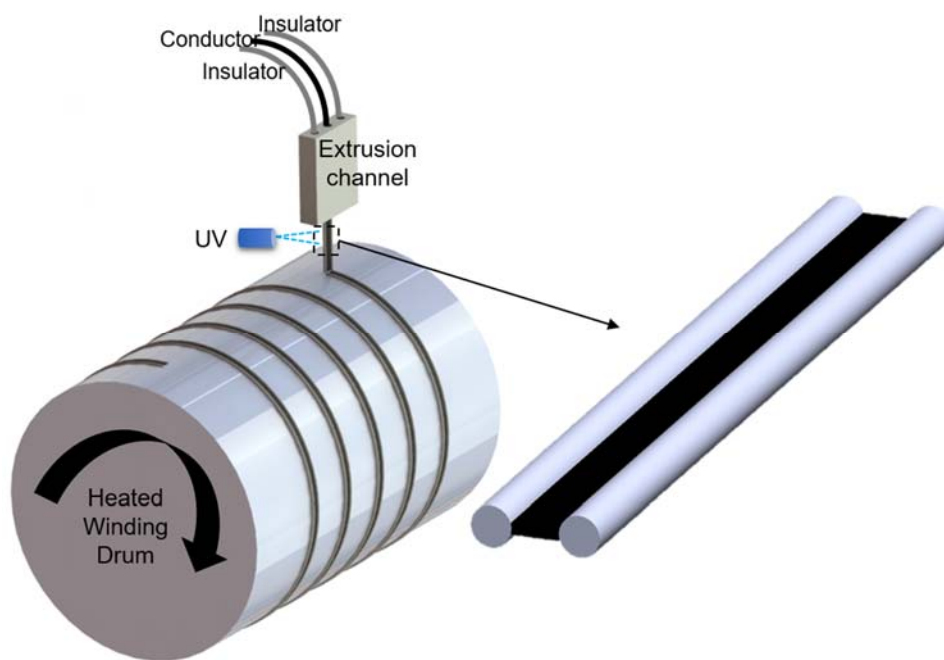


Figure 84: Schematic of fiber extrusion

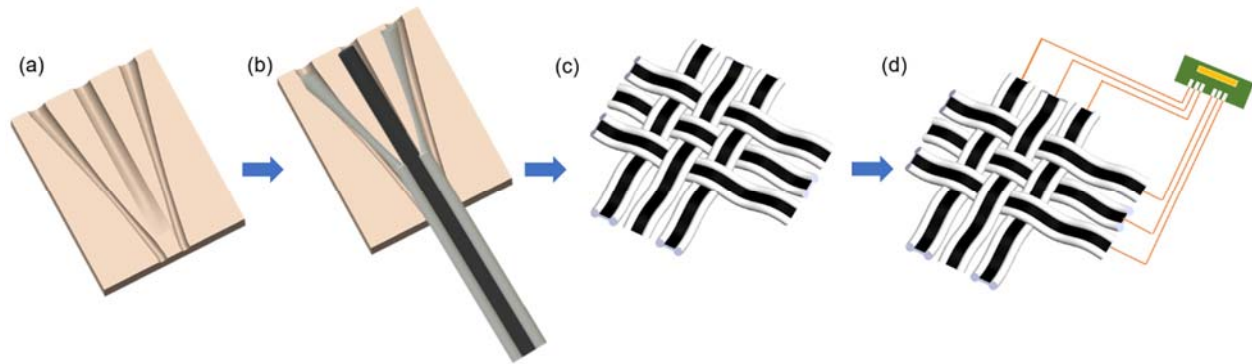


Figure 85: Schematic of sensor array fabrication process: (a) Fabrication of three channel extrusion device. (b) Fiber extrusion. (c) Weaving, and (d) Fabrication of electrical interconnects.

### 6.2.2 Benchtop sensor characterization

In the benchtop characterization the capacitive woven sensing arrays were evaluated for their contactless sensing capability. These tests were conducted on a load frame (MTS-30G) by attaching a small (5 mm x 5 mm) grounded copper tip to the crosshead in compression mode while the sensor was placed underneath, to simulate a human finger approaching the sensor array, see Figure ?? . The capacitance was continuously recorded while the finger-like the tip mover closer and away from the sensor. The change in capacitance,  $\Delta C$ , was calculated from the difference ( $C_{base} - C_{proximity}$ ), where  $C_{base}$  is the initial capacitance of woven sensor and  $C_{proximity}$  is the capacitance of sensor when a conductive object approaches the sensor. Since the fringe field couples with the conductive object, the value of  $C_{proximity}$  is always lower than that of  $C_{base}$  . Therefore, a negative value of  $\Delta C$  indicates presence of an object in the proximity of the sensor. This also means that hypothetically, closer the conductive object to the sensor, larger is the drop in capacitance which corresponds to larger negative value of  $\Delta C$  [9], [12]. In the first set of evaluation, the sensor pixel of the woven array was positioned underneath the grounded copper tip 18 mm away as that was the maximum distance of proximity at which sensor was sensitive to

proximity of conductive object (see Figure 86a). The crosshead was then moved towards and subsequently away from the sensor at a constant speed of 20mm/min. During three separate initial excursions, the finger-like copper tip was brought as close as 2, 6, and 10 mm from the sensing pixel while the capacitance was recorded continuously as a function of time, see Figure 86b, and c. As expected, in all cases, the capacitance values dropped as the tip approached the sensing pixel and the largest drop was observed for the closest proximity (2 mm) of the copper tip. The sensory output during the movement closer and away were mirror images of each other and maybe more importantly, the sensor output was the same for all proximity values irrespective of how close the tip came at the end of its traverse (see Figure 86d). It should also be noted that sensor array becomes more sensitive as the probe comes closer to the sensor pixel.

Based on these initial observations, the rest of the evaluations were performed with the tip traversing as close as 2 mm from the sensor pixel. The data for multiple cycles of approach presented in Figure 87a show remarkably repeatable response of the sensor. Figure 87a shows 2mm proximity test at 40mm/min repeated for 100 cycles and exhibits good reliability with complete recovery of capacitance after removing the conductive object.

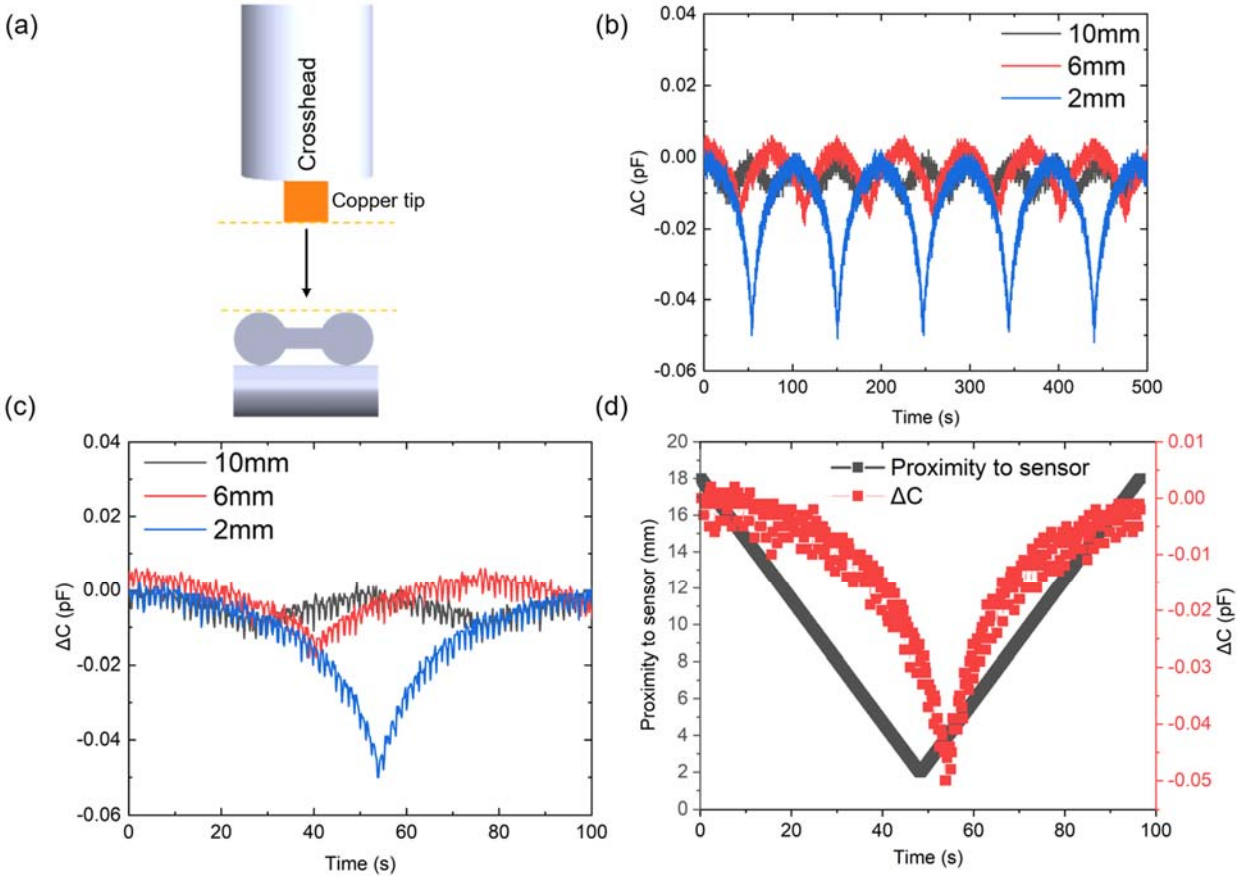


Figure 86: Effect of the proximity of grounded conductive object on capacitance. (a) Schematic of the experimental setup showing grounded copper tip attached to movable crosshead. (b) Effect of three different proximity distances. (c) Zoomed in single cycles of three different proximity distances shown in (b). (d) Proximity to sensor and change in capacitance plotted as a function of time.

The change in the output of the sensor while the copper tip is held in position over time (2 mins) at a fixed proximity (2 mm) was recorded as a measure of drift in sensor response. The drop in capacitance ( $\Delta C$ ) of -0.045 pF was recorded and there was no change in capacitance during the 2 minute intervals of (Figure 87b) over 10 cycles. A variation of  $\pm 0.005$  pF was well within the noise level of the data collection system. The time necessary for a sensor output to change from its current state to a stable new value due to an instantaneous change in the physical signal, called response time, is also a critical measure of its performance. The response time of the sensor pixel was assessed by varying the speed of approach toward the sensor pixel Figure 87c shows the

response of the sensor to 2 mm proximity of the conductive tip at approach speeds of 20, 30, and 40 mm/min. The response of the sensor was plotted over 500 s and it was observed that for all approach speeds, the output was repeatable and consistent ( $\Delta C$  of -0.05pF).

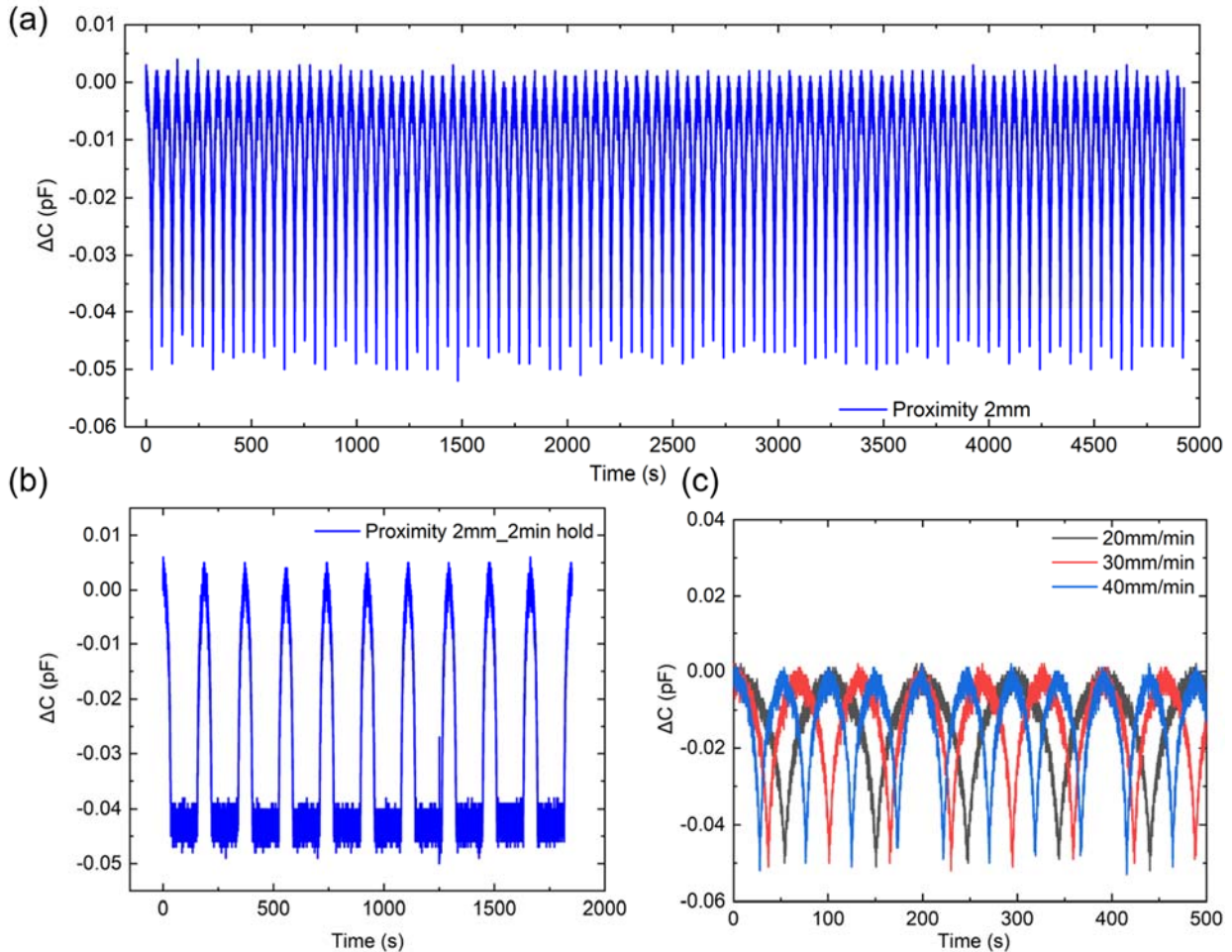


Figure 87: (a) Capacitive response of 100 cycles of 2mm proximity of conductive copper tip to the sensor. (b) Capacitive response of sensor when the conductive copper tip is held 2mm away for 2 minutes for 10 cycles. (c) Effect of three different speeds of approaching of conductive copper tip 2mm away from the sensor.

As mentioned earlier that capacitive sensors are commonly used in pressure sensing so the dual mode operation of these sensors i.e. capacitance-based pressure and proximity sensing was tested. In this experiment, the conductive object approached the sensor and compressed it to simulate gentle touch during which the capacitance was recorded. The  $\Delta C$  response curve to the

conductive object's position showed capacitance decrease during the approach, capacitance increase during compression and capacitance recovery when moving away from the sensor (Figure 88a). The drop in capacitance due to approach was  $\Delta C$  was  $-0.075$  pF and increase in capacitance during compression was  $+0.05$  pF. The different response of the capacitance for approaching and pressing shows that a single sensor could be used for detecting contact pressures as well as proximity of the conducting object. The gentle compression was confirmed from the recorded force of  $0.2$  N during contact (Figure 88b). Further, 10 cycles of approaching and pressing of the sensor were done and repeatable response was obtained (Figure 88c).

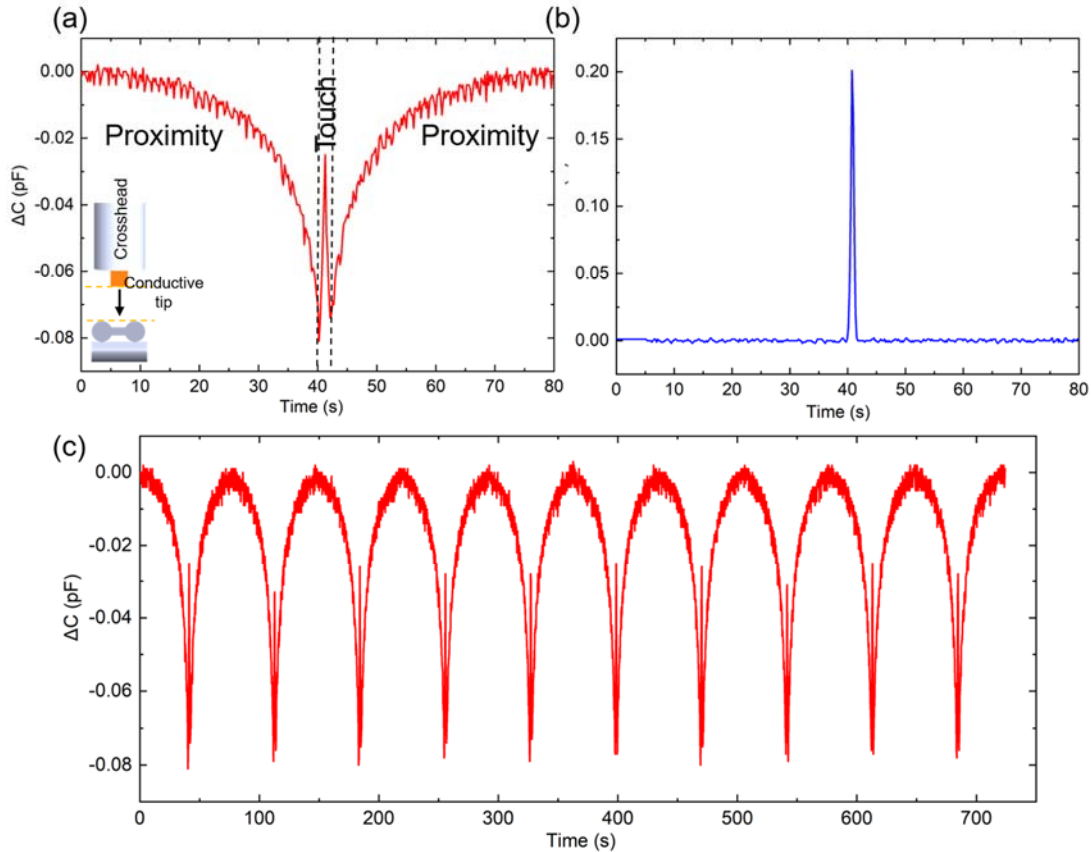


Figure 88: Dual-mode operation of the capacitive sensor. (a) Capacitance change during approaching, pressing and distancing from the sensor showing capacitance decrease during the approach, capacitance increase when pressed and capacitance recovery during retraction of the crosshead. (b) Force recorded during the pressing of the sensor. (c) 10 cycles of approaching-pressing of the sensor.

### 6.2.3 *Gesture recognition*

Based on the performance of the woven sensor array in proximity and motion sensing, we explored one of the obvious potential practical applications of this in gesture recognition. Textile fabrics with these capabilities can offer an alternative user interface for providing real-time communication with personal electronic devices. Gesture is a natural human body language and in this case can be defined as a physical movement, e.g. distinctive touch or swipe that can be interpreted by the sensor. In order to use gesture as an interface for communication in this instance it has to be in the close proximity of the clothing we use. For these experiments, we use the woven array with 96 sensory pixels, described earlier. For data interpretation and gesture tracking purposes, each of the 96 pixels was assigned a specific number based on their position in the woven matrix, see

Figure 97 in supplementary information. In the first demonstration, two fingers namely, the index and long finger were simultaneously brought above pixel 10 and pixel 19 respectively (Figure 89a), which led to a drop in capacitance of those two pixels with  $\Delta C$  values ranging from -0.03pF to -0.06 pF (Figure 89c). The heat map, presented in Figure 89b, represents the sensor response upon the two-finger approach with lowering of capacitance values of pixel 10 and 19. It is also observed that the long finger has a larger value of  $|\Delta C|$  than that for the index finger due to longer length than index finger. The drop in capacitance at same time demonstrates the multi-touch capability also. The sensor array produced repeatable output for all of the five similar gestures and showed simultaneous drop with larger drop for long finger (Figure 89d).

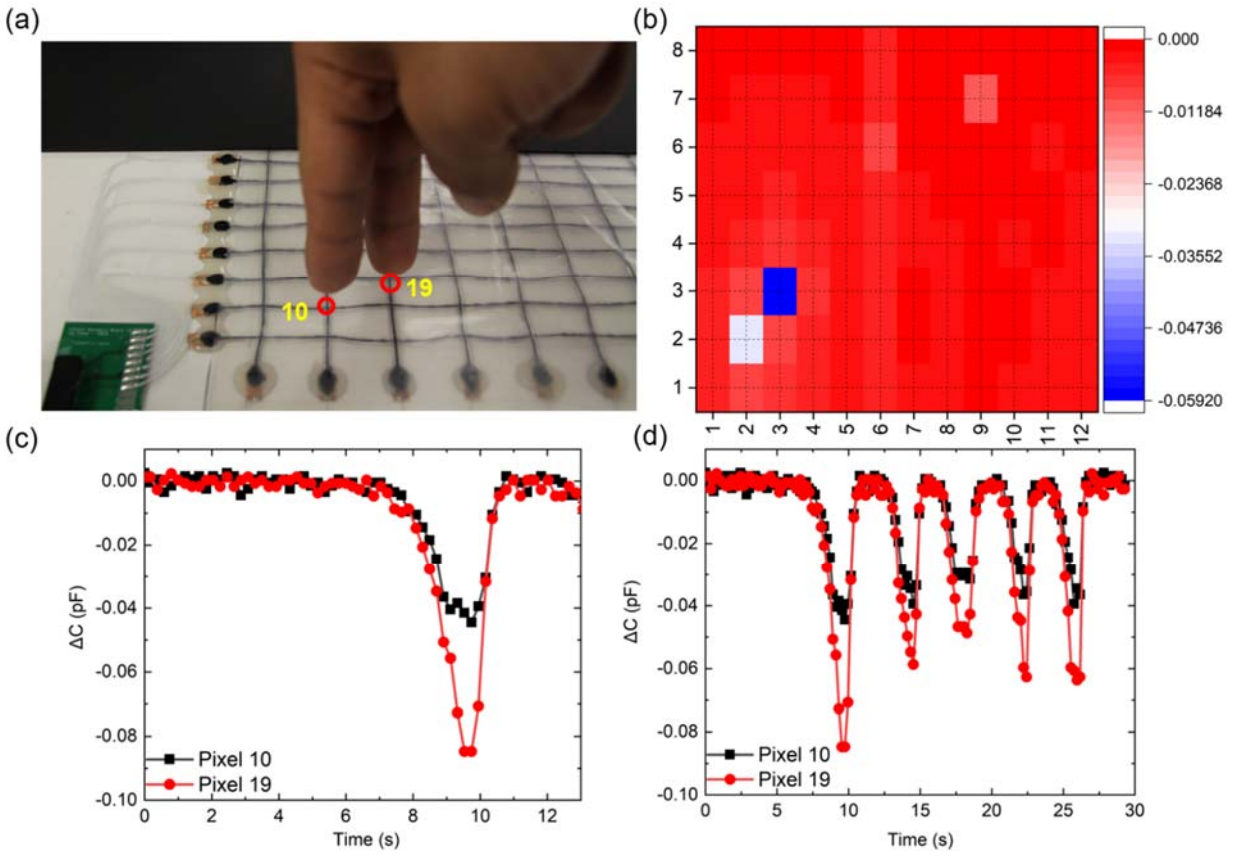


Figure 89: Two finger simultaneous approach detection. (a) Index and long finger in proximity of pixel 10 and pixel 19 respectively. (b) Heatmap of change in capacitance of sensor array with pixel 10 and pixel 19 displaying a lower capacitance compared to other pixels. (c) Change in capacitance of pixel 10 and pixel 19 with time when approached by index and long finger simultaneously. (d) 5 cycles of approach and retraction of index and long finger from pixel 10 and pixel 19.

As a next step, three fingers, namely, the index, long and ring fingers were simultaneously brought in the close proximity of pixels 10, 21 and 28, respectively (Figure 90a). The heat map of the response of the sensor array shows pixel 10, 21, and 28 displaying a lower capacitance compared to other pixels (Figure 90b). In this case, also, the long finger showed the highest signal intensity (Figure 90c). Once again, tests over five cycles of three-finger approach were carried out to demonstrate the repeatability (Figure 90d). Overall, the finger movement experiments demonstrate the ability of the woven sensor array to detect multi-touch, sense human finger proximity as well as pattern, over multiple cycles.

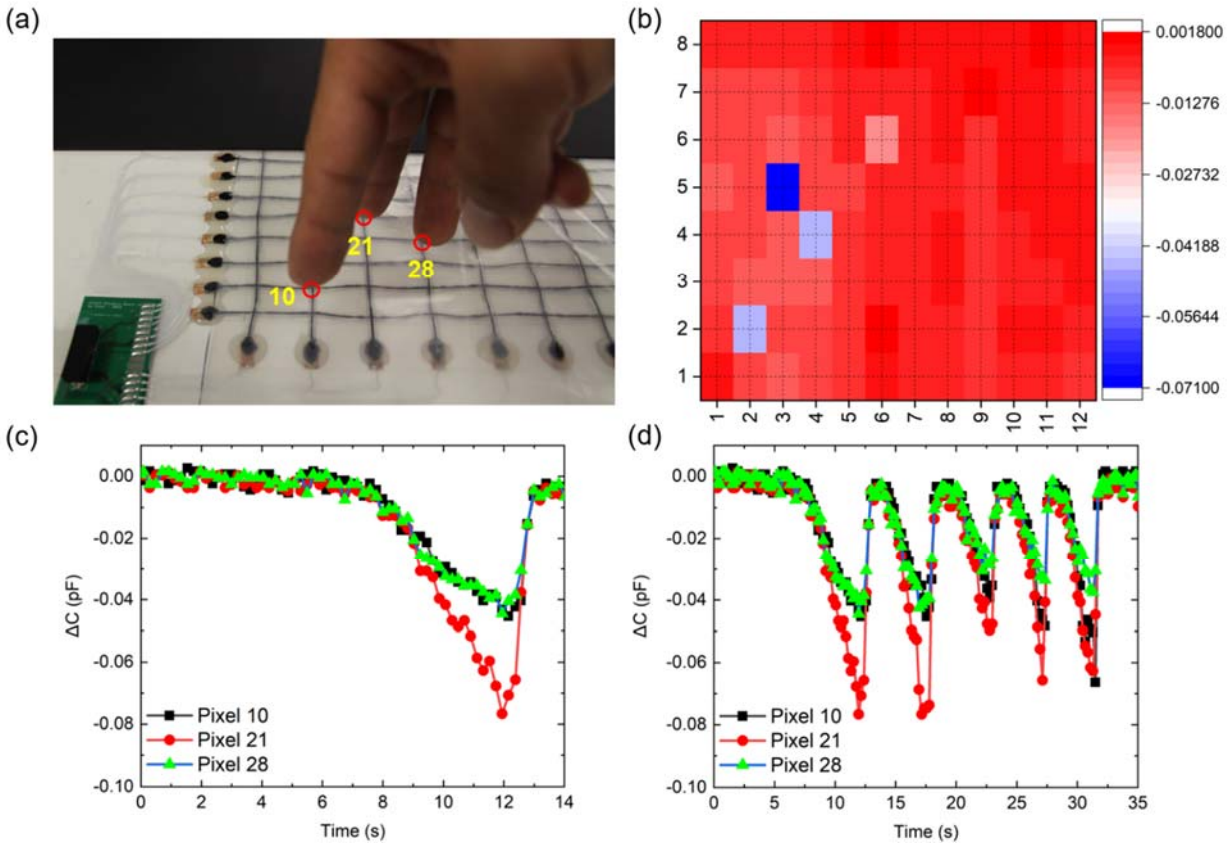


Figure 90: Three finger simultaneous approach detection. (a) Index, long and ring finger in proximity of pixel 10, pixel 21 and pixel 28 respectively. (b) Heatmap of change in capacitance of sensor array with pixel 10, pixel 21 and pixel 28 displaying a lower capacitance compared to other pixels. (c) Change in capacitance of pixel 10, pixel 21 and pixel 28 with time when approached by index, long and ring finger simultaneously. (d) 5 cycles of approach and retraction of index, long and ring finger from pixel 10, pixel 21 and pixel 28.

The quasi-static human-finger approach experiments targeting specific pixels, were followed by evaluation of the sensor array in swipe gestures. Contactless swipe or similar gestures are increasingly being investigated for use as human-machine interface [16], [18]–[21]. In the first instance, the index finger was moved over column 3 of the sensor array beginning at pixel 21 and ending at pixel 17, see Figure 91a. The change in the capacitance of these 5 pixels (21, 20, 19, 18, and 17) along with others in the vicinity during the event is plotted in the form of a heat map in Figure 91b. The heat map is plotted such that it represents the physical orientation of the sensor

array and captures the overall gesture performed. The bottom axis (x-axis) of the heat map represents 12 columns and the vertical axis (y-axis) represents 8 rows. The intersection of each grid line represents a sensing pixel and will be referred to by the pixel number defined in Figure 97 in describing the sensory response to the gesture. In the heat map in Figure 9b, the pixels with a shade of blue indicate a larger drop in capacitance indicative of proximity of the human finger. The gesture of swipe along the y-axis is clearly visible in this heat map (Figure 91b). More information about the gesture was obtained by plotting the sensory response of pixels with time. The  $|\Delta C|$  vs time graph of the gesture shows capacitance drop of various pixels involved in the gesture response at different points in time (Figure 91c). In this particular swipe gesture, the response of the sensor array, beginning with pixel 21 to 20 and all the way to 17 shows the expected sequential drop due to the movement. This means that it is possible to determine the direction of gesture performed on the array using this information. In this orientation of the sensor array, pixel 21 is on a higher row than pixel 17 which means that the swipe was a downward movement. The swipe gesture was performed three times as shown in Figure 9d, where the measured capacitance values of pixels, 21 to 17, is shown in three groups separated by  $\sim 5$ s of elapsed time in between each swipe (Figure 91d).

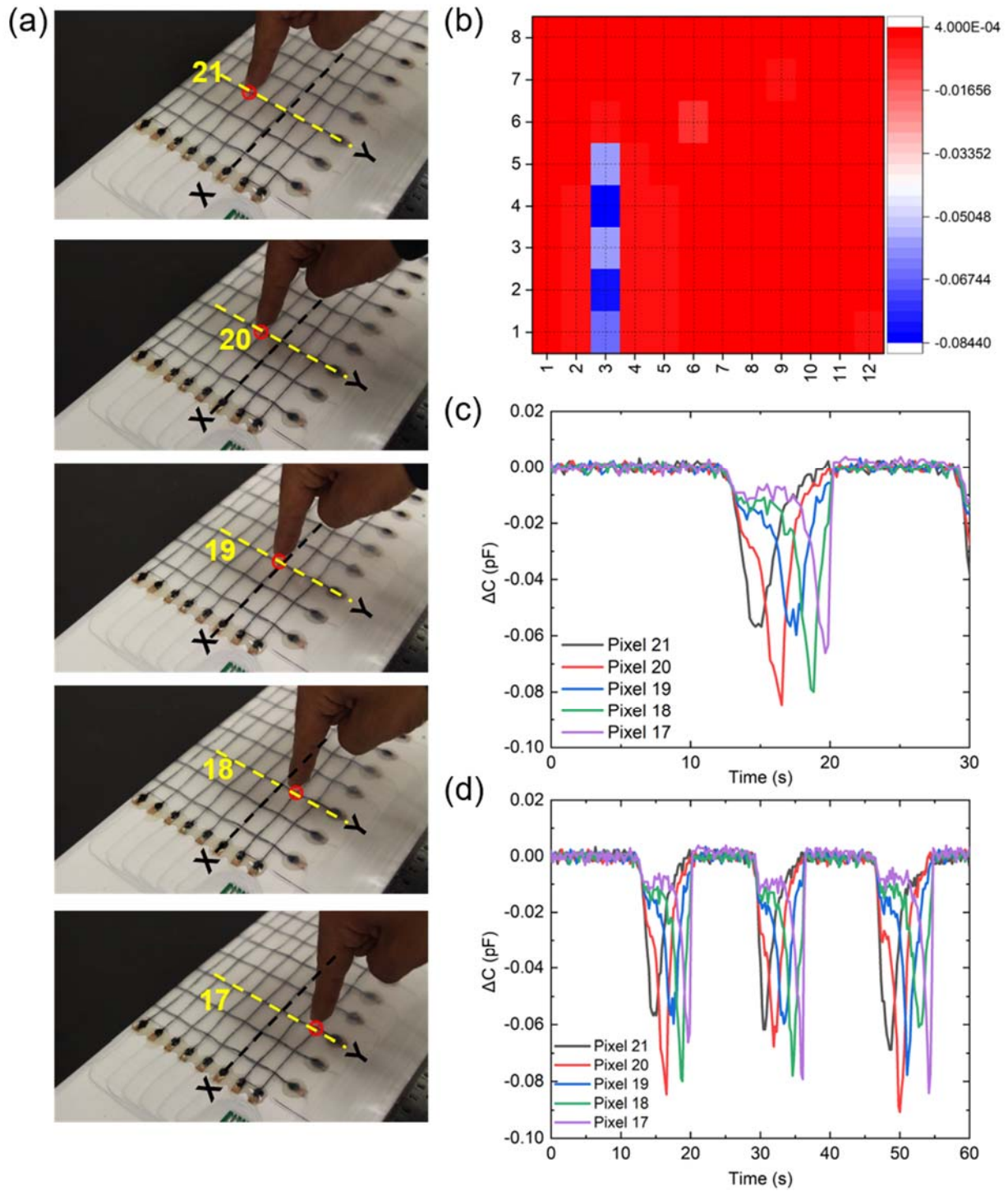


Figure 91: Touchless swipe gesture using index finger. (a) Swipe motion on column 3 with images of index finger at every pixel from pixel 21 to pixel 17 during swipe. (b) Swipe gesture on column 3 represented in the form of heatmap. (c) Drop in capacitance of pixels 21 to 17 during swipe with time. (d) Change in capacitance of pixels 21 to 17 during 3 swipe gestures.

Since the simple linear swipe could be interpreted, exactly, more complex motions were investigated. Figure 10 shows the sensory response of the woven array when the index finger was moved in two linear swipes to cross each other to create the pattern of the arithmetic notation of addition. The heat map shows the final gesture performed by the user on specific pixels of column 3 and row 4 (Figure 92b). The  $\Delta C$  vs time plot presented in Figure 92c, clearly shows the first swipe along the y direction or column 3, followed by horizontal swipe along row 4. That is because in column 3, pixel 22 showed first drop peak and pixel 18 last. It is also seen that the two swipes were separated by a few seconds between them. The crossover point of these two swipes happened at pixel 20 as it had two drop-peaks in separate swipes.

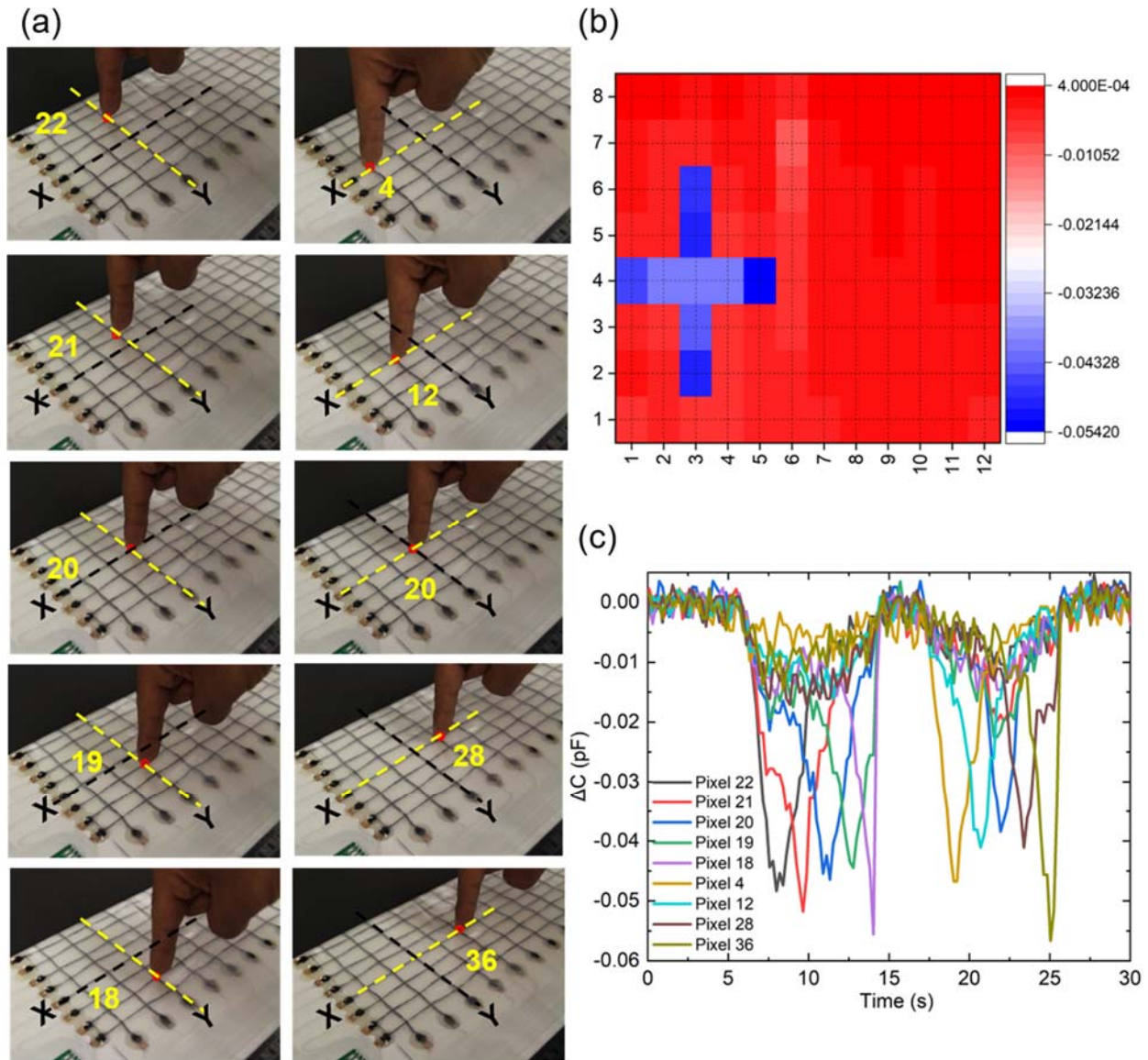


Figure 92: Touchless addition sign gesture using index finger. (a) Vertical and horizontal swipe motions on column 3 and row 4 respectively with images of index finger at every pixel of interest in that region. (b) Addition sign gesture represented in the form of heatmap. (c) Drop in capacitance of pixels of interest during vertical and horizontal swipes with time.

In real life scenarios, a user could hover over the sensor array in not only along the row or column directions but also diagonally. One of the gestures, which captures this effect, is the checkmark motion. The motion as well as the corresponding signal recorded from the sensor array is presented in Figure 93. In this instance, the checkmark sign using the index finger (Figure 93a),

influenced eight pixels. The diagonal movement caused capacitance drop in different pixels spanning across multiple rows and columns. The results showed that pixels 6, 12, 18 formed the left hand part of the checkmark sign and pixels 27, 36, 45, 54, 63 created the longer right hand part.

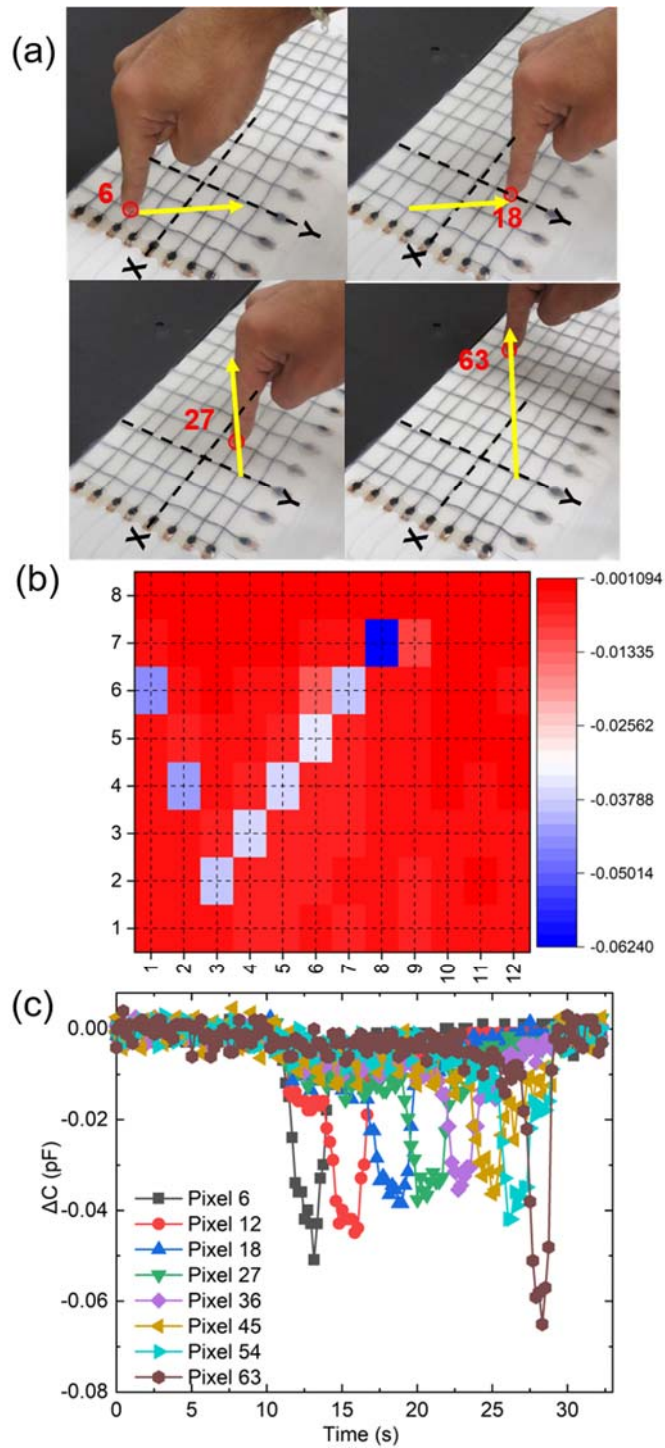


Figure 93: Touchless check mark sign gesture using index finger. (a) Images of the index finger at different pixels across columns creating a check mark sign. (b) Check mark sign gesture represented in the form of heatmap. (c) Drop in capacitance of pixels of interest during creating a check mark sign with time.

The gestures demonstrated thus far could be interpreted as binary commands (on & off) or the more complicated ones (dial phone), etc. But if the sensor interface can decipher simple common words which might then be translated to voice commands then it can be a very useful wearable sensor interface to differently abled subjects. With this motivation, touchless writing of a simple greeting message such as 'HI' was attempted (see Figure 94a). Firstly, the word H was written and then I. For writing 'H', two vertical swipes were separated by one column to create the horizontal bridge of letter H and then a vertical swipe was used to represent the letter 'I.' Pixels 6 to 2 on 1<sup>st</sup> column represent left bar of letter H, pixels 4 to 20 represent middle bridge of letter H (top right), pixels 22 to 18 (column 3) represent right bar of letter H (bottom left) and pixel 38 to 34 (column 5) represents letter I (bottom right). The capacitive response of these pixels represented on a heatmap displays the word HI (Figure 94b). Careful tracking of capacitance values of pixels in the order of hovering described above and in the images, shows four clusters of peaks corresponding to various parts of letter H and I with multiple peaks of certain pixels indicating they were hovered over more than once while creating that gesture (Figure 94c). It can be observed that the  $\Delta C$  vs time graph becomes increasingly complex to decipher in terms of the fact that which pixel responded first or which gesture was performed first. More sophisticated data analysis techniques will be required for complex gestures but heatmaps provide sufficient information about the gesture.

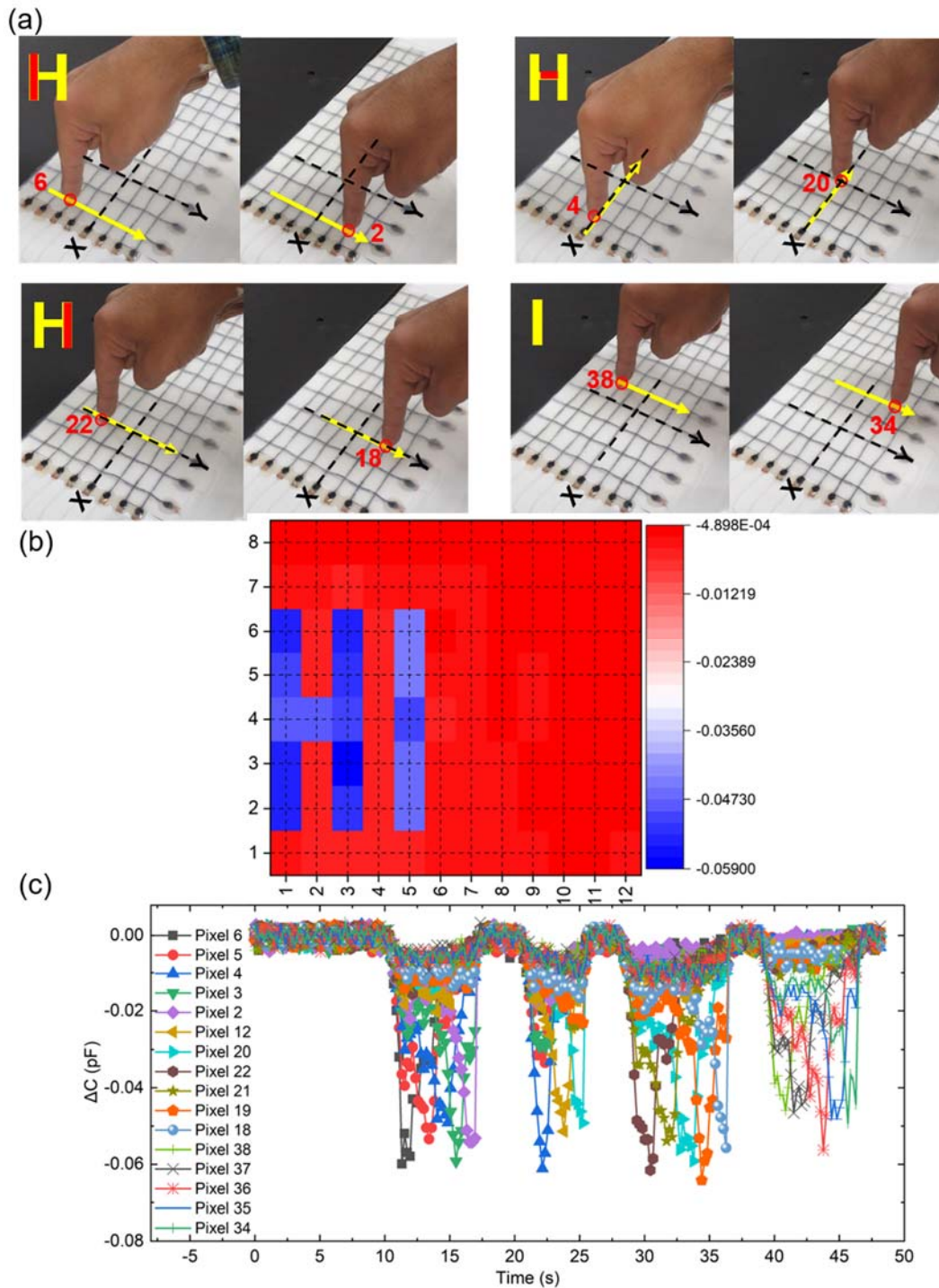


Figure 94: Touchless writing of word HI using index finger. (a) Images of the index finger at different pixels during creating a pattern of the word HI where hovering from pixel 14 to 10 represents left bar of letter H (top left), hovering from pixel 12 to 28 represents middle bridge of letter H (top right), hovering from pixel 30 to 26 represents right bar of letter H (bottom left) and hovering from pixel 38 to 34 represents letter I (bottom right). (b) Word HI represented in the form of a heatmap. (c) Drop in capacitance of pixels of interest during writing word HI with time.

### **6.3 Conclusion**

In summary, a large area fiber-based woven capacitive sensor array with 96 sensing pixels was fabricated through simple fabrication processes including benchtop extrusion and hand weaving. Benchtop characterization experiments were conducted to evaluate the contactless sensing capabilities of the sensor array for proximity detection of conducting objects. Further, gesture sensing capabilities ranging from multifinger static gestures to dynamic gestures using finger including contactless swipe to contactless writing were demonstrated. This study provides a promising route toward emerging electronic textile based contactless gesture interfaces as remote controllers or assistive communication devices.

## 6.4 Supplementary information

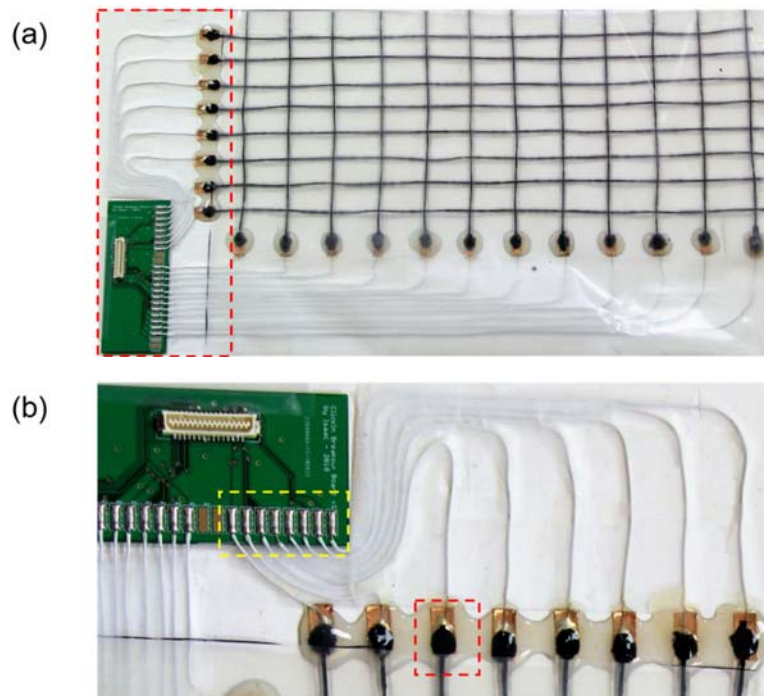


Figure 95: (a) Image of 96 channel sensor array showing 8 rows and 12 columns connected to breakout board. (b) Electrical connection of fiber to copper tape with CPC paste (black) encapsulated by silicone.

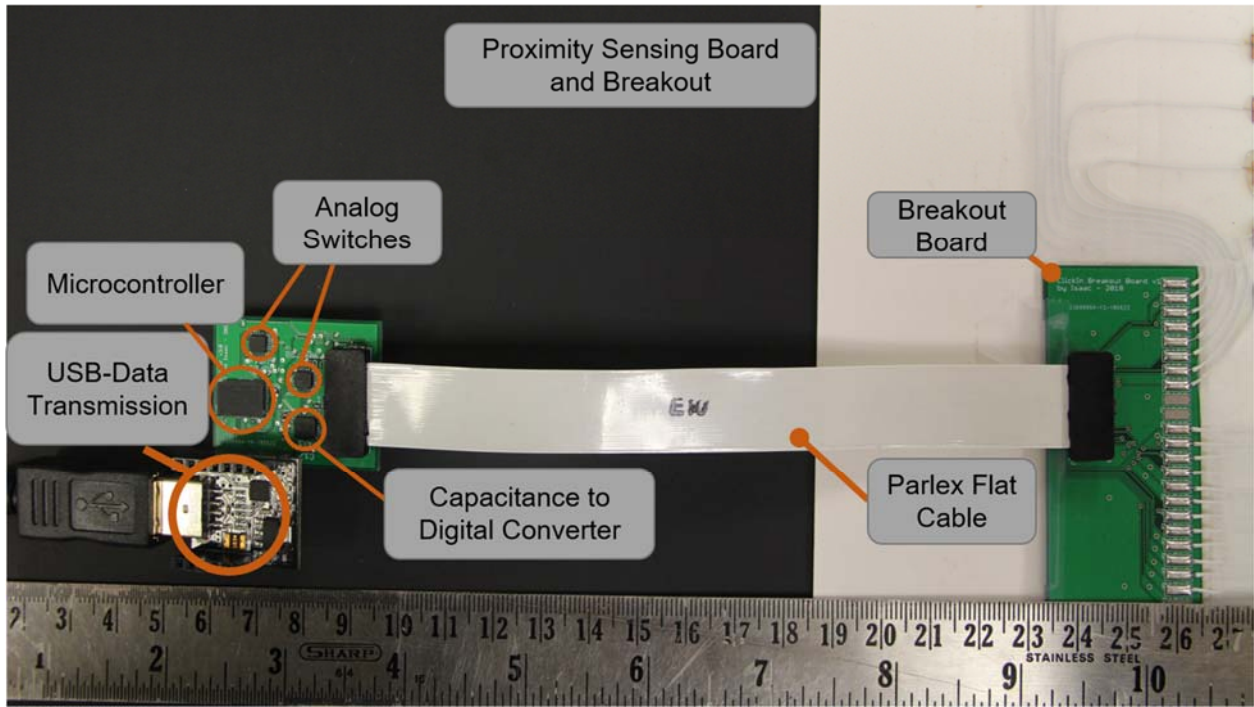


Figure 96: Different parts of data collection system to record capacitance from 96 channels.

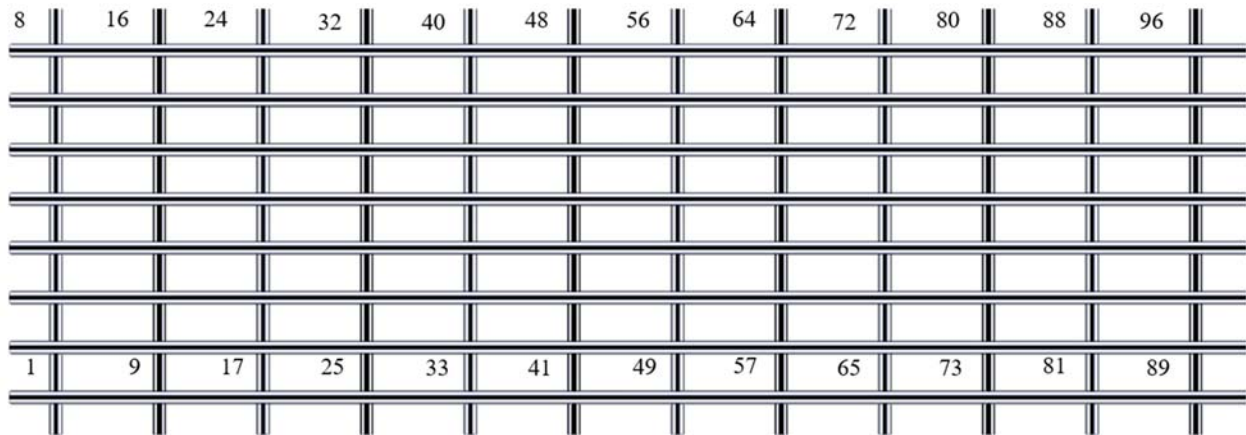


Figure 97: Schematic of the 96 (8 rows x 12 columns) sensor proximity sensing array with each pixel assigned a particular number for data analysis during gesture decoding.

## References

- [1] M. Orth, J. R. Smith, E. R. Post, J. A. Strickon, and E. B. Cooper, "Musical jacket," in *ACM SIGGRAPH 98 Electronic art and animation catalog*, Orlando, Florida, USA, 1998, p. 38, doi: 10.1145/281388.281456.
- [2] "Firefly Dress." [http://www.maggiorth.com/art\\_Jacket.html](http://www.maggiorth.com/art_Jacket.html) (accessed Feb. 24, 2020).
- [3] S. Takamatsu, T. Kobayashi, N. Shibayama, K. Miyake, and T. Itoh, "Fabric pressure sensor array fabricated with die-coating and weaving techniques," *Sens. Actuators Phys.*, vol. 184, pp. 57–63, Sep. 2012, doi: 10.1016/j.sna.2012.06.031.
- [4] O. Atalay, A. Atalay, J. Gafford, and C. Walsh, "A Highly Sensitive Capacitive-Based Soft Pressure Sensor Based on a Conductive Fabric and a Microporous Dielectric Layer," *Adv. Mater. Technol.*, vol. 3, no. 1, p. 1700237, 2018, doi: 10.1002/admt.201700237.
- [5] J. Lee *et al.*, "Conductive Fiber-Based Ultrasensitive Textile Pressure Sensor for Wearable Electronics," *Adv. Mater.*, vol. 27, no. 15, pp. 2433–2439, 2015.
- [6] X. You *et al.*, "Stretchable capacitive fabric electronic skin woven by electrospun nanofiber coated yarns for detecting tactile and multimodal mechanical stimuli," *J. Mater. Chem. C*, vol. 6, no. 47, pp. 12981–12991, 2018, doi: 10.1039/C8TC03631D.
- [7] M. Kang, J. Kim, B. Jang, Y. Chae, J.-H. Kim, and J.-H. Ahn, "Graphene-Based Three-Dimensional Capacitive Touch Sensor for Wearable Electronics," *ACS Nano*, Jul. 2017, doi: 10.1021/acsnano.7b02474.
- [8] Y. Hu *et al.*, "12.2 3D gesture-sensing system for interactive displays based on extended-range capacitive sensing," in *2014 IEEE International Solid-State Circuits Conference Digest of Technical Papers (ISSCC)*, 2014, pp. 212–213, doi: 10.1109/ISSCC.2014.6757404.

- [9] B. Zhang *et al.*, “Dual functional transparent film for proximity and pressure sensing,” *Nano Res.*, vol. 7, no. 10, pp. 1488–1496, Oct. 2014, doi: 10.1007/s12274-014-0510-3.
- [10] Q. Hua *et al.*, “Skin-inspired highly stretchable and conformable matrix networks for multifunctional sensing,” *Nat. Commun.*, vol. 9, no. 1, p. 244, Jan. 2018, doi: 10.1038/s41467-017-02685-9.
- [11] X. Zhao, Q. Hua, R. Yu, Y. Zhang, and C. Pan, “Flexible, Stretchable and Wearable Multifunctional Sensor Array as Artificial Electronic Skin for Static and Dynamic Strain Mapping,” *Adv. Electron. Mater.*, vol. 1, no. 7, p. 1500142, 2015, doi: 10.1002/aelm.201500142.
- [12] H.-K. Lee, S.-I. Chang, and E. Yoon, “Dual-Mode Capacitive Proximity Sensor for Robot Application: Implementation of Tactile and Proximity Sensing Capability on a Single Polymer Platform Using Shared Electrodes,” *IEEE Sens. J.*, vol. 9, no. 12, pp. 1748–1755, Dec. 2009, doi: 10.1109/JSEN.2009.2030660.
- [13] S. Walia, I. Mondal, and G. U. Kulkarni, “Patterned Cu-Mesh-Based Transparent and Wearable Touch Panel for Tactile, Proximity, Pressure, and Temperature Sensing,” *ACS Appl. Electron. Mater.*, vol. 1, no. 8, pp. 1597–1604, Aug. 2019, doi: 10.1021/acsaelm.9b00330.
- [14] S. Yao and Y. Zhu, “Wearable multifunctional sensors using printed stretchable conductors made of silver nanowires,” *Nanoscale*, vol. 6, no. 4, pp. 2345–2352, 2014, doi: 10.1039/C3NR05496A.
- [15] Zhenhai Chen and R. C. Luo, “Design and implementation of capacitive proximity sensor using microelectromechanical systems technology,” *IEEE Trans. Ind. Electron.*, vol. 45, no. 6, pp. 886–894, Dec. 1998, doi: 10.1109/41.735332.

- [16] I. Poupyrev, N.-W. Gong, S. Fukuhara, M. E. Karagozler, C. Schwesig, and K. E. Robinson, “Project Jacquard: Interactive Digital Textiles at Scale,” in *Proceedings of the 2016 CHI Conference on Human Factors in Computing Systems*, New York, NY, USA, 2016, pp. 4216–4227, doi: 10.1145/2858036.2858176.
- [17] C. Holz and P. Baudisch, “Understanding touch,” in *Proceedings of the SIGCHI Conference on Human Factors in Computing Systems*, Vancouver, BC, Canada, 2011, pp. 2501–2510, doi: 10.1145/1978942.1979308.
- [18] J. T. Muth *et al.*, “Embedded 3D Printing of Strain Sensors within Highly Stretchable Elastomers,” *Adv. Mater.*, vol. 26, no. 36, pp. 6307–6312, Sep. 2014, doi: 10.1002/adma.201400334.
- [19] M. Amjadi, A. Pichitpajongkit, S. Lee, S. Ryu, and I. Park, “Highly stretchable and sensitive strain sensor based on silver nanowire–elastomer nanocomposite,” *ACS Nano*, vol. 8, no. 5, pp. 5154–5163, 2014.
- [20] L. Haslinger, S. Wasserthal, and B. G. Zagar, “P3.1 - A capacitive measurement system for gesture recognition,” *Proc. Sens. 2017*, pp. 616–620, May 2017, doi: <http://dx.doi.org/10.5162/sensor2017/P3.1>.
- [21] Y. Ye, C. He, B. Liao, and G. Qian, “Capacitive Proximity Sensor Array With a Simple High Sensitivity Capacitance Measuring Circuit for Human–Computer Interaction,” *IEEE Sens. J.*, vol. 18, no. 14, pp. 5906–5914, Jul. 2018, doi: 10.1109/JSEN.2018.2840093.

## CHAPTER 7: Summary and Future work

In this research, a dumbbell shaped bicomponent fiber was fabricated consisting of insulating and conducting components. The individual fiber acts as a resistive sensor and woven assembly of the fibers forms a capacitive sensor at each cross-over point in the fabric leading to more than one sensing functionality along with multimodality. This approach allows us to harness inherent orthogonal interlacement of fibers/yarns in a woven textile structure. In this work, silicone elastomer was used as the base fiber forming material and carbon black-silicone polymer composite as conductive material to fabricate the fibers. The bicomponent fibers were fabricated using custom developed extrusion based benchtop techniques namely (a) extrusion printing and (b) coextrusion. In extrusion printing, insulating segments were printed first followed by conducting segment whereas in coextrusion process an extrusion channel was used to shape the polymeric fluids to the desired dumbbell cross-section. Coextrusion process produced longer fiber lengths with higher production rate. Capacitance and resistance were the primary electrical measurements conducted to characterize the sensing response of fibers. These fiber based sensors were used as capacitive sensors to monitor tactile forces, impedance sensors to detect wetness/moisture and as dry electrodes to monitor biopotentials like ECG (heart rate). A real world application in biomedical field for inner prosthetic environment monitoring of transtibial amputees using these woven fiber based sensor arrays was demonstrated. The sensor arrays were tested in three phases namely, artificial limb testing, able bodied testing, and amputee testing. These tests showed that fiber based sensors integrated within prosthetic environment can successfully track weight shifts as well as walking. This research provides a proof of concept of implementation of fiber-based sensors for inner prosthetic environment monitoring for the first time. Lastly, a large area sensor array was created and used for contactless sensing of gestures based on capacitive

sensing. Gesture sensing capabilities ranging from multifinger static gestures to dynamic gestures including contactless swipe were demonstrated. This particular study provides a promising route toward emerging e-textile based contactless gesture interfaces as remote controllers or assistive communication devices.

This interdisciplinary research covered multiple areas including preparation of conductive materials, conductive fiber production, electrical interconnect fabrication for connecting conductive fibers to data collection system, sensor response characterization and the application of these sensors in biomedical field with potential application as human-machine interface. Based on these research works, multiple future research directions were identified which are listed below:

*(a) Different fiber cross sections with different fiber forming materials*

This research only focused on one specific dumbbell shaped fiber cross-section and demonstrated its multifunctional sensing capabilities. So far this is the first ever use of a dumbbell fiber design for sensing applications. Results of this work will be very helpful for understanding and designing sensory fibers with other cross-sections such as core-sheath (see Figure 98). Carbon black was the only conductive filler used to prepare the conducting polymer composite forming the middle conducting segment of dumbbell fibers so other conducting fillers like carbon nanotubes, silver flakes can be used based on required properties. Use of transparent conducting materials particularly, will eliminate the requirement of heat for conductive material curing and the whole fiber can be cured using UV light, enhancing the process efficiency and improving chances of success in producing unique multicomponent fibers. Innovative designs like sandwich structures could be created with a dielectric material separating conductive electrodes preventing electrical shorting under high forces, making it useful for applications like footsteps detection (see Figure 99) for security and surveillance applications.



Figure 98: Core-sheath fiber design. Image shows a hollow silicone tube filled with carbon-black silicone composite.

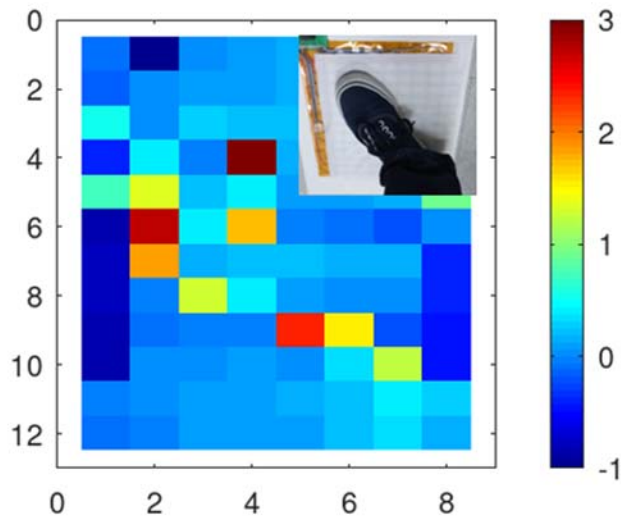


Figure 99: Capacitance increase of pixels of sensor array due to force exerted by left of the subject upon stepping plotted as heatmap

*(b) Polymer flow modeling within extrusion device*

The choice of flow path lengths, die orifice dimensions, no-wall zone lengths within extrusion device along with flow rates was based on experimental observations. Flow modeling of fiber forming materials within extrusion device using COMSOL Multiphysics simulations (see

Figure 100) can help in predicting flow behaviors, understanding influence of viscosity and fluid velocities on final fiber shape and reduce the number of experiments required to optimize the extrusion process parameters to produce the desired fiber cross-section.

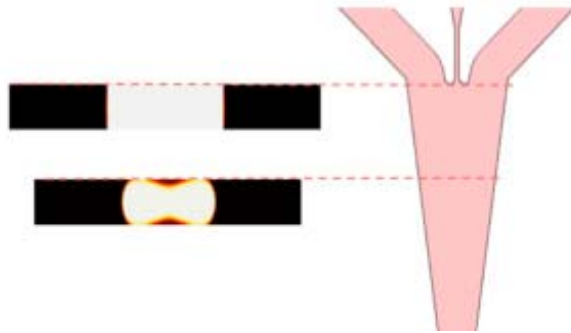


Figure 100: Fluid flow simulation using COMSOL multiphysics. [Adapted from Sharifi, Farrokh, Diamant Kurteshi, and Nastaran Hashemi. "Designing highly structured polycaprolactone fibers using microfluidics." *journal of the mechanical behavior of biomedical materials* 61 (2016): 530-540.]

*(c) Hoop and longitudinal strain sensing*

The sensing fibers produced in this work were evaluated for their sensing response to tensile, compressive and shear forces. Fiber shaped sensors can also be used for hoop and longitudinal strain sensing on the surface of inflated cylindrical structures with known internal pressure (see Figure 101). The piezoresistive response of individual fibers will be recorded for longitudinal and hoop strain sensing along with the capacitive signal at crossover point of fibers. Such complex deformation sensing fibers could be useful for monitoring soft inflatable actuators deployed in various environments.

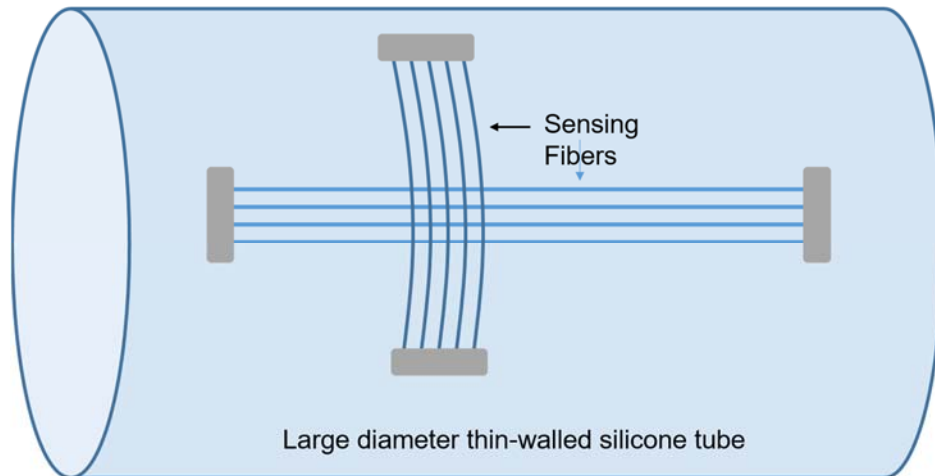


Figure 101: Sensing fiber placement on silicone tubing for hoop and longitudinal stress sensing

*(d) Electromyography (EMG) signal recording*

One of the multiple sensing functionalities of these fibers was biopotential measurement where the conducting segment of the fibers was used as a dry electrode to record electrical activity of heart in form of an ECG signal. As preliminary experiment, the conducting polymer composite film of fibers was used to record the EMG signal of gastrocnemius muscle of the subject. Two custom polymeric dry electrodes along with commercial bipolar electrodes (Ambu Neuroline 715) were placed on the right leg of the subject and the Maximum Voluntary Contraction (MVC) of the gastrocnemius muscle of the leg was measured by asking the subject to rise on the toes through the full available range of ankle plantar flexion, keeping the knee extended. Results showed that these dry polymeric electrodes were able to capture the EMG signal but had a lower signal-to-noise (S/N) ratio compared to commercial electrodes (see Figure 102) due to lack of complete skin contact. Further research using this conductive polymer composite material in form of fibers and as coating on prosthetic liners can open new avenues for monitoring EMG along with other parameters within prosthetic environment.

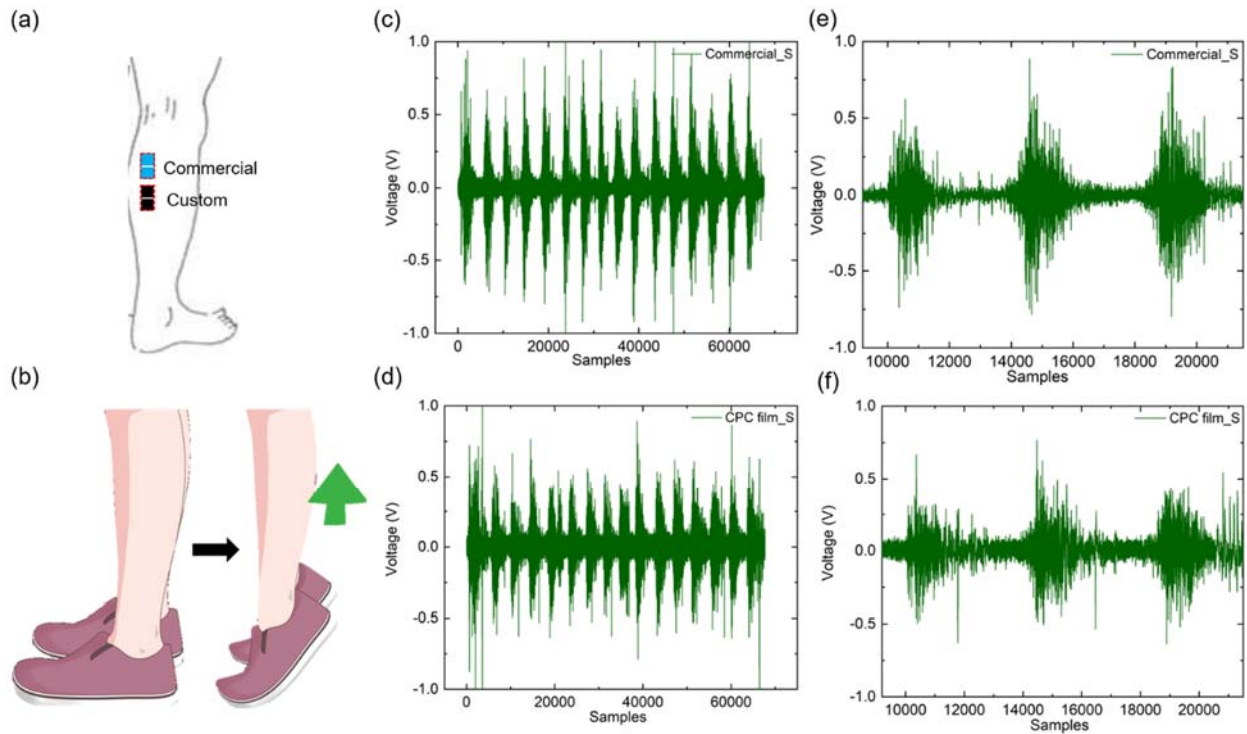


Figure 102: (a) Placement of electrodes on right gastrocnemius muscle. (b) Maximum Voluntary Contraction (MVC) of the gastrocnemius muscle of the leg by rising on toes. (c) Voltage response of commercial sensor during multiple cycles of rising on toes and relaxing. (d) Voltage response of custom developed (CPC-conductive polymer composite) sensor during multiple cycles of rising on toes and relaxing. (e) Zoomed in 3 cycles of commercial sensor. (f) Zoomed in 3 cycles of CPC sensor indicative of S/N ratio.

*(e) Woven fiber based sensors for Diabetic Ulcer Prevention*

Woven arrays of capacitive fibers in the form of socks or shoe insoles can be used for monitoring pressure levels during walking in patients who have decreased sensation in their feet to prevent diabetic foot ulcers. The sensor information collected over time could be used to notify patient for repositioning or modifying their walking behavior to avoid damage to their feet.

*(f) Fibers as actuators*

The conductive polymer composite consisting of polydimethylsiloxane (PDMS) and carbon black upon exposure to UV light displayed actuation due to conversion of UV light into thermal energy

by carbon black particles, causing thermal expansion in the composite (see Figure 103). Therefore, these fibers can also be used as actuators.

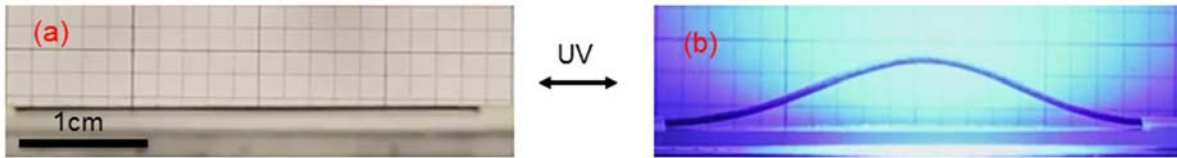


Figure 103: Light actuation of conductive polymer composite film. (a) Initial flat configuration of film taped at both ends, and (b) Buckling response of both sides taped film when illuminated by UV light